Advanced Instability Methods using Spectral/*hp* Discretisations and their Applications to Complex Geometries

by

Gabriele Rocco

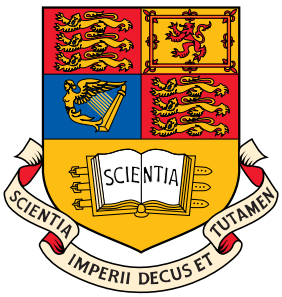

Department of Aeronautics
Imperial College London

This thesis is submitted for the degree of Doctor of Philosophy of Imperial College London

2014

"*Omnes discere cupiunt artem oratoriam, sed nemo magistris vel rhetoribus debitam dignamque laboris molestissimi mercedem vult solvere.*"

Decimus Iunius Iuvenalis,
SatiræXVI.

Declaration

This is to certify that the work presented in this thesis has been carried out at Imperial College London, and has not been previously submitted to any other university or technical institution for a degree or award. The thesis comprises only my original work, except where due acknowledgement is made in the text.

The copyright of this thesis rests with the author and is made available under a Creative Commons Attribution Non Commercial No Derivatives licence. Researchers are free to copy, distribute or transmit the thesis on the condition that they attribute it, that they do not use it for commercial purposes and that they do not alter, transform or build upon it. For any reuse or redistribution, researchers must make clear to others the licence terms of this work.

Gabriele Rocco

Acknowledgements

This thesis marks the end of my journey towards the PhD. As the old chestnut goes: "life is what happens in between", and, first and foremost, I am indebted to life for this literally transforming experience. Every twist and turn, every achievement and, above all, every disappointment helped to scratch all my granitic beliefs and widen my horizons, not just from a scientific point of view. Too many people are worth mentioning, but the first acknowledgement cannot be anyone else but my supervisor, Prof. Spencer Sherwin, who gave me this opportunity and made this thesis possible with his scrupulous help and commitment. I would also like to thank Dr. Tamer Zaki for his constant helpfulness and assistance and Prof. Hugh Blackburn for all the stimulating discussions and the stunning hospitality in the sun-kissed Australia. A thanks goes to the Imperial Italian gang: Alessandro in particular, to my former and present colleagues (and friends), Chris, Dave, Andrew, David and Julien. Thank you guys, it would not have been the same without all of you. I cannot forget all my friends, who helped to keep my sanity during the extenuating research days, in U.K., in Italy (Luca and Paola deserve a special mention) and in U.S. At this point two people $1,000$ miles away are probably complaining about not having being mentioned so far. Well, I am saving the best for last. I really could not have made it without your unconditional love and support. You are the invisible presence who sustained me at every step of the journey, you are the most powerful constants behind all my equations. Therefore, words are not eloquent enough to describe my deep gratitude towards you. All I can say is a simple "*vi voglio bene*".

Abstract

Controlling wakes of flows past bluff bodies is a fundamental problem in a wide range of engineering applications. In the present work, we investigate such problems theoretically and numerically using linear stability analysis. We initially consider a flow past a cylinder in a fully developed vortex shedding regime, and we apply sufficiently high spanwise forcing on the surface of the cylinder to stabilise the near-wake. The effects on the aerodynamic forces, the wake topology and the dynamics of the vorticity are investigated using spanwise sinusoidal and Gaussian forcing. Stability analysis of the linearised Navier-Stokes equations is then performed on the fully three-dimensional flow to investigate the role of the spanwise modulation on the absolute instability associated with the von-Kármán street. The three-dimensional global modes allows us to detect the regions where the instability acts, and the interactions of the perturbations with the base flow shed light on the most relevant mechanism for the wake stabilisation. Additional relevant information on the design of an efficient control device are provided by receptivity analysis and the structural sensitivities.
A similar approach is used to study the stability of a flow through a compressor passage at a $Re = 138,500$. Due to the complexity of both the geometry and dynamics of the flow, a phase-averaging technique is used to generate a globally periodic basic flow, extracting only the organised structures and neglecting all the background unsteadiness. This approach allows us to perform Floquet and transient growth analyses to detect the structure of the global modes and the presence of convective instabilities.

A voi tre.

Contents

List of Figures

List of Tables

Chapter 1

Introduction

> *"Begin at the beginning," the King said, gravely, "and go on till you come to an end; then stop.*
>
> Lewis Carroll, *Alice in Wonderland*

In the last decade there has been a surge of interest to reduce the fuel consumption and the CO_2 emissions produced by the civil aviation and road transport, which are responsible of about 30% of all global emissions. Recent estimations forecast an increase of the fuel consumption in the aviation of about 160% by 2030, with consequent CO_2 emissions rising to 1250 million tonnes (Leschziner *et al.* 2011, Horton 2006, Peters *et al.* 2005). A drag reduction of 1% on an aircraft in cruise conditions generates a decrease of 0.75% in the fuel consumption, leading to a potential reduction of the pollutant emissions of about nine million tonnes per 1% of drag reduction. Currently, the skin friction constitutes about 60% of the total drag (Goldhammer 2009), therefore it remains the main area of investigation to improve the design of aircraft.

Driven by the necessity to maximise the drag reduction, several innovative techniques have been developed in laboratories, but most of them are not suitable for practical applications, which require efficient and reliable operating conditions over a wide range of parameters. Several engineering constraints generally inhibit the exploitation of advanced concepts and techniques in control, hence most aeronautical industries still rely on simple passive devices, generally riblets and vortex generators, while the only active control technique of industrial interest is open-loop suction (Spalart & McLean 2011, Boeing Commercial Airplanes). However, the EU has ap-

proved a highly demanding plan to reduce the CO_2 emission by 50% by 2020 with respect to 2000, forcing both the academic and industrial community to investigate new control methods.
Currently one of the biggest difficulties in the adoption of novel control techniques in industrial applications is that it is necessary to modify the flows efficiently and quickly, making the aerodynamic design an intricate problem. Following Leschziner *et al.* 2011, at present the research of control strategies for drag reduction can be classified in three main categories:

1. the delay of transition, which can be achieved by passive techniques such as roughness elements, or closed-loop control methods, where sensors detect the instabilities and apply appropriate countermeasures.

2. reduction of the near-wall turbulence using oscillations or travelling-wave motions induced by wall movement and plasma actuators.

3. suppression of separation and control of vortex shedding from semi-infinite walls and airfoils by means of open and closed-loop control techniques.

As will be discussed more in detail in the following sections and chapters, in this thesis we investigate techniques described in the last point. Specifically, we will not take into considerations feedback techniques, but we will focus only on passive and open-loop control methods, which are still preferred because of their simple implementation and cost-effectiveness. Together with the adoption of an efficient control technique, gaining a thorough understanding of the underlying physical phenomena is essential. However, even at this formative stage, it is important to specify that an exhaustive knowledge of the involved flow physics is still not available, despite the remarkable advancement garnered in the last few years. In particular, noteworthy strides have been achieved thanks to the potential of computational fluid dynamics (CFD), which has been able to shed light on many unanswered questions arising from conflicting results in different experimental techniques. In this context, spectral/*hp* element methods offer a promising computational technique to solve complex problems since they combine the geometrical flexibility of finite element methods with the superior accuracy and convergence properties of spectral approaches. Therefore, such numerical methods can be extremely helpful in investigating the dynamics of several mechanisms exploited by actuators and might represent a good *trait d'union* between the flow physics and control theories. Besides this, the fast-paced evolution of computer hardware and the development of new efficient

algorithms to solve partial differential equations provide the possibility to perform accurate DNS of industrial flows. This can lead to a new approach in the control design, which combines simultaneously the physical insight into the flow with new control theories. Therefore, in the present work, the discussion of the design of a suitable control device is intrinsically related to the evaluation of the physical phenomena, overtaking previous approaches which considered fluid dynamics and control theory separately. As we will see, some the control methodologies explicitly exploit certain linear mechanisms typical of transitional flows, and their successful adoption in several applications suggests the importance of such mechanisms to understand the dynamics of non-linear flows.

1.1 Stability theory: harbinger of the flow transition

The main theoretical framework behind flow transition is known as hydrodynamic stability theory. A solid understanding of such theory, even in its simplest formulation, provides important insights into the mechanisms behind some of the successful control methodologies. An explanatory example is the simple control technique based on the introduction of a small cylinder in the wake of a bluff body, which was found to reduce, or even suppress, the vortex shedding in a specific range of Reynolds numbers. Strykowski & Sreenivasan (1990) studied experimentally and numerically the best placement of the secondary cylinder, but the same results can be achieved if we think that the effect of the control cylinder is to weaken or eliminate the absolute instability in the near-wake region. These concepts will be explained more in detail in chapter 4, but should give the reader a hint about the essential interconnection between control theory and fluid dynamics.
Despite practical applications of the hydrodynamic stability being quite recent, the concept of stability of a state of a physical or mathematical system dates back to the eighteenth century and is explained clearly by Maxwell (Drazin & Reid, 1981):

> *"When...an infinitely small variation of the present state will alter by an infinitely small quantity the state at future time, the condition of the system, whether at rest or in motion, is said to be stable; but when an infinitely small variation in the present state may bring about a finite difference in the state of the system in a finite time, the condition of the system is said to be unstable"*

This definition is very general and does not have a direct link to fluid dynamics, highlighting that the study of the stability of a fluid state is not dissimilar to analogous studies in other fields, such as magnetohydrodynamics, plasma physics, elasticity, rheology, combustion or general relativity. The main formulation of hydrodynamic stability is due to Helmholtz, Kelvin, Rayleigh and, above all, Reynolds. In 1883 Osborne Reynolds performed several experiments on the dynamics of a flow in a pipe[1].

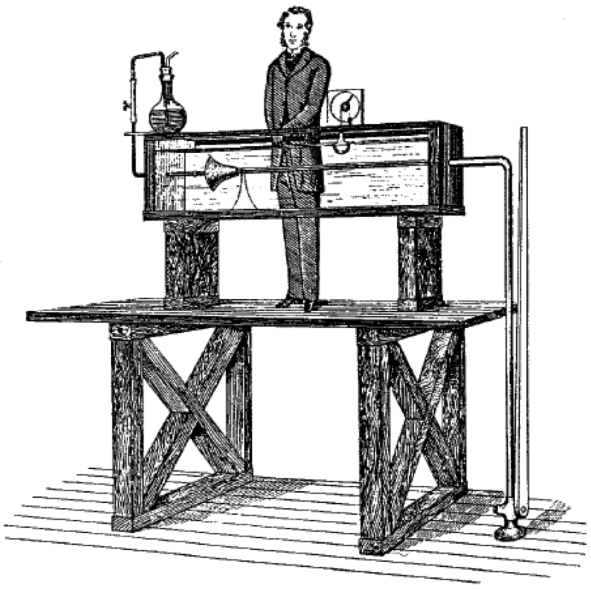

Figure 1.1: Configuration of Reynolds's experiment. Adapted from Drazin & Reid 1981

Reynolds showed that the smooth flow, typical at sufficiently low velocities, tends to break down when a specific parameter, UD/ν, exceeds a critical value[2], with the subsequent appearance of *flashes* at specific points in the pipe. This experiment is the precursor of our modern classification of laminar and turbulent flows and the parameter UD/ν is now called *Reynolds number*. Moreover, Reynolds noticed that:

[1]The experimental apparatus still survives in Manchester and was used in 1970 to repeat Reynolds's experiments.

[2]D is the diameter of the pipe, U the maximum velocity of the water in the pipe and ν the kinematic viscosity

> *"the critical velocity was very sensitive to disturbance in the water before entering the tubes...*
> *This at once suggested that the condition might be one of instability for disturbance of a certain magnitude and [stability] for smaller disturbances."*

Reynolds introduced the central problem of hydrodynamic stability: to understand whether a given laminar flow is unstable when it is perturbed by a disturbance and if so, how it breaks down into a turbulent or some other laminar flow. Methods to study the stability of dynamical systems were known at Reynolds's time and were widely applied to systems of particles and rigid bodies. These methods consist in linearising Newton's or Lagrange's equations around the steady state of the system and decomposing the perturbations into independent modes of the form $e^{\lambda t}$, where λ is a complex number. It is the evaluation of the real part of λ which provides information about the stability of the system, since if it is positive the system is unstable because an arbitrary small perturbation would grow exponentially. Stokes, Kelvin and Rayleigh extended this method to fluid mechanics, overcoming the remarkable difficulties related to the presence of partial differential equations rather than ordinary differential equations.
A comprehensive discussion of hydrodynamic stability analysis is beyond the scope of this thesis and interested readers may refer to Drazin & Reid (1981) and Schmid & Henningson (2001). However, in order to provide a general overview of such a complex field, it is useful to mention the four different approaches:

1. Linear stability theory: this represents the foundation of the theory and is the oldest and still most used approach. It consists of linearising the Navier-Stokes equations around a given base flow and then evaluating the temporal evolution of arbitrary small perturbations of the basic state.

2. Weakly non-linear theory: this is an extension of linear stability theory and takes into account the presence of the non-linear effects, which become gradually more relevant as the amplitude of the perturbations grows. Assuming a wavelike behaviour for the disturbances, the evolution of each Fourier component is not independent from the others, but they are all coupled together through wave-triad interactions. In weakly non-linear theory, the amplitude of the perturbations is assumed to be *weakly* time-dependent, therefore it varies at a much

longer time scale than the wavelike part of the disturbance. Relevant investigations on the role of the non-linearities were performed by means of the non-linear parabolised stability equations. In this context Haynes & Reed (1996) studied the development of stationary crossflow vortices over a 45-degree swept NFL(2)-0415 airfoil and showed that the adoption of non-linear parabolised stability equations overcome the differences between experimental results and the linear stability theory.

3. Theory of bifurcation and chaos: this evaluates the bifurcations of a dynamical system from one regime to another when a certain parameter is increased (i.e. the Reynolds number for fluids). It generally requires relevant numerical calculations, but the most common routes to chaos can be detected via the qualitative mathematical theory.

4. Strongly non-linear theory: this is the most rigorous theory and it assumes arbitrarily large perturbations. It is based on Serrin's theorem and Liapunov's direct method, but it is of difficult applicability, providing generally bound conditions for the stability of flows.

In this project we will only consider linear stability theory, since all the other approaches are still not mature to be applied to complex flows. Although we will only focus on the simplest level of hydrodynamic stability theory, a further discussion is required within the linear approximation. The first approach is to consider the base flow as a function of just one coordinate, e.g. y, $\boldsymbol{U} = U(y)$, and then analyse the stability of such profile. This simplification is usually valid for several simple flows and it known as local stability analysis. In the context of local stability, we can distinguish between two different types of instabilities: absolute and convective respectively. If an arbitrary small perturbation, localised in space, grows at that fixed spatial location, the flow is absolutely unstable, whereas if it propagates as it grows, decaying at any fixed point in space, then the instability is said to be convective (Huerre & Monkewitz 1995). An illustration of these two possibilities is shown in figure (1.2).
However, the strong assumption of one-dimensional base flow is not valid for more complex problems. Thus, the base flow often needs to be resolved in two or three-dimensions, $\boldsymbol{U}(x, y, z, t)$, and the stability analysis is performed with respect to two or three-dimensional perturbations $\boldsymbol{u}' = \boldsymbol{u}'(x, y, z, t)$, which are assumed to have the modal form $\boldsymbol{u}' = \hat{\boldsymbol{u}}'(x, y, z) \exp(\lambda t)$. This approach is called global stability analysis and has been extremely effective in determining the global instabilities in many complex flows, both

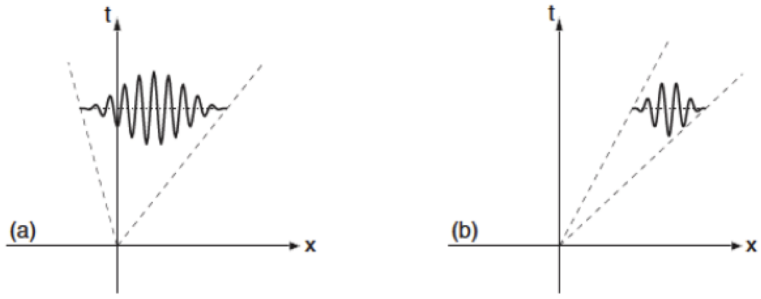

Figure 1.2: Sketch on the dynamics of the absolute (a) and convective (b) instabilities. Adapted from (Huerre & Monkewitz 1995)

open and closed (Barkley & Henderson 1996, Blackburn 2002a, Sherwin & Blackburn 2005). According to the different structures of the base flows, we can perform a further classification of the possible approaches in global stability analysis (Theofilis (2011)). TriGlobal stability analysis is the most generic methodology and assumes a basic state which is inhomogeneous in all the spatial directions. However, TriGlobal approach is often numerically demanding and unfeasible for most applications, therefore several simplifications are required. The three-dimensional parabolised stability equations (3D-PSE) assume a base flow which shows a slow variations along one spatial direction, leading to an initial value problem to be solved along the slow direction. On the other hand, BiGlobal approach assumes the basic state to be purely two-dimensional and the perturbations are assumed to be periodic in the third direction (§ 4.24). Within the global stability analysis, a distinction between absolute and convective instabilities cannot be made as easily as in the local approach because the convective instabilities do not show a modal behaviour. Therefore, global stability analysis cannot be applied to detect the convective instabilities which arises in problems with inflow and outflow conditions; a large-scale eigenvalue analysis does not detect such behaviour. These instabilities generally result from the linear transient growth of the perturbation energy, which is associated to the non-normality of the eigenmodes. Therefore, an exhaustive study of the global instabilities cannot disregard the non-modal analysis, which shows that transient response due to the presence of local convective instabilities is the energy transient amplification of the infinitesimal perturbations. This leads to an additional investigation, peculiar of the global stability analysis, which is known as transient growth analysis. All these concepts will be discussed more rigorously in chapter 4, but they are useful to contextualise the present project

within the current research on hydrodynamic stability.

1.2 Scope of the research

The maturity of the linear stability theory has led to successful applications to delay the transition in boundary layers flows (Semeraro *et al.*, 2013) and attenuate the vortex shedding of flows past bluff bodies (Giannetti & Luchini 2007, Hwang & Choi 2006). This poses the question of whether linear stability studies can be applied to more complex cases of direct industrial impact. The task is surely challenging and it requires a strong interaction between university-based scientists and engineers in industry, with each group recognising and responding to the priorities and constraints of the others. One of the main difficulties that hinders the adoption of stability analysis for industrial problems is the necessity to deal with very complex problems, both in terms of geometries and flow features. Even the most challenging studies by means of global stability analysis are generally limited to two-dimensional base flows, assuming that the problem has one direction of homogeneity. However, the three-dimensionality of the flows has long been recognised to play a fundamental role in reducing the drag coefficient and weakening the vortex shedding. For example, wavy trailing edges are a common practice in engineering, such as in the design of wings in Formula 1, as shown in figure (1.3). Hence, simplifying assumptions on the two dimensionality of the base flow might be too restrictive for an adequate control design, in particular if the potential of the three-dimensional modifications is taken into consideration.

Therefore, the philosophy that drives the investigations presented in this thesis is the necessity to extend the stability analysis to three-dimensional base flows and apply it to the complex geometries found in common engineering applications. This task is obviously very ambitious and it is clear that providing general conclusions valid in a wide range of applications is difficult. Moreover, the lack of a solid theoretical understanding on the dynamics of fully three-dimensional instabilities, even in simple problems, make such a goal out of reach. However, as a first step, we can deal with these two aspects separately, directing our efforts to gain the broadest insight into the mechanisms leading to the development of three-dimensional instabilities and, at the same time, applying the conventional approaches of the hydrodynamic stability theory to realistic configurations. Although it is the combination of these two aspects that will lead to noteworthy improvements in the aerodynamic design, these studies are useful to acknowledge

Figure 1.3: Photo of the rear wing trailing edge of McLaren Mercedes MP4/22 (courtesy of McLaren Racing).

the possibilities and limitations of each approach.
In the first part of this thesis, we will focus on the characterisation of the instabilities in fully three-dimensional flows (TriGlobal stability, Theofilis 2011). Such three-dimensionality is not an artificial expedient, but a direct consequence of the application of spanwise forcing on the surface of a bluff body; this configuration represents in fact an efficient control technique, which was seen to generate a noteworthy reduction of the fluctuations of the aerodynamic forces and an attenuation of the typical unsteadiness that characterises the vortex shedding (Kim & Choi 2005, Darekar & Sherwin 2001). With the aim of extending the above-mentioned investigations, we consider then the simple case of a flow past a circular cylinder, since its extensively studied dynamics lends itself well to be the starting point of our research. Previous studies (Kim & Choi 2005) detected the optimal intensity of spanwise forcing and the regions where its effects are more relevant. However, reasonable explanations of the obtained results are still scarce, despite few attempts have been recently given by means of the local stability analysis (Hwang *et al.* 2013, Del Guercio *et al.* 2014). Keeping this in mind, we investigate the problem from a global stability perspective and we try to identify how the spanwise modulation, the alteration of the vortex shedding and the change in the dynamics of the instabilities are intrinsically related. Besides this, we pose an important question from a control point of view: is sinusoidal forcing the optimal choice or other functions can lead to a more efficient control of the instabilities? We remark once again that it is the

synergy of the stability analysis and control theory that provides adequate answers to these questions. Ignoring the results provided from the control theory may lead to effective but highly inefficient manners of controlling the wake, while disregarding the stability features of the flow hides to the designer all of the mechanisms which need to be exploited.
If the complexity of the first application presented in this thesis relies on the advanced instability method, while the geometry is intentionally kept simple, in the second part of the thesis we will consider the reverse problem: we will investigate by means of the BiGlobal stability analysis the instabilities arising in a flow through a compressor passage. The adopted geometry comes in fact from the results of previous experimental investigations on a linear low-pressure (LP) compressor cascade (Hilgenfeld & Pfitzner 2004). Starting from the studies of Zaki *et al.* (2009, 2010), we investigate the role of transition and the separation in such configuration, where such effects are enhanced by the strong adverse pressure gradients that the flow experiences, in contrast with the more commonly studied low-pressure (LP) turbines (Wu & Durbin 2001, Wissink & Rodi 2006, Abdessemed *et al.* 2009*b*). Several issues were addressed *en route*, specifically the necessity to extend the conventional Floquet analysis to flows with localised periodicities. Common engineering applications might not show a well-defined periodic behaviour all over the computational domain, but just in a specific region. Therefore, Floquet analysis, which requires a global periodicity of the flow field, cannot be applied. Such problem was solved using the phase-averaging technique, a common methodology used especially in experimental fluid-mechanics. This provides evidence of the fact that the applications of well-established theories to complex problems are often more than mere academic exercises, but can actually lead to extensions or revisions of the conventional approaches.

1.3 Computational effort

All the investigations discussed in the present work were performed computationally; the complexity of the considered cases requires the proper combination of efficient time-integration schemes, spatial discretisation and a high geometric flexibility. Therefore, the adoption of a suitable numerical code was a key factor in the success of the present project. With this in mind, the choice fell on *Nektar++* (Kirby & Sherwin 2006), an open-source software developed at Imperial College London (Department of Aeronautics) in collaboration with the University of Utah (School of Computing). Since *Nektar++* is an ongoing project, not all the required features for the present research were present. Therefore, a relevant computational effort has been

made to implement, validate and debug all the necessary C++ classes and algorithms. More specifically the following tasks have been performed:

- validation and debugging of the incompressible Navier-Stokes solver based on the projection method introduced by Karniadakis *et al.* (1991).
- Implementation,validation and debugging of the additional advection terms (linearised and adjoint) required for the stability analysis.
- Implementation, validation and debugging of the routines of Arnoldi algorithms to solve the stability eigenproblems.
- Efficient extension of the code to solve BiGlobal and TriGlobal stability problems [3]
- Temporal Fourier interpolation of the base flow to perform Floquet stability analysis.
- Development of the necessary post-processing routines to visualise the results and calculate most relevant physical quantities (such as Q-criterion, perturbation energy, sensitivities.)
- Implementation, validation and debuugging of specific routines to compute phase-averages.
- Development of basic classes aimed at extending the code to integrate Navier-Stokes equations in cylindrical coordinates.

1.4 Layout of the thesis

Before concluding this chapter, it is appropriate to provide an overview of the remaining chapters of this thesis.
Chapter 2 discusses the numerical methodologies used in the present studies. Despite the plethora of methods that can be used to solve CFD problems, in the present work the spectral/*hp* element method was chosen.
In first part of chapter 3, we present the mechanisms behind the onset of the vortex shedding and, more generally, the wake transition. Herein the

[3]The implementation of the BiGlobal and TriGlobal stability analysis was performed via a Fourier interpolation in the third direction (§2.3.6). To study complex geometries, it was important to implement these techniques efficiently, minimising the number of planes (two or one for the BiGlobal approach, as described in §4.24) and trying to implement a parallel implementation of the Arnoldi eigensolver.

discussion of the problem is more from a physical point of view, without lingering on the underlying mathematical formulation. In the second part of the chapter the most common techniques to control the flow past bluff bodies are overviewed, discussing their advantages and disadvantages in terms of both implementation and efficiency. Chapter 4 is dedicated to a mathematical introduction to the modal and non-modal hydrodynamic stability theory; particular emphasis is given to the receptivity analyses and their implications on the design of controllers. All the concepts are then applied to a flow past a cylinder, which provides to be an important driving example for the following chapters. Chapter 5 presents the studies on the instabilities arising in a flow subject to spanwise forcing (often referred as surface bleed). At first, we discuss the results from direct numerical simulations to characterise the optimal features of forcing and to understand the physical mechanisms involved. TriGlobal stability analyses are then used to investigate the role of the spanwise modulation on the near-wake instabilities. Energy and receptivity studies are adopted to shed light on the high efficiency of such approach to control vortex shedding and provide useful indications on the design of an appropriate controller. Chapter 6 presents a BiGlobal stability analysis of a flow in a compressor passage. After an introductory discussion on the main physical mechanisms, a phase-average technique is used to generate a "globally periodic" base flow, which allows us to perform Floquet analyses of the periodic orbits and detect the presence of convective instabilities. Finally, the conclusions of our findings and suggestions for further work are presented in chapter 7. In addition, Appendix A contains a description of the Arnoldi methods, which were used in the present thesis to solve the stability eigenproblems.

Chapter 2

The Spectral/*hp* element method

> *It is unworthy of excellent men to lose hours like slaves in the labor of calculation which could be relegated to anyone else if machines were used.*
>
> Gottfried Willhelm von Leibniz, *Machina Arithmetica*

In this chapter, the fundamental concepts behind the spectral/*hp* element method are illustrated. This method was used to discretise the partial differential equations that describe all the physical phenomena investigated in this thesis.

2.1 Introduction to the Navier-Stokes equations

Let us consider an incompressible Newtonian viscous fluid. Its motion is described by the Navier-Stokes equations which, in a Cartesian coordinate system, read:

$$\frac{\partial \boldsymbol{u}^+}{\partial t^+} + (\boldsymbol{u}^+ \cdot \nabla)\boldsymbol{u}^+ = -\frac{1}{\rho}\nabla p^+ + \nu \nabla^2 \boldsymbol{u}^+ \tag{2.1}$$

$$\nabla \cdot \boldsymbol{u}^+ = 0 \tag{2.2}$$

where $\boldsymbol{u}^+ \equiv \boldsymbol{u}(x^+, y^+, z^+, t^+) \equiv (u^+, v^+, w^+)(t^+)$ is the velocity field, t^+ the time, p^+ the pressure, ρ the constant density and ν the kinematic viscosity of

the fluid, which is assumed to be constant. These equations can be rewritten in the following non-dimensional form:

$$\frac{\partial \boldsymbol{u}}{\partial t} + (\boldsymbol{u} \cdot \nabla)\boldsymbol{u} = -\nabla p + \frac{1}{Re}\nabla^2 \boldsymbol{u} \tag{2.3}$$

$$\nabla \cdot \boldsymbol{u} = 0 \tag{2.4}$$

where $x = x^+/L$, $y = y^+/L$, $z = z^+/L$, $t = t^+ u_\infty/L$, $\boldsymbol{u} = (u, v, w)(t) = \boldsymbol{u}^+/u_\infty$, $p = (p^+ - p_\infty)/(\rho u_\infty^2)$ and $Re = u_\infty L/\nu$. Here, L, u_∞ and p_∞ represent the characteristic length, velocity and pressure respectively.
In this thesis, we will consider these equations just in their non-dimensional formulation and they will be solved by means of a quasi 3D-approach. As we will describe in the following sections, this method consists in approximating the flow variables by a Fourier series along the z-direction, such that the three-dimensional equations are then reduced to a set of two-dimensional problems with different wavenumbers. Each set of 2D-equations is then spatially discretised by means of a spectral/*hp* element method (Karniadakis & Sherwin, 2005) and evolved temporally using a velocity-correction scheme (Karniadakis *et al.* 1991).

2.2 Numerical discretisations

Before describing in details the spectral/*hp* element method, we introduce briefly the Finite Element and the Spectral methods; the spectral/*hp* element methods combine the properties of both finite element and spectral methods, making it particularly suitable to solve partial differential equations defined in complex domains, which are typical in a wide range of applications.

2.2.1 Finite Element Method

The first implementation of the finite element method originated in the field of structural engineering and it is based on the solution of the Rayleigh-Ritz problem, expressed by the following theorem:

Theorem

Given the sufficiently continuous real functions $p(x)$, $u(x)$ and $f(x)$, the functional

$$\mathcal{F}(u) = \int_0^1 \left[p(x)(\frac{du}{dx}(x))^2 + q(x)u^2(x) - 2f(x)u(x) \right] dx \qquad (2.5)$$

has a minimum with respect to the variation in $u(x)$, which is given by the following Euler equation:

$$-\frac{d}{dx}\left(p(x)\frac{du(x)}{dx} \right) + q(x)u(x) = f(x) \qquad (2.6)$$

Finding the solution of equation (2.6) is equivalent to finding the function $u(x)$ that minimise the functional (2.5). The Rayleigh-Ritz approach consists in approximating the solution using a finite number of functions $u(x) = \sum_i^N q_i \Phi_i(x)$ to determine the unknown weights q_i that minimise the functional of equation (2.5). The Rayleigh-Ritz method is the starting point to introduce the finite element method, and in fact the weak integral of equation (2.6) gives the Galerkin formulation of the problem, which can be then reduced to an algebraic system to be solved numerically (Courant & Hilbert 1989).
Therefore, the main idea behind the finite element method is to divide the physical domain Ω into a set of subdomains Ω_i with a characteristic size h, usually called *elements*, and locally approximate the solution by piecewise interpolation functions. Algebraic convergence is achieved by reducing the size of the elements (h-type refinement). The error in the numerical solution decays by refining the mesh, which is equivalent to introducing more elements while keeping the order of the interpolation fixed. The possibility to use unstructured meshes makes the method attractive to study problems defined on complex geometries.

2.2.2 Spectral Method

In spectral methods, the solution is approximated by a global p-expansion within the whole computational domain. The expansion is generally made of high-order orthogonal functions, typically Fourier, Chebyshev or Legendre

series (Gottlieb & Orszag 1977). Exponential convergence is achieved by increasing the number of modes in the expansion (p-type refinment). The main difficulty of the spectral method is in constructing a continuous expansion across the computational domain, and so these methods are generally limited to simple geometries. Spectral methods show better convergence properties and higher accuracy than traditional finite element methods. Interested readers can find an extensive overview of spectral methods in Canuto *et al.* (2006).

2.2.3 Spectral/*hp* element method

The spectral/*hp* element method encompasses the methods previously described and aims at combining the geometrical flexibility of the finite element methods with the superior convergence and accuracy of the spectral methods. The computational domain is discretised into a subset of elements where the solution is locally approximated using high-order functions (hp-type discretisation). Convergence can be achieved by both h or p-type refinement. In the following section, the spectral/*hp* method will be discussed, starting from the method of the weighted residuals and the deriving Galerkin formulation.

2.2.4 The method of the weighted residuals

The approximation of the solution of a partial differential equation in a spatial domain Ω requires the replacement of an infinite series expansion with a finite representation. The choice of some specific conditions to be satisfied determines the type of numerical method. Similarly to the finite element method, the spectral/*hp* element method relies on the method of the weighted residuals in order to determine the weight functions which appear when the weak formulation of a partial differential equations is considered. Let us consider a linear differential equation in a domain Ω, denoted by

$$\mathbb{L}(u) = 0 \tag{2.7}$$

and subject to appropriate initial and boundary conditions. The approximated solution of (2.7) can be expressed as

$$u^{\delta}(\boldsymbol{x}, t) = u_0(\boldsymbol{x}, t) + \sum_{i=0}^{N_{dof}} \hat{u}_i(t)\Phi_i(\boldsymbol{x}), \tag{2.8}$$

where $\Phi_i(\boldsymbol{x})$ are analytic functions called *trial* (or *expansion*) *functions*, $\hat{u}_i(t)$ are the N_{dof} unknown coefficients, and $u_0(\boldsymbol{x}, t)$ is a function satisfying

the initial and boundary conditions. The functions $\Phi_i(x)$ need to satisfy only any homogeneous boundary conditions which are present, since the boundary conditions are already satisfied by $u_0(\boldsymbol{x}, t)$. Substituting (2.8) into equation (2.7), a non-zero residual R is obtained:

$$\mathbb{L}(u^\delta) = R(u^\delta). \tag{2.9}$$

In order to have a unique way of determining the coefficients $\hat{u}_i(t)$, a restriction should be applied on the residual R such that equation (2.9) is reduced to a system of ordinary differential equations in $\hat{u}_i(t)$. If equation (2.7) is time-independent then the coefficients $\hat{u}_i$ can be determined directly from the solution of an algebraic system.
In the method of the weighted residuals we adopt a restriction on R such that the inner product of the residual with respect to a *weight* (or *test*) function is equal to zero:

$$\langle v(\boldsymbol{x}), R \rangle = 0. \tag{2.10}$$

where the function $v(\boldsymbol{x})$ is a test or weight function, while $\langle \cdot, \cdot \rangle$ denotes the inner product between two C^0 functions, f and g, defined over Ω:

$$\langle f, g \rangle = \int_\Omega f(\boldsymbol{x}) g(\boldsymbol{x}) d\boldsymbol{x}. \tag{2.11}$$

Let us choose $\boldsymbol{v}(\boldsymbol{x})$ as an arbitrary linear combination of a finite set of known functions $v_j(\boldsymbol{x})$:

$$v(\boldsymbol{x}) = \sum_{j=1}^{N_{dof}} b_i v_j(\boldsymbol{x}) \tag{2.12}$$

When $N_{dof} \to \infty$, the residual $R(\boldsymbol{x}) \to 0$ since the approximated solution tends to the analytical one, $u^\delta \to u(\boldsymbol{x})$, independently from the choice of the test function $v_j(\boldsymbol{x})$. However, due to the finite number of degrees of freedom, the nature of the scheme is determined by the choice of the expansion functions $\Phi_i(\boldsymbol{x})$ and test function v_j.
Let us substitute equation (2.9) into equation (2.10) :

$$\int_\Omega \sum_{j=1}^{N_{dof}} v_j(\boldsymbol{x}) \mathbb{L}(u^\delta) d\boldsymbol{x} = 0 \tag{2.13}$$

If we assume that the operator $\mathbb{L}$ is time-independent and use expression (2.8) to evaluate (2.13), we obtain :

$$\int_\Omega \sum_{j=1}^{N_{dof}} v_j(\boldsymbol{x}) \mathbb{L} \left(u_0(\boldsymbol{x}) + \sum_{i=0}^{N_{dof}} \hat{u}_i \Phi_i(\boldsymbol{x}) \right) d\boldsymbol{x} = \sum_{j=1}^{N_{dof}} \left[\int_\Omega v_j(\boldsymbol{x}) \mathbb{L}(u_0(\boldsymbol{x})) + \int_\Omega v_j(\boldsymbol{x}) \mathbb{L} \left(\sum_{i=1}^{N_{dof}} \hat{u}_i \Phi_i(\boldsymbol{x}) \right) d\boldsymbol{x} \right] = 0 \tag{2.14}$$

where we used the linearity of the operator $\mathbb{L}$ to split (2.14) in two terms, and the interchangeability of the integral and summation is guaranteed by the continuity of the inner product. This expression leads to a set of algebraic equations to determine $\hat{u}_j$:

$$\sum_{i=1}^{N_{dof}} \left[\hat{u}_i \int_\Omega v_j(\boldsymbol{x}) \mathbb{L} \left(\Phi_i(\boldsymbol{x}) \right) \right] d\boldsymbol{x} = - \int_\Omega v_j(\boldsymbol{x}) \mathbb{L}(u_0(\boldsymbol{x})) d\boldsymbol{x} \quad j = 1, \ldots, N_{dof} \tag{2.15}$$

This set of equations can be expressed in a matrix form:

$$\boldsymbol{A}\hat{\boldsymbol{u}} = \boldsymbol{f} \tag{2.16}$$

where $\hat{\boldsymbol{u}}$ is the vector of coefficients $\hat{u}_i$, $\boldsymbol{A}$ is the system matrix, where elements are expressed by:

$$\boldsymbol{A}[i][j] = \int_\Omega v_j(\boldsymbol{x}) \mathbb{L} \left(\Phi_i(\boldsymbol{x}) \right) \tag{2.17}$$

and the vector $\boldsymbol{f}$ is given by:

$$\boldsymbol{f}[j] = - \int_\Omega v_j(\boldsymbol{x}) \mathbb{L} \left(u_0(\boldsymbol{x}) \right) \tag{2.18}$$

As previously mentioned, the specific choice of the expansion and test functions defines the numerical scheme. A list of the commonly used test functions and the resulting computational methods is reported in table 2.1. In this work, the Galerkin scheme, which uses the same function spaces for both the test and trial functions, is used.

2.3 Generalities on the spectral/*hp* discretisations

Similarly to finite element methods, the starting point to derive the spectral/*hp* method is the discretisation of a domain Ω into a subset of elements Ω_i, for example quadrilaterals or triangles. Each element Ω_i can be transformed, by means of a unique mapping $\chi = (\chi, \chi)$, from its arbitrary original

Test/weight function	Type of computational method
$v_j(\boldsymbol{x}) = \delta(\boldsymbol{x} - \boldsymbol{x}_j)$	Collocation
$v_j(\boldsymbol{x}) = \begin{cases} 1, & \text{inside} \quad \Omega^j \\ 0, & \text{outside} \quad \Omega^j \end{cases}$	Finite volume (subdomain)
$v_j(\boldsymbol{x}) = \frac{\partial R}{\partial \hat{u}_j}$	Least-squares
$v_j(\boldsymbol{x}) = \Phi_j$	Galerkin
$v_j(\boldsymbol{x} = \Psi_i (\neq \Phi_j)$	Petrov-Galerkin

Table 2.1: Test function $v_j(\boldsymbol{x})$ used in the method of weighted residuals and the resulting method.

shape in the physical space (x_1, x_2) into a standard element Ω_{st}, defined in a reference space (ξ_1, ξ_2):

$$x_1 = \chi_1(\xi_1, \xi_2), \qquad x_2 = \chi_2(\xi_1, \xi_2). \tag{2.19}$$

Operations involving elements in the physical space will be referred as *local*, while operations in the reference space as *standard*.

2.3.1 Quadrilateral expansion bases

The quadrilateral standard element is defined as a bi-unit square $\mathcal{Q}^2$:

$$\Omega_{st} = \mathcal{Q}^2 = \{\xi_1, \xi_2 : |\xi_1, \xi_2| \leq 1\} \tag{2.20}$$

The simplest way to construct the expansion bases is by taking the tensor product of a one-dimensional basis. In the present work, two type of basis will be used:

- Modal (C^0 continuous) basis:

$$\phi_p(\xi) = \begin{cases} \psi_0^a(\xi) = \frac{1-\xi}{2}, & p = 0, \\ \psi_p^a(\xi) = \left(\frac{1-\xi}{2}\right)\left(\frac{1+\xi}{2}\right) P_{p-1}^{1,1}, & 0 < p < P \\ \psi_P^a(\xi) = \frac{1+\xi}{2}, & p = P \end{cases} \tag{2.21}$$

  where ξ represents the one-dimensional local coordinate, spanning from -1 to 1, whereas $P_p^{1,1}$ is the Jacobi polynomial of order p, which has the property of being orthogonal to all polynomials of order less than p if integrated with respect to $(1 - \xi)(1 + \xi)$:

$$\int_{-1}^{1}(1-\xi)(1+\xi)P_n^{1,1}P_m^{1,1}=0, \quad n\neq m. \tag{2.22}$$

A fundamental property of the modal expansion is that it can be decomposed into *boundary* and *interior* modes. Boundary modes are the modes with non-zero support on the boundaries of the standard region, while interior modes are modes with zero values on all boundaries. This decomposition is convenient when a C^0 global expansion is required, since a a global expansion can be generated from the local expansions by matching the shapes of the individual boundary modes.

- Nodal (C^0 continuous) basis:

$$\phi_p(\xi)=\frac{1}{P(P+1)L_p(\xi_p)}\frac{(1-\xi^2)L'_P(\xi)}{\xi-\xi_p}, \quad 0\leq p\leq P, \tag{2.23}$$

where $L_p(\xi)$ is a Legendre polynomial of order P, while ξ_p denotes the Gauss-Lobatto points in $[-1,1]$. An important property of the Legendre polynomial is that they are orthogonal with respect to the inner product on the interval $\xi=[-1,1]$.

The two-dimensional expansion functions can be obtained from the tensor product of these one-dimensional functions:

$$\phi_{pq}(\xi_1,\xi_2)=\phi_p(\xi_1)\phi_q(\xi_2), \quad 0\leq p,q,\ \ p\leq P_1, q\leq P_2 \tag{2.24}$$

Let us note that the polynomial order of the multi-dimensional expansions may be different in each coordinate direction, in fact P_1 and P_2 are not necessarily the same.

2.3.2 Triangular expansion bases

When the mesh is composed of triangular elements, some difficulties arise, since the Cartesian coordinates (ξ_1,ξ_2) are not bounded by constant limits, as in the case for quadrilaterals, but are dependent upon each other. The structure of the triangular standard element is $\mathcal{T}^2=\{-1\leq\xi_1,\xi_2:\xi_1+\xi_2\leq 0\}$, which does not allow us to define the tensor product expansion as easily as in §2.3.1. However, we can define an artificial coordinate system where the local coordinates have independent bounds and define a transformation that maps the triangular region into a rectangular one. This coordinate system is called *collapsed* and it is used to represent the triangles in the

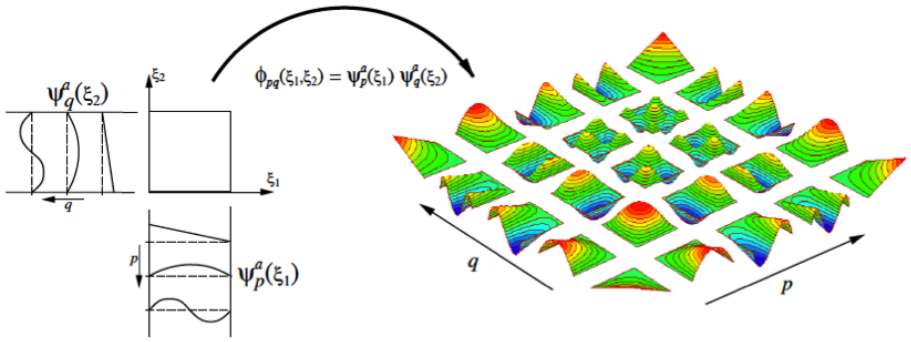

Figure 2.1: Construction of a two-dimensional modal expansion basis from the tensor product of two one-dimensional expansions of order $P = 4$. Adapted from Karniadakis & Sherwin (2005)

standard region Ω_{st}. A suitable collapsed coordinate system is defined by the Duffy transformation:

$$\begin{aligned} \eta_1 &= 2\frac{1+\xi_1}{1-\xi_2} - 1, \\ \eta_2 &= \xi_2 \end{aligned} \tag{2.25}$$

and the respective inverse transformation is:

$$\begin{aligned} \xi_1 &= \frac{(1+\eta_1)(1-\eta_2)}{2} - 1 \\ \xi_2 &= \eta_2 \end{aligned} \tag{2.26}$$

The new coordinates (η_1, η_2) define the standard triangular region by:

$$\mathcal{T}^2 = \{(\eta_1, \eta_2) | -1 \leq \eta_1, \eta_2 \leq 1\} \tag{2.27}$$

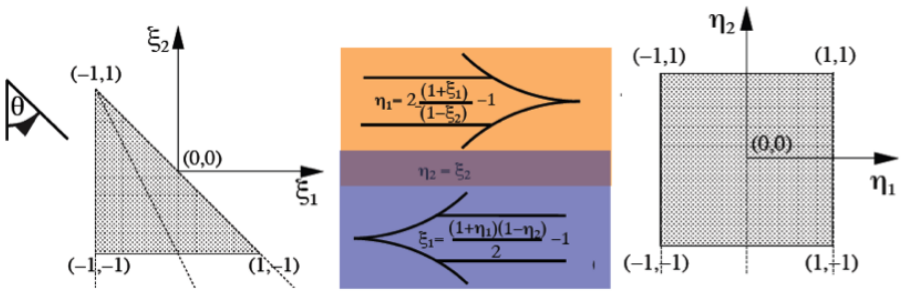

Figure 2.2: Triangle-to-rectangle transformation. Adapted from Karniadakis & Sherwin (2005).

By means of this (2.25), the definition of the triangular region in the collapsed coordinate system is identical to the definition of the standard quadri-

lateral region we introduced in §2.3.1. It is now possible to define the expansion bases in the collapsed system similarly to quadrilateral elements:

$$\phi_{pq}(\xi_1, \xi_2) = \psi^a_p(\eta_1)\psi^b_{pq}(\eta_2) \tag{2.28}$$

where $\psi_{pq}(\eta)$ is the modified one-dimensional expansion base (Karniadakis & Sherwin (2005)):

$$\psi^b_{pq}(\eta) = \begin{cases} \psi^a_q(\eta), & p = 0, 0 \leq q \leq Q, \\ \left(\frac{1-\eta}{2}\right)^{p+1}, & 0 < p < P, q = 0, \\ \left(\frac{1-\eta}{2}\right)^{p+1} \frac{1+\eta}{2} P^{2p+1,1}_{q-1}(\eta), & 0 < p < P, 0 < q < Q, \\ \psi^a_q(\eta), & 0 < p < P, 0 < q < Q \end{cases} \tag{2.29}$$

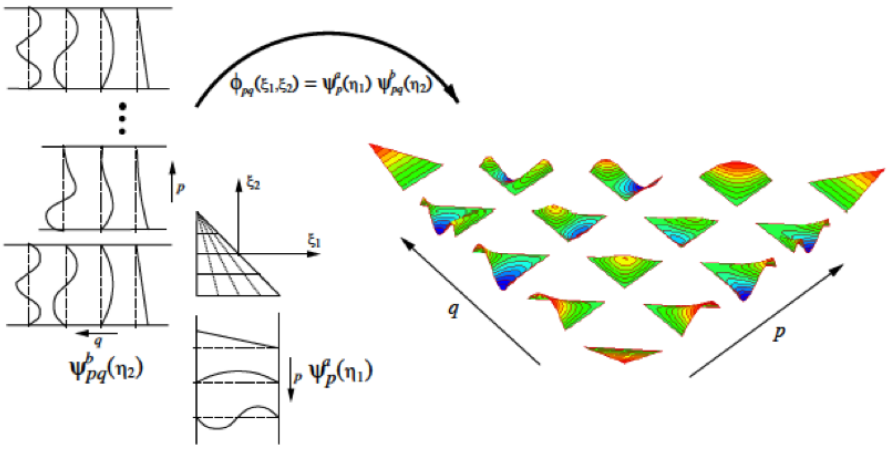

Figure 2.3: Construction of a two-dimensional modal expansion basis from the tensor product of two one-dimensional expansions of order $P = 4$. Adapted from Karniadakis & Sherwin (2005).

This basis allows us to perform once again the decomposition into boundary and interior modes, facilitating the tessellation of the elements into a global expansion, preserving the C^0-continuity of the solution. One of the main advantage of tensorial bases is the possibility to use the *sum-factorisation* technique, which reduces significantly the number of operations, generating a noteworthy gain in terms of computational efficiency. Further details can be found in Karniadakis & Sherwin (2005).

2.3.3 Elemental operations in the standard reference space

As explained in section §2.2.4, the weak Galerkin formulation requires the differentiation and integration of functions in the computational domain in order to evaluate the matrix $\boldsymbol{A}$ and the vector $\boldsymbol{f}$ expressed by (2.17) and (2.18). These operations will be introduced initially in the standard region Ω_{st} and their value in the local system will be evaluated using the inverse mapping. Finally, the contributions of each element are summed up to assemble the global matrix system.

2.3.3.1 Numerical integration

In order to calculate the integrals present in the weak Galerkin formulation, it is necessary to introduce some discrete integration rules, commonly known as *numerical quadrature*. In this thesis, Gaussian quadrature is adopted due to its high accuracy when sufficiently smooth functions are considered.
Let us consider the integral:

$$\int_{-1}^{1} u(\xi)d\xi, \tag{2.30}$$

and approximate the integral with the following finite summation:

$$\int_{-1}^{1} u(\xi)d\xi \approx \sum_{i=0}^{Q-1} w_i u(\xi_i) \tag{2.31}$$

where w_i are specified constants that will be referred as *weights* and ξ_i are $Q-1$ distinct points in the interval $-1 \leq \xi_i \leq 1$.
In Gaussian quadrature the integrand is presented as a Lagrange polynomial $h_i(\xi)$ through Q points ξ_i:

$$u(\xi) = \sum_{i=0}^{Q-1} u(\xi_i)h_i(\xi) + \varepsilon(u) \tag{2.32}$$

where $\varepsilon(u)$ represents the approximation error. (2.30) can then be expressed as:

$$\int_{-1}^{1} u(\xi)d\xi = \sum_{i=0}^{Q-1} w_i u(\xi_i) + R(u) \tag{2.33}$$

where:

$$w_i = \int_{-1}^{1} h_i(\xi)d\xi \tag{2.34}$$

$$R(u) = \int_{-1}^{1} \varepsilon(u) d\xi \tag{2.35}$$

Expression (2.34) defines the weights w_i in terms of the integral of the Lagrange polynomial, but we still need to evaluate ξ_i. Since $u(\xi)$ is represented by a polynomial of order $Q-1$, the approximation will be exact if $u(\xi)$ is a polynomial of order $Q-1$ or less (in this case $R(u)=0$). However, there is a choice of zeros which permits the exact integration of polynomials of order higher than $Q-1$ and this is the main idea behind Gaussian quadrature. The zeros used in the Gaussian quadratures are the zeros of the Jacobi polynomials. There are three different choices of the zeros, leading to three different types of Gaussian quadratures, known as Gauss, Gauss-Radau and Gauss-Lobatto. Gauss quadrature uses zeros where the points are interior to the interval $-1 < \xi_i < 1$ for $i = 0, \ldots, Q-1$ and is able to integrate exactly polynomials of order less than $2Q-1$. In Gauss-Radau quadrature, the zeros include one of the end-points, generally $\xi = -1$ and it is possible to integrate exactly polynomials up to order $2Q-2$. Finally, if the zeros include both the end-points ($\xi = \pm 1$), then we have the Gauss-Lobatto quadrature and an exact integration is possible for polynomials up to order $2Q-3$.
The extension to two-dimensional problems for the standard quadrilateral region can be performed easily using two one-dimensional integrals:

$$\int_{\mathcal{Q}^2} u(\xi_1,\xi_2) d\xi_1 d\xi_2 = \int_{-1}^{1} \left\{ \int_{-1}^{1} u(\xi_1,\xi_2)|_{\xi_2} \right\} d\xi_2 \simeq \sum_{i=0}^{Q_1-1} w_i \left\{ \sum_{j=0}^{Q_2-1} w_j u(\xi_{1i},\xi_{2j}) \right\} \tag{2.36}$$

where Q_1 and Q_2 are the number of quadrature points in the ξ_1 and ξ_2 directions respectively.
The extension for the two-dimensional standard triangular region is a little bit more complex, requiring the transformation from the Cartesian to the collapsed system, and it is expressed by (2.25).

$$\int_{\mathcal{T}^2} u(\xi_1,\xi_2) d\xi_1 d\xi_2 = \int_{-1}^{1} \int_{-1}^{1} u(\eta_1,\eta_2) \left| \frac{\partial(\xi_1,\xi_2)}{\partial(\eta_1,\eta_2)} \right| d\eta_1 d\eta_2 \tag{2.37}$$

where $\partial(\xi_1,\xi_2)/\partial(\eta_1,\eta_2)$ is the Jacobian of the transformation and is expressed by:

$$\frac{\partial(\xi_1,\xi_2)}{\partial(\eta_1,\eta_2)} = \frac{1-\eta_2}{2} \tag{2.38}$$

Using a one-dimensional Gaussian quadrature for each integral, we obtain:

$$\int_{-1}^{1}\int_{-1}^{1} u(\eta_1,\eta_2)\frac{1-\eta_2}{2}d\eta_1 d\eta_2 = \sum_{i=0}^{Q_1-1} w_i \left\{ \sum_{j=0}^{Q_2-1} w_j u(\eta_{1i},\eta_{2j})\frac{1-\eta_{2j}}{2} \right\} \tag{2.39}$$

where η_{1i} and η_{2j} are the quadrature points in the η_1 and η_2 directions respectively. However, it is possible to consider a more general quadrature rule, which we shall refer as *Gauss-Jacobi* quadrature which is very convenient for triangles. This quadrature includes the factor $(1-\xi)^\alpha(1+\xi)^\beta$ in the integrand:

$$\int_{-1}^{1}(1-\xi)^\alpha(1+\xi)^\beta u(\xi)d\xi = \sum_{i=0}^{Q-1} w^{\alpha,\beta}u(\xi_i^{\alpha,\beta}), \tag{2.40}$$

where $w^{\alpha,\beta}$ and $\xi_i^{\alpha,\beta}$ are the weights and zeros, which both depend on the choice of the exponents α and β. If $\alpha=\beta=0$, then standard Gaussian quadrature is recovered. The Gauss-Jacobi is particularly convenient to define the integration in the standard triangular region since the Jacobian term $(1-\eta_2)/2$ can be directly included into the quadrature weights by setting $\alpha=1,\beta=0$. The integration scheme over $\mathcal{T}^2$ is then:

$$\int_{-1}^{1}\int_{-1}^{1} u(\eta_1,\eta_2)\frac{1-\eta_2}{2}d\eta_1 d\eta = \sum_{i=0}^{Q_1-1} w_i^{0,0} \left\{ \sum_{j=0}^{Q_2-1} \hat{w}_j^{1,0} u(\eta_{1i},\eta_{2j}) \right\}, \tag{2.41}$$

where:

$$\hat{w}_j^{1,0} = \frac{w_j^{1,0}}{2}. \tag{2.42}$$

For triangles, the Gauss-Jacobi rules uses fewer quadrature points than the standard Gauss-integration to achieve an equivalent accuracy. Generally the Lobatto-type quadrature is preferred because it includes the end points of the interval $[-1,1]$, which is helpful in setting the boundary conditions. However, when triangles are used, the Radau distribution in η_2 (which includes the point at $\eta_2=-1$) is preferred because it avoids the explicit calculations of terms at the degenerate vertex ($\eta_1=-1,\eta_2=1$). This vertex does not cause problems when integrating over $\mathcal{T}^2$, but adds complications in the differentiation.

2.3.3.2 Collocation differentiation

The application of the method of the weighted residuals involves the evaluation of the derivatives of a function inside the integral. Therefore, we need

to evaluate the function derivatives at the quadrature points ξ_i; in this thesis we will use a method called *collocation differentiation* or differentiation in physical space.
Let us assume that the approximate solution $u^\delta(\xi)$ is a polynomial of order equal or less than P; we can express it exactly in terms of Lagrange polynomials $h_i(\xi)$ through a set of Q nodal points ξ_i:

$$u(\xi) = \sum_{i=0}^{Q-1} u(\xi_i) h_i(\xi), \qquad h_i(\xi) = \frac{\prod_{j=0, j\neq i}^{Q-1} (\xi - \xi_j)}{\prod_{j=0, j\neq i}^{Q-1} (\xi_i - \xi_j)} \tag{2.43}$$

where $Q \geq P + 1$. Therefore, we can write the derivative of $u(\xi)$ as:

$$\frac{du(\xi)}{d\xi} = \sum_{i=0}^{Q-1} u(\xi_i) \frac{dh_i(\xi)}{d\xi} \tag{2.44}$$

The derivative at the nodal points ξ_i is therefore given by:

$$\frac{du(\xi)}{d\xi} = \sum_{j=0}^{Q-1} d_{ij} u(\xi_j) \tag{2.45}$$

where:

$$d_{ij} = \left. \frac{dh_j(\xi)}{d\xi} \right|_{\xi=\xi_i} \tag{2.46}$$

is the differentiation matrix.

These concepts can be extended to two-dimensional cases. For a standard quadrilateral region $\mathcal{Q}^2$, let us consider the general expansion:

$$u^\delta(\xi_1, \xi_2) = \sum_{p=0}^{P_1} \sum_{q=0}^{P_2} \hat{u}_{pq} \phi_{pq}(\xi_1, \xi_2) \tag{2.47}$$

and write it in terms of Lagrange polynomials:

$$u^\delta(\xi_1, \xi_2) = \sum_{p=0}^{Q_1-1} \sum_{q=0}^{Q_2-1} u_{pq} h_p(\xi_1) h_q(\xi_2), \tag{2.48}$$

where:

$$u_{pq} = u^\delta(\xi_{1p}, \xi_{2q}), \quad Q_1 > P_1, \quad Q_2 > P_2 \tag{2.49}$$

and ξ_{1p} and ξ_{2q} are the zeros of an appropriate Gaussian quadrature. The partial derivative with respect to ξ_1 is:

$$\frac{\partial u^{\delta}}{\partial \xi_1}(\xi_1, \xi_2) = \sum_{p=0}^{P_1} \sum_{q=0}^{P_2} u_{pq} \frac{dh_p(\xi_1)}{d\xi_1} h_q(\xi_2). \tag{2.50}$$

Noting that the Lagrange polynomials at the nodal points assume the value of the Kronecker delta, $h_p(\xi_i) = \delta_{pi}$, we can write the derivative with respect to ξ_1 at the nodal points (ξ_{1i}, ξ_{2j}) as:

$$\frac{\partial u^{\delta}}{\partial \xi_1}(\xi_{1i}, \xi_{2j}) = \sum_{p=0}^{P_1} \sum_{q=0}^{P_2} \left\{ u_{pq} \left. \frac{dh_p(\xi_1)}{d\xi_1} \right|_{\xi_{1i}} \delta_{qj} \right\} = \sum_{p=0}^{P_1} u_{pj} \left. \frac{dh_p(\xi_1)}{d\xi_1} \right|_{\xi_{1i}} \tag{2.51}$$

The derivative with respect to ξ_2 can be evaluated in a similar way:

$$\frac{\partial u^{\delta}}{\partial \xi_2}(\xi_{1i}, \xi_{2j}) = \sum_{p=0}^{P_2} u_{iq} \left. \frac{dh_p(\xi_2)}{d\xi_2} \right|_{\xi_{2j}} \tag{2.52}$$

For the triangular region $\mathcal{T}^2$, the polynomial expansion can be represented in terms of Lagrange polynomials using the collapsed coordinates η_1 and η_2:

$$u^{\delta}(\xi_1, \xi_2) = \sum_{p=0}^{P_1} \sum_{q=0}^{P_2} \hat{u}_{pq} \phi_{pq}(\eta_1, \eta_2) = \sum_{p=0}^{P_1} \sum_{q=0}^{P_2} u_{pq} h_p(\eta_1) h_q(\eta_2) \tag{2.53}$$

where $u_{pq} = u^{\delta}(\eta_{1p}, \eta_{2p})$ and η_{1p}, η_{2q} refer to the nodal points of the Lagrange polynomials. The partial derivative with respect to the Cartesian system (ξ_1, ξ_2) is expressed by the following expression:

$$\begin{pmatrix} \frac{\partial}{\partial \xi_1} \\ \frac{\partial}{\partial \xi_2} \end{pmatrix} = \begin{pmatrix} \frac{2}{1-\eta_2} \frac{\partial}{\partial \eta_1} \\ 2\frac{1+\eta_1}{1-\eta_2} \frac{\partial}{\partial \eta_1} + \frac{\partial}{\partial \eta_2} \end{pmatrix} \tag{2.54}$$

Similarly to the quadrilaterals, the extension to triangles can be performed considering that the partial derivatives with respect to η_1 and η_2 at the nodal points are given by:

$$\frac{\partial u^{\delta}}{\partial \eta_1}(\eta_{1i}, \eta_{2j}) = \sum_{p=0}^{P_1} u_{pj} \left. \frac{dh_p(\eta_1)}{d\eta_1} \right|_{\eta_{1i}}, \tag{2.55a}$$

$$\frac{\partial u^{\delta}}{\partial \eta_2}(\eta_{1i}, \eta_{2j}) = \sum_{p=0}^{P_2} u_{iq} \left. \frac{dh_q(\eta_2)}{d\eta_2} \right|_{\eta_{2j}}. \tag{2.55b}$$

Substituting equations (2.55a) and (2.55b) into equation (2.54), we obtain the partial derivative of the function u with respect to the Cartesian coordinates (ξ_1, ξ_2).

2.3.3.3 Backward and forward transformation

As discussed in §2.3.3.1 and §2.3.3.2, the derivation and integration might be performed in two different spaces. Hence, it is necessary to introduce a transformation to evaluate the physical values from the expansion basis coefficients (*backward transformation*) and *vice-versa* (*forward transformation*). The backward transformation can be defined as:

$$u^{\delta}(\xi_{1i}, \xi_{2j}) = \sum_{p,q} \hat{u}_{p,q} \phi_{pq}(\xi_{1i}, \xi_{2j}) \tag{2.56}$$

which merely evaluates the spectral/*hp* element expansion at the quadrature points. To derive a mathematical expression for the forward transformation, let us consider a generic function $u(\xi_1, \xi_2)$ and calculate the error $R(u)$ between the approximation u^{δ} and $u(\xi_1, \xi_2)$:

$$u^{\delta}(\xi_1, \xi_2) - u(\xi_1, \xi_2) = \sum_{p,q} \hat{u}_{p,q} \phi_{pq}(\xi_1, \xi_2) - u(\xi_1, \xi_2) = R(u) \tag{2.57}$$

Similarly to the method of weighted residuals discussed in §2.2.4, we take the inner product of both sides by an undefined function $v(\xi_1, \xi_2)$ and set $\langle v, R(u) \rangle = 0$. We obtain:

$$\left\langle v, \sum_{p,q} \hat{u}_{pq} \phi_{pq} \right\rangle = \langle v, u \rangle . \tag{2.58}$$

The choice of the function $v(\xi_1, \xi_2)$ defines the type of projection. In the collocation projection we choose $v(\xi_1, \xi_2) = \delta(\xi_{1i}, \xi_{2j})$ where $\delta(\xi_{i1}, \xi_{2j})$ is the Kronecker delta function at the nodal points, implying that $R(u(\xi_{1i}, \xi_{2j}) = 0$. This technique can be used to interpolate a function within the region $(\xi_1, \xi_2) \in \Omega_{st}$. In the Galerkin projection the weight functions are chosen to be the same as the expansion basis, $v(\xi_1, \xi_2) = \phi_{rs}(\xi_1, \xi_2)$. Noting that the coefficients $\hat{u}_{pq}$ are independent of ξ_1 and ξ_2, equation (2.58) can be then written as:

$$\sum_{p,q} \langle \phi_{rs}, \phi_{pq} \rangle \, \hat{u}_{pq} = \langle \phi_{rs}, u \rangle \tag{2.59}$$

Equation (2.59) represents a linear system, which can be solved to determine $\hat{u}_{pq}$, where $\langle \phi_{rs}, \phi_{pq} \rangle$ represent the components of the coefficient matrix.

2.3.4 Elemental operation within general-shaped elements

In the previous sections, the methodology to integrate and differentiate within the standard region Ω_{st} was described. However, we need to gen-

eralise the concepts in order to perform these operation in the elemental local region Ω^e, which can have a generic shape and orientation. The idea is to define a mapping $\chi^e = (\chi_1^e, \chi_2^e)$ between the Cartesian coordinates (x_1, x_2) and the local Cartesian coordinates in the standard region (ξ_1, ξ_2), which can be expressed by:

$$x_1 = \chi_1^e(\xi_1, \xi_2), \qquad x_2 = \chi_2^e(\xi_1, \xi_2). \tag{2.60}$$

Let us consider straight-side elements, which require just information of the vertices. The mapping for a triangle defined by the vertices $\{(x_1^A, x_2^A), (x_1^B, x_2^B), (x_1^C, x_2^C)\}$ is:

$$x_i = \chi_i^e(\eta_1, \eta_2) = x_i^A \frac{1-\eta_1}{2}\frac{1-\eta_2}{2} + x_i^B \frac{1+\eta_1}{2}\frac{1-\eta_2}{2} + x_i^C \frac{1+\eta_2}{2}, \quad i = 1, 2 \tag{2.61}$$

This mapping can be expressed in the Cartesian coordinate system, recalling equation (2.25):

$$x_i = \chi_i(\xi_1, \xi_2) = x_i^A \frac{-\xi_2 - \xi_1}{2} + x_i^B \frac{1+\xi_1}{2} + x_i^C \frac{1+\xi_2}{2}, \quad i = 1, 2 \tag{2.62}$$

Similarly, for quadrilateral elements defined by the vertices $\{(x_1^A, x_2^A), (x_1^B, x_2^B), (x_1^C, x_2^C), (x_1^D, x_2^D)\}$:

$$\begin{aligned} x_i = \chi_1(\xi_1, \xi_2) = x_i^A \frac{1-\xi_1}{2}\frac{1-\xi_2}{2} + x_i^B \frac{1+\xi_1}{2}\frac{1-\xi_2}{2} + \\ x_i^C \frac{1+\xi}{2}\frac{1+\xi_2}{2} + x_i^D \frac{1-\xi_1}{2}\frac{1+\xi_2}{2}, \quad i = 1, 2. \end{aligned} \tag{2.63}$$

To extend these results to curvilinear elements, we define the following mapping:

$$x_i = \chi_i(\xi_1, \xi_2) = \sum_{p=0}^{P_1} \sum_{q=0}^{P_2} \hat{x}_{pq}^i \phi_{pq}(\xi_1, \xi_2) \tag{2.64}$$

Equation (2.64) expresses the geometry of the problem as an expansion with the same form and polynomial order of the unknown variables; this type of mapping is called *iso-parametric*. Mappings (2.62) and (2.63) are particular cases of (2.64), where the coefficients of all but the vertex modes are zero (Karniadakis & Sherwin, 2005). The integration within a general-shaped elemental region Ω^e can be expressed as:

$$\int_{\Omega^e} u(x_1, x_2) dx_1 dx_2 = \int_{\Omega_{st}} u(\xi_1, \xi_2) |J| d\xi_1 d\xi_2. \tag{2.65}$$

where J is the Jacobian due to the transformation:

$$J = \begin{vmatrix} \frac{\partial x_1}{\partial \xi_1} & \frac{\partial x_1}{\partial \xi_2} \\ \frac{\partial x_2}{\partial \xi_1} & \frac{\partial x_2}{\partial \xi_2} \end{vmatrix} = \frac{\partial x_1}{\partial \xi_1}\frac{\partial x_2}{\partial \xi_2} - \frac{\partial x_1}{\partial \xi_2}\frac{\partial x_2}{\partial \xi_1}. \tag{2.66}$$

To differentiate, we apply the chain rule:

$$\begin{bmatrix} \frac{\partial}{\partial x_1} \\ \frac{\partial}{\partial x_2} \end{bmatrix} = \begin{bmatrix} \frac{\partial \xi_1}{\partial x_1}\frac{\partial}{\partial \xi_1} + \frac{\partial \xi_2}{\partial x_1}\frac{\partial}{\partial x_2} \\ \frac{\partial \xi_1}{\partial x_2}\frac{\partial}{\partial \xi_1} + \frac{\partial \xi_2}{\partial x_2}\frac{\partial}{\partial x_2} \end{bmatrix}. \tag{2.67}$$

Since the mapping is iso-parametric, we have that $\xi_i = \chi_i^{-1}(\xi_1, \xi_2)$, so we can apply the chain rule directly to ξ_1 and ξ_2:

$$\begin{bmatrix} \frac{\partial}{\partial x_1} \\ \frac{\partial}{\partial x_2} \end{bmatrix} = \begin{bmatrix} \frac{\partial \xi_1}{\partial x_1} & \frac{\partial \xi_2}{\partial x_1} \\ \frac{\partial \xi_1}{\partial x_2} & \frac{\partial \xi_2}{\partial x_2} \end{bmatrix} \begin{bmatrix} \frac{\partial}{\partial \xi_1} \\ \frac{\partial}{\partial \xi_2} \end{bmatrix} = \frac{1}{J} \begin{bmatrix} \frac{\partial x_2}{\partial \xi_2} & -\frac{\partial x_2}{\partial \xi_1} \\ -\frac{\partial x_1}{\partial \xi_2} & \frac{\partial x_1}{\partial \xi_1} \end{bmatrix} \begin{bmatrix} \frac{\partial}{\partial \xi_1} \\ \frac{\partial}{\partial \xi_2} \end{bmatrix} \tag{2.68}$$

In this thesis, collocation differentiation will be used to compute the metric terms $\partial \xi_i / \partial x_j$ and the derivatives with respect to ξ_1 and ξ_2.

2.3.5 Global operations

All the operations described so far are performed on a single element and share no information with any other element. However, to calculate the global solution on the domain Ω some form of continuity or transfer of information between the elements needs to be imposed. In this thesis, the classical Galerkin method is adopted, which consists of imposing C^0-continuity between the element boundaries. This is achieved by means of a global assembly process, often referred as *direct stiffness summation* or *global assembly*. At this stage, it is important to recall the decomposition of the elemental bases into boundary/interior modes, in fact we need to match only the boundary modes of similar shape. The most advantageous computational approach for the global assembly is to perform most operations in a local environment and then assemble all the local contributions into a global system. This method requires a mapping to relate the global system to the local one. Let us consider a function $u(x_1, x_2)$, which can be expanded as:

$$u(x_1, x_2) = \sum_{e=1}^{N_{el}} \sum_{p=0}^{P_1} \sum_{q=0}^{P_2} \phi_{pq}^e(x_1, x_2) \hat{u}_{pq}^e, \tag{2.69}$$

where N_{el} is the number of elements in the domain, $\hat{u}_{pq}^e$ the local expansion coefficients and $\phi_{pq}^e(x_1, x_2)$ the expansion modes in a specific element e.

The vector representing all the local degrees of freedom[1] can be obtained by concatenation of all the local expansion coefficients:

$$\hat{\boldsymbol{u}}_l = \underline{\hat{\boldsymbol{u}}}^e = \begin{bmatrix} \hat{\boldsymbol{u}}^1 \\ \hat{\boldsymbol{u}}^2 \\ \vdots \\ \hat{\boldsymbol{u}}^{N_{el}} \end{bmatrix}, \tag{2.70}$$

where the underlined vector implies the extension over all the elemental regions. The mapping from the global to the local degrees of freedom can be expressed by the matrix $\boldsymbol{\mathcal{A}}$, which is sparse with entries generally ± 1 or 0:

$$\hat{\boldsymbol{u}}_l = \boldsymbol{\mathcal{A}} \hat{\boldsymbol{u}}_g \tag{2.71}$$

The global assembly can then be expressed by the transpose of the matrix $\boldsymbol{\mathcal{A}}$ and can be captured by the integral operation. Let us consider the inner product of a function $u(x_1, x_2)$ with respect to the global basis $\Phi_m(x_1, x_2)$:

$$\hat{\boldsymbol{I}}_g[m] = \int_\Omega u(x_1, x_2) \Phi_m(x_1, x_2) dx_1 dx_2, \quad 0 \leq m < N_{dof} \tag{2.72}$$

Equation (2.72) can be expressed using each elemental contribution:

$$\hat{\boldsymbol{I}}_g[m] = \int_\Omega u(x_1, x_2) \Phi_m(x_1, x_2) dx_1 dx_2 = \int_{\Omega^e} u(x_1, x_2) \phi_n(x_1, x_2) dx_1 dx_2, \tag{2.73}$$

where $m(n, e)$ expresses each modal contribution n over each element e. We can then write equation (2.73) as:

$$\hat{\boldsymbol{I}}_g = \boldsymbol{\mathcal{A}}^T \hat{\boldsymbol{I}}_l = \boldsymbol{\mathcal{A}}^T \underline{\hat{\boldsymbol{I}}}^e \tag{2.74}$$

This methodology is summarised in figure (2.4).

2.3.5.1 Static and multi-level static condensation

Let us consider the following Helmholtz equation:

$$\nabla^2 u - \lambda u = f \tag{2.75}$$

[1] the local degrees of freedom are defined as all the elemental expansion coefficients over all the elements.

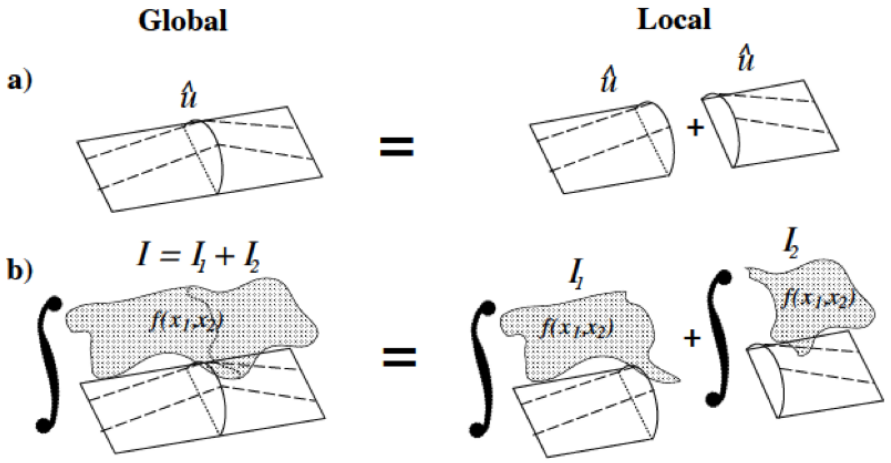

Figure 2.4: Illustration of local to global assembly. If we have a global expansion as represented in figure *(a)* it can be decomposed into two elemental contributions multiplied by the same global coefficient $\hat{u}$. To integrate a function $f(x_1, x_2)$ with respect to the global mode (figure *(b)*), the integration in the global region is split into the sum of the integration within the local regions (Karniadakis & Sherwin, 2005).

defined in a local quadrilateral region Ω^e. The weak formulation of the problem can be written in a matrix notation as

$$\boldsymbol{H}^e\hat{\boldsymbol{u}}^e = [\boldsymbol{L}^e + \lambda\boldsymbol{M}^e]\hat{\boldsymbol{u}}^e. \tag{2.76}$$

Expression (2.76) is similar to (2.16), where $\boldsymbol{L}^e$ represents the Laplacian operator, while $\boldsymbol{M}^e$ is called *elemental mass matrix* and is defined as:

$$\boldsymbol{M}^e[m][n] = \int_{\Omega^e} \Phi^e_m(x_1, x_2)\Phi^e_n(x_1, x_2)dx_1dx_2 \tag{2.77}$$

Following the procedure described in §2.3.5, we can construct the global matrix, starting from the elemental contributions using the matrix $\boldsymbol{\mathcal{A}}$:

$$\boldsymbol{M} = \boldsymbol{\mathcal{A}}^T\underline{\boldsymbol{M}}^e\boldsymbol{\mathcal{A}}, \tag{2.78}$$

$\underline{\boldsymbol{M}}^e$ is a block diagonal matrix that concatenates the single elemental matrices $\boldsymbol{M}^e$:

$$\underline{\boldsymbol{M}}^e = \begin{bmatrix} \boldsymbol{M}^1 & 0 & 0 & \cdots & 0 \\ 0 & \boldsymbol{M}^2 & 0 & \cdots & 0 \\ 0 & 0 & \boldsymbol{M}^3 & \cdots & 0 \\ \vdots & \vdots & \vdots & \ddots & \vdots \\ 0 & 0 & 0 & \cdots & \boldsymbol{M}^{N_{el}} \end{bmatrix} \tag{2.79}$$

Each of the elemental matrices $\boldsymbol{M}^e$ can be split into four sub-matrices, which contain the boundary and interior contributions respectively:

$$\boldsymbol{M}^e = \begin{bmatrix} \boldsymbol{M}_b^e & \boldsymbol{M}_c^e \\ (\boldsymbol{M}_c^e)^T & (\boldsymbol{M})i^e \end{bmatrix} \tag{2.80}$$

where $\boldsymbol{M}_b^e$ represents the components of the $\boldsymbol{M}^e$ resulting from the boundary-boundary interactions, $\boldsymbol{M}_c^e$ the components of $\boldsymbol{M}^e$ from the coupling between the boundary-interior modes, and $\boldsymbol{M}_i^e$ the components of $\boldsymbol{M}^e$ resulting from the interior-interior mode interactions. In the global assembly operation, when the mapping $\boldsymbol{\mathcal{A}}$ is built, the global boundary degrees of freedom are listed first, followed by the global interior degrees of freedom. Furthermore, the global interior degrees of freedom are numbered consecutively. The resulting system then has the form shown in figure (2.5). In this figure $\boldsymbol{M}_b$ is the global assembly matrix of the elemental boundary-boundary mode interaction from $\boldsymbol{M}_b^e$, and similarly $\boldsymbol{M}_c$, $\boldsymbol{M}_i$ correspond to the global assembly matrices of the elemental boundary-interior coupling and interior-interior systems $\boldsymbol{M}_c^e$ and $\boldsymbol{M}_i^e$.
Let us assume that we need to solve a system of the form:

$$\boldsymbol{M}\boldsymbol{x} = \boldsymbol{\mathcal{A}}^T \underline{\boldsymbol{M}}^e \boldsymbol{\mathcal{A}}\boldsymbol{x} = \boldsymbol{f}. \tag{2.81}$$

and let us split $\boldsymbol{x}$ and $\boldsymbol{f}$ into the boundary and interior components respectively:

$$\boldsymbol{x} = \begin{bmatrix} \boldsymbol{x}_b \\ \boldsymbol{x}_i \end{bmatrix}, \quad \boldsymbol{f} = \begin{bmatrix} \boldsymbol{f}_b \\ \boldsymbol{f}_i \end{bmatrix}. \tag{2.82}$$

Therefore equation (2.81) can be rewritten as:

$$\begin{bmatrix} \boldsymbol{M}_b^e & \boldsymbol{M}_c^e \\ (\boldsymbol{M}_c^e)^T & (\boldsymbol{M})i^e \end{bmatrix} \begin{bmatrix} \boldsymbol{x}_b \\ \boldsymbol{x}_i \end{bmatrix} = \begin{bmatrix} \boldsymbol{f}_b \\ \boldsymbol{f}_i \end{bmatrix}. \tag{2.83}$$

If we pre-multiply the system by the matrix:

$$\begin{bmatrix} \boldsymbol{I} & -\boldsymbol{M}_c\boldsymbol{M}_i^{-1} \\ 0 & \boldsymbol{I} \end{bmatrix} \tag{2.84}$$

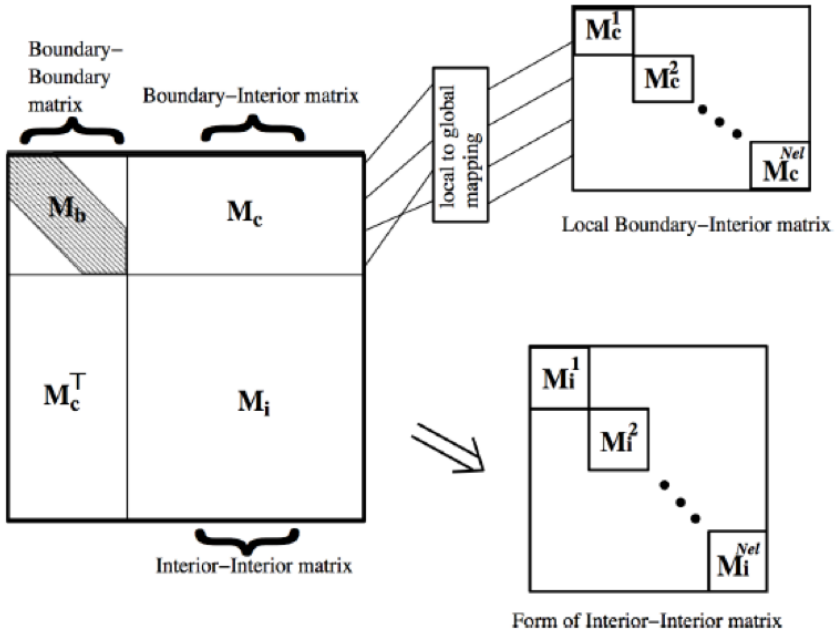

Figure 2.5: Structure of the global matrix system. Adapted from Karniadakis & Sherwin (2005).

we obtain:

$$\begin{bmatrix} \boldsymbol{M}_b - \boldsymbol{M}_c \boldsymbol{M}_i^{-1} \boldsymbol{M}_c^T & 0 \\ (\boldsymbol{M}_c)^T & \boldsymbol{M})i \end{bmatrix} \begin{bmatrix} \boldsymbol{x}_b \\ \boldsymbol{x}_i \end{bmatrix} = \begin{bmatrix} \boldsymbol{f}_b - \boldsymbol{M}_c \boldsymbol{M}_i^{-1} \boldsymbol{f}_i \\ \boldsymbol{f}_i \end{bmatrix} \tag{2.85}$$

The equation for the boundary unknowns is:

$$(\boldsymbol{M}_b - \boldsymbol{M}_c \boldsymbol{M}_i^{-1} \boldsymbol{M}_c^T) \boldsymbol{x}_b = \boldsymbol{f}_b - \boldsymbol{M}_c \boldsymbol{M}_i^{-1} \boldsymbol{f}_i \tag{2.86}$$

Once $\boldsymbol{x}_b$ is known, x_i can be determined from the second row of equation (2.85):

$$\boldsymbol{x}_i = \boldsymbol{M}_i^{-1} \boldsymbol{f}_i - \boldsymbol{M}_i^{-1} \boldsymbol{M}_c^T \boldsymbol{x}_b \tag{2.87}$$

The solution of the system (2.81) has been split into three operations. The first is the evaluation and inversion of $\boldsymbol{M}_b - \boldsymbol{M}_c \boldsymbol{M}_i^{-1} \boldsymbol{M}_c^T$ (usually referred to as the *Schur complement*). The second one is the computation $\boldsymbol{M}_i^{-1}$, while the final step is the evaluation of $\boldsymbol{M}_c \boldsymbol{M}_i^{-1} = [\boldsymbol{M}_i^{-1} \boldsymbol{M}_c^T]^T$. Both the second and third operations can be performed at a local elemental level. The most expensive operation of this procedure is the computation of the Schur complement, in fact the inverse matrix $\boldsymbol{M}_i^{-1}$ is generally full. This

method is known as *static condensation*. A further optimisation can be achieved by means of the multi-level static condensation (often referred as *subtracting*). The same idea behind the static condensation can be applied to the remaining boundary degrees of freedom to solve the Schur complement system. An appropriate numbering of the boundary system generates a block diagonal Schur complement matrix and the static condensation can be then reapplied to this new level. Further details on this method can be found in Karniadakis & Sherwin (2005).

2.3.6 Fourier-Spectral/*hp* element method

In this thesis, the three-dimensional solution of the underlying PDEs (equations (2.3) and (2.4)) is computed by means of a Fourier-spectral/*hp* element method (Karniadakis, 1990). This method consists of a combination of a spectral/*hp* element approach to discretise the variables in a series of two-dimensional planes ($x-y$ for instance) and then a spectral Fourier method is applied in the third direction, (generally the z direction), as shown in figure (2.6).
To use a spectral method in the spanwise direction, we need to consider a periodic solution of equations (2.3)-(2.4) along the span, so that

$$\boldsymbol{u}(x,y,z,t) = \boldsymbol{u}(x,y,z+L_z,t) \tag{2.88}$$

where L_z represents the length in the spanwise dimension. Let us expand the solution in the spanwise direction using a discrete Fourier series with K modes:

$$\boldsymbol{u}(x,y,z,t) = \sum_{k=-K/2}^{K/2} \hat{\boldsymbol{u}}_k(x,y,t) e^{i\frac{2k\pi}{L_z}} \tag{2.89}$$

The equations that describe the evolution of each coefficient $\hat{\boldsymbol{u}}_k$ can be obtained by taking the Fourier transform $\mathcal{F}$ of equations (2.3)-(2.4):

$$\frac{\partial \hat{\boldsymbol{u}}_k}{\partial t} = \mathcal{F}[\mathbf{N}(\boldsymbol{u})] - \tilde{\nabla} p_m + \frac{1}{Re}\tilde{\nabla}^2 \boldsymbol{u}_k \tag{2.90a}$$

$$\tilde{\nabla} \cdot \hat{\boldsymbol{u}}_k = 0 \tag{2.90b}$$

where $\mathbf{N}(\boldsymbol{u})$ is the non-linear term of the Navier-Stokes equations, while operators $\tilde{\nabla}$ and $\tilde{\nabla}^2$ are respectively:

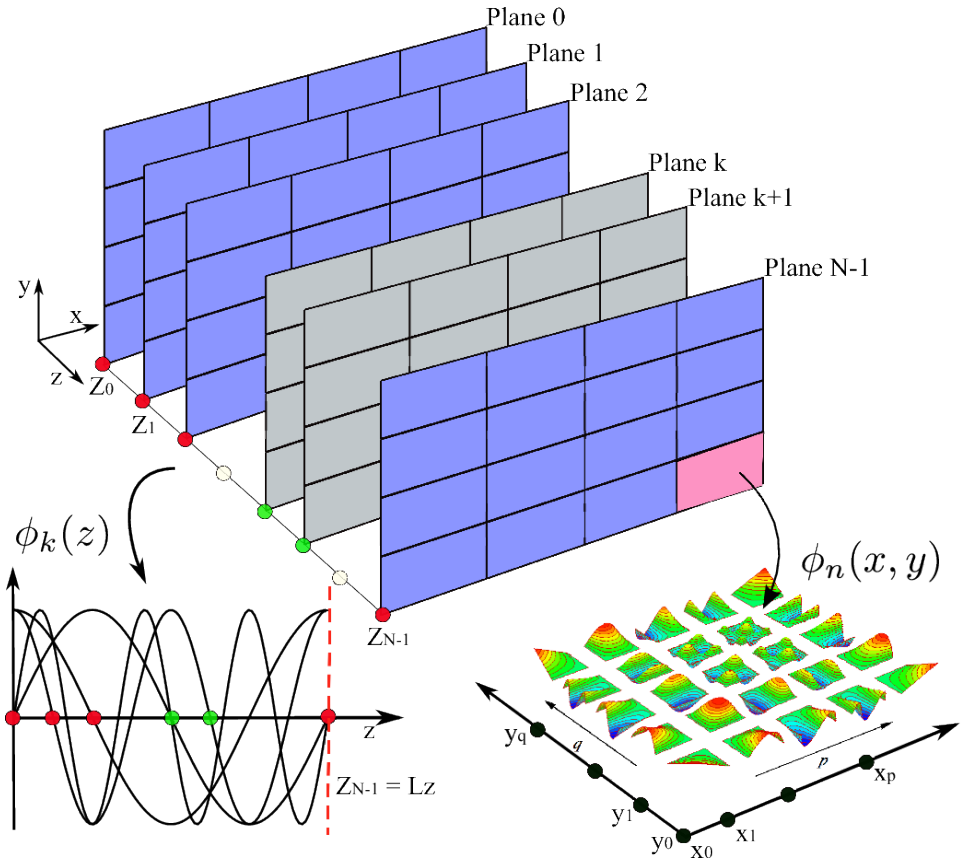

Figure 2.6: Geometric interpretation of the Fourier spectral/*hp* element method. Spectral/*hp* element discretisation is adopted on each xy plane and a spectral method in the z-direction. Adapted from Bolis (2013)

$$\tilde{\nabla} = \begin{pmatrix} \frac{\partial}{\partial x} \\ \frac{\partial}{\partial y} \\ i\beta_k \end{pmatrix} \qquad \tilde{\nabla}^2 = \frac{\partial^2}{\partial x^2} + \frac{\partial^2}{\partial y^2} - \beta_k^2 \qquad \text{with} \qquad \beta_m = \frac{2\pi k}{L_z} \tag{2.91a}$$

Each mode can be evaluated independently from the others and the only coupling is through the non-linear terms. The solution of the equations is then reduced to a series of two-dimensional problems over the Fourier planes. This has important advantages in term of efficiency and it facilitates the parallelisation of the algorithms (Bolis, 2013).

2.4 Time evolution of the Navier-Stokes equations

In the previous sections, the spatial discretisation using spectral/*hp* element method was introduced, but no mention was made about the method adopted to evolve the unsteady Navier-Stokes equations (2.3) and (2.4) in time. In this work, a *stiffly stable time splitting scheme* (Karniadakis *et al.*, 1991) was used. This algorithm is a velocity-correction projection scheme that decouples the velocity from the pressure, leading to an explicit evolution of the advection term and an implicit evolution of the diffusive terms. The semi-discrete system is written as:

$$\frac{\hat{\boldsymbol{u}} - \sum_{q=0}^{J_i-1} \alpha_q \boldsymbol{u}^{n-q}}{\Delta t} = -\sum_{q=0}^{J_e-1} \beta_q \left[\boldsymbol{u} \cdot \nabla \boldsymbol{u}\right]^{n-q} \tag{2.92a}$$

$$\frac{\hat{\hat{\boldsymbol{u}}} - \hat{\boldsymbol{u}}}{\Delta t} = -\nabla (p')^{n+1} \tag{2.92b}$$

$$\frac{\gamma_0 (\boldsymbol{u})^{n+1} - \hat{\hat{\boldsymbol{u}}}}{\Delta t} = \nu \nabla^2 \boldsymbol{u}^{n+1} \tag{2.92c}$$

where J_e is the order of the time integration for the explicit terms (advection terms), J_i the implicit ones (diffusion terms), and γ_0, α_q and β_q are the coefficients of the multi-step implicit scheme, whose values are reported in table (2.2). The scheme requires the definition of appropriate boundary conditions for velocity and pressure; for the pressure, the following high-order boundary condition is adopted:

$$\frac{\partial p^{n+1}}{\partial n} = -\left[\frac{\partial \boldsymbol{u}}{\partial t}^{n+1} + \nu \sum_{q=0}^{J_e-1} \beta_q (\nabla \times \nabla \times \boldsymbol{u})^{n-q} + \sum_{q-0}^{J_e-1} \beta_q [(\boldsymbol{u} \cdot \nabla) \boldsymbol{u}^{n-q}\right] \cdot \boldsymbol{n} \tag{2.93}$$

Coefficient	1st order	2nd order	3rd order
γ_0	1	3/2	11/6
α_0	1	2	3
α_1	0	-1/2	-3/2
α_2	0	0	1/3
β_0	1	2	3
β_1	0	-1	-3
β_2	0	0	1

Table 2.2: Stiffly stable splitting scheme coefficients

The high-order boundary conditions for the pressure are important because without these conditions the method cannot recover the appropriate temporal convergence (Karniadakis *et al.* 1991).

Chapter 3

Wake transition and control of flows past bluff bodies

> *The more you explain it, the more I don't understand it.*
>
> Mark Twain, *A Complaint about Correspondents*

The scope of this chapter is to outline the different types of instabilities in wakes of flows past bluff bodies, specifically circular cylinders. In the first part of the chapter, after a general introduction to the problem, a classification of the different regimes of vortex shedding is presented, discussing in details the presence of three-dimensional effects. The second part of the chapter describes the main techniques used to attenuate or suppress the instabilities in flows past bluff bodies, focusing on their efficiency.

3.1 Introduction to the problem

In this thesis, we will refer a body immersed in a flow as *bluff* when, at sufficiently high Reynolds number, the flow separates over an extended part of its surface. An alternate shedding of vortices in the near wake is observed and it is responsible for significant fluctuations of the aerodynamic forces, with consequent structural vibrations, noise or resonance. Bluff bodies are encountered in a wide range of engineering applications (heat exchanger tubes, risers in marine technology, road vehicles, buildings and bridges) and

the dynamics of their wakes are complex to predict. However, an efficient control of the unsteadiness of their wakes is a fundamental problem since it might cause severe damages to the body. A prototype to investigate the physical mechanisms responsible for the development of wakes is the flow past a circular cylinder, due to its simplicity for both experimental and computational investigations; one of the main difficulties of such studies is related to the different behaviours the wake shows when the Reynolds number is increased. In the following sections, the wake patterns and the occurring instabilities in flows past a cylinder will be discussed, laying down important concepts to understand the background of the present research.

3.2 Vortex dynamics in the wake of the flow past a cylinder

The study of flows past a circular cylinder has been widely studied in the last two centuries. The first experimental investigations date back to Strouhal in 1878, who studied the effect of the wind blowing over a wire or a string (Aeolian tones). The pitch of the aeolian tone, generated by the relative motion of the wire and the air, was found to be independent from the length and the tension of the wire, but it is related just to the diameter D and the speed of the relative motion U. Within certain limits, the relation between the frequency n and the ratio U/D can be expressed by:

$$n = 0.185U/D \tag{3.1}$$

In 1879 Lord Rayleigh discussed Strouhal's work in light of the dimensional analysis, introducing a non-dimensional number known as *Strouhal number* $St = nD/U$ and showed that this non-dimensional parameter is a function of the Reynolds number of the flow, Re. His final formula, introduced in 1915 is:

$$St = 0.195\left[1 - \frac{20.1}{Re}\right] \tag{3.2}$$

At the beginning of the 20th century, Bénard and other scientists performed some experiments in water by towing a cylinder and noticed the presence of several dimples on the surface of the cylinder, produced by the presence of a staggered array of vortices rotating with opposite sign. This periodic phenomenon was called *vortex shedding* and it was found to be responsible for the Aeolian tones. However, the theoretical connection between vortex shedding and the oscillation of the drag of the bluff body was presented

by von-Kármán only in 1912. He was convinced that the wake oscillations and the alternate generation of vortices were strictly related and he investigated the linear stability of the vortex street. He found that two rows of opposite-signed vortices were unstable in both symmetric and antisymmetric configuration, with the exception of a particular arrangement characterised by $b/a = 0.28056$, where a is the distance between to vortex rows and b the inter-vortex spacing between two rows.

The analyses performed by von-Kármán left several open questions, in particular how these results were related to the vortex formation or the periodic shedding. A first physical description of the vortex formation in the near-wake was formulated by Gerrard (1966). Gerrard suggested that a forming vortex draws the opposite shear layer across the wake, eventually cutting off the supply of vorticity to the growing vortex. A better understanding of the this phenomen was given by Perry *et al.* (1982) and it is summarised in figure (3.1). At the beginning of the process, a symmetrical pair of equal and opposite recirculating-flow regions is present; when the vortices start to shed, these regions are disrupted and instantaneous patterns of fluid penetrate into the wake. According to Gerrard's interpretation, the counterclockwise vortex A grows from (a) to (d), gaining circulation from its connected shear layers, until a saddle point S is formed at the lower side of the body (e), interrupting the supply of circulation. The vortex is then shed and advected downstream.

Huerre & Monkewitz (1990) provides a description of the wake dynamics in terms of local and global modes, which are related to absolute and convective instabilities and the near wake of a bluff body is identified as a region of absolute instability. This view is crucial for this thesis and will be described in details in §5.6. Several physical quantities influence the dynamics of wakes, specifically the Strouhal number, the drag and lift coefficients, the base pressure coefficient $C_{pb} = (p_b - p_\infty)/\left(\frac{1}{2}\rho U_\infty^2\right)$ (where p_b is the pressure at a point located at 180 degrees from the stagnation point and p_∞ the static pressure at infinity), the location of the separation points, the surface shear stress, the mean velocity, the Reynolds stresses and estimates of the length and width of the domain of the vortex formation region. Bearman (1965) using a splitter place discovered that the base suction coefficient $-C_{pb}$ is inversely proportional to the formation length[1] L_f. More generally an increase in the formation length was found to be associated with a decrease in the level of the velocity fluctuations u'_{rms}/U_∞ , the two-dimensional Reynolds

[1] the vortex formation length is the point downstream of the bluff body where the velocity fluctuations are grown to maximum (Bearman 1965, Griffin & Ramberg 1974)

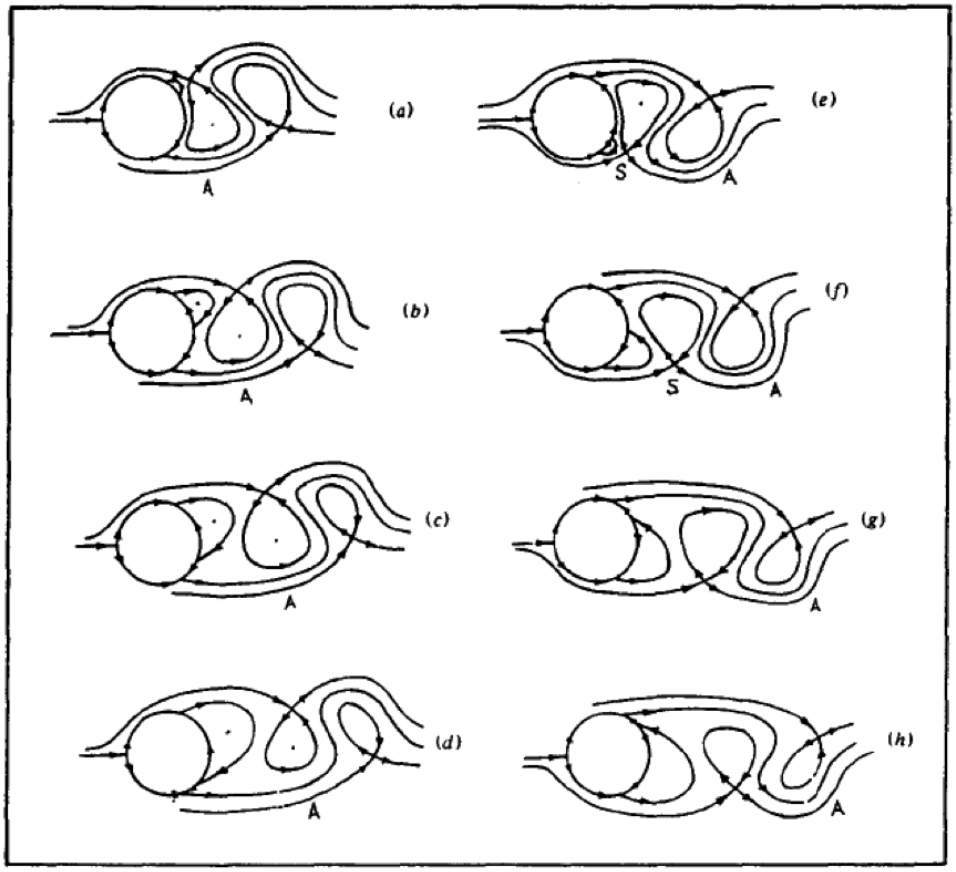

Figure 3.1: Model of vortex shedding from Perry *et al.* (1982)

stresses ($-\rho u'v'$), and in the base suction, which generates a drag reduction. However, the main parameter that governs the dynamics of the system is the Reynolds number $Re = U_\infty D/\nu$. The dependence of vortex shedding on the Reynolds number will be extensively discussed in the next section.

3.3 Classification of vortex shedding regimes

The first classification of the flow regimes as function of the Reynolds number Re is due to Roshko (1955*a*). A wide range of Reynolds numbers was investigated, from 40 to 10,000, together with measurements of the velocity fluctuations and the shedding frequency. A stable periodic laminar vortex shedding was detected for $47 < Re < 150$, a transition regime for $150 < Re < 300$ and an irregular regime for $300 < Re < 10,000$, where the velocity fluctuations showed distinct irregularities. Similar results were obtained later by Bloor (1964). Significant information about the physical mechanisms involved in the formation of vortex shedding can be obtained by plotting the variation of the base pressure coefficient C_{pb}, or the Strouhal number St, over the Reynolds number Re (figure (3.2) and (3.3) respectively). The base suction coefficient was seen to be sensitive to the process of vortex formation in the near-wake, which itself is strongly affected by the evolution of the two and three-dimensional instabilities. Increasing the Reynolds number the flow shows different types of laminar and three-dimensional transition regimes, affecting significantly the dynamics of vortex shedding.

3.3.1 Laminar Steady Regime, $0 < Re \approx 49$

When the Reynolds number is below around 49, the flow is steady, so the Strouhal number is zero. In particular for very low Reynolds number $Re < 5$, the inertial effects are negligible, thus viscous phenomena are dominant. This type of regime is called *Stokes flow*. Above $Re = 5$, the boundary layers separate from the surface and two symmetrical vortices are present on each side of the wake. The near-wake is closed and becomes more elongated when the Reynolds number is increased.

3.3.2 Laminar Vortex Shedding Regime, $49 < Re < 140 - 194$

If the Reynolds number is around 49, the behaviour becomes very different from the steady wake regime previously described. Instabilities arise at the end of the near-wake and their strength and amplification grow with Re. The onset of the wake instability near $Re = 49$ (often referred as *primary*

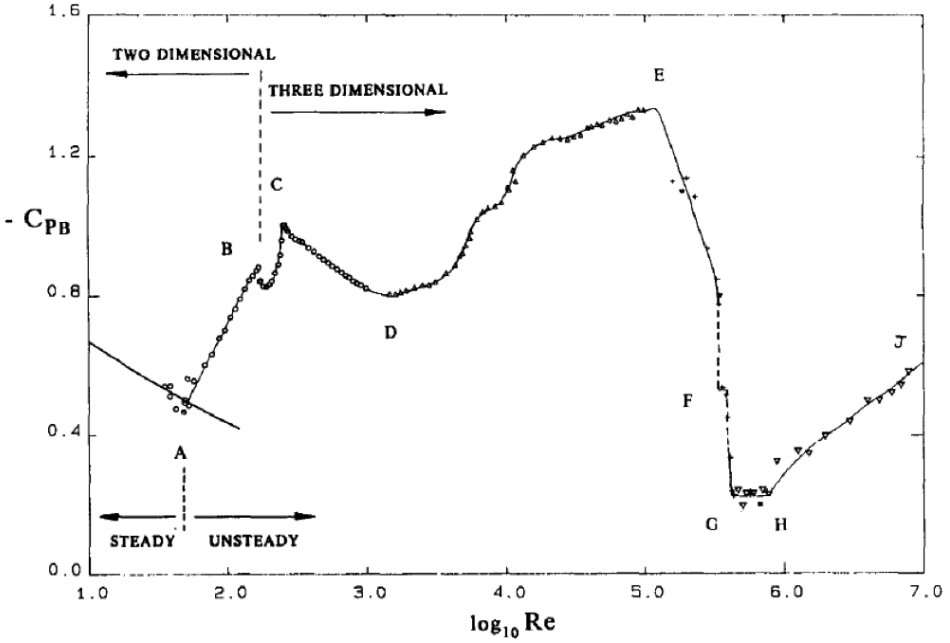

Figure 3.2: Plot of the base suction coefficient $-C_{pb}$ over Reynolds number (Williamson, 1996b).

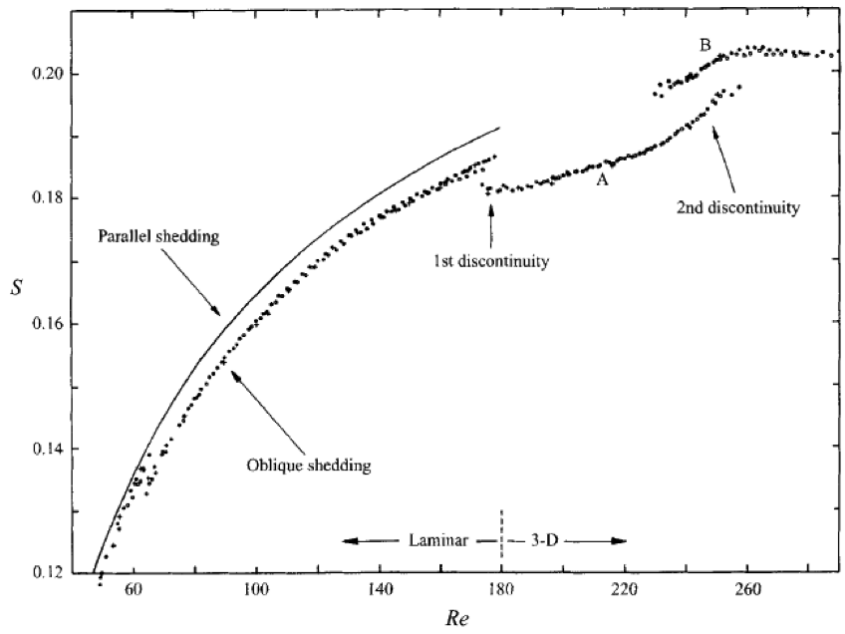

Figure 3.3: Plot of the Strouhal number over Reynolds number (Williamson, 1996b).

instability) was found to be a Hopft bifurcation[2] and the flow can be modelled as a dynamical system using the Stuart-Landau equation (Provansal *et al.*, 1987). As the instabilities arise, the Reynolds stresses in the near-wake region increase and the formation length decreases, together with a relevant increase in the base suction. The flow is two-dimensional, laminar and the wake oscillation are purely periodic, with a single frequency if vortex shedding is parallel in the spanwise direction[3]. Furthermore, the Strouhal number increases with the Reynolds number as a consequence of the unsteadiness of the flow.

3.3.3 3-D Wake Transition, $190 < Re < 1000$

Transition phenomena occur when the Reynolds number approaches 190 and the wake develops a secondary instability, which is three-dimensional and streamwise vortex pairs appear (Williamson 1996b, 1996a); this type of instability is referred as "Mode A" and can be detected from the discontinuity in the variation of the Strouhal number or the base suction, as shown in figures (3.3) and (3.2). Increasing further the Reynolds number, a second discontinuity appears over a range of Re from 230 to 250, where there is a gradual transfer of energy from Mode A to a new mode, known as "Mode B", characterised by finer scale streamwise vortices, with a spanwise length scale of around one diameter. In this regime, local shedding-phase dislocations along the span cause large-scale spots, which are known as *vortex dislocations* (Williamson 1992a, Lewis & Gharib 1992). The appearance of Mode A and B was confirmed by the results obtained by Barkley & Henderson (1996) using stability analysis, as we will discuss in details in §3.4.2.

3.3.4 Shear-Layer Transition regime, $1000 < Re < 200,000$

In this regime, the boundary layer is still laminar and separation effects are observed at around 80°. In the free shear-layers a Kelvin-Helmholtz instability is developed and small vortices are observed, known as Bloor-Gerrard vortices. Bloor (1964) showed that these vortices generate a frequency in the wake which varies roughly as $Re^{3/2}$, differently from the Karman vortices, which cause a frequency with a linear dependence on the Reynolds number. In this regime, the base suction and the Reynolds stress level increase again, while the Strouhal number and the formation length both decrease.

[2] A Hopf bifurcation typically occurs when a complex conjugate pair of eigenvalues of the linearised dynamical system at a fixed point becomes purely imaginary

[3] This condition can be achieved by a proper manipulation of the boundary conditions (Henderson 1994, 1995).

Three-dimensional structures on the scale of the shear layer vortices are present, as well as on the scale of the von-Kármán vortices (Wei & Smith 1986, Williamson et al. 1995).

3.3.5 Critical Transition Regime, $200,000 < Re < 700,000$

In the critical transition regime, a separation/re-energisation bubble is observed; this bubble re-energises the boundary layer, which separates further downstream at about 140°, and produces a reduction of the width of the downstream wake with respect to the laminar case. This phenomenon generates a noteworthy reduction of drag and base suction. The separation/re-energisation bubble might occur on only one side of the bluff body, causing a bistable configuration with large mean lift forces ($C_L = 1$), as found by Bearman (1969) and Shewe (1983).

3.3.6 Supercritical regime, range G-H

In the supercritical regime, the flow is symmetric and presents two separation-reattachment bubbles on each side of the body. The wake is particularly thin and fluctuations are observed at large Strouhal numbers (around 0.4), as shown by Bearman in 1969. The Reynolds stresses of the boundary layer are considerably high, allowing the boundary layer to survive the strong adverse pressure gradient (Roshko, 1993).

3.3.7 Post-Critical Regime, range H-J

When the Reynolds number is further increased, the transition point moves further upstream, until the flow becomes turbulent.

As discussed in this section, the progressive increase of the Reynolds number is associated with three main types of shear flow instabilities, namely a wake transition, followed by the shear layer transition and boundary layer transition. In the present work, we will consider just the first stage (wake transition); in the next section we will describe the three-dimensional effects of the laminar vortex shedding, which is important for the studies we will perform in the following chapters.

3.4 Three-dimensionality in the laminar vortex shedding regime

An important feature of the nominally two-dimensional flows around bluff bodies is the presence of relevant three-dimensional effects. A flow is said to be *nominally two-dimensional* if the physical quantities show anisotropic irregularities along the span, therefore only their time-averaged values are zero in the spanwise direction. As discussed by Williamson (1996b), there are two mechanisms responsible for the three-dimensional effects observed in the laminar vortex shedding regime: external effects, which are generally end effects associated with the aspect ratio of the bluff body, and the natural instabilities arising in the flow.

3.4.1 End effects: oblique shedding

Evidence that vortices can shed at an oblique angle with respect to the axis of the cylinder has been recognised since the seventies; this phenomenon is known as *oblique shedding* and it was first discussed by Berger & Wille in 1972, who found typical oblique angles of 15-20°. Earlier experiments performed by Tritton in 1959 showed discontinuities in the dependence of the Strouhal number on the Reynolds number in the laminar shedding regime. The relation between these two phenomena was investigated for over thirty years, producing a large amount of scattered measurements, until in 1989 Williamson showed that the discontinuity observed by Tritton is caused by a change from one mode of oblique shedding to another. The boundary conditions at the end of the cylinder are the critical factor and are responsible for the angle of shedding over the span. Williamson performed experiments in a towing tank and wind tunnel and found that the initial parallel shedding is distorted by the end effects of the cylinder. The vortices formed an oblique or periodic *chevron* pattern and the $St-Re$ discontinuity seen in figure (3.4) was observed.

In the context of oblique waves, an interesting result was obtained by means of the Squire's transformation (1933). For a given wake profile and Reynolds number, in a parallel flow, if the frequency and the temporal growth of the most unstable 2D-wave are f_o and σ_o, then for an oblique wave at angle θ, the most unstable frequency and growth are $f_\theta = f_o \cos\theta$ and $\sigma_\theta = \sigma_o \cos\theta$. respectively. From such theoretical considerations, Williamson showed it is possible to define a universal Strouhal curve and the oblique shedding Strouhal number St_θ can be collapsed onto the parallel shedding Strouhal number St_o by the transformation $St_o = St_\theta / \cos\theta$. These results suggested

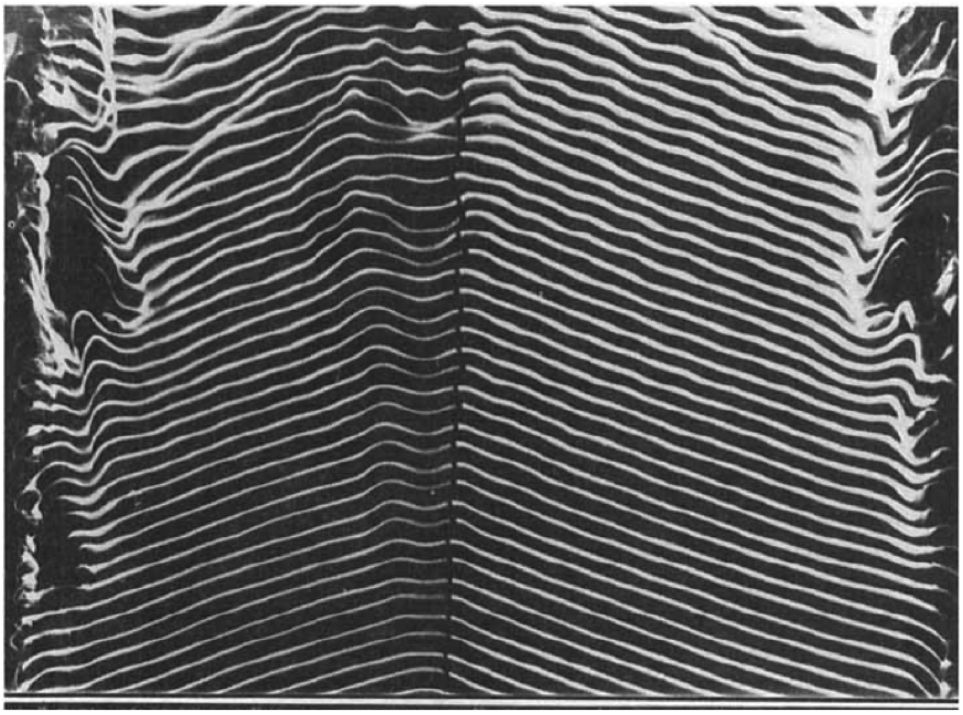

Figure 3.4: Oblique shedding mode in the wake of a circular cylinder at $Re = 85$ (flow is upwards past a horizontal cylinder). The oblique vortices have propagated inwards from the end to form a chevron-shaped pattern that covers the whole span of the cylinder (Williamson, 1989).

that it is possible to promote parallel shedding by manipulations of the end conditions. This phenomenon can be achieved by several mechanical devices: angling inwards the leading endplates (Williamson 1988a, 1989), ending the span with larger coaxial cylinder (Eisenlohr & Eckelmann 1989), using suction tubes from downstream (Miller & Williamson 1994) or using control cylinders orthogonal to the test cylinder (Hammache & Gharib 1991). These techniques are shown in figure (3.5).

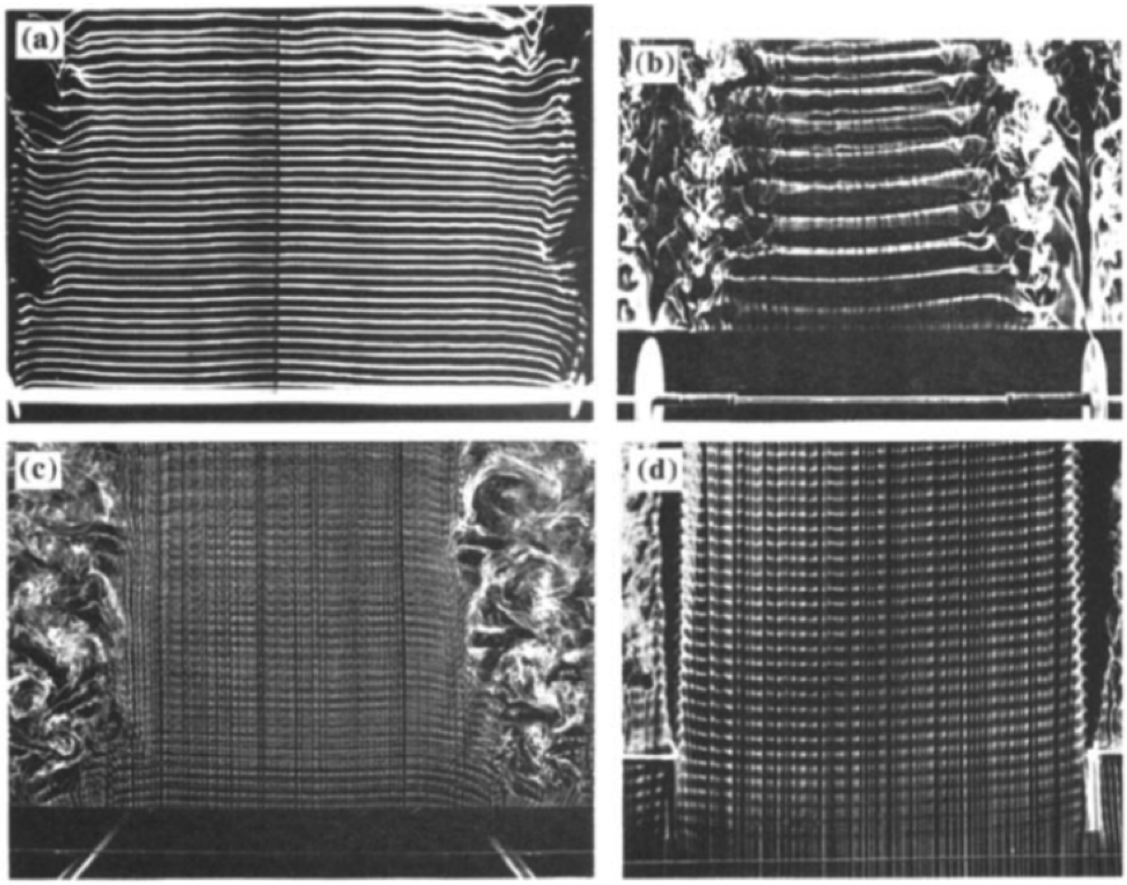

Figure 3.5: Parallel two-dimensional shedding induced by manipulations the end boundary conditions: (a): angled end (Williamson, 1988a), (b): coaxial end cylinder (Eisenlohr & Eckelmann, 1989), (c: control cylinders orthogonal to the test cylinder (Hammache & Gharib, 1991), (d): suction tubes from downstream (Miller & Williamson, 1994).

3.4.2 Natural three-dimensional effects in the transition regime

A second type of three-dimensional effects arising in flows past cylinders are independent from the boundary conditions and are instead associated with the natural instabilities of the wake. Roshko (1955*a*) suggested the presence of transitional phenomena in the separating shear layers, before the vortices were fully formed and shed from the cylinder, and detected high frequency oscillations of the velocity. Hama (1957) related these oscillations to the appearance of three-dimensional effects in the near-wake, which appeared as a three-dimensional waviness on the primary von-Kármán vortices, which Gerrard (1978) called "fingers of dye". Williamson (1988b, 1992a) showed that these "fingers" are associated with the vortex loops and streamwise vortices, similarly to other free shear flows. Further investigations were carried on in the eighties: Wei & Smith (1986) related the high-frequency velocity oscillations to the development of secondary vortices, hypothesising that the 3D-stretching of these secondary vortices are responsible for the appearance of the streamwise vortices in the wake. Williamson (1988b, 1992a) performed a wide range of experiments to determine the variation of the Strouhal number with the Reynolds number (see figure (3.3)), noting that the wake has a two-dimensional behaviour until a critical Reynolds number is reached ($Re = 180 - 194$), with a consequent discontinuity in the curve. This behaviour is called mode A (see section § 3.3.2) and it is characterised by a wavy deformation of the vortices along the spanwise direction, with characteristic wavelengths around 3-4 diameters. This process is self-sustaining due to the Biot-Savart induction from one loop to the next and shows similar length scales to the "in-phase" mode, related to the formation of the vortex loops in an unseparated wake (Meiburg & Lasheras, 1988). When the Reynolds number is further increased ($Re = 230 - 250$), a new type of three-dimensional instability appears, which is known as mode B. This instability presents finer-scale vortices, which are more regulara than those found in Mode A and have smaller wavelengths, usually around one diameter. The structures of these two instabilities are reported in figure (3.6).

A peculiar feature of the three-dimensional transition is the appearance of large-scale structures, of order 10-20 diameters, between spanwise cells with different shedding frequencies. These structures were widely investigated by Williamson (1992a), Lewis & Gharib (1992), Bearman (1992), Eisenlohr & Eckelmann (1989), Papangelou (1992) and they are called vortex dislocations. Their presence helps to explain the large intermittent velocity irregularities found by Roshko (1955*a*) in 1954 and they have a prominent role in

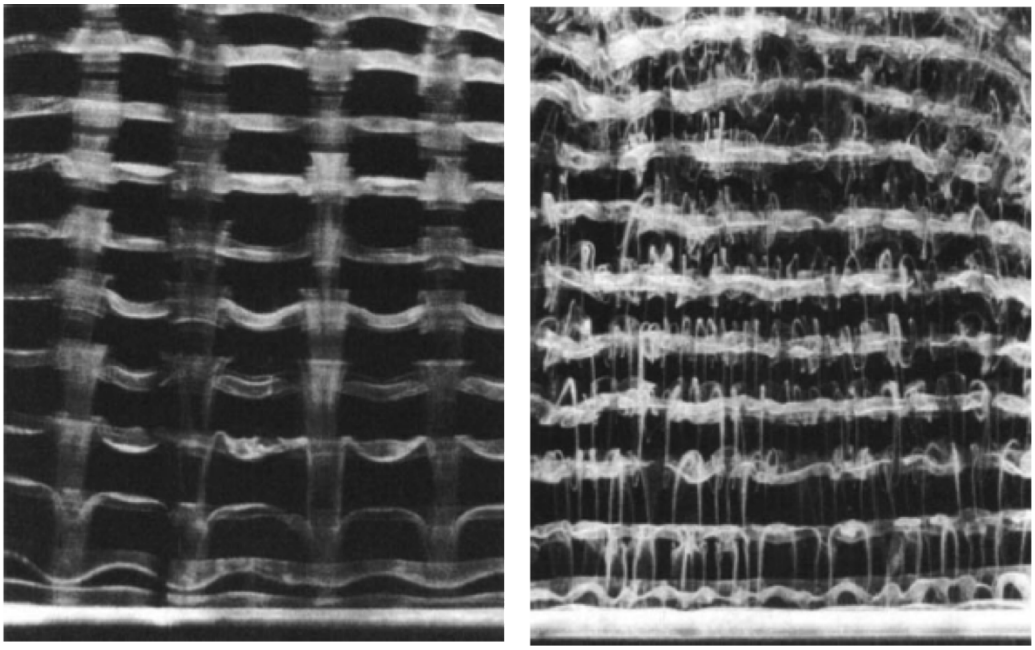

Figure 3.6: Experimental visualisation of mode A (left) and mode B (right) instabilities. The flow streams from the bottom to top (Williamson, 1992a).

explaining the mechanism leading to turbulence. To study the structure of the vortex dislocations Williamson (1992) forced the generation of the dislocations using a small ring on a cylinder, creating spanwise cells shedding at different frequencies. The ring generated low-frequency periodic structures f_R, which evolved into the vortex dislocations with a frequency $f_C - f_R$, where f_C is the frequency associated with the main cylinder. Vortex dislocations were found to spread rapidly along the spanwise direction and tend to be generated in the regions where the vortex loops evolve.

The first computational studies of the wake transition were performed by Karniadakis & Triantafyllou in 1992 using spectral/*hp* element methods, but the main conclusions were later proved to be incorrect due to the small size of the domain, which was incapable of capturing the underlying physical mechanisms. Zhang *et al.* in 1995 repeated the computations with a larger domain and were able to reproduce the mode A and B instabilities in accordance with the experimental investigations. Furthermore, they found an additional three-dimensional instability (mode C); this instability was observed when a thin wire was placed parallel to the cylinder axis in the near wake, slightly offset from the wake centreline. This mode was seen to

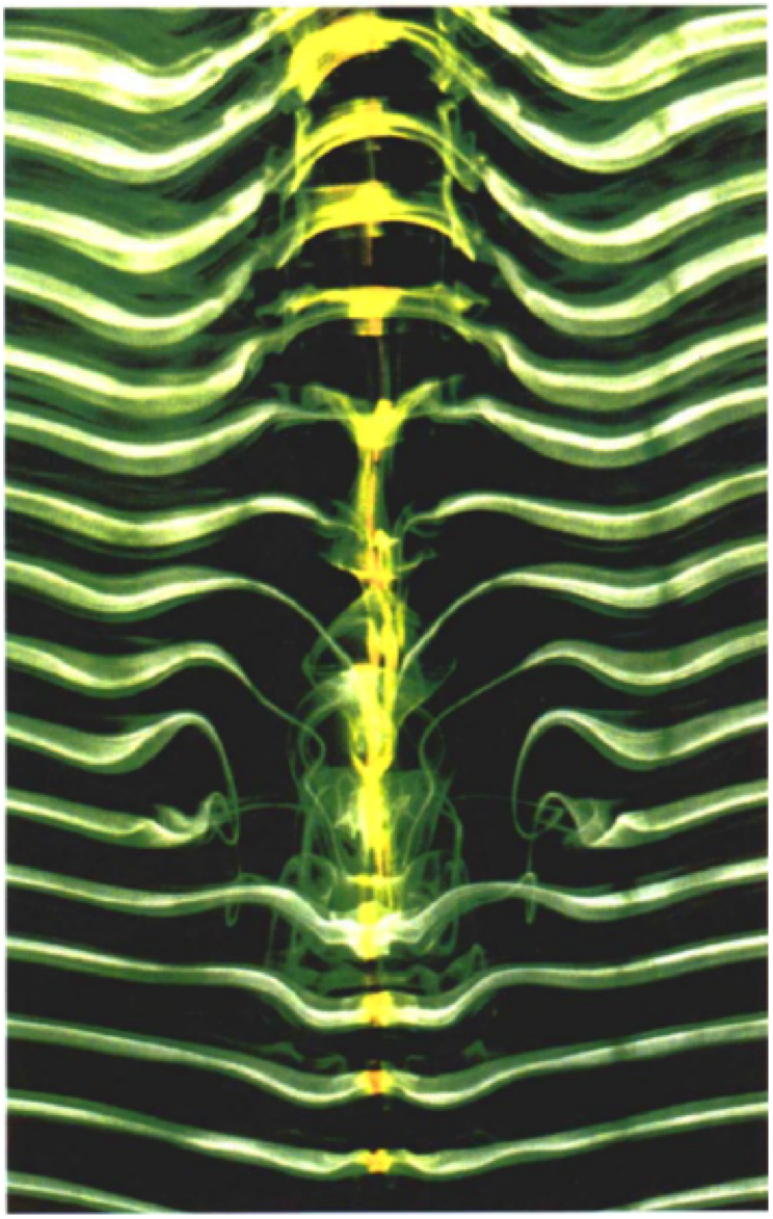

Figure 3.7: Vortex dislocation induced by means of a small ring disturbance around the cylinder. Flow is upwards past an horizontal cylinder at Re=140 (adapted from Williamson, 1992a).

affect the forces acting on the cylinder more intensely than mode A and B, and it was suggested it was not related to the asymmetry in the wake.
From the middle nineties, computational investigations of the flow past a cylinder were combined with results from the global stability analysis (we will discuss it in chapter §4), providing fundamental improvements in the description of the relevant mechanisms behind the instabilities. Barkley & Henderson (1996) performed a three-dimensional Floquet stability analysis of the wake in a specific range of Reynolds numbers ($140 \leq Re \leq 300$). They showed that the two-dimensional wake becomes absolutely unstable via a secondary instability. The main parameters that characterise the instability are the Reynolds number, Re, and the wavenumber of the spanwise perturbations, $\beta = 2\pi/\lambda_z$, where λ_z is the corresponding wavelength. A first critical Reynolds number was found at $Re = 188.5$ and a critical spanwise wavelength $\lambda_z = 3.96D$. This corresponds to Mode A reported by Williamson (1988). A second instability was detected at $Re = 259$ for a spanwise length $\lambda_z = 0.822D$, which corresponds to Mode B. The important role of the end effects was discussed and the hysteresis in bifurcation behind Mode A, already detected in the experiments, was confirmed. Despite the extensive investigations on the structure of the three-dimensional wakes in the transition regime, the physical mechanisms responsible for the onset of the instabilities were highly debated. Brede *et al.* (1996) proposed that Mode A is a centrifugal instability of the braid region between the primary vortices, while Mode B is caused by the three-dimensional effects of the separated shear layers in the near-wake. Williamson (1996) suggested instead that Mode A originates from an elliptic instability in the vortex cores, while Mode B is due to a hyperbolic instability of the braid shear layer. However, Henderson (1997) pointed out that the classification of Mode A as elliptic is not appropriate since the Floquet analysis shows that the maximum amplification occurs between the vortices rather than in their cores. Thompson *et al.* (2000) showed that despite Mode A is not purely elliptic, it shows some distinctive elliptic features. Starting from a Floquet analysis, the leading mode was split into two mutually exclusive parts. The first part is characterised by a velocity field which is zero in the region where the elliptic instability indicated that the flow as not elliptic. For the second, the reverse was done. Therefore, the velocity field was split into an elliptic and hyperbolic component. The evolution of these components, showed that after many shedding cycles they both evolve back to the Floquet mode. However, the first component evolved more quick than the second one. A quantitative comparison showed that mode A is 2/3 elliptic and 1/3 hyperbolic and the dominance of the elliptic instability in the initiation and

maintenance of the perturbations was further confirmed in 2001 by Thompson, Leweke & Williamson.
Finally, Blackburn & Lopez (2003a) investigated an additional unstable mode in the wake of a cylinder at higher Reynolds number, $Re = 377$. This mode is called mode QP, for quasi-periodic, and has a wavenumber between those of mode A and B; Blackburn *et al.* (522) used the concept of the symmetry theory, introduced by Marques *et al.* (2004), to study the bifurcations of wakes of bluff bodies.

3.5 Control of flows over bluff bodies

As mentioned at the beginning of the chapter, the presence of vortex shedding in wakes of bluff bodies generates a significant pressure drop on the rear of the body in a wide range of Reynolds number, causing structural vibrations, acoustic noise and resonance, enhanced mixing and a significant increase in the the drag and lift fluctuations. Therefore, an effective control to weaken or suppress vortex shedding is fundamental in many applications; in the following section, an overview of the most significant control methods is given.

3.5.1 Overview and classification of the control methods

Control methods of flows past bluff bodies can be classified in three main categories: passive, active open-loop and active closed-loop (or feedback control) respectively (Choi *et al.*, 2008). Passive controls are characterised by the absence of a power input, while a power input is always present in active control techniques. Active open-loop controllers do not use any feedback to control the output, while close-loop controllers use sensors to monitor the system output and then feed the data back to the controller where the signal is adjusted properly. Another important classification can be introduced considering the presence of eventual geometric modifications in the spanwise direction. Two-dimensional control techniques are characterised by a constant control input in the spanwise direction; an example is the introduction of a short splitter plate, of about one diameter in length, behind the bluff body. Roshko (1955*b*) was the first to adopt this technique and showed that the splitter plate was able to create a strong interference with vortex shedding, which was eventually suppressed. Base bleed is another two-dimensional control technique and its application dates back to Wood (1964) and Bearman (1967). The introduction of bleed air through a hole in the centre of the base generates a profile of vorticity of opposite sign with

respect to the one introduced by the boundary layers separating from the body surface, leading to the suppression of vortex shedding. Other successful two-dimensional passive control techniques include the end plates (Nishioka & Sato 1974; Stansby 1974) and secondary small cylinders (Strykowski & Sreenivasan, 1990). Three-dimensional control techniques are characterised instead by a variation of the actuation property along the spanwise direction; some examples are reported in figure (3.8): Zdravkovich (1981) introduced helical strakes to reduce the fluctuations of the aerodynamic forces, which were recently studied in a linear stability context (Gomez *et al.* 2014), Tanner (1972), Rodriguez (1991), Petrusma & Gai (1994) studied the effect of a segmented trailing edge. Tombazis & Bearman (1997) introduced a wavy trailing edge and found that the waviness produces vortex dislocations in the wake, with a subsequent increase in the base pressure. Bearman & Owen (1998) used a spanwise waviness in the front stagnation face of a rectangular cylinder, obtaining a complete suppression of vortex shedding. However, a waviness on the rear surface was found not to reduce the drag since the separation occurs at the front edge. Owen *et al.*(2000, 2001) applied the same methodology to a circular cylinder and obtained similar results inserting a waviness along the axis of the cylinder and spirally attaching hemispherical bumps on the surface. Darekar & Sherwin (2001) performed DNS of a flow past a cylinder with a wavy stagnation face at low Reynolds number and showed that the von-Kármán street can be suppressed into a steady and symmetric structure. They pointed out that the suppression is caused by a distortion of the shear layers and found that the optimal wavelength is close to the wavelength of Mode A instability. Park *et al.* (2006) proposed a small-size tab on the upper and lower trailing edges. The height (l_y) and width (l_z) of the tabs were changed, together with the spacing between two adjacent tabs (λ). The drag was seen to be reduced and the optimal configuration produced an increase of 3% in the base pressure. The presence of the tabs caused the vortices to lose their eventual two-dimensional nature and vortex dislocations occurred. Vortex shedding completely disappeared right behind the bluff body but occurred weakly at farther downstream locations. The main mechanism of drag reduction related to the adoption of tabs was found to be the introduction of a phase mismatch in vortex shedding, which can break the nominally two-dimensional nature of the phenomenon. Yoon (2005) applied tabs to stabilise the wake of a flow past circular cylinder and found that tabs located near the separation point attenuate vortex shedding, and the optimal spacing of the adjacent tabs is similar to the optimal wavelenght of the waviness found by Darekar & Sherwin (2001).

However, active open-loop control techniques have not attracted the atten-

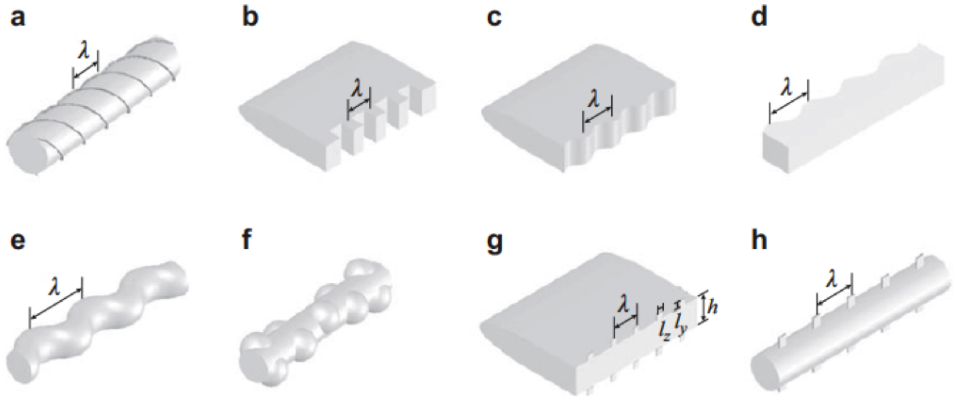

Figure 3.8: Three-dimensional passive control technique: *(a)* helical strake, *(b)* segmented trailing edge, *(c)* wavy trailing edge, *(d)* wavy stagnation face, *(e)* sinusoidal axis, *(f)* hemispherical bump (*g*),*(h)* small-size tab. Adapted from Choi *et al.* (2008).

tion of the scientific community until the nineties, with the exception of the base bleed (Bearman 1967, Wood 1964). The main reason is probably their complexity and rather low efficiency, despite their effectiveness to reduce the drag (Choi *et al.* 2008). The first theoretical studies on active controllers were performed by Blevins (1990), who showed that, when a time-periodic open-loop force is applied on the surface of the bluff body, vortex shedding is locked in phase to the forcing, hence the forcing strengthens the von-Kármán street and increases the mean drag and lift fluctuations. Tokumaru & Dimotakis (1991) were able to suppress vortex shedding in a flow past a circular cylinder by means of high-frequency rotations. More recently Kim & Choi (2005) investigated the effect of a three-dimensional forcing on the surface a circular cylinder. In their analysis they considered a wide range of Reynolds number ($47 < Re < 3900$) and imposed a steady blowing and suction profile on two slots, located at the upper and lower surfaces of the cylinder, expressed by the following equation:

$$\phi_1(z) = \phi_2(z) = \phi_0 \sin\left(\frac{2\pi z}{\lambda}\right) \tag{3.3}$$

where ϕ_1 and ϕ_2 are the radial velocities at the upper and slower slots, respectively, z is the spanwise direction, ϕ_0 the forcing amplitude and λ the forcing wavelength. This technique was seen to be very effective, leading to a complete suppression of vortex shedding at moderate/low Reynolds numbers, while it weakly reappears in the far wake for higher Reynolds numbers. Kim *et al.* (2004) applied the distributed forcing to a turbulent flow over a

two-dimensional model vehicle with a blunt trailing edge, obtaining a noteworthy drag reduction. Due to the effectiveness and versatility of this control method, a similar technique will be used in the chapter 5 to investigate the main features underlying to the suppression of the von-Kármán street.

Feedback control methods require a further classification, specifically single-sensor feedback controls, optimal/suboptimal controls and controls based on ROMs. Since at Reynolds numbers just above the critical value, the wake has generally just one unstable mode, resulting from the von-Kármán vortex shedding, a single-sensor actuator feedback loop is sufficient. The first applications date back to 1967 when Berger actuated a bimorph cylinder with signals from a hot-wire sensor located in the wake. Williams & Zhao (1989) reduced the velocity fluctuations of vortex shedding at $Re = 400$ using a loudspeaker controlled by the velocity phase of a specific point of the wake. Roussopoulos in 1993 conducted a similar experiment and came to the conclusion that a single-sensor feedback loop cannot stabilise the wake at high Reynolds numbers. Huang (1996) used a control device that measured the velocity in the region of the upper shear layer of a circular cylinder and used it to drive a loudspeaker, which generated sound from the slot on the upper surface. The feedback sound was able to suppress vortex shedding even if the controller acted just one side of the cylinder, demonstrating that vortex shedding is associated with an instability involving two parallel shear flows. More recently, Zhang *et al.* (1995) developed an efficient proportional-integral-derivative (PID) controller to suppress the in-phase vortex shedding and vortex-induced vibrations on a spring supported square cylinder at the resonance conditions.

Optimal control theory[4] has sparked noteworthy interest recently, but its applications in real situations is not possible since it requires the knowledge of the full flow field, for a global time period, to solve the adjoint equations. A feasible approach is instead the suboptimal feedback control algorithm, which consists of seeking an optimal condition over a short time period. Min & Choi (1999) applied this method to a circular cylinder at $Re = 100$ and 160; they chose the difference of the real and potential pressures on the surface of the cylinder as a cost function to be minimised, while the control input was the instantaneous surface pressure. One of the main difficulties of the suboptimal approach relies on its strong dependance on the cost function. For example, as shown by Min & Choi (1999), the reduction of the drag is better achieved when the cost function is the difference of the real

[4]It is a mathematical optimisation method, firstly derived by Pontryagin. It generally involves the solution of an adjoint system of equations. Further information can be found in Abergel & Teman (1990)

and potential flow surface pressures rather than the drag itself. The explanation is the non-linearity of the cost function with respect to the control input, requiring an *a priori* physical knowledge of the flow physics. Single-sensor measurement is a suitable technique at low Reynolds numbers, when the wake has just one unstable mode resulting from the von-Kármán vortex shedding. However, at higher Reynolds numbers multiple unstable modes are present, hence several feedback sensors to estimate the flow field are required. The main technique used in these cases is the *Reduced-Order Models* (ROM); the idea is to extract the most relevant energetic modes from the flow field by means of a proper orthogonal decomposition, often referred as POD, and use them to design a low-dimensional controller (Holmes *et al.* 1996). Graham *et al.* (1999) used this method to control the flow past a rotating circular cylinder at $Re = 100$. The control input was the cylinder rotation and they were able to reduce the unsteadiness of the wake, although the prediction errors were seen to increase during the control, so, to overcome this problem, they had to reset the ROM periodically. Other applications of ROM are the adoptions of vortex models when the wake is mainly governed by vortices. Such approach was firstly used by Cortelezzi (1996) in a boundary layer context and then extended to bluff bodies by Li & Aubry (2003) , who successfully suppressed the lift fluctuations at $Re = 100$ and 200 (Föppl's potential flow model). The main problem of ROM comes from its non-equivalence to the full Navier-Stokes equations and this issue might lead to a local optimum of the original dynamical system. Besides, controllability and observability of the retained modes are two important problems of ROM.

A last important classification of the control methods considers what region needs to be modified: the boundary layer or the wake respectively. In boundary layer control methods the drag reduction is achieved by changing the structure of the boundary layer from laminar to turbulent, delaying the separation. This control is particularly suitable for bluff bodies with a movable separation points and an important application is the adoption of a surface roughness. Achenbach (1972, 1974) showed that the introduction of a roughness element on the bluff body results in a local minimum of the drag coefficient at a specific critical Reynolds number, which was seen to decrease with the increasing effect of the roughness. Another technique to enhance the direct transition to turbulence is a vortex generator at the leading edge, which introduces streamwise vorticity into the boundary layer, causing strong near-wall momentum and a consequent delay of the main separation. A further boundary layer control is based on the generation of strong near-wall momentum by early separation and reattachment

of the flow, which generates a separation bubble above the surface of the bluff body. This effect can be achieved by means of a trip wire at the front surface (Maxworthy, 1969), transverse groove (Kimura & Tsutahara, 1991), free-stream turbulence (Blackburn & Melbourne 1996, Kiya *et al.* 1982), surface dimples (Choi *et al.*, 2006). Conversely, another methodology to control vortex shedding is by a direct-wake modification, delaying the interaction of the shear layers (splitter plates and base bleed) or changing the wake directly, through geometric or dynamic change in the system (wavy trailing edge and distributed forcing).
A last interesting control device is the synthetic jet, which was introduced by Glezer and his co-workers in the nineties (Glezer & Amitay 2002, Smith & Glezer 1998). The main idea is to generate vortices at the edge of an orifice by the time-periodic motion of a flexible diaphragm in a seal cavity; a non-negligible amount of momentum is transferred to the flow, despite the net mass flux is zero. The synthetic jet was applied to a flow over a circular cylinder at several high Reynolds numbers ($Re = 31,000$ and $131,000$), and the application of a high-frequency forcing from the synthetic jet produced a noteworthy drag reduction, despite the lift was increased due to the installation of the actuator at just one side of the cylinder. The problem was found to be insensitive to the forcing frequency.

3.5.2 Estimation of the control efficiency

An important problem is the definition of a suitable efficiency for the control method. This issue is particularly complex for active controllers since it depends on the specific device. Choi *et al.* (2008) defined the control efficiency as the ratio of the saved power to the control input power, neglecting any additional loss inside the mechanism of the controller. If the control input is a forcing over the bluff body surface, similar to the method adopted in chapter 5 of this thesis , the ideal control efficiency is given by:

$$\eta_1 = \frac{(D_u - D_c)u_\infty}{\int_A \left(\frac{1}{2}\rho\phi^3 + p_w\phi\right) dA} \tag{3.4}$$

where D_u and D_c are the drags of the uncontrolled and controlled problem respectively; A is the body surface, ρ the density, p_w the surface pressure and ϕ the control velocity. The first term inside the integral represents the energy convection, whereas the second the pressure work. However, this definition describes an ideal efficiency, since it is hypothesised that the control can fully utilise all the available power sources. A slightly different definition can then be introduced, which takes into account the fact that it

is not possible to use entirely the power sources available in the flow system:

$$\eta_2 = \frac{(D_u - D_c)u_\infty}{\int_A \left(\left| \frac{1}{2}\rho\phi^3 \right| + |p_w\phi| \right) dA} \tag{3.5}$$

Equation (3.5) is a good method to evaluate the efficiency of a controller and, if $\eta_2 \gg 1$, the additional losses inside the device are not particularly relevant. Kim & Choi (2005) showed that the suppression of the shedding via distributed forcing is highly efficient, in fact $\eta_1 \approx 150$ and $\eta_2 \approx 30$. For the base bleed, $\eta_2 \approx 3.8$, while η_1 is negative because $p_w\phi < 0$.

Chapter 4

Hydrodynamic stability theory

> *Philosophy is written in that great book which ever lies before our eyes - I mean the universe - but we cannot understand it if we do not first learn the language and grasp the symbols, in which it is written. This book is written in the mathematical language, and the symbols are triangles, circles and other geometrical figures, without whose help it is impossible to comprehend a single word of it.*
>
> Galileo Galilei, *The Assayer*

In this chapter the hydrodynamic stability theory is introduced; this theory is useful to investigate both qualitatively and quantitatively the dynamics of the instabilities and provides useful information on the implementation of efficient controllers. In the first part of the chapter the theoretical framework of the direct stability analysis is outlined, starting from the problem of defining the stability of a given flow and then introducing the local and global approaches. The second part of the chapter is dedicated to the introduction of the adjoint Navier-Stokes equations and the solution of the adjoint stability problem, which is directly connected to the receptivity of the flow to momentum forcing and mass injection. The concomitant evaluation of the direct and adjoint modes leads to the concept of structural sensitivity, which is necessary to detect the core of the instabilities. Besides, the transient growth methodology is explained in order to study the dynamics of the convective instabilities within the global stability analysis. Finally,

all these concepts are applied to a two-dimensional flow past a cylinder, and, in particular, emphasis is given to their implications on the passive control of the wake.

4.1 Derivation of the linearised Navier-Stokes equations

Hydrodynamic instability is a field of fluid mechanics which deals with the response of a laminar flow to disturbances of small or moderate amplitudes. A first intuitive approach to the concept of stability is to check if a given flow, perturbed by arbitrary small perturbations, returns to its original state or evolves into a new different state. In the former case, we can define the flow as stable, in the latter as unstable. Instabilities can often result in a turbulent flow, but sometimes they lead to a different laminar state. The equations which describe the evolution of disturbances can be obtained considering a base flow (or basic state) $(\boldsymbol{U}, P)$ and a perturbed state $(\boldsymbol{U} + \varepsilon\boldsymbol{u'}, P + \varepsilon p')$, with $\varepsilon \ll 1$, which both satisfy the Navier-Stokes equations. Substituting the perturbed state into the Navier-Stokes equations (2.3)-(2.4), we obtain:

$$\nabla \cdot \boldsymbol{U} + \varepsilon \nabla \cdot \boldsymbol{u'} = 0 \tag{4.1a}$$

$$\begin{aligned} &\left(\frac{\partial \boldsymbol{U}}{\partial t} + \boldsymbol{U} \cdot \nabla \boldsymbol{U} + \nabla P - \frac{1}{Re}\nabla^2 \boldsymbol{U}\right) + \\ &+ \varepsilon \left(\frac{\partial \boldsymbol{u'}}{\partial t} + \boldsymbol{U} \cdot \nabla \boldsymbol{u'} + \boldsymbol{u'} \cdot \nabla \boldsymbol{U} + \varepsilon \boldsymbol{u'} \cdot \nabla \boldsymbol{u'} + \nabla p' - \frac{1}{Re}\nabla^2 \boldsymbol{u'}\right) = 0. \end{aligned} \tag{4.1b}$$

Since the base flow $(\boldsymbol{U}, P)$ satisfies the Navier-Stokes equations, the first terms on the left hand sides of (4.1a) and (4.1b) are zero; the non-linear terms $\boldsymbol{u'} \cdot \boldsymbol{u'} \sim o(\varepsilon^2)$ are one order of magnitude smaller than the other ones, hence they can be neglected. These considerations lead to the linearised Navier-Stokes equations:

$$\nabla \cdot \boldsymbol{u'} = 0 \tag{4.2a}$$

$$\frac{\partial \boldsymbol{u'}}{\partial t} + \boldsymbol{U} \cdot \nabla \boldsymbol{u'} + \boldsymbol{u'} \cdot \nabla \boldsymbol{U} = -\nabla p' + \nu \nabla^2 \boldsymbol{u'} \tag{4.2b}$$

However, to describe properly the evolution of an initial disturbance, it is important to define a quantity to measure its size. A suitable choice is the kinetic energy of the disturbance E_V contained in a control volume V:

$$E_V = \frac{1}{2}\int_V \boldsymbol{u'} \cdot \boldsymbol{u'} dV. \tag{4.3}$$

The choice of the control volume V generally depends on the particular geometry of the flow.

4.2 Definition of stability and critical Reynolds numbers

The formal definition of stability of a flow state is based on the disturbance kinetic energy E_V, which is expressed by expression (4.3) (Schmid & Henningson, 2001). A first definition considers an asymptotic limit of the disturbance kinetic energy for large times.

Definition

A solution $\boldsymbol{U}$ to the Navier-Stokes equations is *asymptotically stable* to perturbations if the perturbation kinetic energy satisfies the following condition:

$$\lim_{t\to\infty} \frac{E_V(t)}{E_V(0)} = 0; \tag{4.4}$$

According to this definition, the stability of a system depends only on the asymptotic behaviour of the ratio of the disturbance energy with respect to its value at the initial time. However, the stability of the problem could depend on the initial energy of the perturbation, therefore a definition of conditional stability is required:

Definition

A solution $\boldsymbol{U}$ to the Navier-Stokes equations is said to be *conditionally stable* if there exists a threshold energy $\delta > 0$ such that the flow is stable when $E(0) < \delta$.

A special case of conditional stability is the concept of global stability:

Definition

If a flow is conditionally stable and the threshold energy is infinite ($\delta \to \infty$), the flow is said to be *globally stable*.

Finally, one last definition can be given, considering a flow whose perturbation energy decreases for all times, not just in the asymptotic limit.

Definition

A solution $\boldsymbol{U}$ to the Navier-Stokes equations is said to be *monotonically stable* if:

$$\frac{dE_V}{dt} < 0, \quad \forall t > 0 \tag{4.5}$$

From these definitions of stability, it is possible to introduce the *critical Reynolds numbers*, which provide information about the physical conditions that destabilise a flow. A first critical Reynolds number, Re_E, can be defined such that the flow is monotonically stable if $Re < Re_E$. This value can be deduced from the energy theory using the Reynolds-Orr equation, which will be introduced in §4.3. Another critical Reynolds number, Re_G, is the value below which the flow is globally stable, $Re < Re_G$. This value is difficult to derive analytically and it can be determined by means of the bifurcation analysis. Sometimes it is assumed to be the lowest Reynolds number for which turbulence can be sustained. However, this assumption is not valid for all flows, so it is necessary to introduce an additional critical Reynolds number, Re_T, below which the flow relaminarises. A last definition considers a Reynolds number, Re_L, above which the flow is linearly unstable or not conditionally stable, $Re > Re_L$. According to this definition, there exists at least one infinitesimal disturbance which is unstable.
As evident, the problem of defining a critical Reynolds number is complex and table (4.1) shows the critical Reynolds number for some simple flows. For a plane Couette flow Re_G and Re_T are different, implying the existence of non-turbulent equilibrium solutions, which were found by Nagata (1990) and later verified to be stable (Lundbladh 1993). For the plane Poiseuille

Flow	Re_E	Re_G	Re_T	Re_L
Hagen-Poiseuille	81.5	-	2000	∞
Plane Poiseuille	49.6	-	1000	5772
Plane Couette	20.7	125	360	∞

Table 4.1: Critical Reynolds number for wall-bounded shear flows.

and circular pipe flow such non-turbulent equilibrium solutions have not been found for $Re < Re_T$.

4.3 The Reynolds-Orr equation

In the previous section the concepts of stability and the critical Reynolds number were introduced. Moreover their strong connection to the disturbance energy was discussed. The evolution equation for the kinetic disturbance energy can be obtained by scalar multiplying the nonlinear disturbance equations by the perturbation velocity $\boldsymbol{u'}$ and then enforcing the divergence-free condition, expressed by equation (4.2a). This yields:

$$\begin{aligned}\frac{\partial(\boldsymbol{u'}\cdot\boldsymbol{u'})}{\partial t} = &-\boldsymbol{u'}\otimes\boldsymbol{u'}:\nabla\boldsymbol{U}-\frac{1}{Re}\nabla\boldsymbol{u'}:\nabla\boldsymbol{u'}- \\ &\nabla\cdot\left[-\frac{1}{2}(\boldsymbol{u'}\cdot\boldsymbol{u'})\otimes\boldsymbol{U}-\frac{1}{2}(\boldsymbol{u'}\cdot\boldsymbol{u'})\otimes\boldsymbol{u'}-\boldsymbol{u'}\cdot p\boldsymbol{I}+\frac{1}{Re}\boldsymbol{u'}\cdot\nabla\boldsymbol{u'}\right]\end{aligned} \tag{4.6}$$

where $\boldsymbol{I}$ represents the unit tensor. Let us integrate equation (4.6) over the volume V and assume the disturbance to be localised or spatially periodic; using the divergence theorem, the last term on the right hand side of equation (4.6) does not give any contribution and we obtain the following equation, which is known as *Reynolds-Orr equation*:

$$\frac{dE_V}{dt} = -\int_V \boldsymbol{u'}\otimes\boldsymbol{u'}:\nabla\boldsymbol{U}dV-\frac{1}{Re}\int_V\nabla\boldsymbol{u'}:\nabla\boldsymbol{u'}dV. \tag{4.7}$$

The two terms on the right hand side of equation (4.7) represent the exchange of energy with the base flow and the energy dissipation due to viscous effects respectively. One of the main conclusions that can be derived from the Reynolds-Orr equation is that the instantaneous growth rate $\left(\frac{1}{E_V}\frac{dE_V}{dt}\right)$ is independent from the disturbance amplitude. This means that the growth rate of a finite-amplitude disturbance can be found at each instant using an infinitesimal disturbance of identical shape. Therefore, the

instantaneous growth rate is given by the mechanisms associated to the linearised equations and the total growth of the disturbance can be regarded as the sum of the growth rates associated with each linear mechanism. This is a consequence of the conservative nature of the non-linear terms in the Navier-Stokes equations (Schmid & Henningson, 2001).

4.4 Stability as eigensolution to the viscous problem

After having introduced the concept of stability, we will show that the study of the stability of a flow can be reduced to the solution of an eigenproblem. We start by discussing the local stability analysis and then extend this approach to more general cases (global stability analysis).

4.4.1 Local stability analysis

Let us consider a parallel base flow $\boldsymbol{U} = [U(y), 0, 0]^T$ and substitute it into the linearised Navier-Stokes equations (4.2a) and (4.2b):

$$\frac{\partial u'}{\partial x} + \frac{\partial v'}{\partial y} + \frac{\partial w'}{\partial z} = 0 \tag{4.8a}$$

$$\frac{\partial u'}{\partial t} + U(y)\frac{\partial u'}{\partial x} + v'\frac{dU}{dy} = -\frac{\partial p'}{\partial x} + \frac{1}{Re}\nabla^2 u' \tag{4.8b}$$

$$\frac{\partial v'}{\partial t} + U(y)\frac{\partial v'}{\partial x} = -\frac{\partial p'}{\partial y} + \frac{1}{Re}\nabla^2 v' \tag{4.8c}$$

$$\frac{\partial w'}{\partial t} + U(y)\frac{\partial w'}{\partial x} = -\frac{\partial p'}{\partial z} + \frac{1}{Re}\nabla^2 w' \tag{4.8d}$$

Taking the divergence of the linearised momentum equations (4.8b)-(4.8d) and using the continuity equation (4.8a), we can deduce an equation for the perturbation pressure:

$$\nabla^2 p' = -2\frac{dU}{dy}\frac{\partial v'}{\partial x}. \tag{4.9}$$

This equation can be used with equation (4.8c) to eliminate p':

$$\left[\left(\frac{\partial}{\partial t} + U\frac{\partial}{\partial x}\right)\nabla^2 - \frac{d^2U}{dy^2}\frac{\partial}{\partial x} - \frac{1}{Re}\nabla^4\right] v' = 0 \tag{4.10}$$

To describe the three-dimensional flow field, we need a second equation. A convenient choice is the equation for the normal vorticity $\eta = \frac{\partial u}{\partial z} - \frac{\partial w}{\partial x}$:

$$\left[\frac{\partial}{\partial t} + U\frac{\partial}{\partial x} - \frac{1}{Re}\nabla^2\right]\eta = -\frac{dU}{dy}\frac{\partial v'}{\partial z} \tag{4.11}$$

Let us consider a general wavelike solution to equations (4.10) and (4.11):

$$v'(x,y,z,t) = \tilde{v}(y)e^{i(\alpha x+\beta z-\alpha ct)} \tag{4.12a}$$

$$\eta'(x,y,z,t) = \tilde{\eta}(y)e^{i(\alpha x+\beta z-\alpha ct)} \tag{4.12b}$$

where $c \in \mathbb{C}$ is the phase speed, while α and $\beta \in \mathbb{R}$ the streamwise and spanwise wavenumbers respectively. The choice of the complex frequency $\omega = \alpha c$ and the real wavenumbers defines the temporal stability problem: the spatial structure of the wavelike perturbation does not change in time, but its amplitude can grow or decay. Substituting (4.12a) and (4.12b) into (4.10) and (4.11), we obtain the equations for the normal velocity and vorticity, known as *Orr-Sommerfeld equation* (Orr 1907, Sommerfeld 1908), (4.13a), and *Squire equation* (Squire 1933), (4.13b), respectively:

$$\left[(-i\omega + i\alpha U)\left(\frac{d^2}{dy^2} - k^2\right) - i\alpha\frac{d^2U}{dy^2} - \frac{1}{Re}\left(\frac{d^2}{dy^2} - k^2\right)^2\right]\tilde{v} = 0 \tag{4.13a}$$

$$\left[(-i\omega + i\alpha U) - \frac{1}{Re}\left(\frac{d^2}{dy^2} - k^2\right)\right]\tilde{\eta} = -i\beta\frac{dU}{dy}\tilde{v} \tag{4.13b}$$

where $k^2 = \alpha^2 + \beta^2$. The Orr-Sommerfeld equation (4.13a) poses an eigenvalue problem of a second-order differential operator, where ω is the associated complex eigenvalue. Since the coefficients of this equation are real, the eigenvalues appear as complex conjugate pairs; if the imaginary part of the eigenvalue is greater than zero, $\mathcal{I}(\omega) > 0$, the disturbance grows exponentially, otherwise it decays exponentially. Thus, to study the stability of the flow, we must solve the eigenproblem defined by the Orr-Sommerfeld equation and then use the solution to solve the Squire equation (4.13b), where $\tilde{v}$ appears as a forcing term.

Another important conclusion that can be derived from the local stability analysis is the relation between two and three-dimensional solutions. Let us consider the Orr-Sommerfeld equation for a three-dimensional flow, (4.14a), and two-dimensional flow, (4.14b), respectively:

$$(U-c)\left(\frac{d^2}{dy^2} - k^2\right)\tilde{v} - \frac{d^2U}{dy^2}\tilde{v} - \frac{1}{i\alpha Re}\left(\frac{d^2}{dy^2} - k^2\right)^2\tilde{v} = 0 \tag{4.14a}$$

$$(U-c)\left(\frac{d^2}{dy^2}-\alpha_{2D}^2\right)\tilde{v}-\frac{d^2U}{dy^2}\tilde{v}-\frac{1}{i\alpha_{2D}Re_{2D}}\left(\frac{d^2}{dy^2}-\alpha_{2D}^2\right)^2\tilde{v}=0 \quad (4.14b)$$

If $\beta = 0$, these equations have the same solution if and only if the following relations are satisfied:

$$\alpha_{2D} = k = \sqrt{\alpha^2+\beta^2} \quad (4.15)$$

$$\alpha_{2D}Re_{2D} = \alpha Re \quad (4.16)$$

We have then the following condition:

$$Re_{2D} = Re\frac{\alpha}{k} < Re \quad (4.17)$$

This results is known as *Squire's transformation* and it expresses the fact that a three-dimensional mode is equivalent to a two-dimensional one at a *lower* Reynolds number. This result can be used to prove the following theorem (*Squire's theorem*):

Theorem

Given the critical Reynolds number Re_L for the onset of linear instabilities and a given pair of wavenumbers α, β, the Reynolds number below which no exponential instabilities exist for any wavenumbers satisfies the following relation:

$$Re_c \equiv \min_{\alpha,\beta} Re_L(\alpha,\beta) = \min_{\alpha,\beta} Re_L(\alpha,0) \quad (4.18)$$

Therefore, if a given three-dimensional mode is unstable, the corresponding two-dimensional mode for $\beta = 0$ will be unstable at lower Reynolds number. Consequentially, results from two-dimensional stability analyses do not provide any information on the stability of the corresponding three-dimensional flows.

4.4.2 Global stability analysis

The study of instabilities using the local approach has been used with mixed success. Despite its ability to predict correctly the instability waves on a flat plate boundary layer, it fails to determine the instability of the Poiseuille flow in a pipe at *all* Reynolds numbers, even if the base flow is truly parallel. Therefore, a generalisation of the approach presented in §4.4.1 needs to be introduced. Following an approach similar to Hall & Horseman (1991) and Henningon (1987), let us consider a generic base flow $\boldsymbol{U}$, which is assumed to be a solution of the Navier-Stokes equations, and let us take the divergence of the momentum equations (4.2b), enforcing the divergence-free condition expressed by (4.2a); we obtain:

$$\nabla^2 p' = \nabla \cdot (\boldsymbol{U} \cdot \nabla \boldsymbol{u'} + \boldsymbol{u'} \cdot \nabla \boldsymbol{U}) = \nabla \cdot \Big((\boldsymbol{U} \cdot \nabla + (\nabla \boldsymbol{U})^T) \boldsymbol{u'} \Big) \tag{4.19}$$

Substituting equation (4.19) into (4.2b), it is then possible to rewrite the linearised equations in an operator form without the explicit dependence on p' (Tuckerman & Barkley, 2000):

$$\frac{\partial \boldsymbol{u'}}{\partial t} = \mathcal{L} \boldsymbol{u'} = \mathcal{A}(\boldsymbol{U}) \boldsymbol{u'} \tag{4.20}$$

We can choose the solution of our problem to be in the following form:

$$\boldsymbol{u'}(\boldsymbol{x}, t) = \tilde{\boldsymbol{u}}(\boldsymbol{x}) e^{st}, \quad \text{where} \quad s = \sigma + i\omega 3 \tag{4.21}$$

which substituted into (4.20) gives:

$$\mathcal{A}(\boldsymbol{U}) \tilde{\boldsymbol{u}}(\boldsymbol{x}) = s \tilde{\boldsymbol{u}}(\boldsymbol{x}). \tag{4.22}$$

This approach is referred as *global* and represents the most general way to study the instabilities arising in a flow (Theofilis 2003, 2011). The term "global" stability analysis was introduced by Joseph (1966), discussing a methodology to evaluate the lower bounds for flow instability considering the evolution of the perturbation energy. However, the approach to global stability analysis as the eigensolution to a viscous problem appeared only in the early 1980s with the pioneering work of Pierrehumbert & Widnall (1982), Eriksson & Rizzi (1985), Pierrehumbert (1986). Pierrehumbert & Widnall (1982) solved the perturbed form of the Euler equation using spectral methods, whereas Henningon (1987) solved the two-dimensional Rayleigh equation. The first viscous instability of an open flow was performed by Zebid (1987) to study the wake of a circular cylinder, while Amon & Patera (1989) performed the same analysis in a closed system, specifically a

grooved channel. The solution of three-dimensional viscous eigenproblems (TriGlobal stability analysis) represents the most challenging methodology in the linear stability analysis and there has been a surge of interest in the last decade. The first three-dimensional viscous eigenproblem was solved for the first time by Tezuka & Suzuki (2006) to study the flow around a sphere and a prolate spheroid. Morzynski & Thiele (2008) analysed the stability in the wake of cylinder and spheres, Bagheri *et al.* (2009) performed the stability analysis of a jet-in-cross-flow, while Giannetti *et al.* (2009) studied the instability in a cubic lid-driven cavity. Throughout this thesis, we will use this approach, but, in practice, the construction of the matrix which represents the operator $\mathcal{A}$ is not feasible due to the large dimensions of the problem. Hence, an equivalent standard time-stepping approach will be used to integrate both the non-linear and linearised Navier-Stokes equations (Eriksson & Rizzi 1985, Barkley *et al.* 2008). This approach consists of constructing a Krylov subspace by a repeated application of the time-dependent operator $\mathcal{L}$ at different equidistant time steps $t_i = i\Delta t$, starting from an initial vector of arbitrary amplitude $\boldsymbol{u'_0}$:

$$\mathcal{K} = span(\boldsymbol{u'}_0, \mathcal{A}(\Delta t)\boldsymbol{u'}_0, \mathcal{A}(2\Delta t)\boldsymbol{u'}_0, \ldots, \mathcal{A}((n-1)\Delta t) \tag{4.23}$$

Therefore, this approach allows us to advance in time a generic initial condition $\boldsymbol{u'_0}$ circumventing the matrix formation. Moreover, the large dimensions of the systems imply that the eigenvalues and eigenvectors of the system cannot be computed via a QR algorithm, therefore alternative techniques must be used. In this thesis, an Arnoldi algorithm was adopted. A detailed description of such numerical methods is provided in Appendix A.

4.4.3 Direct stability analysis: BiGlobal approach

An intermediate approach between the local and global stability consists in assuming base flows which depend on just two spatial directions, while the perturbations are imposed to be periodic in the third homogeneous one, as expressed in equations (4.24). This method is usually referred as *BiGlobal approach*.

$$\boldsymbol{U}(\boldsymbol{x}, t) = \begin{bmatrix} U(x, y, t) \\ V(x, y, t) \\ W(x, y, t) \end{bmatrix} \tag{4.24a}$$

$$\boldsymbol{u'}(\boldsymbol{x}, t) = \hat{\boldsymbol{u}}' e^{i\beta z} = \begin{bmatrix} \hat{u}' e^{i\beta z} \\ \hat{v}' e^{i\beta z} \\ \hat{w}' e^{i\beta z} \end{bmatrix} \tag{4.24b}$$

In equations (4.24b), $\beta = 2\pi/L_z$ is the spanwise wavenumber, while L_z is the corresponding wavelength. In this case, $\hat{\boldsymbol{u}}'$ is a complex vector and the evolution operator $\mathcal{A}$, expressed in (4.22), is complex. If the flow is completely two-dimensional, $W(x, y, t) = 0$, then the system can be reduced to a problem containing only the real part of the streamwise and transverse perturbation velocities, $\hat{u}' \cos(\beta_z)$ and $\hat{v}' \cos(\beta z)$, and the imaginary part of the spanwise component, $\hat{w}' \sin(\beta_z)$, halving the number of degrees of freedom in the system. However, if the eigenvalues are complex then the full system must be considered to recover the correct eigenmodes.

4.4.4 Floquet stability analysis

An extension of the stability theory considered so far can be performed for a time-periodic base flow $\boldsymbol{U}(t)$ over an interval T: $\boldsymbol{U}(t) = \boldsymbol{U}(t + T)$. Since the flow is periodic with period T, the linearised operator, which depends only on the base flow, will also be time-dependent and T-periodic. Let us integrate equation (4.20) from an initial time t_0 to a generic time $t_0 + t$:

$$\boldsymbol{u'}(t_0 + t) = \exp\left(\int_{t_0}^{t_0+t} \boldsymbol{A}(\boldsymbol{U}(\tau))d\tau\right)\boldsymbol{u'}(t_0) \tag{4.25}$$

Equation (4.25) defines an evolution operator $\boldsymbol{C} = \int_{t_0}^{t_0+t} \boldsymbol{A}(\boldsymbol{U}(\tau))d\tau$ over the period T, evolving an initial perturbation $\boldsymbol{u'}(t_0)$ around a periodic orbit and giving the value at time t_0+t. The stability of the system is then determined by the eigenvalues of the matrix $\boldsymbol{C}$, often referred as *monodromy matrix*. The solution of this eigenproblem is called *Floquet stability analysis* and it requires the knowledge of the base flow $\boldsymbol{U}(t)$ at each time step (Tuckerman & Barkley 2000, Blackburn 2002*b*). Due to the periodicity of the base flow, a time interpolation (usually in terms of Fourier series) is required. The eigenvalues μ of $\boldsymbol{C}$ are known as Floquet multipliers and can be expressed as:

$$\mu = \exp(\sigma T) \tag{4.26}$$

where σ is called the Floquet exponent. In general, both σ and μ can be complex, indicating a travelling wave solution in the flow. Although in this thesis Floquet analysis was only adopted to study flows past bluff bodies, it is important to stress how this theory had a fundamental importance to characterise the secondary instability of boundary layers. Let us restrict our attention to the simple two-dimensional boundary layer along a flat surface. The flow is subject to an initial stage of linear instability, known as primary instability, characterised by two dimensional travelling

waves (Tollmien-Schlichting waves), which break-up the uniformity of the flow in the streamwise direction, redistributing spanwise vorticity into periodic concentrations near the critical layer, where wave speed and mean speed coincide (Herbert 1988). However, the primary mode does not lead to a breakdown to turbulence, but to a secondary instability mechanism: the TS waves grow and distort the base flow, which is not anymore of Blasius type, and generate inflection points in the velocity profile and a rapid breakdown to turbulence. In a coordinate system moving with the phase speed of the wave, the flow can be considered periodic in the streamwise direction. Therefore, Floquet stability analysis was able shed light on several unanswered questions on the dynamics of secondary instabilities in boundary layers, providing a good agreement with previous results of Klebanoff *et al.* (1962), Cornelius (1985), Kachanov & Levchenko (1984). The leading Floquet multiplier was found to be unstable and the secondary mode was seen to be in phase with the TS waves and travel at the same phase speed. As in a plane Poiseuille flow, a second mode with a smaller positive growth rate was found, making the transition scenario more complex.

4.5 BiGlobal stability analysis of the flow past a cylinder

In this section an application of the Floquet stability analysis is presented. Specifically, we will study the stability of two-dimensional periodic flows past a circular cylinder with respect to three-dimensional perturbations; this problem was studied by Barkley & Henderson (1996) and provides a benchmark case for the results which will be discussed in the following chapters. The mesh and the specific computational parameters used to perform these simulations are the same ones described in details in chapter §5.2.
Following Barkley & Henderson (1996), a validation of the computational domain size has been performed by comparing the shedding frequency and the vorticity distribution on different meshes. The shedding frequency was seen to increase when the cross-flow length (L_c in figure 5.1) was decreased; this phenomenon is related an upward shift in the local Reynolds number when the flow accelerates around the cylinder. Since no difference in the vortex shedding frequency was detected for $L_c > 22$, confirming the results obtained from Barkley & Henderson (1996), $L_c = 45$ was chosen in this thesis. The profile of the vorticity was used to check the resolution of the flow downstream from the cylinder and study the effect of the outflow boundary conditions; specifically a downstream length $L_O = 50$ was found

to be sufficient to produce the correct wake. The base flows used for the Floquet analyses were computed using a Fourier interpolation through 32 equispaced time slices, which were extracted from a single vortex shedding period T. The results of the Floquet analyses are reported in figure (4.1), which shows the dependence of the absolute value of the dominant Floquet multiplier $|\mu|$ over the spanwise wavenumber β at three different Reynolds numbers; at $Re = 220$ the multipliers have an absolute value less than unity $|\mu| < 1$ for $\beta \gtrsim 2.5$, hence the flow is stable in this range of wavenumbers. The wavenumber of maximum growth is approximately $\beta \approx 2$. When β is large (β>15), the multipliers are approximately zero. This behaviour is related to dominance of the viscous term in the linearised equations when $\beta \sim Re^{1/2}$, thus for larger values of β no further instabilities can arise (Barkley & Henderson, 1996). As already discussed in chapter §3, two different three-dimensional unstable modes can arise in the range of Reynolds numbers we are considering, which are known as mode A and B respectively. Mode A is the first to appear and it corresponds to the first peak of the curves, at the smaller wavenumbers β. Mode B corresponds instead to the second peak, when β is larger, and it is present only at $Re = 300$ (the curve at $Re = 220$ shows a peak, but $|\mu| < 1$). In order to evaluate the critical Reynolds numbers for the onset of these instabilities, the curves of neutral stability were computed (figure (4.2)); the neutral curve defines the boundary areas where exponentially growing solutions exist and where they do not (Schmid & Henningson, 2001). Thus, along these curves there exists a neutrally stable solution, characterised by a multiplier $|\mu| = 1$, while the region on the right of these curves identifies the solutions which are linearly unstable to three-dimensional perturbations. The critical Reynolds number and the corresponding wavelengths are $Re_A = 190$, $L_{z,A} = 3.98$ ($\beta_A = 1.578$) for mode A and $Re_B = 260$, $Lz, B = 0.825$ ($\beta_B = 7.616$) for mode B.

Let us consider mode A at $Re = 220$ and $\beta = 1.57$. This mode shows a reflectional symmetry with respect to the centreline $y = 0$, similarly to the base flow, and which is known as RT symmetry[1] (Robichaux *et al.*, 1999):

$$\text{Mode A} = \begin{cases} \hat{u}(x, y, z, t) = \hat{u}(x, -y, z, t + T/2) \\ \hat{v}(x, y, z, t) = -\hat{v}(x, -y, z, t + T/2) \\ \hat{w}(x, y, z, t) = \hat{w}(x, -y, z, t + T/2) \end{cases} \tag{4.27}$$

This symmetry holds also for the streamwise component of the perturbation vorticity ω_x, which can be obtained taking the curl of (4.27):

[1] R for reflection in space and T for translation in time

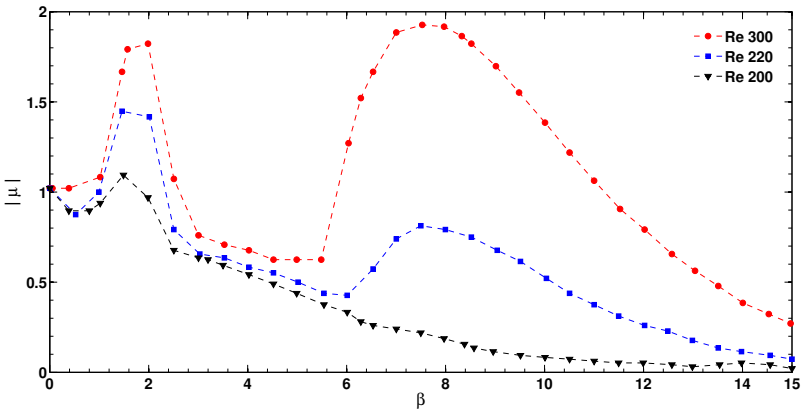

Figure 4.1: Dominant Floquet multipliers as function of the spanwise wavenumber β at $Re = 200$, $Re = 220$ and $Re = 300$.

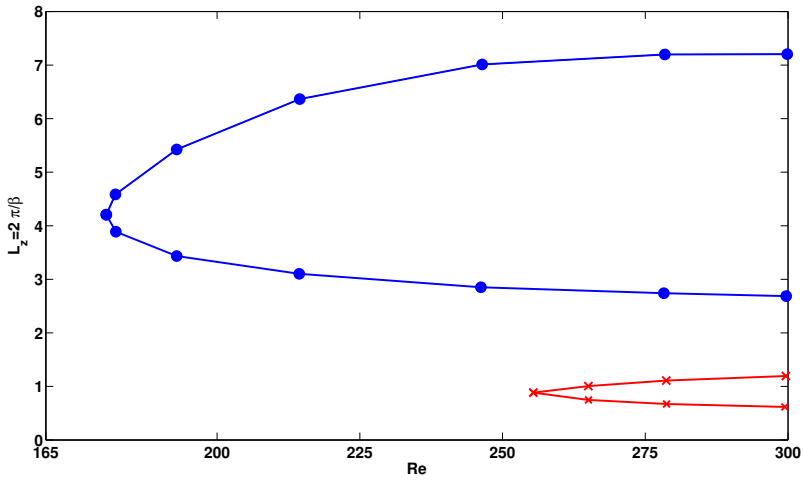

Figure 4.2: Neutral stability curves. In the region on the right of the curve the wake is unstable to three-dimensional perturbations. ∘ - mode A, × - mode B.

$$\hat{\omega}_x(x, y, z, t) = \hat{\omega}_x(x, -y, z, t + T/2). \tag{4.28}$$

This behaviour is highlighted in figure (4.3): the streamwise vorticity has different signs on each side of the wake centreline and it is more intense in the vortex cores of the base flow.

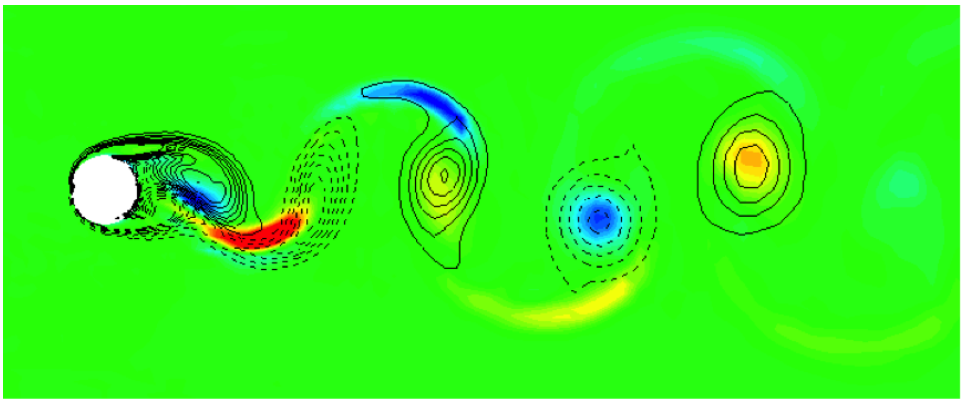

Figure 4.3: Contours of the streamwise vorticity ω_x of the Floquet mode and isolines of the spanwise vorticity Ω_z of the base flow. Red contours and solid lines represent positive vorticity, blue contours and dashed lines negative.

4.6 Adjoint Navier-Stokes equations

The concept of *adjoint* of a linear operator is very important in functional analysis and has a fundamental role in characterising the flow instabilities.

Definition

Let us consider a continuous linear operator $A : H \to H$ where H is a Hilbert space. There exists a unique continuous operator $A^* : H \to H$ such that:

$$\langle Ax, y \rangle = \langle x, A^* y \rangle , \quad \forall x, y \in H \tag{4.29}$$

A^* is called *adjoint operator* of A.

Following Barkley *et al.* (2008) and Hill (1992), let us write the linearised Navier-Stokes equation in the compact form:

$$\mathcal{H}\boldsymbol{q} = 0 \tag{4.30}$$

where $\boldsymbol{q} = (\boldsymbol{u}', p')^T$ and $\mathcal{H}$ is the evolution operator:

$$\mathcal{H} = \left(\begin{array}{c|c} -\partial_t - (\boldsymbol{U}\cdot\nabla) + (\nabla\boldsymbol{U})\cdot + \frac{1}{Re}\nabla^2 & -\nabla \\ \hline \nabla\cdot & 0 \end{array} \right) \tag{4.31}$$

Following definition (4.29), we can introduce the adjoint operator $\mathcal{H}^*$:

$$\langle \mathcal{H}\boldsymbol{q}, \boldsymbol{q} \rangle = \langle \boldsymbol{q}, \mathcal{H}^*\boldsymbol{q}^* \rangle \tag{4.32}$$

where $\boldsymbol{q}^*$ denotes the adjoint velocity and pressure. Integrating by parts:

$$\begin{aligned} &\langle \mathcal{H}\boldsymbol{q}, \boldsymbol{q} \rangle - \langle \boldsymbol{q}, \mathcal{H}^*\boldsymbol{q}^* \rangle = -\int_\Omega -[\boldsymbol{u}\cdot\boldsymbol{u}^*]_0^\tau d\Omega dt + \\ &\int_0^\tau \int_\Omega \nabla\cdot\left\{ -\boldsymbol{U}(\boldsymbol{u}'\cdot\boldsymbol{u}^*) + \boldsymbol{u}p^* - \boldsymbol{u}^*p + \frac{1}{Re}\left[(\nabla\boldsymbol{u})^T\cdot\boldsymbol{u}^* - (\nabla\boldsymbol{u}^*)^T\cdot\boldsymbol{u} \right] \right\} \mathrm{d}\Omega\mathrm{d}t \end{aligned} \tag{4.33}$$

Employing the divergence theorem, equation (4.33) can be expressed using only the boundary terms:

$$\begin{aligned} &\langle \mathcal{H}\boldsymbol{q}, \boldsymbol{q} \rangle - \langle \boldsymbol{q}, \mathcal{H}^*\boldsymbol{q}^* \rangle = -\int_\Omega [\boldsymbol{u}'\cdot\boldsymbol{u}^*]_0^\tau dv + \\ &\int_0^\tau \oint_{\partial\Omega} \mathbf{n}\cdot\left\{ -\boldsymbol{U}(\boldsymbol{u}'\cdot\boldsymbol{u}^*) + \boldsymbol{u}'p^* - \boldsymbol{u}^*p + \frac{1}{Re}\left[(\nabla\boldsymbol{u}')^T\cdot\boldsymbol{u}^* - (\nabla\boldsymbol{u}^*)^T\cdot\boldsymbol{u}' \right] \right\} \mathrm{d}S\mathrm{d}t. \end{aligned} \tag{4.34}$$

where $\mathbf{n}$ is a unit outward normal on the spatial boundary of the domain $\partial\Omega$, while dS is the surface differential. For $\boldsymbol{q}$, $\boldsymbol{q}^*$ with compact support, the boundary terms vanish and condition (4.32) is satisfied. The adjoint equations corresponding to the linearised Navier-Stokes equations can then be expressed as :

$$\mathcal{H}^*\boldsymbol{q}^* = 0 \tag{4.35}$$

The explicit formulation is:

$$-\frac{\partial\boldsymbol{u}^*}{\partial t} + (\boldsymbol{U}\cdot\nabla)\boldsymbol{u}^* + (\nabla\boldsymbol{U})^T\cdot\boldsymbol{u}^* = -\nabla p^* + \frac{1}{Re}\nabla^2\boldsymbol{u} \tag{4.36a}$$

$$\nabla\cdot\boldsymbol{u}^* = 0 \tag{4.36b}$$

It is interesting to note the negative sign in front of the temporal derivative, which implies that the adjoint runs backward in time, differently from the linearised Navier-Stokes operator.

4.6.1 Lagrange identity and receptivity analysis

Another meaningful manner of deriving the Navier-Stokes adjoint equations is by means of the Lagrange identity (Ince, 1926).
Given a linear operator L, its adjoint operator L^*, and any pair of C^2-functions u, v defined in $\mathbb{R}^n$, the following identity holds:

$$vL(u) - uL^*(v) = \nabla \cdot \boldsymbol{M} \tag{4.37}$$

where:

$$M_i = \sum_{j=1}^{n} a_{ij} \left(v\frac{\partial u}{\partial x_j} - u\frac{\partial v}{\partial x_j} \right) + uv \left(b_i - \sum_{j=1}^{n} \frac{\partial a_{ij}}{\partial x_j} \right) \tag{4.38}$$

This identity is known as *Lagrange identity*; if we consider the linearised Navier-Stokes operator, equation (4.37) gives:

$$\begin{aligned} &\left[\left(\frac{\partial \boldsymbol{u'}}{\partial t} + \boldsymbol{L}(\boldsymbol{U}, Re)\boldsymbol{u'} + \nabla p \right) \cdot \boldsymbol{u}^* + \nabla \cdot \boldsymbol{u'} p^* \right] + \\ &+ \left[\boldsymbol{u'} \cdot \left(\frac{\partial \boldsymbol{u}^*}{\partial t} + \boldsymbol{L}^*(\boldsymbol{U}, Re)\boldsymbol{u}^* + \nabla p^* \right) + p \nabla \cdot \boldsymbol{u}^* \right] = \frac{\partial (\boldsymbol{u'} \cdot \boldsymbol{u}^*)}{\partial t} + \nabla \cdot \boldsymbol{J}(\boldsymbol{q}, \boldsymbol{q}^*) \end{aligned} \tag{4.39}$$

where $\boldsymbol{L}$ represents the sum of the diffusive and advection terms of the linearised Navier-Stokes equations, while $\boldsymbol{L}^*$ its adjoint. $\boldsymbol{J}(\boldsymbol{q}, \boldsymbol{q}^*)$ is called *bilinear concomitant* and reads:

$$\boldsymbol{J}(\boldsymbol{q}, \boldsymbol{q}^*) = \boldsymbol{U}(\boldsymbol{u'} \cdot \boldsymbol{u}^*) + \frac{1}{Re}(\nabla \boldsymbol{u}^* \cdot \boldsymbol{u'} - \nabla \boldsymbol{u'} \cdot \boldsymbol{u}^*) + p^* \boldsymbol{u'} + p \boldsymbol{u}^* \tag{4.40}$$

The adjoint equations (4.36) can be defined considering the second term in the square brackets on the left hand side of (4.39). The Lagrange identity has a fundamental role, since a proper manipulation of the left hand side of equation (4.39) leads to important considerations on the underlying physical meaning of the adjoint equations . The adjoint equations can be used to evaluate the effect of a generic set of initial conditions and forcing on the time-asymptotic behaviour of the perturbations. Following Giannetti & Luchini (2007), let us consider the Laplace transform in time of (4.2b) of $\boldsymbol{q} = (\boldsymbol{u'}, p')$:

$$\tilde{\boldsymbol{q}}(\boldsymbol{x}, s) = \int_0^{+\infty} \boldsymbol{q}(\boldsymbol{x}, t) \exp(-st) \mathrm{d}t \tag{4.41}$$

Substituting (4.41) into (4.2b) we obtain:

$$s\tilde{\boldsymbol{u}}' + \boldsymbol{L}(\boldsymbol{U}, Re)\tilde{\boldsymbol{u}}' + \nabla\tilde{p} = \tilde{\boldsymbol{f}} + \boldsymbol{u}_{in} \tag{4.42a}$$

$$\nabla \cdot \tilde{\boldsymbol{u}}' = \tilde{m} \tag{4.42b}$$

where $\boldsymbol{u}_{in}(\boldsymbol{x}) = \boldsymbol{u}(\boldsymbol{x}, t = 0)$ denotes the initial condition to solve the linearised Navier-Stokes equations, while $\tilde{\boldsymbol{f}}$ and $\tilde{m}$ the Laplace transforms of two generic forcing functions introduced in equations (4.2a) and (4.2b). These terms represent a momentum forcing and a mass injection respectively. The solution in the time domain can be recovered using the Bromwich integral:

$$\boldsymbol{q}(\boldsymbol{x}, t) = \frac{1}{2\pi i} \lim_{T\to\infty} \int_{\gamma-iT}^{\gamma+iT} \tilde{\boldsymbol{q}}(\boldsymbol{x}, s) \exp(st) ds \tag{4.43}$$

where $\gamma \in \mathbb{R}$ is sufficiently large such that all the singularities are located on the left of the integration path. Let us consider a system with just one pole with a positive real part, i.e. s_1, as shown in figure (4.4)[2].

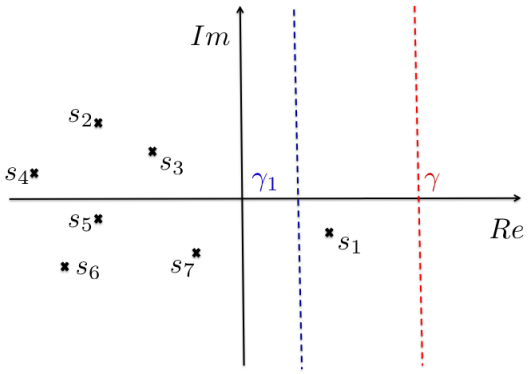

Figure 4.4: Schematic representation of the Bromwich integration path and the poles in the complex plane.

We can rewrite the integral (4.43) along a lower value γ_1, taking into account the role of the pole s_1 through the residue theorem:

[2] this assumption postulates the presence of an unstable global mode with an eigenvalue s_1.

$$\boldsymbol{q}(\boldsymbol{x},t) = \mathcal{R}[\tilde{\boldsymbol{q}}(\boldsymbol{x},s)]_{s=s_1}\exp(s_1 t) + \frac{1}{2\pi i}\lim_{T\to\infty}\int_{\gamma_1-iT}^{\gamma_1+iT}\tilde{\boldsymbol{q}}(\boldsymbol{x},s)\exp(st)\mathrm{d}s \tag{4.44}$$

where $\mathcal{R}[\tilde{\boldsymbol{q}}(\boldsymbol{x},s)]_{s=s_1}$ denotes the residue of $\tilde{\boldsymbol{q}}(\boldsymbol{x},s)$ evaluated at $s=s_1$. Let us assume that $s=s_1$ is a simple pole, then we can calculate the residue as:

$$\mathcal{R}[\tilde{\boldsymbol{q}}(\boldsymbol{x},s)]_{s=s_1} = \lim_{s\to s_1}(s-s_1)\tilde{\boldsymbol{q}}(\boldsymbol{x},s) = A_1\tilde{\boldsymbol{q}}_1(\boldsymbol{x},s_1) \tag{4.45}$$

where $\tilde{\boldsymbol{q}}_1(\boldsymbol{x},s_1)$ is the global mode associated to the eigenvalue $s=s_1$. The amplitude of the global mode A_1 can be determined by applying the Lagrange identity to the following fields:

$$\boldsymbol{q}(\boldsymbol{x},t) = \tilde{q}(\boldsymbol{x},s)\exp(st) \tag{4.46}$$

$$\boldsymbol{q}_1^*(\boldsymbol{x},t) = \tilde{q}_1^*(\boldsymbol{x},s_1)\exp(-s_1 t) \tag{4.47}$$

where $\tilde{\boldsymbol{q}} = (\tilde{\boldsymbol{u}},\tilde{p})$ comes from the solution of the Laplace transformed equations (4.42), while $\tilde{\boldsymbol{q}}_1^* = (\tilde{\boldsymbol{u}}_1^*,\tilde{p}_1^*)$ is the adjoint global mode corresponding to s_1. Integrating the Laplace-transformed Lagrange identity over the domain Ω and using the divergence theorem, we obtain:

$$\begin{aligned}
&\int_\Omega\left[(s\tilde{\boldsymbol{u}} + \boldsymbol{L}(\boldsymbol{U},Re)\tilde{\boldsymbol{u}} + \nabla p)\cdot\tilde{\boldsymbol{u}}_1^* + \nabla\cdot\tilde{\boldsymbol{u}}\tilde{p}_1^*\right]d\Omega + \\
&+\int_\Omega\left[\tilde{\boldsymbol{u}}\cdot(-s_1\tilde{\boldsymbol{u}}_1^* + \boldsymbol{L}^*(\boldsymbol{U},Re)\tilde{\boldsymbol{u}}_1^* + \nabla\tilde{p}_1^*) + \tilde{p}\nabla\cdot\tilde{\boldsymbol{u}}_1^*\right]d\Omega = \\
&=\int_\Omega(s-s_1)\tilde{\boldsymbol{u}}\cdot\tilde{\boldsymbol{u}}_1^* d\Omega + \oiint_{\partial\Omega}\boldsymbol{J}(\tilde{\boldsymbol{q}},\tilde{\boldsymbol{q}}_1^*)\cdot\boldsymbol{n}\mathrm{d}S.
\end{aligned} \tag{4.48}$$

This expression relates the Laplace-transformed variables to the adjoint global mode. Taking the limit for $s\to s_1$ and recalling equations (4.36), (4.42) and (4.45), we obtain:

$$A_1 = \frac{\int_\Omega\tilde{\boldsymbol{u}}_1^*\cdot(\boldsymbol{u}_{in}+\tilde{\boldsymbol{f}})d\Omega + \int_\Omega\tilde{p}_1^*\tilde{m}d\Omega + \oiint_{\partial\Omega}\left[\frac{1}{Re}\nabla\tilde{u}_1^*\cdot\tilde{\boldsymbol{u}}_{\partial\Omega} + \tilde{p}_1^*\tilde{\boldsymbol{u}}_{\partial\Omega}\right]\cdot\boldsymbol{n}d\Omega}{\int_\Omega\tilde{\boldsymbol{u}}_1^*\cdot\tilde{\boldsymbol{u}}_1\mathrm{d}\Omega} \tag{4.49}$$

where $\tilde{\boldsymbol{u}}_{\partial\Omega}$ is the Laplace-transformed boundary condition. Expression (4.49) relates the amplitude of the global mode to the forcing functions, the boundary and initial conditions. The first term of the numerator shows that the initial conditions and an eventual momentum source are weighted by the adjoint eigensolution. Therefore, this term quantifies the influence of initial

conditions and forcing terms on the excitation of the instability. Analogously, the second term shows that the adjoint pressure is a significant measure of the effect of an eventual mass injection on the flow instability (Hill (1992), Hill (1995)). Finally, the last term shows how strongly the boundary motion is coupled with the instability.

4.6.2 Receptivity to spatially localised feedbacks: structural sensitivity

From the previous sections, it is evident that the dynamics of the instabilities requires the evaluation of both the direct and the adjoint modes. In particular, it is important to investigate the region where a modification of the structure of the problem generates the most significant drift of the leading eigenvalues (Giannetti & Luchini, 2007). This allows us to determine whether a generic structural perturbation is acting on the "core" of the instability mechanisms and has a role in exciting the global mode. Let us consider the Laplace transform of the linearised Navier-Stokes equations (4.42) and perturb them via two linear differential operators $\delta\boldsymbol{H}(\tilde{\boldsymbol{u}}_p, \tilde{p}_p)$ and $\delta R(\tilde{\boldsymbol{u}}_p, \tilde{p}_p)$, where the subscript p denotes the perturbed variables $\tilde{\boldsymbol{u}}_p = \tilde{\boldsymbol{u}}' + \delta\tilde{\boldsymbol{u}}'$, $\tilde{p}_p = \tilde{p}' + \delta\tilde{p}'$:

$$(s + \delta s)\tilde{\boldsymbol{u}}_p + \boldsymbol{L}(\boldsymbol{U}, Re)\tilde{\boldsymbol{u}}_p + \nabla\tilde{p}_p = \delta\boldsymbol{H}(\tilde{\boldsymbol{u}}_p, \tilde{p}_p) \tag{4.50a}$$

$$\nabla \cdot \tilde{\boldsymbol{u}}_p = \delta R(\tilde{\boldsymbol{u}}_p, \tilde{p}_p) \tag{4.50b}$$

Neglecting the quadratic terms, we obtain:

$$s\delta\tilde{\boldsymbol{u}}' + \boldsymbol{L}(\boldsymbol{U}, Re)\delta\tilde{\boldsymbol{u}}' + \nabla\delta\tilde{p}' = -\delta s\tilde{\boldsymbol{u}} + \delta\boldsymbol{H}(\tilde{\boldsymbol{u}}', \tilde{p}') \tag{4.51a}$$

$$\nabla \cdot \tilde{\boldsymbol{u}}' = \delta R(\tilde{\boldsymbol{u}}_1', \tilde{p}') \tag{4.51b}$$

We can now apply the Lagrange identity to the perturbed field $\delta\boldsymbol{q}(\boldsymbol{x}) = \delta\tilde{\boldsymbol{q}}(\boldsymbol{x})\exp(s_1 t)$ and to the adjoint mode $\boldsymbol{q}^* = \tilde{\boldsymbol{q}}^*\exp(-s_1 t)$ associated to the global mode identified by the eigenvalue s_1. Integrating over the domain Ω, using equation (4.51) and taking into account the boundary condition we obtain:

$$\delta s_1 = \frac{\int_\Omega \left[\tilde{\boldsymbol{u}}_1^* \cdot \delta\boldsymbol{H}(\tilde{\boldsymbol{u}}_1, \tilde{p}_1) + \tilde{p}^*\delta R(\tilde{\boldsymbol{u}}_1, \tilde{p}_1)\right] d\Omega}{\int_\Omega \tilde{\boldsymbol{u}}_1^* \cdot \tilde{\boldsymbol{u}}_1' d\Omega} \tag{4.52}$$

Equation (4.52) relates the drift of the eigenvalue s_1 to the perburted operators and the adjoint field. Therefore expression (4.52) is called *sensitivity*. We will consider perturbations which are localised in space. Let us consider the sensitivity of the eigenvalue with respect to a generic force-velocity

coupling, which is equivalent to introducing in the domain a device able to excite the flow with a force whose direction and intensity depend just on the velocity perturbation:

$$\boldsymbol{f} = \boldsymbol{C}(\boldsymbol{x}) \cdot \boldsymbol{u}' \tag{4.53}$$

If this structural perturbation is localised in space, at a generic point $\boldsymbol{x_0}$, we can write equation (4.53) as:

$$\boldsymbol{f} = \boldsymbol{C_0}\delta(\boldsymbol{x} - \boldsymbol{x_0}) \cdot \boldsymbol{u}_1' \tag{4.54}$$

where δ denotes the Kronecker delta function. Let us assume that no perturbation acts on the continuity equation ($\delta R(\tilde{\boldsymbol{u}}_1, \tilde{p}_1) = 0$) and $\delta \boldsymbol{H}(\tilde{\boldsymbol{u}}', \tilde{p}) = \boldsymbol{C_0}\delta(\boldsymbol{x} - \boldsymbol{x_0}) \cdot \tilde{\boldsymbol{u}}_1'$, we obtain the following relation:

$$|\delta s_1| = \frac{\left|\int_\Omega \tilde{\boldsymbol{u}}_1^* \cdot \boldsymbol{C}(\boldsymbol{x}) \cdot \tilde{\boldsymbol{u}}_1' d\Omega\right|}{\left|\int_\Omega \tilde{\boldsymbol{u}}_1^* \cdot \tilde{\boldsymbol{u}}_1' d\Omega\right|} \leq \|\boldsymbol{C}_0\| \, \lambda(\boldsymbol{x_0}) \tag{4.55}$$

where:

$$\lambda(\boldsymbol{x}) = \frac{\|\tilde{\boldsymbol{u}}_1^*(\boldsymbol{x})\| \, \|\tilde{\boldsymbol{u}}_1'(\boldsymbol{x})\|}{\left|\int_\Omega \tilde{\boldsymbol{u}}_1^* \cdot \tilde{\boldsymbol{u}}_1' d\Omega\right|} \tag{4.56}$$

Therefore the product of the direct and adjoint modes gives the maximum coupling among the velocity components and $\lambda(\boldsymbol{x})$ identifies the regions where the instability mechanism acts. This quantity is called *structural sensitivity* (Giannetti & Luchini, 2007) and it is an indicator of the receptivity to spatially localised feedbacks in a flow. It is important to stress that this methodology assumes a perturbation localised in a single point of the domain. The problem of understanding how more complex structural modifications (e.g. two localised structural perturbations) affect the instability mechanisms is difficult and it is not possible to provide a straightforward solution. Generally the solution to such problems requires the concomitant comparison of direct numerical simulations and the results of stability analyses.

4.6.3 Structural sensitivity to base flow modifications

Another approach to study the receptivity of a flow is the evaluation of the drift of an eigenvalue due to a structural perturbation acting on the base flow (Bottaro *et al.*, 2003). We will see that this is particularly significant for analysis that will be presented in §5, where the stabilisation of the wake is achieved by modifications of the base flow velocity profile. The structural sensitivity with respect to base flow modifications was firstly introduced

by Marquet *et al.* (2008a) using a Lagrange multiplier technique and then extended by Luchini *et al.* (2008)-(2009) and Pralits *et al.* (2010) by means of the Lagrange identity. Let us consider an infinitesimal perturbation of the base flow $\boldsymbol{U}_p = \boldsymbol{U} + \delta\boldsymbol{U}$ and substitute it into the Laplace transformed Navier-Stokes equations. We obtain:

$$s\delta\tilde{\boldsymbol{u}}' + \boldsymbol{L}(\boldsymbol{U}, Re)\delta\tilde{\boldsymbol{u}}' + \nabla\delta\tilde{p}' = -\delta s\tilde{\boldsymbol{u}} - \delta\boldsymbol{C}(\delta\boldsymbol{U}, \tilde{u}) \tag{4.57a}$$

$$\nabla \cdot \delta\tilde{\boldsymbol{u}}' = 0 \tag{4.57b}$$

where $\delta\boldsymbol{C}$ is the bilinear operator and it expresses the variation of the linear operator $\boldsymbol{L}$ with respect to the variation of the base flow:

$$\delta\boldsymbol{C}(\delta\boldsymbol{U}, \tilde{\boldsymbol{u}}) = \delta\boldsymbol{U} \cdot \nabla\tilde{\boldsymbol{u}}' + \tilde{\boldsymbol{u}}' \cdot \nabla\delta\boldsymbol{U} \tag{4.58}$$

We can now apply the same methodology described in section §4.6.2; let us apply the Lagrange identity to the perturbed field $\delta\boldsymbol{q}(\boldsymbol{x}, t) = \delta\tilde{\boldsymbol{q}}(\boldsymbol{x})\exp(s_1 t)$, which satisfies equations (4.57a), and to the adjoint field, $\boldsymbol{q}^*(\boldsymbol{x}, t) = \tilde{\boldsymbol{q}}^*(\boldsymbol{x})\exp(-s_1 t)$. Integrating over the domain and taking into account the boundary conditions, we obtain:

$$\delta s_1 = -\frac{\int_\Omega \tilde{\boldsymbol{u}}_1^* \cdot \delta\boldsymbol{C}(\delta\boldsymbol{U}, \tilde{\boldsymbol{u}}')d\Omega}{\int_\Omega \tilde{\boldsymbol{u}}_1^* \cdot \tilde{\boldsymbol{u}}_1' d\Omega} \tag{4.59}$$

Expression (4.59) relates the drift of the eigenvalue s_1 with respect to the modifications of the base flow (encapsulated in $\delta\boldsymbol{C}$) and the adjoint field. Integrating by parts we obtain:

$$\delta s_1 = \frac{\int_\Omega \delta\boldsymbol{U} \cdot \delta\boldsymbol{C}^*(\tilde{\boldsymbol{u}}^*, \tilde{\boldsymbol{u}}')d\Omega - \cancel{\oint\!\!\!\oint}_{\partial\Omega}(\delta\boldsymbol{U} \cdot \tilde{\boldsymbol{u}}^*)\tilde{\boldsymbol{u}}' \cdot \boldsymbol{n}dS}{\int_\Omega \tilde{\boldsymbol{u}}^* \cdot \tilde{\boldsymbol{u}}' d\Omega} \tag{4.60}$$

where the second integral in the numerator vanishes if the solution decays at infinity. In this expression $\delta\boldsymbol{C}^*$ is the adjoint of $\delta\boldsymbol{C}$:

$$\delta\boldsymbol{C}^*(\tilde{\boldsymbol{u}}^*, \tilde{\boldsymbol{u}}') = \tilde{\boldsymbol{u}}' \cdot \nabla\tilde{\boldsymbol{u}}^* - \nabla\tilde{\boldsymbol{u}}' \cdot \tilde{\boldsymbol{u}}' \tag{4.61}$$

Expression (4.61) is directly related to the sensitivity to a generic modification of the base flow (Marquet *et al.*, 2008a) and it is the sum of two terms. The first one, $(\tilde{\boldsymbol{u}}' \cdot \nabla\tilde{\boldsymbol{u}}^*)$, represents the transport of perturbations, while the second one, $(\nabla\tilde{\boldsymbol{u}}' \cdot \tilde{\boldsymbol{u}}')$, the production of perturbations by the base flow modifications. The comparison of the intensity of these two terms highlights whether the transport or production processes are responsible for

the sensitivity. To obtain an expression analogous to (4.56), let us consider the variation of a steady base flow due to a generic structural perturbation:

$$\mathbf{L}(\boldsymbol{U}, Re)\delta\boldsymbol{U} + \nabla\delta P = \delta\boldsymbol{M}\cdot\boldsymbol{U} \tag{4.62a}$$

$$\nabla\cdot\delta\boldsymbol{U} = 0 \tag{4.62b}$$

where $\delta\boldsymbol{M}$ represents the coupling matrix that characterises the feedback process, and has a role similar to $\delta\boldsymbol{H}$ in equation (4.50). Applying the Lagrange identity to the base flow $(\boldsymbol{U}, P)$ and the adjoint field $(\boldsymbol{U}^*, P^*)$, and integrating by parts, we obtain:

$$\int_\Omega \delta\boldsymbol{U}\cdot\delta\boldsymbol{C}^*(\tilde{\boldsymbol{u}}^*, \tilde{\boldsymbol{u}})d\Omega = -\int_\Omega \boldsymbol{U}^*\cdot\delta\boldsymbol{M}\cdot\boldsymbol{U}d\Omega + \oiint_{\partial\Omega} \boldsymbol{J}(\delta\boldsymbol{U}, \delta P, \delta\boldsymbol{U}^*, \delta P^*)\cdot\boldsymbol{n}dS \tag{4.63}$$

where $\boldsymbol{J}$ is the bilinear concomitant expressed by (4.40), while $(\boldsymbol{U}^*, P^*)$ denotes the adjoint base flow ,which can be determined by the following equations (4.64):

$$\boldsymbol{L}^*(\boldsymbol{U}, Re)\boldsymbol{U}^* + \nabla P^* = \delta\boldsymbol{C}^*(\tilde{\boldsymbol{u}}^*, \tilde{\boldsymbol{u}}) \tag{4.64a}$$

$$\nabla\cdot\boldsymbol{U}^* = 0 \tag{4.64b}$$

where $\boldsymbol{L}^*$ is the adjoint Navier-Stokes operator:

$$\boldsymbol{U}\cdot\nabla\boldsymbol{U}^* - \nabla\boldsymbol{U}\cdot\boldsymbol{U}^* + \frac{1}{Re}\nabla^2\boldsymbol{U}^* \tag{4.65}$$

Therefore, given the steady base flow $\boldsymbol{U}$, the direct and adjoint velocity eigenvectors ($\boldsymbol{u}'$ and $\boldsymbol{u}^*$ respectively), we can evaluate the adjoint base flow $\boldsymbol{U}^*$ by solving the steady adjoint base flow equations (4.64), where the forcing term is $\delta\boldsymbol{C}^*(\tilde{\boldsymbol{u}}^*, \tilde{\boldsymbol{u}})$, introduced in equation (4.61). Similarly to the approach used in §4.6.2, let us assume that the feedback is localised in space, $\delta\boldsymbol{M} = \delta\boldsymbol{M}_0\delta(\boldsymbol{x}-\boldsymbol{x}_0)$. Using equation (4.60) and (4.61) with the appropriate boundary conditions, we obtain:

$$|\delta s_1(\boldsymbol{x}_0)| = \left|\frac{\int_\Omega \boldsymbol{U}^*\cdot\delta\boldsymbol{M}\cdot\boldsymbol{U}d\Omega}{\int_\Omega \tilde{\boldsymbol{u}}_1^*\cdot\tilde{\boldsymbol{u}}_1 d\Omega}\right| = \frac{|\boldsymbol{U}^*(\boldsymbol{x}_0)\cdot\delta\boldsymbol{M}_0\cdot\boldsymbol{U}(\boldsymbol{x}_0)|}{|\int_\Omega \tilde{\boldsymbol{u}}_1^*\cdot\tilde{\boldsymbol{u}}_1 d\Omega|} \leq \|\delta\boldsymbol{M}_0\|\,\Lambda(\boldsymbol{x}_0) \tag{4.66}$$

where:

$$\Lambda(\boldsymbol{x}) = \frac{\|\boldsymbol{U}^*(\boldsymbol{x})\| \, \|\boldsymbol{U}(\boldsymbol{x})\|}{\int_\Omega \tilde{\boldsymbol{u}}_1^* \cdot \tilde{\boldsymbol{u}}_1 d\Omega}. \tag{4.67}$$

$\Lambda(\boldsymbol{x})$ represents the structural sensitivity with respect to a local base flow modification. While expression (4.56) represents the eigenvalue drift due to a time-periodic forcing with the frequency of the instability mode, expression (4.67) assumes a local steady forcing which is proportional to the local base flow velocity and it induces variations of the base flow. Both the sensitivities $\lambda(\boldsymbol{x})$ and $\Lambda(\boldsymbol{x})$ are useful to study the stability of the problem and detect the different instability mechanisms.

4.7 Transient growth and convective instabilities

In the framework we presented in the previous sections we implicitly used the definition of *asymptotic stability*, discussed in §4.2, which implies a decay of the perturbation energy just for $t \to \infty$. However, an asymptotic stable flow might exhibit a non-negligible transient energy response, unless a condition of monotonic stability can be provided. The presence of transient growth phenomena is common in many applications, for example in open flows, where a particularly complex geometry might produce a steep variation of the base flow. Therefore, the main question to answer is related to the existence of bounded solutions which exhibit large growth before inevitably decaying. Let us consider the energy of a perturbation at a generic time τ, normalised with respect to its initial value. An initial perturbation with unitary energy, which implies $\|\boldsymbol{u'}(0)\| = 1$, leads to:

$$\frac{E(\tau)}{E(0)} = \langle \boldsymbol{u'}(\tau), \boldsymbol{u'}(\tau) \rangle \tag{4.68}$$

Recalling the evolution operator defined in (4.20), it is possible to express (4.68) as the following:

$$\frac{E(\tau)}{E(0)} = \langle \mathcal{A}(\tau)\boldsymbol{u'}(0), \mathcal{A}(\tau)\boldsymbol{u'}(0) \rangle \tag{4.69}$$

It is now possible to recast the previous expression introducing the adjoint evolution operator $\mathcal{A}^*(\tau)$ in the L_2 inner product:

$$\frac{E(\tau)}{E(0)} = \langle \boldsymbol{u'}(0), \mathcal{A}^*(\tau)\mathcal{A}(\tau)\boldsymbol{u'}(0) \rangle \tag{4.70}$$

The most common task in hydrodynamic stability theory is the quest for the most dangerous initial condition that results in the largest amplification

of the perturbation energy. This is equivalent to a search for the maximum amplification $G(\tau)$ of the initial energy over a specified time interval. Thus, the transient growth analysis consists of an optimisation problem over all initial conditions for a given time τ:

$$G(\tau) \equiv \max_{\|\boldsymbol{u'}(0)\|=1} \frac{E(\tau)}{E(0)} \tag{4.71}$$

From (4.70), it is evident that the largest possible growth is dictated by the dominant eigenvalue of operator $\mathcal{A}^*(\tau)\mathcal{A}(\tau)$, although even the first few sub-dominant eigenvalues may also be of interest[3]. It can be demonstrated that this approach is equivalent to finding the largest singular value of the operator $\mathcal{A}$. The eigenfunction $\boldsymbol{v}$ associated to the largest eigenvalue of operator , $\mathcal{A}^*(\tau)\mathcal{A}(\tau)$ gives in fact an initial perturbation $\boldsymbol{u'}(0)$ that generates a growth λ at time τ. Therefore:

$$\mathcal{A}(\tau)\boldsymbol{v} = \sigma\boldsymbol{u}, \quad \|\boldsymbol{u}\| = 1 \tag{4.72}$$

where $\sigma = \|\boldsymbol{u'}(\tau)\|$. This is the singular value decomposition of $\mathcal{A}(\tau)$.
The phenomenon of transient growth can be explained by considering the non-normality of the linearised Navier-Stokes evolution operator. This fact can be simply understood using the simple geometric example shown in figure (4.5). Let us assume a unit-length vector $\boldsymbol{f}$ represented in a non-orthogonal basis .This vector is defined as the difference of the two nearly collinear vectors $\boldsymbol{\Phi_1}$ and $\boldsymbol{\Phi_2}$. With the time progression, the component of these two vectors decrease respectively by 20% and 50%. The vector $\boldsymbol{f}$ increases substantially in length before decaying to zero. Thus, the superposition of decaying non-orthogonal eigenmodes can produce in short-term a growth in the norm of the perturbations (Schmid, 2007).

4.8 Stability, receptivity and transient growth analysis of a flow past a cylinder

In this section the stability, receptivity and transient growth analysis will be applied to a flow past a two-dimensional cylinder at $Re = 40$. This study is important because it allows us a direct comparison with several results reported in the literature (Giannetti & Luchini 2007, Marquet *et al.* 2008a, Pralits *et al.* 2010, Giannetti *et al.* 2010) and provides useful insights that

[3]let us note that $\mathcal{A}^*(\tau)\mathcal{A}(\tau)$ is a self-adjoint operator, therefore its leading eigenvalues will be real and positive, consistently with the fact that it is associated to the energy of the perturbations.

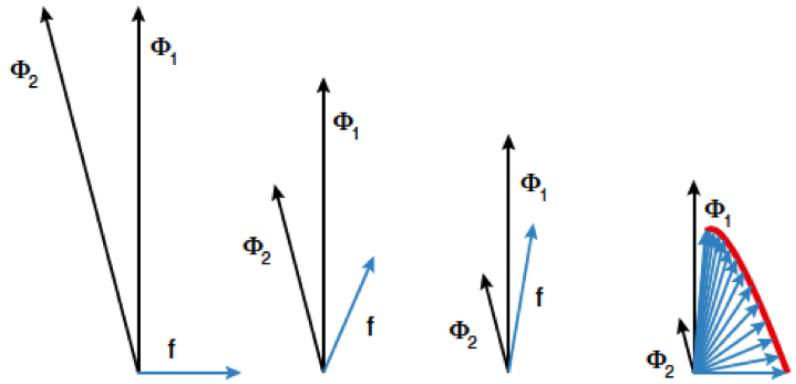

Figure 4.5: Geometric interpretation of the transient growth. Adapted from (Schmid, 2007).

will be further addressed in chapter 5. Information about the mesh and the choice of the main computational parameters are the same ones discussed in §(5.2).
Figure (4.6) shows the profile of the steady base flow, which was used to perform such analyses. The drag coefficient and the length of the recirculation bubble are in accordance with the data available in the literature, as reported in table (4.2).

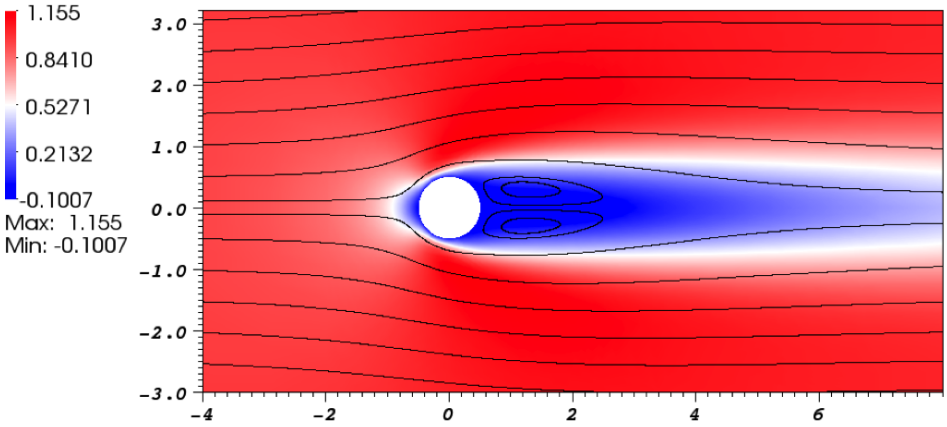

Figure 4.6: Detail of the velocity and streamlines at $Re = 40$.

By means of direct stability analysis, the flow is seen to be stable to two-

	C_D	L_B
Dennis & Chang (1970)	1.52	2.35
Coutanceau & Bouard (1977)	–	1.89
Fornberg (1980)	1.5	2.24
Ye *et al.* (1999)	1.52	2.27
Kim *et al.* (2001)	1.51	–
Giannetti & Luchini (2007)	1.54	2.24
Present work	1.52	2.26

Table 4.2: Drag coefficient C_D and length of the wake bubble L_B measured from the rear stagnation point.

dimensional perturbations and the decay rate[4] was seen to be $\sigma = -2.1 \times 10^{-2}$, while the frequency $\omega = \pm 7.3 \times 10^{-1}$, in accordance with the results in the literature (Zebid 1987, Hill 1992) . Figures (4.7a) and (4.7b) show the components of the direct mode, normalised such that the Euclidean norm is unity. The dominant eigenmodes are structurally identical, although they are shifted by the frequency ω. The transverse component of the perturbation v' is symmetric about the centreline, while the streamwise component u' is skew-symmetric. The base flow shows an exactly opposite behaviour, hence the superposition of the steady base flow and the disturbance will not show any symmetry. Consequently, the instabilities arising in this flow can be considered symmetry-breaking bifurcations (Tang 1997, Mittal 2010).

To study the regions of maximum receptivity, the adjoint mode was calculated using the same numerical technique used for the direct stability analysis. Figures (4.8a) and (4.8b) show the spatial distribution of the $\|\boldsymbol{u}^*\|$ and $|p^*|$, pointing out the regions of maximum receptivity to momentum forcing/initial conditions and mass injection respectively. The adjoint mode is located close to the cylinder surface and decays rapidly upstream and downstream. The large separation of the direct and adjoint mode is related to the non-normality[5] of the linearised Navier-Stokes equations and it is responsible for the strong sensitivity to forcing (Giannetti & Luchini 2007, Trefethen *et al.* 1993, Schmid & Henningson 2001).

In order to identify the region where the instability mechanisms are more

[4]We define the growth/decay rate as $\sigma = \log(\mathcal{R}(s))/T$ and the frequency $\omega = \mathcal{I}(s)/T$, where s is the dominant eigenvalue and T the time horizon used to integrate the linearised Navier-Stokes equations.

[5]A a operator N on a complex Hilbert space H is called *normal* if it commutes with its hermitian adjoint: $NN* = N * N$.

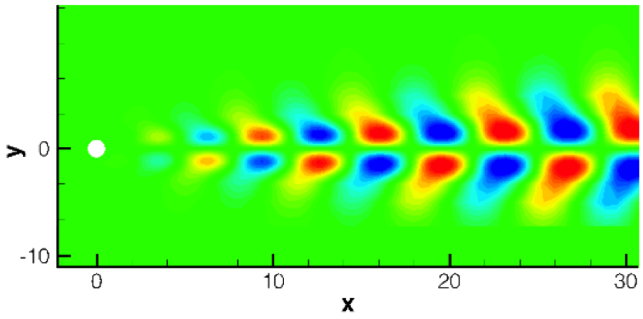

(a)

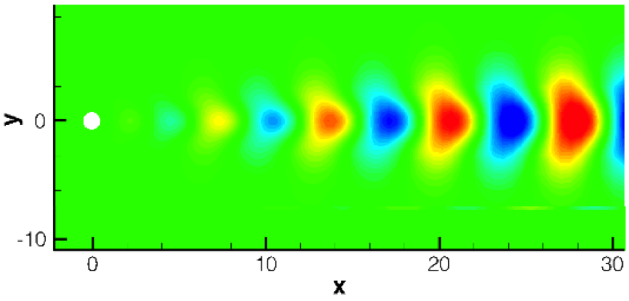

(b)

Figure 4.7: Direct eigenmode at $Re = 40$. (a): streamwise perturbation velocity u', (b): transverse perturbation velocity v'.

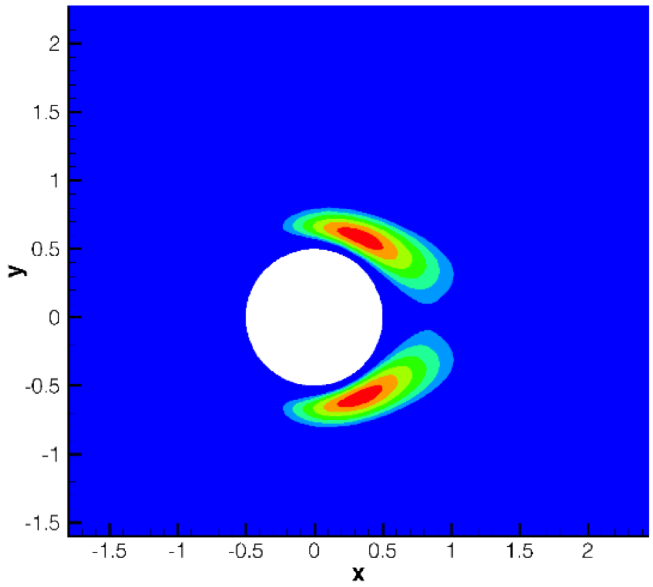

(a)

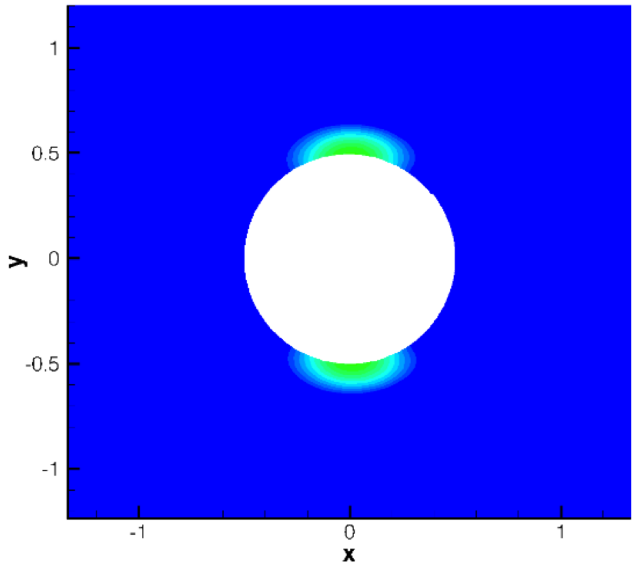

(b)

Figure 4.8: (a): receptivity to momentum forcing and initial conditions $\|\boldsymbol{u}^*\|$, (b): receptivity to mass injection $|p^*|$.

prominent, we cannot consider the direct and adjoint modes separately. Therefore, the structural sensitivity $\lambda(x, y)$ was evaluated by computing the spectral norm of the product of the direct and adjoint modes. As discussed in §4.6.2, the structural sensitivity provides information about the regions where the feedback from the velocity to force is most effective and it is equivalent to introducing in the flow a small device that generates a force whose direction and intensity depend on the value of the local velocity perturbation. Figure (4.9) shows the profile of $\lambda(x, y)$: the maxima are located in two symmetric lobes across the separation bubble, while its intensity is very small in proximity of the cylinder surface and far from it, suggesting that these regions do not have a crucial role on the dynamics of the instabilities.

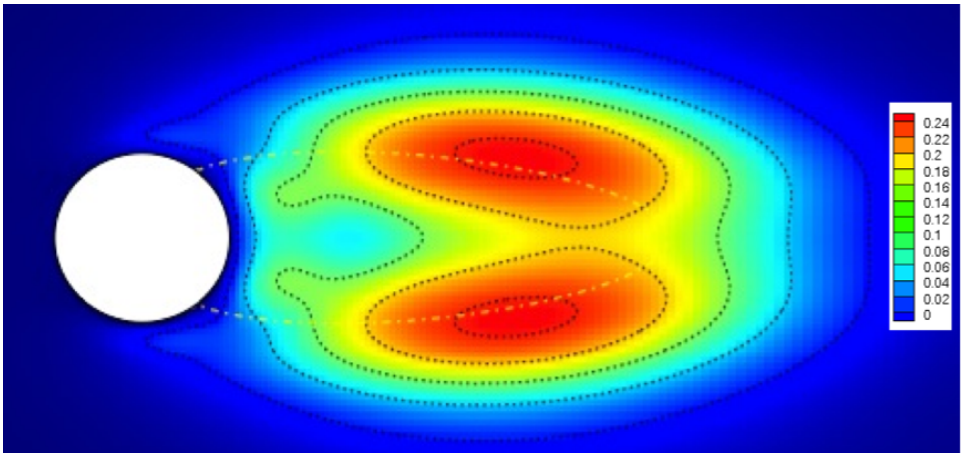

Figure 4.9: Contour plot of the sensitivity to a local feedback at $Re = 40$.

Finally, figure (4.10) shows the structural sensitivity with respect to base flow modifications $\Lambda(x, y)$. This sensitivity assumes a local force proportional to the local base flow velocity and identifies regions which are different from the structural sensitivity $\lambda(x, y)$. Despite two symmetric lobes being identified, similar to ones found for the structural sensitivity $\lambda(x, y)$, the maxima are located in the region just above and below the cylinder; this result shows that the most effective disruption to vortex shedding results from variations of the peripheral velocity of the cylinder , with subsequent modifications of the location of the stagnation point (this approach will be used in chapter §5).

Finally we can study the presence of convective instabilities in the flow. As explained in §4.7, the largest energy growth $G(\tau)$ associated with a specific time horizon τ, can be determined by computing the leading eigenvalue of operator $\mathcal{A}(\tau)\mathcal{A}^*(\tau)$. For $\tau = 60$, t a leading eigenvalue equal to $\lambda \simeq 670.5$

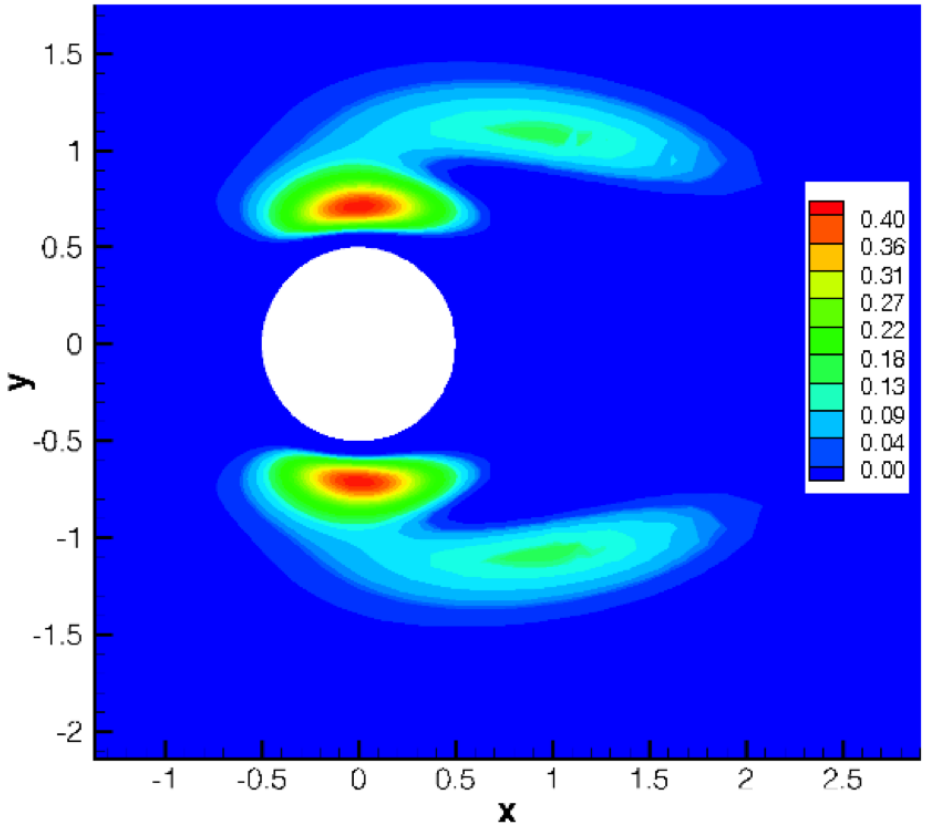

Figure 4.10: Contour plot of the sensitivity to base flow modifications at $Re = 40$.

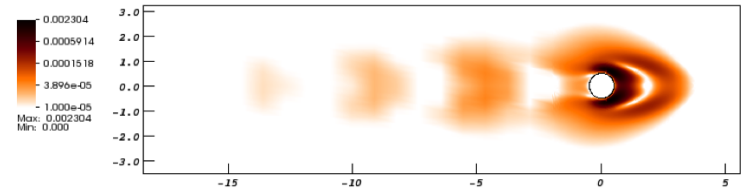

(a)

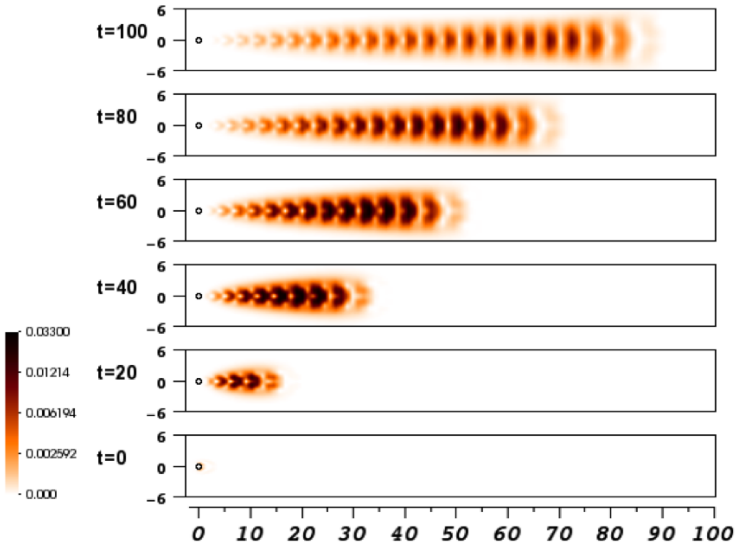

(b)

Figure 4.11: (a): magnitude of the optimal initial perturbation. (b): evolution of the optimal initial disturbance, showing the dynamics of the convective instabilities.

was found. This result points out the presence of convective instabilities, in fact λ represents the largest energy amplification that a perturbation with unitary magnitude might experience at the specified time horizon. The optimal initial disturbance and its evolution is shown in figure (4.11).

Following usual approaches for the transient growth analysis (Cantwell & Barkley 2010, Blackburn *et al.* 2008), figure (4.12a) shows the optimum envelope $G(\tau)$ and four transient responses. These curves follow from those initial conditions which produce the optimal energy growth at the specific time horizon τ and meet the optimum envelope at the corresponding times; optimal curves are in fact an envelope of the transient responses, even if the

individual transients have behaviours which are similar both qualitatively and quantitatively to the envelope. Figure (4.12) shows a comparison of the optimal envelope curve with to the results obtained in a similar study by Cantwell & Barkley (2010).

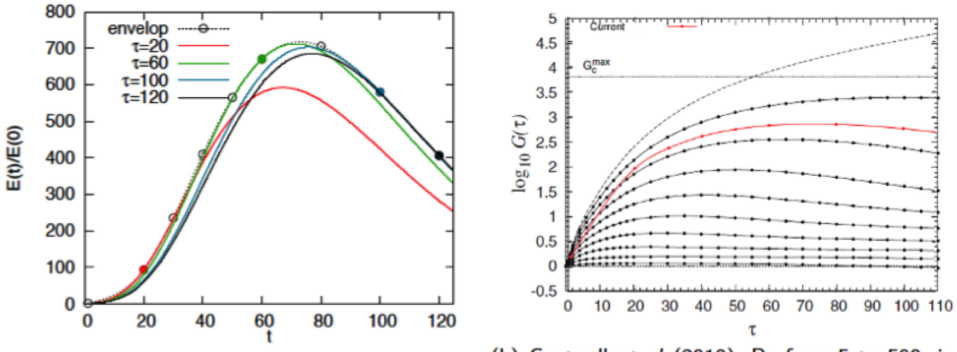

(a) Current

(b) Cantwell *et al* (2010), Re from 5 to 500, in increments of 5

Figure 4.12: *(a)*: linear energy evolution starting from three optimal initial conditions for specific values of $\tau = 20, 60$ and 100 and the envelope of the two-dimensional optima. *(b)*: envelope of the two-dimensional optima for the present case compared with previous findings (Cantwell & Barkley 2010).

4.9 Application of the hydrodynamic instability to the control of vortex shedding

As discussed throughout this chapter, the hydrodynamic stability theory provides a solid theoretical framework to understand the dynamics of the instabilities. This issue is particularly relevant to study the mechanisms behind the vortex shedding in a flow past a bluff body, which was seen to be directly related to the presence of a region with an absolute instability (Chomaz 2005, Huerre & Monkewitz 1995). In particular, the physical insights given by these analyses can be used to stabilise vortex shedding. Efficient control techniques generate change in the near-wake region, which act as a wavemaker, and lead to the attenuation, or suppression, of the the global instability. A simple but highly instructive application is the control technique suggested by Strykowski & Sreenivasan (1990), who noticed that the proper placement of a small control cylinder in the wake results in the suppression of the vortex shedding in a specific range of Reynolds numbers. In order to achieve the suppression, the control cylinder must

be placed within either of the two regions, which are symmetrical with respect to $y = 0$. The shape of these region is determined by the ratio of the diameters of the main and secondary cylinders (figure(4.13)). A numerical investigation of this technique was performed by Hill (1992), who computed the shift in the growth rate caused by a first-order correction of the eigenfrequency, resulting from the placement of the smaller cylinder. The same results found by Strykowski & Sreenivasan (1990) were retrieved using the adjoint Navier-Stokes equations, confirming that the vortex shedding eventually returns at higher Reynolds numbers with a significantly reduced Strouhal number. Moreover, the map of the shift of the Strouhal number, caused by the small cylinder, showed the regions where the frequency was found to be more prominent. A more general explanation of this methodology can be given by means of the structural sensitivity. The placement of the secondary cylinder generates a force on the fluid that modifies the flow field and leads to a a shift of the eigenvalues. Since the control cylinder has a diameter much smaller than the main one, its presence is equivalent to the effect of a localised perturbation. This issue is reflected in the similarity of figures (4.9) and (4.13) where the differences are due to the finite diameter of the secondary cylinder.
Further considerations can be deduced from the profile of the structural sensitivity to base flow modifications. The largest drift of eigenvalues is obtained by modifying the base flow in the regions close to the surface of the cylinder and in the upper/lower lobes of figure (4.10). However, as discussed by Marquet et al. (2008a), localised modifications of the base flow in the separation regions have a destabilising effect, producing an increase of the growth rate of the instabilities; this explains the reason why no suppression of the vortex shedding is achieved if the localised modification of the base flow is in proximity to the cylinder, as shown in figure (4.13).

4.10 Final remarks

It is important to remember that the methodology presented in this chapter is linear. When the Reynolds number is high, a disturbance that stabilises the frequency of the absolute instability might destabilise other modes. This phenomenon is related to the non-normality of the linearised Navier-Stokes equations. However, methods such as the splitter plates, base bleed and distributed forcing provide good results in a wide range of Reynolds numbers, suggesting that the vortex shedding is still the prime mode and the dynamics can be studied using the linear analysis, similarly to the cases at lower Reynolds numbers.

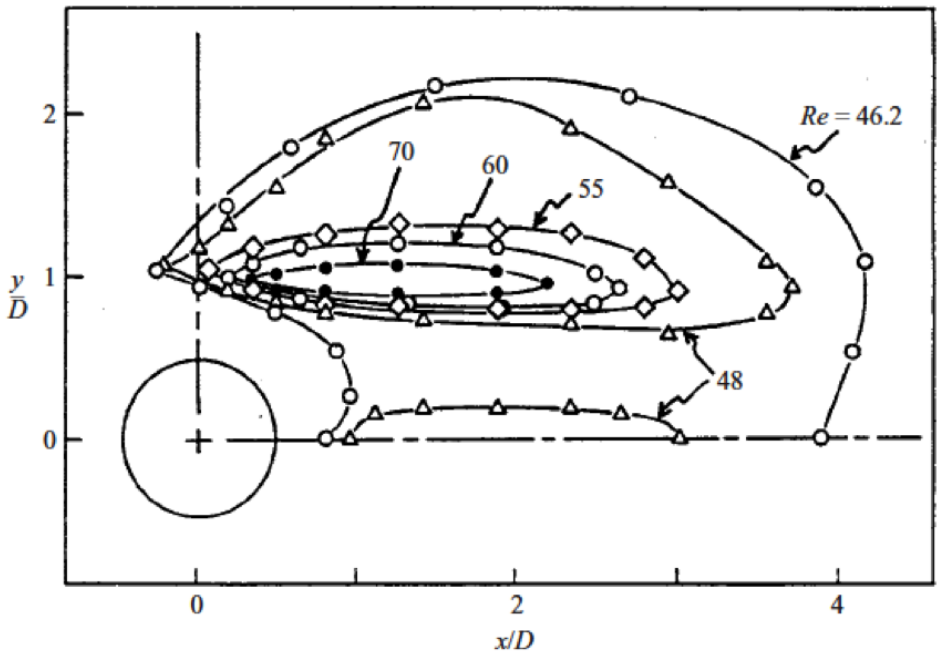

Figure 4.13: Regions where the placement of the secondary cylinder generates a zero growth rate of the temporal mode (adapted from Strykowski & Sreenivasan 1990).

Chapter 5

Suppression of vortex shedding via surface bleed

> *It is a capital mistake to theorise before one has data. Insensibly one begins to twist facts to suit theories, instead of theories to suit facts.*
>
> Sir Arthur Conan Doyle, *The Adventure of Sherlock Holmes*

The main scope of this chapter is to investigate the effects of distributed spanwise forcing on flows past a cylinder. After introducing the main parameters used in the present simulations, the influence of forcing on the suppression of vortex shedding and the stabilisation of the wake are discussed. Stability analysis of the flows is used to understand the physical mechanisms behind the suppression of the von Kármán street and its implications on the design of control devices.

5.1 Introduction

In chapter §3, we discussed the main techniques to suppress the von-Kármán vortex street. In particular, three-dimensional methods were seen to be very efficient, leading to a noteworthy drag reduction. As discussed by Darekar & Sherwin (2001), the effects of spanwise geometric modifications can be taken into account by introducing momentum forcing in the Navier-Stokes equations. This forcing is responsible for the generation of spanwise velocity components along the leading edge surface, which slow down the velocity in some specific regions along the span. These results suggest that an effective

suppression of vortex shedding can be achieved by a combination of a cross-flow velocity at the stagnation face and a slow down effect in the separation regions. Therefore, the application of spanwise distributed forcing along the surface of the cylinder may represent an appropriate manner to control wakes of bluff bodies without introducing any geometric modification. This technique has been extensively used to investigate the vortical dynamics of mixing layers since it affects the evolution of vortices and enhances mixing effects (Lascheras & Choi 1989, Bell & Mehta 1993, Nygaard & Gletzer 1994, Collis *et al.* 1994, Chun *et al.* 1990). Kim & Choi (2005) investigated the effects of spanwise distributed forcing to control wakes generated by flows past bluff bodies and applied sinusoidal blowing/suction along two slots at the upper and lower surfaces of a circular cylinder. In this thesis, a similar technique is used: we apply distributed forcing (or equivalently *surface bleed*) at the top and bottom surfaces of a cylinder by an appropriate modification of the velocity boundary conditions. At first, two in-phase sinusoidal forcing functions are applied to compare their effects with the results obtained by Kim & Choi (2005). Subsequently, the effects of Gaussian profiles are investigated to characterise the configuration that leads to an optimal suppression of vortex shedding. Stability analysis of the linearised Navier-Stokes equations is then performed on the three-dimensional flows to understand the role of spanwise modulation on the classical absolute instability associated with the von-Kármán street. Finally, the computation of the adjoint modes allows us to address the evaluation of the receptivity and the identification of the structural sensitivities, which are fundamental to understand the dynamics of the involved instability mechanisms.

5.2 Parameters of the numerical simulations

Figure (5.1) shows a sketch of the geometry adopted in the present thesis. We consider a cylinder completely immersed in an incompressible Newtonian flow: the upstream boundary L_i is $50D$ from the centre of the cylinder, while the side boundary L_c is $45D$ from the centre of the body. The choice of the inflow and cross-flow length is important to assure the validity of the results obtained by DNS and stability analysis. Cantwell & Barkley (2010) showed that such values lead to errors of the growth rates less than 1%, using a numerical method similar to the one used in the present thesis. The downstream boundary L_o is $50D$, such that eventual instabilities have sufficient space to evolve properly.

Regarding the boundary conditions, Dirichlet boundary conditions were imposed for the velocity at the upstream and side boundaries of the compu-

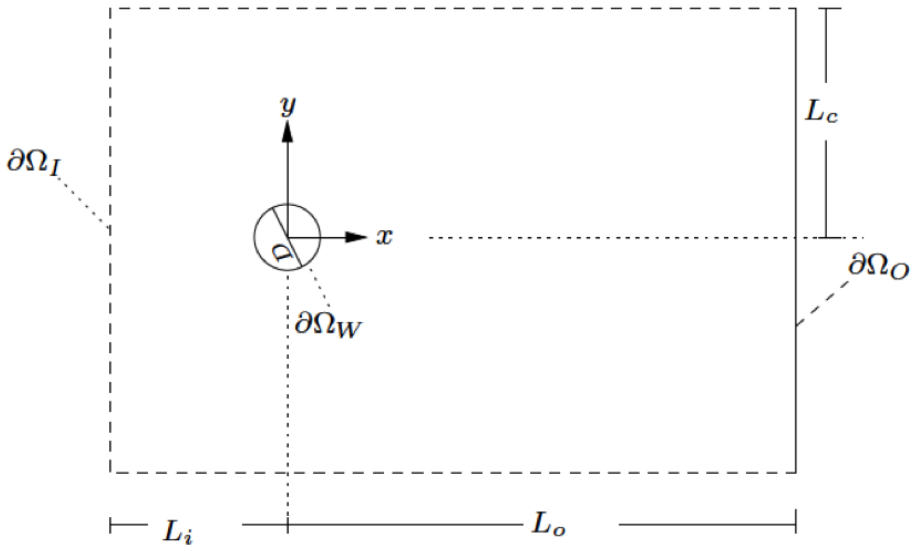

Figure 5.1: Sketch of the geometry of the problem.

tational domain $\partial\Omega_I$. At the downstream boundary $\partial\Omega_O$ outflow Neumann boundary conditions were applied. On the surface of the cylinder $\partial\Omega_W$ a forcing function $\boldsymbol{\phi}(x, y, z)$ was imposed, as we will discuss in §5.4. To summarise, the velocity boundary conditions read:

$$\boldsymbol{u}|_{\partial\Omega_W} = \boldsymbol{\phi}(x, y, z), \tag{5.1a}$$

$$\boldsymbol{u}|_{\partial\Omega_I} = (1, 0, 0)^T, \tag{5.1b}$$

$$\left.\frac{\partial \boldsymbol{u}}{\partial \boldsymbol{n}}\right|_{\partial\Omega_O} = (0, 0, 0)^T. \tag{5.1c}$$

A homogeneous pressure was imposed at the downstream boundary $\partial\Omega_O$, while high order boundary conditions, expressed by (2.93), were adopted on all the others. A structured mesh, shown in figure (5.2), was used. This mesh is composed of 700 quadrilateral elements and the curved boundaries are approximated by a parabolic fitting.
The modal basis described in §2.3.1 was used to interpolate the variables of the problem, while the appropriate polynomial order was chosen using an approach similar to the one discussed by Barkley & Henderson (1996). This approach consists in a convergence study of several physical quantities at $Re = 190$, where we keep the h-refinement fixed and vary the polynomial order P. Results are summarised in table (5.1), which shows the values of some global coefficients when the polynomial order P is progressively

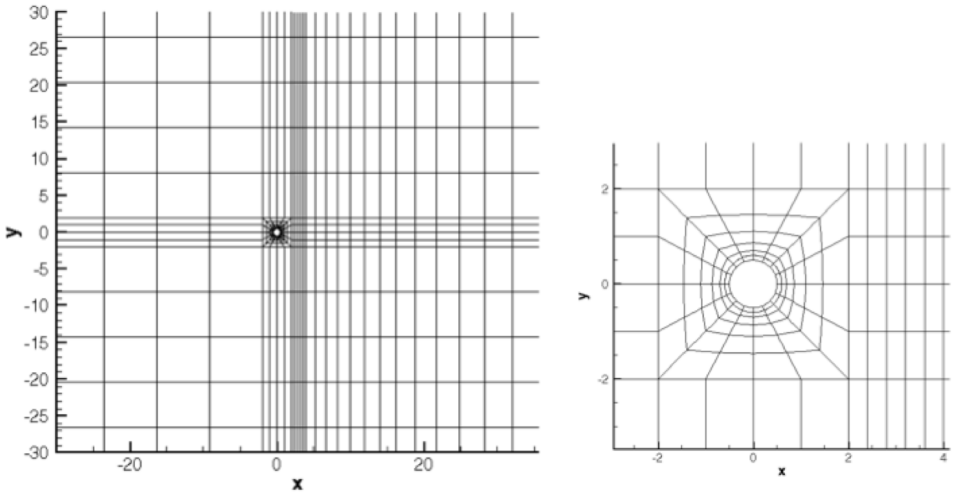

Figure 5.2: Mesh used for the simulations ad a detailed view around the cylinder.

P	Δt	St	$-C_{pb}$	C_D	C'_D	C'_L
5	3×10^{-3}	0.1945	0.9604	1.3768	0.0500	0.5039
6	2×10^{-3}	0.1956	0.9277	1.3487	0.0300	0.4700
7	8×10^{-4}	0.1955	0.9322	1.3447	0.0294	0.4643
8	8×10^{-4}	0.1955	0.9424	1.3445	0.0293	0.4645
9	8×10^{-4}	0.1955	0.9423	1.3445	0.0293	0.4644

Table 5.1: Convergence study of several global parameter at $Re = 190$ with polynomial order P.

increased. In this table St is the Strouhal number ($St = fD/U_\infty$, where f is the frequency of vortex shedding), C_p is the base pressure coefficient, C_D and C'_D the mean and fluctuating drag coefficients, while C_L and C'_L the mean and fluctuating lift coefficients[1]. Considering these results, eighth-order polynomial expansions were adopted for all the simulations described in this chapter.

Let us note that the mesh reported in figure (5.2) is two-dimensional; the three-dimensional simulations were performed using the Fourier-spectral/hp element method described in §2.3.6. The spanwise length of the computational domain L_z was chosen to be $5D$; tests with lengths in the range $L_z = 10D - 20D$ showed differences of about 5% in the values of the aero-

[1]The fluctuating coefficients are calculated as the root mean square of the total coefficients.

dynamic forces, while the wake topologies were seen to be almost identical. The Fourier resolution in the spanwise direction requires further considerations. As described by Henderson (1997), the number of the necessary Fourier modes n_F to capture the dynamics of the system can be estimated by $\beta_D = 2\pi n_F / L_z \sim \sqrt{Re}$. At $Re = 60$, this relation provides $n_F \simeq 8$: eight Fourier modes were found to be sufficient to capture the dynamics of the system and lead to differences in the values of the aerodynamic forces less than 1%. However, simulations at higher Reynolds number required a larger number of modes than the estimated value. Three different resolutions were then tested at $Re = 180$, using 8, 16 and 32 Fourier modes respectively. A large number of modes, $n_F = 32$, was necessary when Gaussian surface bleed was used, due to the particular "sharpness" of the forcing function required for the suppression of vortex shedding.

5.3 Vortex identification

An important aspect of flows past bluff bodies is the fact that their behaviour is governed by the dynamics of the vortices (vortex-dominated flows). Vortices are often viewed as "*the sinews and muscles of turbulence*" (Küchermann 1965) and their identification is hindered by the lack of an accepted mathematical definition (Chakraborty *et al.* 2005). Therefore an important preliminary task is a criterion for a proper identification of the coherent structures. We define as *coherent structure* a localised area in the flow field where swirling and vortical motions are more prominent than the surrounding regions. The vorticity, $\nabla \times \boldsymbol{u}$, might be a tempting quantity to identify the coherent structures but it is often unsuitable, in particular if its magnitude is comparable with the background shear. An example is the vortex sheet, which is not a vortex despite being characterised by a significant amount of vorticity, or the boundary layer on the surface of a bluff body, which does not necessarily contain a vortex. Generally the pressure is able to identify only strong vortices; for instance, in a flow past a cylinder in mode A transition, the pressure within the "fingers of dye", described in §3.4.2, is more intense than at the centre of the spanwise vortices; therefore a single value of the pressure cannot describe properly the features of the flow. Other important examples are the Stokes flows, which are characterised by a very low Reynolds number and are described by the following equations:

$$\frac{1}{Re}\nabla^2 \boldsymbol{u} = \nabla p, \tag{5.2a}$$

$$\nabla \cdot \boldsymbol{u} = 0. \tag{5.2b}$$

Taking the divergence of (5.2a) and using the divergence-free condition expressed by (5.2b), we derive that the pressure follows a Laplace equation: $\nabla^2 p = 0$. Therefore the pressure is a harmonic function and it cannot attain a maximum (or minimum) at any interior points of its domain because of the maximum principle. However, vortex rings are known to occur near the sharp corners, thus the pressure fails to describe properly the presence of coherent structures. Another technique consists in detecting closed or spiral streamlines in the flow. Unfortunately, due to the complex non-linear dynamics that characterises the vortices, a particle might not track a full rotation around the vortex core. Moreover, this method is not Galilean invariant, since the shape of the streamline depends on the speed of the reference system. More precise identification criteria can be introduced using kinematic considerations underlying the velocity gradient tensor $\nabla \boldsymbol{u}$, thereby making them Galilean invariant. The most popular ones are the Q (Hunt *et al.* 1988), λ_2(Jeong & Hussain 1995), Δ (Chong *et al.* 1990) and λ_{ci} (Zhou *et al.* 1990) criteria. In this thesis, the Q-criterion, introduced by Hunt *et al.* in 1998, is used; this criterion identifies the coherent structures as the regions with positive second invariant of the velocity gradient tensor[2] $\nabla \boldsymbol{u}$. In addition, the pressure in the eddy regions should be lower than the ambient pressure. The second invariant Q has the following expression:

$$Q = \frac{1}{2}\left[(\nabla \cdot \boldsymbol{u})^2 - \mathrm{tr}(\nabla \boldsymbol{u})^2\right] \tag{5.3}$$

For an incompressible flow, expression (5.3) can be written as:

$$Q = \frac{1}{2}(\|\boldsymbol{\Omega}\|^2 - \|\boldsymbol{E}\|^2) \tag{5.4}$$

where $\|\boldsymbol{\Omega}\| = \sqrt{\mathrm{tr}(\boldsymbol{\Omega}\boldsymbol{\Omega}^T)}$ and $\|\boldsymbol{E}\| = \sqrt{\mathrm{tr}(\boldsymbol{E}\boldsymbol{E}^T)}$; $\boldsymbol{E}$ and $\boldsymbol{\Omega}$ represents the symmetric and anti-symmetric components of $\nabla \boldsymbol{u}$:

$$\boldsymbol{E} = \frac{1}{2}(\nabla \boldsymbol{u} + (\nabla \boldsymbol{u})^T) \tag{5.5a}$$

$$\boldsymbol{\Omega} = \frac{1}{2}(\nabla \boldsymbol{u} - (\nabla \boldsymbol{u})^T) \tag{5.5b}$$

In an incompressible flow, Q is a local measure of the excess of rotation rate due to the strain rate. However, $Q > 0$ does not necessarily imply the existence of a pressure minimum, but in most cases the pressure condition is included by $Q > 0$ (Jeong & Hussain 1995). Therefore, in this thesis we use the Q-criterion without the additional condition on the pressure.

[2]The invariants of a tensor $\boldsymbol{A}$ are the coefficients of its characteristic polynomial $p(\lambda) = \det(\boldsymbol{A} - \lambda \boldsymbol{I})$.

As an example, the coherent structures found in the wake of a flow past cylinder at $Re = 60$ are reported in figure (5.3). The topology of the wake is characterised by strong spanwise alternating vortex tubes, which clearly identify the von-Kármán vortex street.

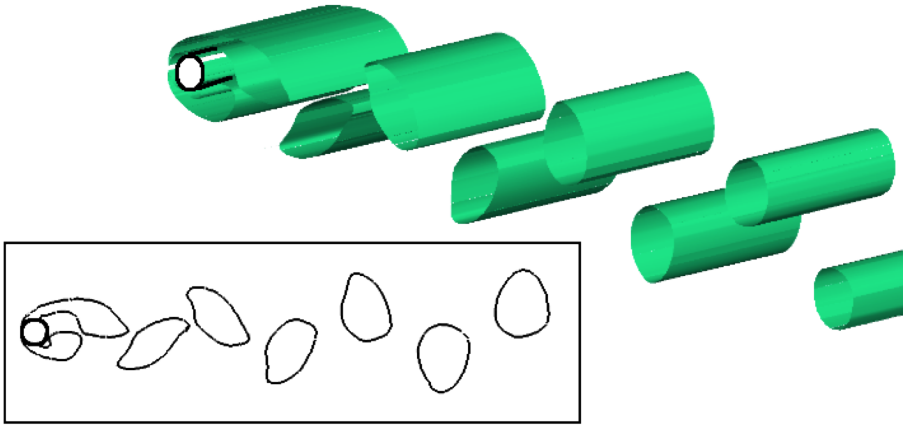

Figure 5.3: Q-isosurfaces for $Q = 0.01$ to show the vortex structure of the von-Kármán street of a flow past circular cylinder at $Re = 60$.

5.4 Suppression via surface bleed

As discussed in §5.1 and in §3.5, non-constant spanwise forcing along the surface of the cylinder is an efficient technique to disrupt vortex shedding and stabilise the wake. Therefore, starting from a fully developed vortex shedding, we apply surface bleed at the top and bottom surfaces of a cylinder, but, differently from the studies of Kim & Choi (2005), the location of the slots is slightly shifted towards the separation regions, where the spanwise vorticity ω_z is more prominent, as shown in figure (5.4). Two Gaussian profiles, centred in $\theta_c = \pi/9$ and $\theta_c = 8/9\pi$, with respect to the y axis, are adopted:

$$\phi_{xy}(\theta)|_{top/bottom} = \exp\left[-\frac{(\theta+\theta_c)^2}{2\zeta_{xy}^2}\right], \tag{5.6a}$$

$$\phi_{xy}(x,y)|_{top/bottom} = \exp\left[-\frac{\left(\arctan\left(\frac{y}{x}\right)+\theta_c\right)^2}{2\zeta_{xy}^2}\right]. \tag{5.6b}$$

The last relation (5.6b) was derived using the polar-cartesian coordinate transformation, while the parameter ζ_{xy} is the standard deviation of the Gaussian profile and represents the width of the forcing slot. In this thesis, ζ_{xy} was set to 0.1, hence forcing spans roughly from θ_A to θ_B reported in figure (5.4) and covers reasonably well the distribution of vorticity along the surface of the bluff body. Changing the position of the two slots, θ_C, within the range $[-\pi/9, \pi/9]$ did not show any significant variations in terms of drag reduction, but the current choice was seen to produce a slightly faster decrease.

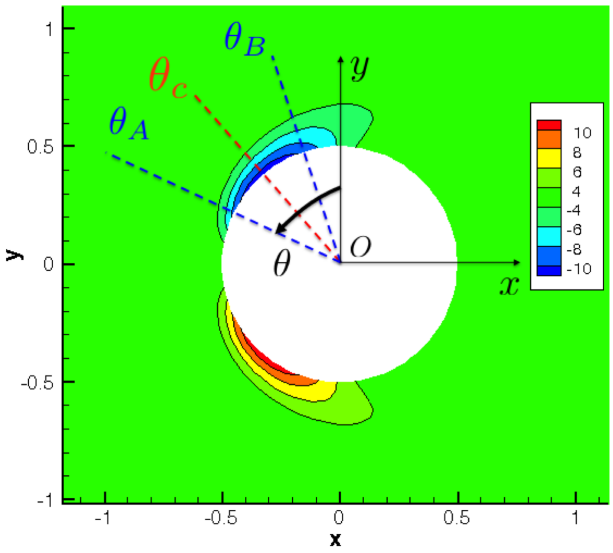

Figure 5.4: Sketch of the spanwise vorticity iso-contours around the cylinder and location of the top forcing slot.

Two different forcing functions were used in the spanwise direction. The first function, reported in (5.7), is a sinusoidal function, where λ_z is the forcing wavelength and ϕ_0 the phase:

$$\phi_z^s(z)|_{top} = \sin\left(\frac{2\pi z}{\lambda_z}\right), \tag{5.7a}$$

$$\phi_z^s(z)|_{bottom} = \sin\left(\frac{2\pi z}{\lambda_z} + \phi_0\right). \tag{5.7b}$$

In the present thesis, in-phase forcing ($\phi_0 = 0$) was used[3]. This choice is justified by the fact that out-of-phase forcing did not produce any drag

[3]the in-phase/out-of-phase is relative to the forcing at the top and bottom of the cylinder.

reduction at low Reynolds numbers and allowed us a direct comparison with previous results in the literature. Kim & Choi (2005) showed that out-of-phase forcing ($\phi_0 = \pi$) generates a reduction of the fluctuations of the aerodynamic forces at high Reynolds number ($Re \approx 3900$), but even in this case the reduction is considerably smaller than in-phase forcing. A second type of surface bleed was considered: a Gaussian function, centred at half of the spanwise length L_z, expressed by equation (5.8). To our knowledge, this is the first investigation of the effects of Gaussian surface bleed on a circular cylinder and represents an interesting case because it introduces modifications in a wider range of wavelengths than sinusoidal forcing, with relevant effects on the stabilisation of the wake.

$$\phi_z^g(z) = \exp\left[-\left(\frac{z - \frac{L_z}{2}}{2\zeta_z^2}\right)^2\right] \tag{5.8}$$

The global forcing function is determined by the product of (5.6b) and (5.7)-(5.8):

$$\phi(x, y, z) = \phi_{xy}(x, y)\phi_z(z). \tag{5.9}$$

This function has been normalised with respect to the integral of its square over the surface of the cylinder is unitary, such that the same amount of energy is introduced in the system for both typologies of spanwise forcing. This normalisation is particularly useful since it allows us to perform direct comparisons among different types of surface bleeds. The final expression of the forcing function reads:

$$\phi(x, y, z) = \frac{A\phi_{xy}(x, y)\phi_z(z)}{\int_\Omega \left[\phi_{xy}(x, y)\phi_z(z)\right]^2 d\Omega} \tag{5.10}$$

where A is the amplitude of forcing. A sketch of the surface bleed used in the present work is reported in figure (5.5). In the following sections we will investigate the effects of the different parameters to study the efficiency to suppress vortex shedding. In the first part of the chapter, we will focus mainly on a flow at $Re = 60$, above the onset of the Hopft bifurcation, while in the last part of this chapter we will discuss a case at a higher Reynolds number.

5.4.1 Spanwise wavelength λ_z and Gaussian width ζ_z

The effects of the spanwise wavelength of sinusoidal forcing, λ_z, and the spanwise standard deviation of Gaussian forcing, ζ_z, have been investigated,

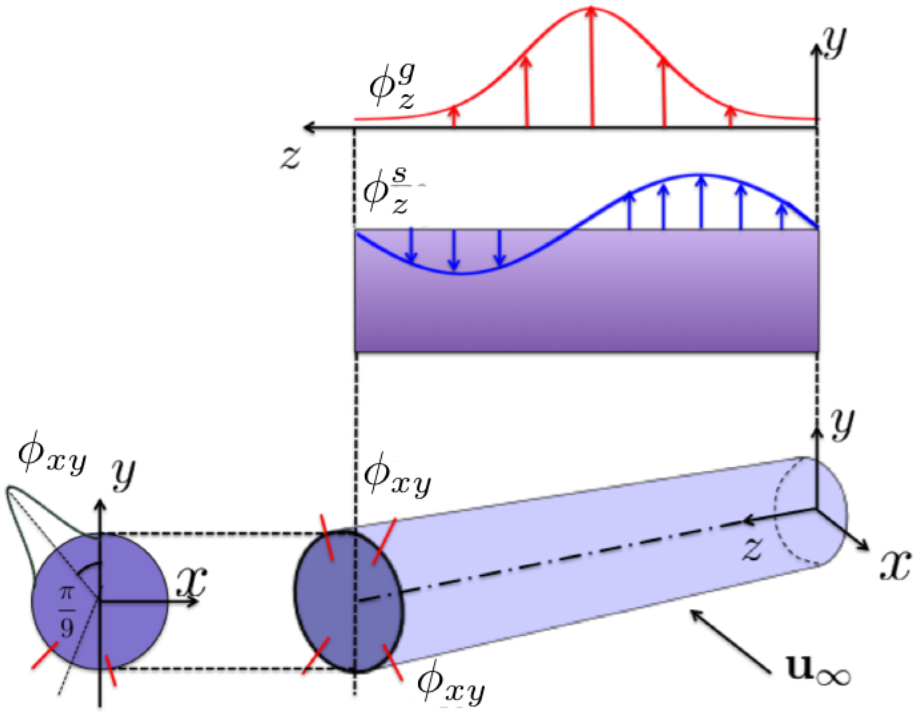

Figure 5.5: Sketch of distributed forcing. Two Gaussian forcing functions ϕ_{xy}, centred at $\theta_c = \pm\pi/9$ with respect to the vertical axis y, are applied in the xy plane. In-phase sinusoidal functions ϕ_z^s or Gaussian functions ϕ_z^g are instead applied along the span.

where we fix the amplitude of global forcing A to be 10% of the free-stream velocity ($A = 0.1u_\infty$). Figure (5.6) shows the time variation of the drag coefficient for different wavelengths of sinusoidal forcing. An increase of the wavelength results in a decrease of drag and a minimum is reached at $\lambda_z = 5D$. A further increase leads to larger values of drag, even though drag is still smaller than the unforced case; at the optimal wavelength, $\lambda_z = 5D$, maximum drag reduction is achieved at about 200 times units. The profile is very similar to the simulations performed by Kim & Choi (2005) and Darekar & Sherwin (2001).

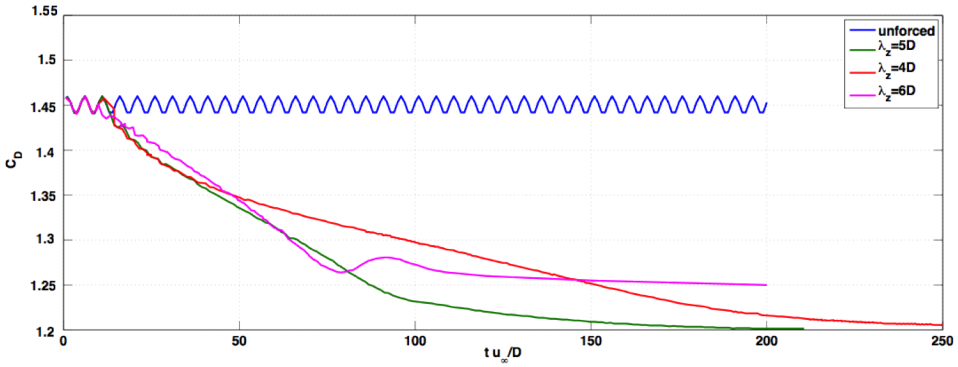

Figure 5.6: Variation of the drag coefficient with the wavelength λ_z at $Re = 60$.

A similar study was performed for the Gaussian spanwise forcing, at the same Reynolds number, where we vary the standard deviation, ζ_z, while we keep the amplitude of forcing fixed ($A = 0.1u_\infty$). When the standard deviation is decreased, which corresponds to a narrower Gaussian function, a reduction of the drag coefficient was observed, as figure (5.7) shows. This reduction is more prominent than sinusoidal forcing (about 20% lower) and it is achieved at about the same time units ($t \approx 200$). An explanation of the higher efficiency of the Gaussian forcing is related the strength of the cross-flow generated by this type of forcing, which produces a more relevant distortion of the shear layers, as we will discuss in the next section. It is important to remember that equation (5.10) guarantees a meaningful comparison between the two different types of forcing, since the controller injects in the system the same amount of energy. For $\zeta_z < 0.1$ the drag coefficient presents a local minimum at about $t \simeq 120$ and for $t \gtrsim 120$ no furtherreduction with respect to $\zeta_z = 0.1$ was detected. A main computational difficulty in the adoption of Gaussian forcing is the larger number of the Fourier modes necessary to obtain a sufficiently accurate approxi-

mation of the solution (errors less than 5%); 8 Fourier modes were seen to be sufficient up to $\zeta_z \leq 0.1$, but $\zeta_z = 0.05$ required 32 modes, which produced a noteworthy increase of the computational demand. Based on these considerations, $\zeta_z = 0.1$ was chosen.

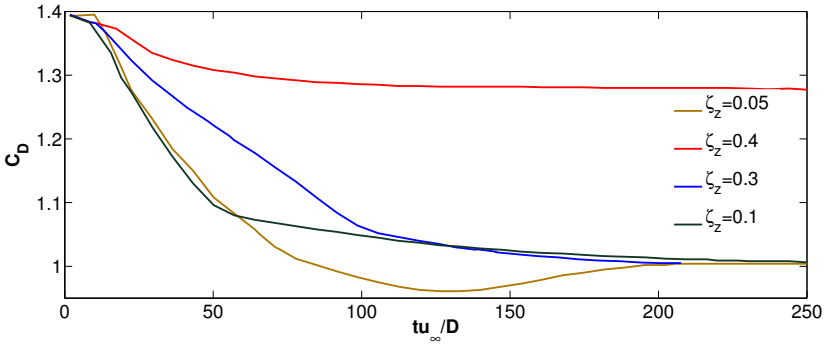

Figure 5.7: Variation of the drag coefficient with the spanwise standard deviation ζ_z at $Re = 60$.

An important question is the minimum value of the amplitude A able to completely suppress vortex shedding. This study was performed by varying A from 0 to 2 and analysing the behaviour of the wake topology and the coherent structures which characterise the von-Kármán street. For this study, the wavelength of sinusoidal forcing was fixed at $\lambda_z = 5D$, while the standard deviation of spanwise Gaussian forcing $\zeta_z = 0.1$. For both types of surface bleed a critical value of the amplitude was found. This value is able to completely suppress vortex shedding and stabilise the wake into a steady configuration. As we will discuss in §5.5, the suppressing of vortex shedding is related to the setup of a growing boundary layer on the leading-edge surface, which generates a spatial redistribution of vorticity. No significant differences in the wake topology were detected for the two different types of surface bleed and the general structure of the wake is shown in figure (5.8). This profile is symmetrical with both vertical and horizontal connections.

The minimal amplitude which leads to the suppression of vortex shedding was found to be $A^s_{cr} = 0.23$ for sinusoidal forcing and $A^g_{cr} = 0.12$ for the Gaussian one. At $Re = 60$, a further increase of the amplitude of forcing did not lead to any change in the wake topology, although this was not the case at higher Reynolds numbers. The critical amplitude of Gaussian forcing is about half the value of the sinusoidal one; these investigations suggest that Gaussian forcing is more efficient than the sinusoidal one because it produces larger drag reduction with a lower control velocity. Using definition (3.5) we

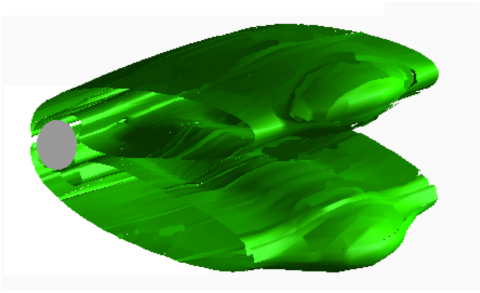

Figure 5.8: Perspective view of the three-dimensional wake at $tu_\infty/D = 300$.

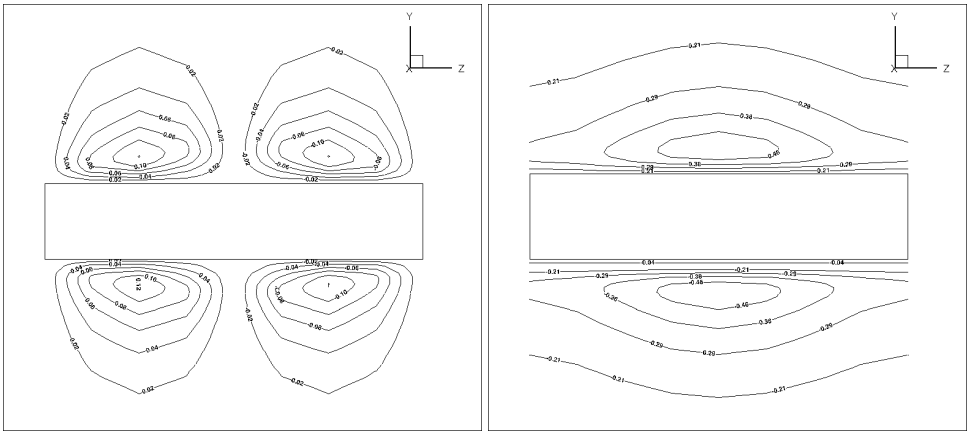

(a) Spanwise velocity w.

(b) Transverse velocity v.

Figure 5.9: Contours of the velocity components at $x = 0$.

found that the efficiency of Gaussian forcing is $\eta_2^g \approx 28$, about 20% higher than sinusoidal forcing ($\eta_2^s = 23$). The explanation of this result is related to the evolution of vorticity. The dynamics of the flow is dictated by the generation of a cross-flow velocity component w, as we can see from figure (5.9). The maximum value of the spanwise velocity w was seen to be about 20% of the free-stream velocity. The cross-flow is responsible for a higher influx of the spanwise velocity at $z = L_z/2$, and generates a higher transverse velocity v within the shear layers than in the region of the stagnation points, as figure (5.9b) points out. Therefore, the presence of a cross-flow component generates streamwise vorticity ω_x.

The streamwise and transverse component of the vorticity are shown in figures (5.10a) and (5.10b) respectively. These components are characterised by elliptical regions centred at $z = L_z/4$ and $3/4L_z$, where the magnitudes were found to be more intense. In figure (5.11) we track the evolution of the

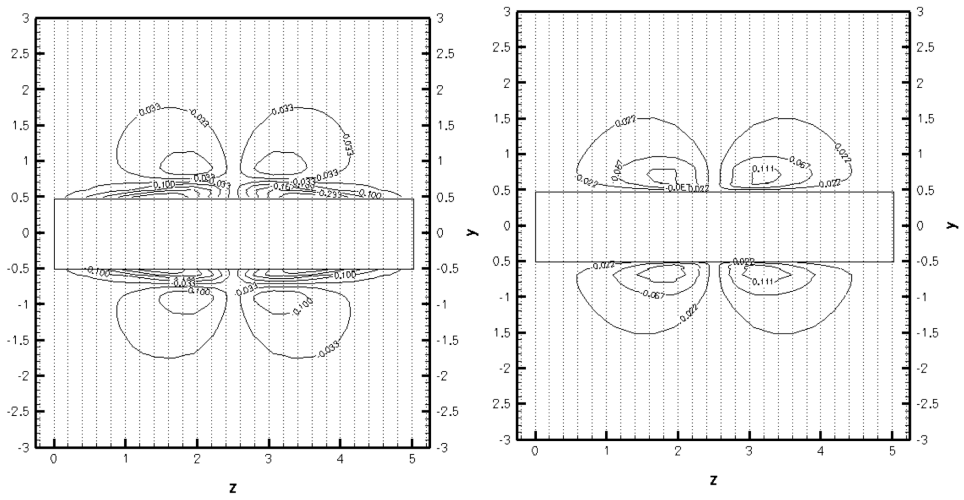

(a) Streamwise vorticity ω_x. (b) Transverse vorticity ω_y.

Figure 5.10: Contours of the vorticity components at $x = 0$.

ratio of the streamwise and spanwise vorticity at $(x, y, z) = (0, 0.7, L_z/4)$, close to one of these points: we can see that this ratio grows monotonically in time. Such three-dimensional redistribution of the vorticity prevents the interactions of the shear layers in the near-wake region and leads to a disruption of the von-Kármán street, as we will discuss in §5.5. The Gaussian profile introduces an amount of streamwise vorticity about 20% higher than the sinusoidal one, hinting the reason of its higher efficiency.

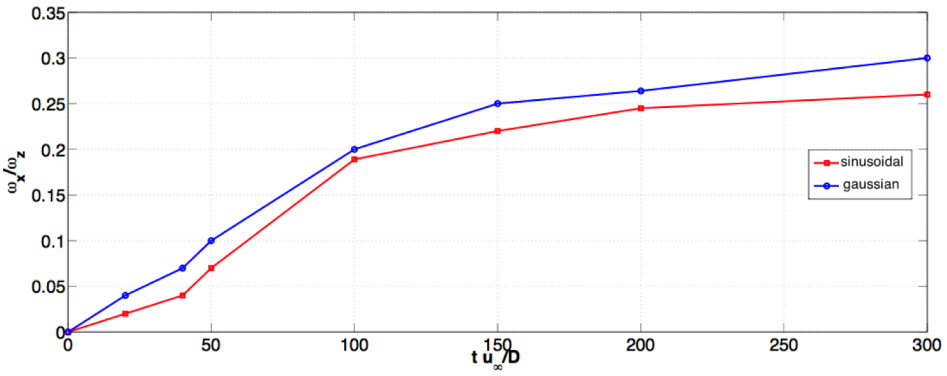

Figure 5.11: Time evolution of the ratio of streamwise and spanwise vorticity ω_x/ω_z at $(x, y, z) = (0, 0.7, L_z/4)$.

5.5 Physical mechanisms underlying the suppression of the von-Kármán street

In the previous section we showed that the introduction of surface bleed generates a cross-flow velocity with the appearance of additional streamwise and transverse components of vorticity. Both these components were found to be more intense in specific locations along the span. This phenomenon was seen to be directly related to the suppression of the von-Kármán street but leads to a key question: can we characterise qualitatively and quantitatively the physical mechanisms responsible for the stabilisation of the wake? Let us consider the development of vortex shedding for the unforced case; the two shear layers separating from the upper and lower surface of body can be regarded as two vortex sheets, which are composed of a series of vortex lines, as figure (5.12) shows.

These vortex sheets are subject to a self-induction motion, described by the Biot-Savart law, hence they tend to bend towards the near-wake region, where they interact, generating vortex shedding. Figure (5.13) shows the vortex lines extracted along a streamline when Gaussian forcing was applied at the critical amplitude; the vortex lines are now deformed along the streamwise and spanwise directions, and at $z = L_z/4$ and $z = 3/4L_z$ two inflections points can be observed. These points correspond to the regions where the streamwise vorticity was found to be more intense. We will refer to these point as *kinematic inflection points* since they are not related to any geometric modification of the problem.

The self-induction mechanism pushes the peaks of the vortex lines away from the centreplane, delaying the interaction of the vortex sheets in the near-wake. Due to the Biot-Savart law, the peaks of the vortex lines, $\boldsymbol{x_E}$ are subject to a positive vertical velocity, while the tips $\boldsymbol{x_T}$ to a negative one. Hence, the peaks of the vortices will move upwards, where the velocity is higher, while the tips are bound in the region with a lower velocity. This mechanism is summarised in figure (5.14) and it is responsible for the suppression of vortex shedding.

An additional quantitative evaluation of the physical suppression mechanisms is given by the time-evolution of the enstrophy of the system, which can be obtained by a scalar multiplication of the equation of vorticity equation by the vorticity itself and then integrating over the domain:

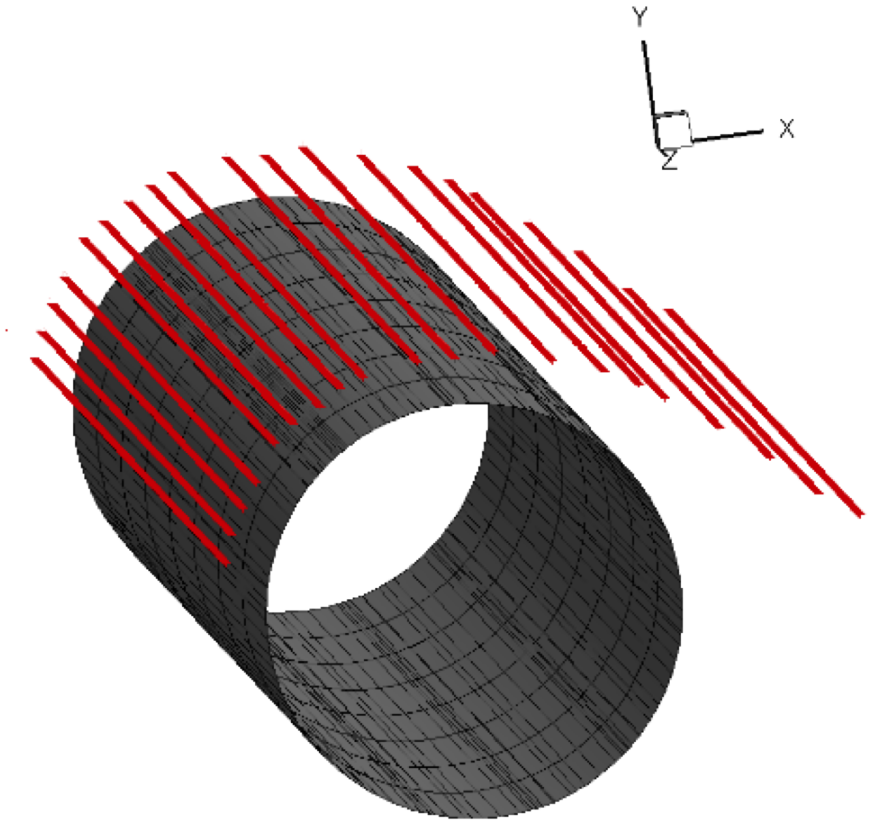

Figure 5.12: Vortex sheet associated the top shear layer for the unforced flow.

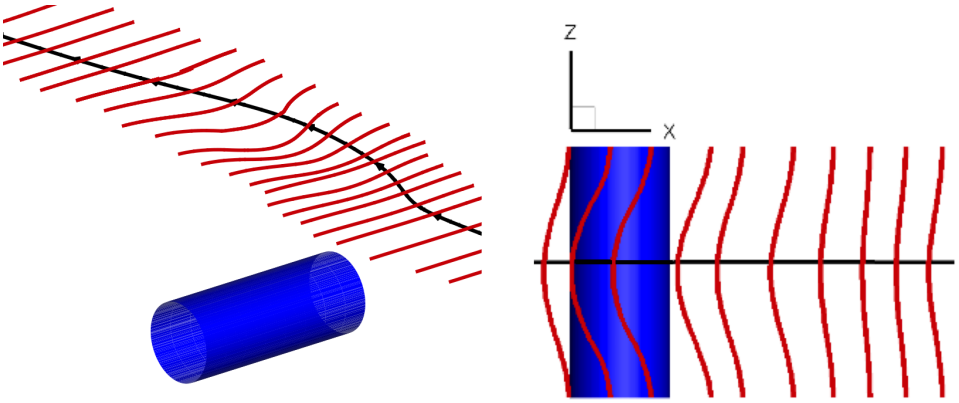

(a) (b)

Figure 5.13: Perspective views of the evolution of the vortex lines along a streamline.

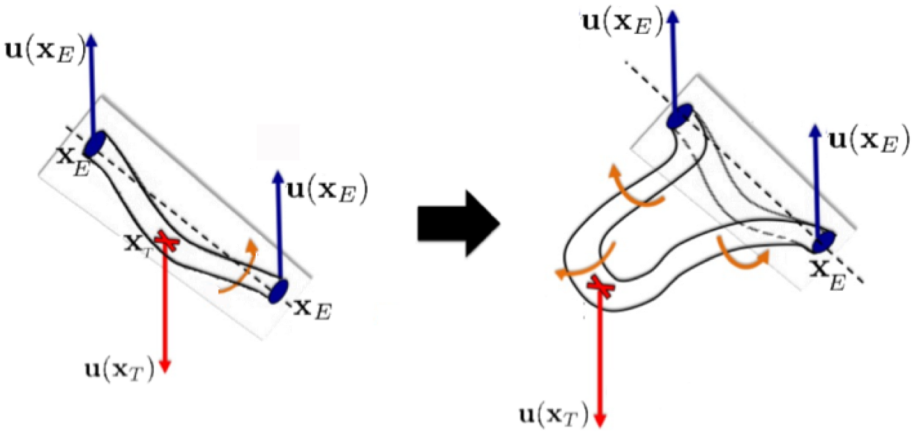

Figure 5.14: Sketch of the deformation mechanism of the vortex lines.

$$\frac{1}{2}\frac{\partial}{\partial t}\int_V \boldsymbol{\omega}\cdot\boldsymbol{\omega}dV = \int_V \boldsymbol{\omega}\otimes\boldsymbol{\omega} : \nabla \boldsymbol{U} dV + \frac{1}{2Re}\int_{\partial V}(\boldsymbol{\omega}\otimes\boldsymbol{\omega})\cdot\boldsymbol{n}dS + \\ - \frac{1}{Re}\int_V \nabla\boldsymbol{\omega} : \nabla\boldsymbol{\omega} dV. \tag{5.11}$$

The first term on the right hand side of (5.11) is a stretching and tilting term, which can raise the enstrophy, the second one is a diffusive flux throughout the boundary and the third one represents the enstrophy dissipation. This last term points out that the diffusive processes tend to attenuate the maxima of vorticity; in the unforced flows the production term is negligible (no streamwise or transverse components of the vorticity are present and the velocity gradient is zero along the spanwise direction). The introduction of distributed forcing enhances stretching and tilting mechanisms: in this case the enstrophy production term was seen to grow and it becomes about one order of magnitude larger than the diffusive contribution (figure 5.15). The prevalence of the enstrophy production mechanisms over the dissipation leads to an increase in the intensity of the vorticity, hence the direction of the shear layers is diverted and the formation of the von-Kármán vortices is inhibited. When vortex shedding is suppressed ($t \approx 200$), no further increase of the production of enstrophy was observed and the rate of change of enstrophy is roughly constant.

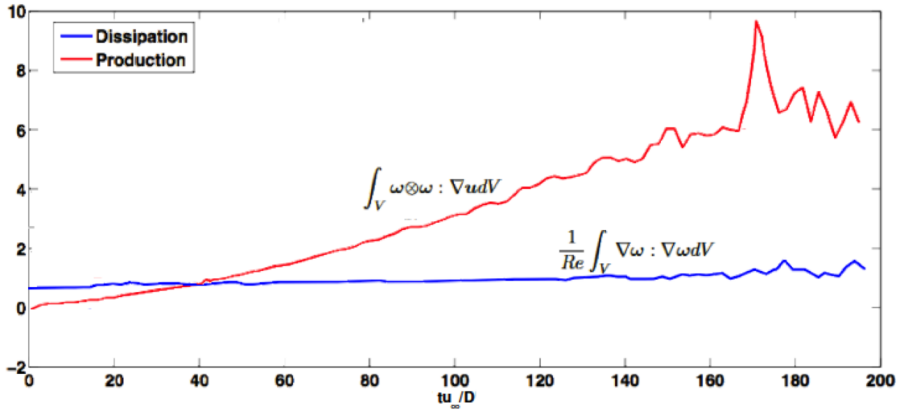

Figure 5.15: Time evolution of the production/dissipation of enstrophy.

Another approach to describe the suppression of vortex shedding can be given analysing the time evolution of the vortical structures. Figure (5.16) shows the evolution of the coherent structures at three-different times. As

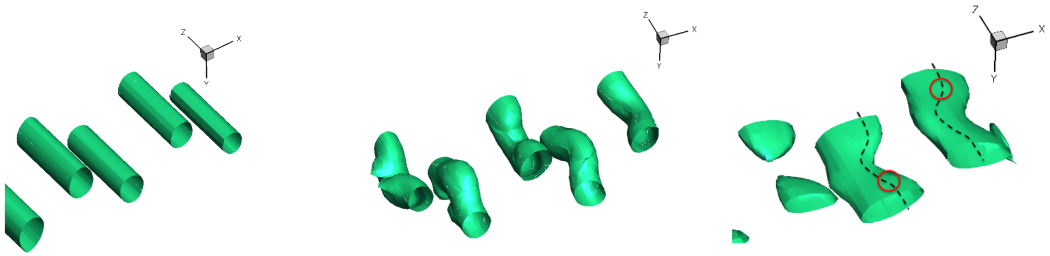

(a) $tu_\infty/D = 5$ (b) $tu_\infty/D = 80$ (c) $tu_\infty/D = 120$

Figure 5.16: Temporal evolution of the vortical coherent structures.

time increases, the structures become deformed in the spanwise direction and at time $tu_\infty/D = 120$, two counter-rotating vortices appear at the same streamwise locations, which correspond to the kinematic inflection points. Following Kim & Choi (2005), let us track the time evolution of the transverse velocity v in these two points; the oscillations of the transverse velocity v decrease in time and at $tu_\infty/D = 120$ they are completely out-of-phase, as shown in figure (5.17). Therefore, two three-dimensional vortices are introduced in the system, which are responsible for the suppression of vortex shedding. To summarise, all these approaches show that the suppression of vortex shedding is mainly determined by the introduction of three-dimensional effects in the flow field: the distortion of the vortex lines are related to the presence of two counter-rotating vortices, which generate a cross-flow velocity and a redistribution of the spanwise vorticity along the streamwise and transverse directions. The evaluation of the enstrophy of the system confirms that the diffusive effects are not able to inhibit this process and a global increase of the maxima of the vorticity is observed until vortex shedding is suppressed.

5.6 The necessity of stability analysis

Despite the fact that the mechanisms presented in the previous section are able to describe accurately the suppression of vortex shedding, some important physical features have not been addressed yet. As already hinted in chapter 4, two different types of instabilities coexist in wakes of flows past a bluff bodies: an absolute instability is generally dominant in the near-wake region, while convective instabilities are prominent in the far-wake. The global oscillations of vortex shedding and the presence of local absolute instabilities were seen to be deeply related (Huerre & Monkewitz

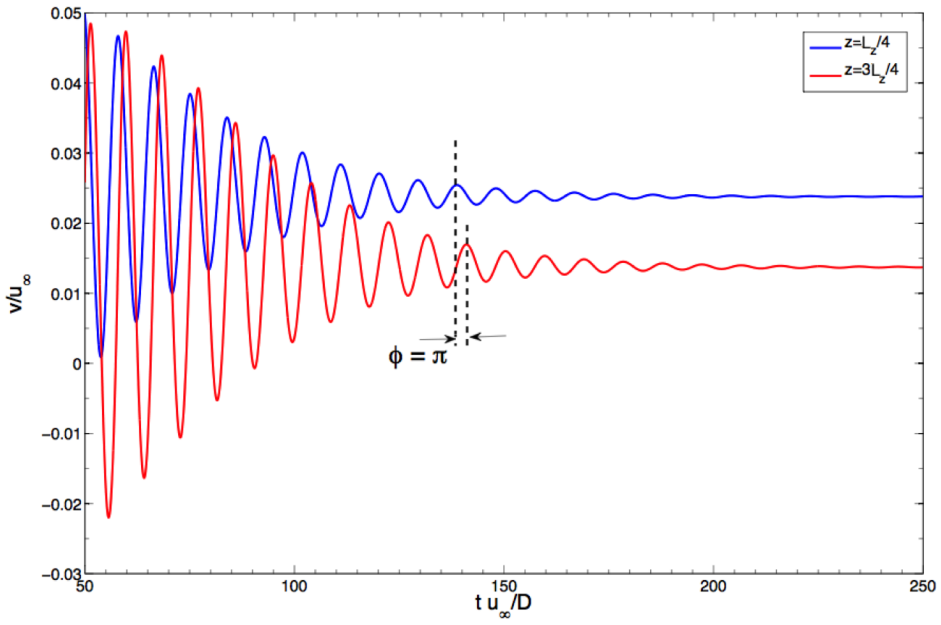

Figure 5.17: Temporal evolution of the transverse velocity at $z = L_z/4$ and $z = 3L_z/4$.

1995, Chomaz 2005).. Within the WKBJ approximation scheme (Bender & Orszag, 1978), the onset of a temporally growing instability was seen to necessitate the presence of a finite region of local absolute instability; more specifically, in flows past bluff bodies, when the Reynolds number exceeds a critical value, a linear global instability is triggered by a Hopf bifurcation and the instability wave is temporally amplified until a limit-cycle oscillation is reached, which is the von-Kármán street. Although, this process in fully non-linear, the non-linearities do not modify the propagation velocity that characterises the front of the "instability wave packet"; this result is very important because it allows us to adopt the ideas of the linear absolute instabilities to predict the behaviour of wakes (Delbende & Chomaz, 1998). Hence, linear stability analysis represents the most appropriate approach to investigate whether the spanwise modifications of the flow are responsible for the stabilisation of the near-wake absolute instability. Hwang *et al.* (2013) provided a first explanation, showing that the spanwise modulation of a parallel wake, modelled by a Monkewitz model, attenuates the absolute instability in a specific range of perturbation wavelengths, which is in accordance with both experimental and numerical results. However, this study does not clarify whether the wake modulations can completely suppress the absolute instability; furthermore, real configurations are very

complicated and the wake model may not be valid, as the authors point out. The control input velocities generally are not sinusoidal (i.e. we determined that Gaussian profiles can be more efficient) and the amplitude of surface bleed can be relatively large, differently from the assumptions made in this study. Moreover, the modulated base flow generally contains several spanwise wave-components and lacks any spanwise uniformity. An attempt to go beyond these limitation is offered by the recent surge of interest in the fully-three-dimensional stability analysis (TriGlobal stability). Similar studies were performed on a jet in cross flow (Bagheri *et al.* 2009, Ilak *et al.* 2012), spheres and discs (Natarajan & Acrivos 1993), but applications to flows past cylinders are still unexplored. Direct comparisons with the results obtained by Hwang *et al.* (2013) are an important part of this work since they allowed us to detect the limitations of the widely used simplifying models and pointed out the actual capabilities of three-dimensional controllers for the stabilisation of wakes.

5.7 Direct stability analysis

In the following section results from direct stability analysis are presented to determine how the dynamics of the global instabilities changes when distributed forcing is applied on the surface of the cylinder.

5.7.1 Methodology

The first step to perform the direct stability analysis is the generation of the base flow. When the amplitude of surface bleed is above the critical value A_{cr}, as discussed in §5.4, the flow was found to be steady, so it can be used to perform stability analysis. A more subtle problem is the study the stability of the unsteady configurations ($A < A_{cr}$), when distributed forcing is not able to completely suppress the oscillations caused by vortex shedding. However, the determination of the global modes in these configurations is important to understand how surface bleed acts on the instabilities. Besides the theoretical relevance of such problem, in some engineering applications a substantial reduction of drag could be more important than a complete suppression of vortex shedding. The lack of any straightforward time-periodicity in this regime makes the Floquet analysis unfeasible; a common methodology is to perform the stability analysis on the time-averaged base flows, which are solutions of the Reynolds-Averaged Navier-Stokes equations (RANS). However, this approach might lead to some difficulties since the base flow is not a genuine solution of the Navier-Stokes

equations due to the presence of the Reynolds-stress term. Moreover, stability analysis might not be able to determine the correct values of the growth rates (Barkley, 2006). Another approach consists in using steady state solutions of the Navier-Stokes equations; this approach has been successfully used in several studies, for instance the stability of the wake of a sphere (Pier, 2008), cavity flows (Akervik *et al.*, 2007), the convective instabilities of a flow past a cylinder (Abdessemed *et al.*, 2009*a*) and more recently in the TriGlobal stability analysis of a jet in crossflow (Bagheri *et al.* 2009, Ilak *et al.* 2012). In this thesis we will use steady base flows to study the stability when forcing does not completely suppress vortex shedding. These steady base flows were computed by inserting a symmetry condition along the centreplane and then time-marching the Navier-Stokes equations until the steady state was reached; figure (5.18) shows a sketch of the geometry used to generate the steady base flows. An additional boundary condition along the centreplane $\pi := \{(x, y, z)|y = 0, z = 0\}$ was used to enforce the steadiness of the solution. This condition is given by $\frac{\partial u}{\partial n} = 0$, $v = 0$ and $\frac{\partial w}{\partial n} = 0$.

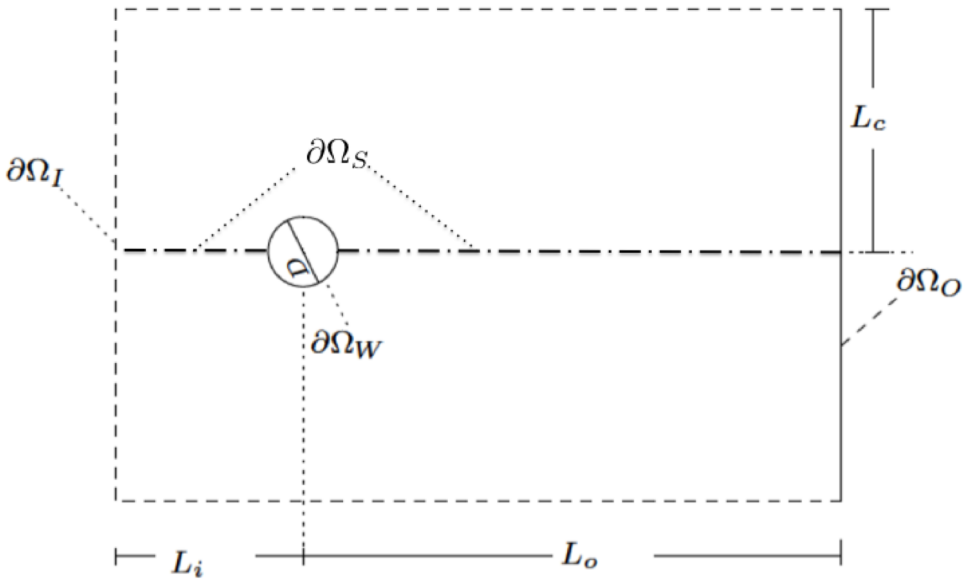

Figure 5.18: Geometry adopted to compute the steady state solution.

In this thesis, global stability analysis was performed using an Arnoldi method (refer to Appendix A for further details). Both the "Modified Arnoldi" (Barkley *et al.* 2008) and `ARPACK` (Lehoucq *et al.* 1998) algorithms

Krylov subspace dimension	Eigenvalues Error
$m = 4$	20%
$m = 6$	17%
$m = 10$	12%
$m = 12$	7%
$m = 14$	4%
$m = 16$	2%

Table 5.2: Error between the absolute values of the dominant eigenvalue for the unforced case and the values reported by Noack & Eckelmann (1994).

were seen to converge to the same dominant eigenvalues, with differences smaller than 10^{-6}. The dimension of the Krylov subspace was set to $m = 16$, which was found to be sufficiently high to capture the dynamics of the system. Table (5.2) shows the error of the absolute value of the dominant eigenvalues of the unforced flow (two-dimensional vortex shedding) with respect to the values reported by Noack & Eckelmann (1994).
The following computations were performed using spanwise Gaussian forcing with a standard deviation $\zeta_z = 0.1$, as discussed in §5.4. The adoption of sinusoidal surface bleed with a wavelength $\lambda = 5D$ did not show any relevant differences in terms of the topology of the global mode and the variation of the growth rate over the amplitude of forcing A.

5.7.2 Eigenvalues and eigenmodes

In this section we will discuss the eigenvalues obtained from the stability analysis and the topology of the global modes at different values for the forcing amplitude A. Figure (5.19) shows the profile of the growth rate σ over the amplitude of the forcing A: an increase of surface bleed results into a progressive weakening of the leading eigenvalue, in fact the growth rate decreases until it becomes zero when the critical amplitude of the forcing is adopted; when $A = A_{cr}$ the flow is neutrally stable and a further increase of the forcing leads to the stabilisation of the wake, with disturbances decaying in time more rapidly. However, this behaviour is observed until $A = 0.22$, when the curve saturates to a decay rate $\sigma \simeq -5 \times 10^{-2}$.

The leading eigenvalues appear as complex-conjugate pairs, therefore a characteristic frequency of the growing/decaying disturbances can be defined.

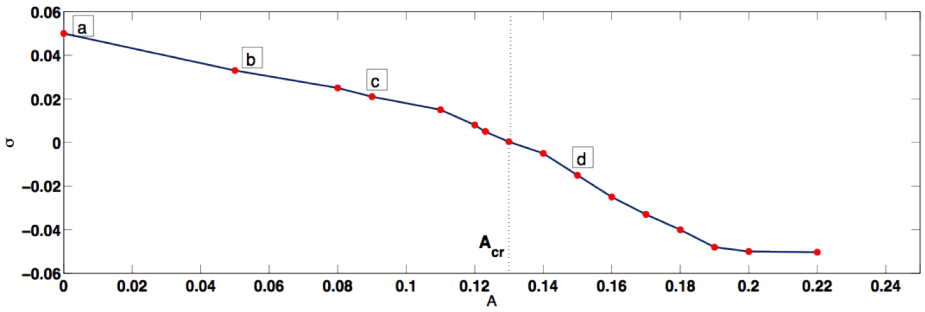

Figure 5.19: Growth rate as a function of the amplitude of the forcing A.

The frequency of the system over the forcing amplitude in reported in figure (5.20).

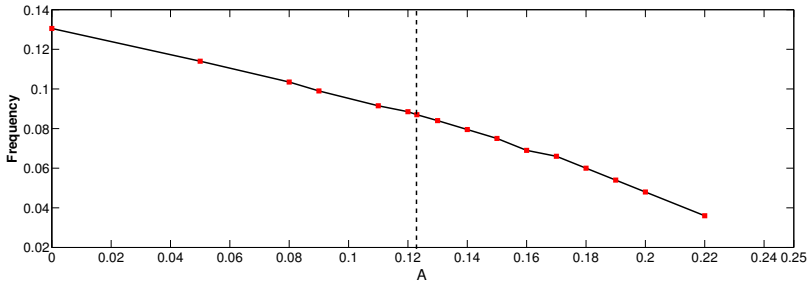

Figure 5.20: Frequency as a function of the amplitude of forcing A.

Let us consider the profiles of the leading eigenmodes for four different amplitudes reported in figure (5.19). When no forcing is applied to the flow the eigenmode shows a row of extended vortices with alternating sign, which are convected downstream, as shown in figure (5.21a). As expected, the mode is purely two-dimensional since no variation was introduced in the spanwise direction. When $A = 5 \times 10^{-3}$ a spanwise variation of the mode can be observed from figure (5.21b); the most pronounced characteristic of the eigenmode is that its magnitude is nearly zero for $x \gtrsim 30D$. This profile might indicate that despite forcing not being large enough to suppress the near-wake absolute instability, it may have an effect in the far-wake region, where convective instabilities occur. Increasing the amplitude, the three-dimensionality of the mode becomes more pronounced and the mode tends to be located in the near-wake region, while it spatially decays downstream (figure (5.21c)).This mechanism continues until the flow become stable (fig-

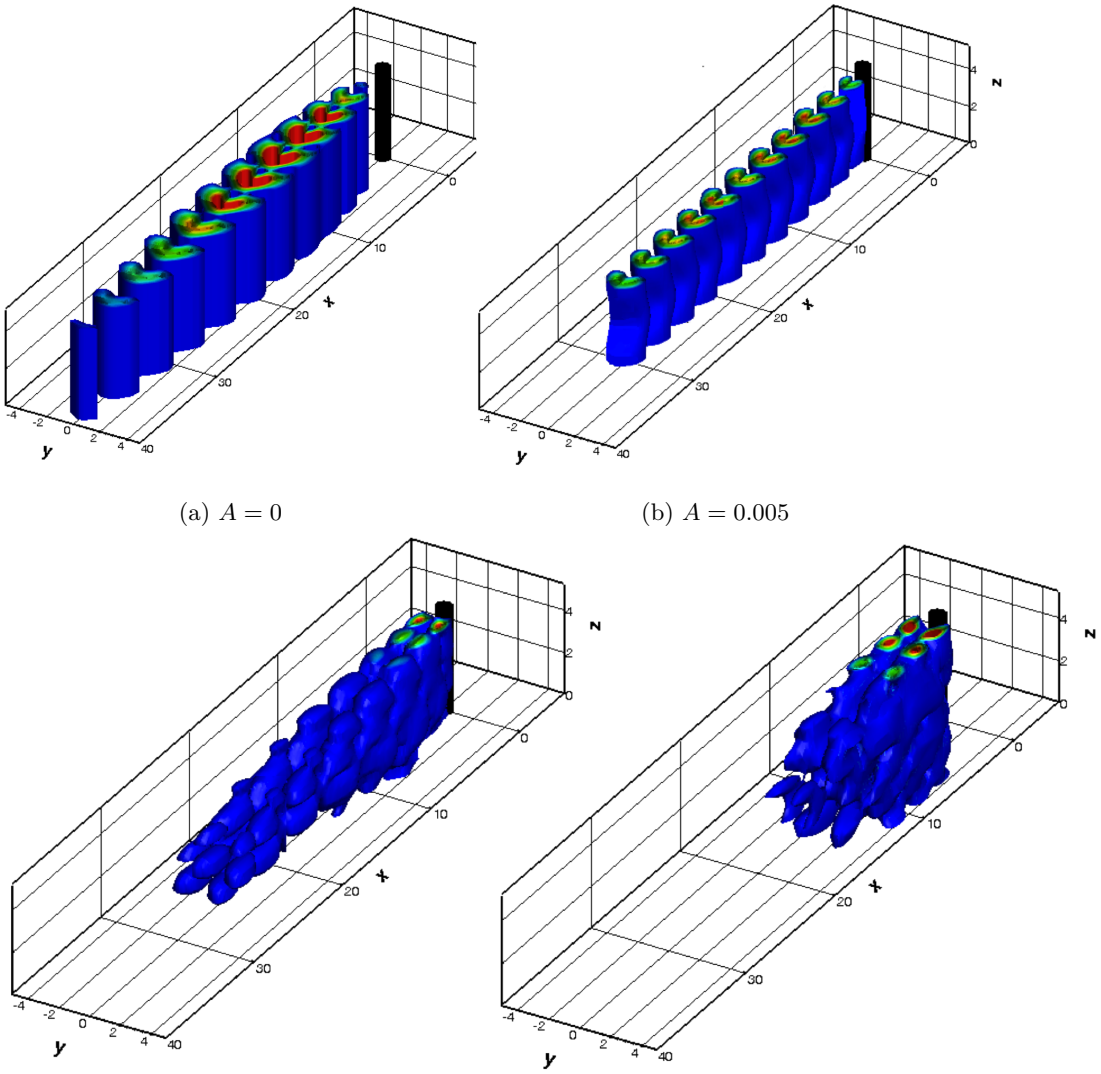

(a) $A = 0$

(b) $A = 0.005$

(c) $A = 0.008$

(d) $A = 0.15$.

Figure 5.21: Topology of the eigemodes for four different amplitudes.

ure (5.21d)), then no significant change in the shape of the mode was detected as A was increased further.

The eigenmodes can be used to study the non-linear behaviour of the transition. We can analyse this behaviour starting from the Landau equation (5.12), which describes the time evolution of the amplitude A of a small perturbation[4]:

[4] A in this case represents the amplitude of the perturbations and should not be confused with the amplitude of forcing introduced in §5.4

$$\frac{dA}{dt} = \lambda_1 A + \lambda_2 |A|^2 A + \lambda_3 |A|^4 A + \cdots + \lambda_n |A|^{2n} A \tag{5.12}$$

In equation (5.12) $\lambda_n \in \mathbb{C}$ are the Landau coefficients. To a first order approximation, the perturbation grows at a rate given by the real part of λ_1, but as time increases non-linear effects become more prominent and the high order terms are fundamental to describe the transition. Provansal, Mathis & Boyer (1987) showed that λ_1 is the eigenvalue obtained by linear stability analysis: the real part, $\mathcal{R}(\lambda_1)$, is the growth rate σ, while the imaginary part, $\mathcal{I}(\lambda_1)$ the frequency ω. Therefore, before the on-set of the non-linearities, the perturbations are subject to an amplification given by the growth rate of linear stability analysis. Let us write the amplitude A in the complex notation $A = |A(t)| \exp(i\phi)$, then equation (5.12) becomes:

$$\frac{d \log |A|}{dt} = \sigma + O(|A|^2) \tag{5.13a}$$

$$\frac{d\phi}{dt} = \omega + O(|A|^2) \tag{5.13b}$$

In the linear approximation, solving the ordinary differential equation given by (5.13a) leads to (5.14):

$$\log |A| = \log |A_0| + \sigma t \tag{5.14}$$

where $|A_0|$ is the amplitude of the perturbation at the initial time t_0. This implies that the slope of the tangent at $t = 0$ represents exactly the growth rate. Following Henderson & Barkley (1996), we can define the amplitude in terms of the flow variables:

$$|A(t)| = \left(\int_\Omega \left| \sum_{i=0}^{N} \hat{\boldsymbol{u}}_i(\boldsymbol{x}, t) \right|^2 \right)^{1/2} \tag{5.15}$$

where $\hat{\boldsymbol{u}}_i$ are the N Fourier coefficients of the velocity field and Ω is the computational domain. Let us superpose the steady base flow with the unstable mode found at $A = 0$, multiplied by a small factor, e.g. $\varepsilon = 10^{-6}$, such that the initial growth is linear. Evolving the non-linear equation we obtain a velocity field which is similar to the vortex street at higher Reynolds number. The profile of the logarithm of the amplitude of the perturbation over time is reported in figure (5.22), which shows that the initial linear growth exactly matches the value determined by stability analysis. As time increases, the non-linearities becomes more prominent until a saturation of the perturbations was detected. This result is important because it provides

a validation of the results we obtained and it clearly shows the limitations of linear analysis.

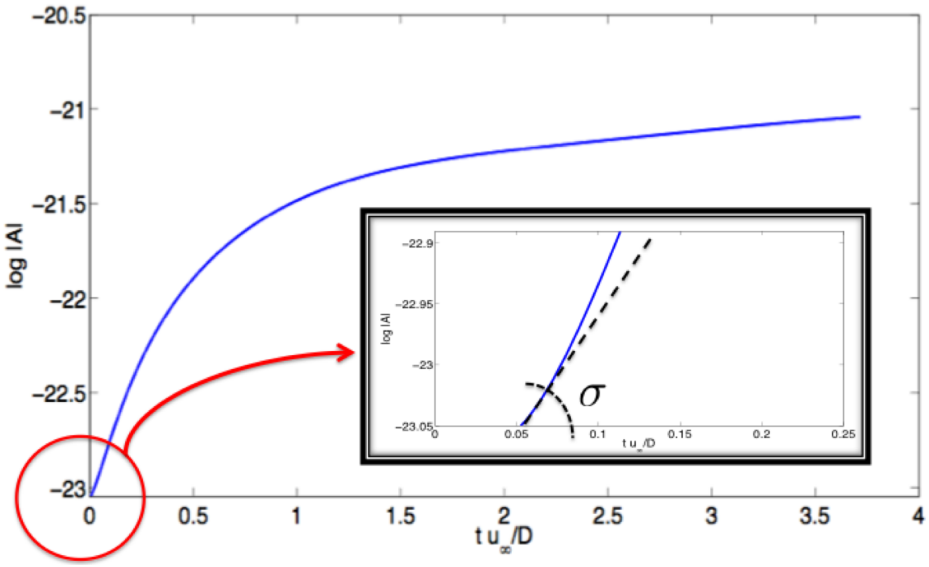

Figure 5.22: Non-linear behaviour of the perturbations

Let us consider now the stable eigenmode obtained at $A = 0.13$, when vortex shedding is completely suppressed. Figure (5.23) shows the vortical structures of the mode obtained by the Q-criterion. As already discussed, the mode is located in the near-wake region of the cylinder, $0.5D < x < 10D$, and its intensity progressively fades away in the streamwise direction. The vortical structures show a waviness along the spanwise direction and the structures become more disrupted as we move downstream, until they are broken down at about $x = 5D$. This result provides a first evidence that the leading perturbations act mainly in the area where the sensitivity is more intense, affecting the core of the absolute instability, as we will discuss in §5.8. This region is known as the wavemaker, and it represents the region where the oscillation originates and from which it propagates to the rest of the fluid.

To study the profile of the eigenmode, we consider a $y - z$ section at $x = D$. The behaviour in the other significant locations ($0.5 < x < 10D$) was found to be qualitatively similar, in accordance with the profile shown in figure (5.23). The contours of figure (5.24) show the normalised absolute value of the three components of the eigenmode, while the superposed isolines indicate the base flow at the same location. The profile of the streamwise

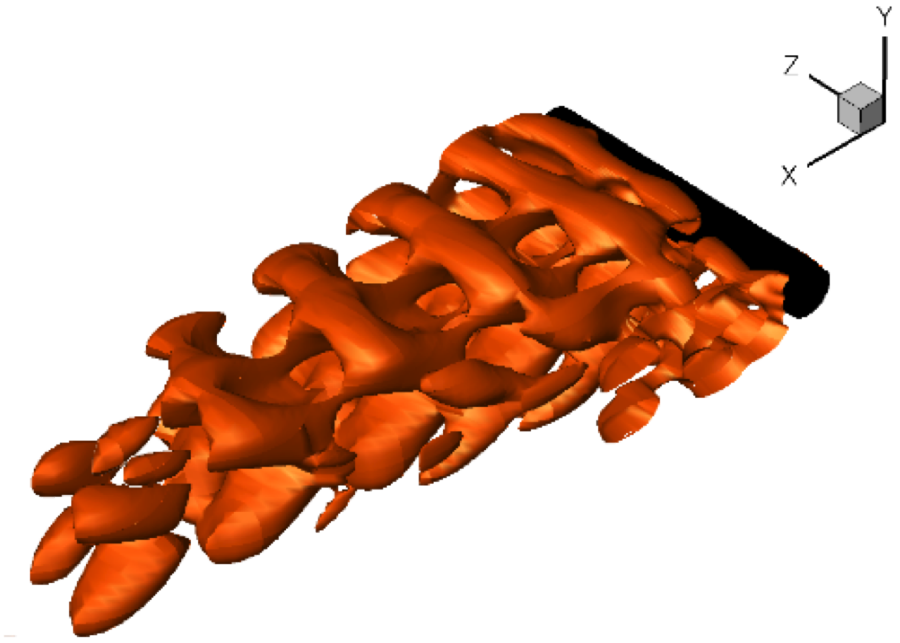

Figure 5.23: Q-isosurface of the eigenmode for $Q = 0.001$.

velocity perturbation u' is located in a narrow spanwise range $1 < z < 4$ and its peak is in the regions just above/below the cylinder, where the perturbations are able to disrupt vortex shedding. The transverse perturbation velocity v' is stronger along the axis $y = 0$ and its intensity is more pronounced in the region where the base flow is slower. Finally, the spanwise perturbation velocity is more prominent at the extremities of the domain ($z = L/4$ and $z = 3/4L$), again in the region just above and below the cylinder, similarly to the transverse component. These results are in accordance with Hwang *et al.* (2013) and provide an indication of how the stabilisation is achieved. The transverse perturbation velocity v' induces a modification of the base flow along the centreplane and prevents the interactions of the top and bottom shear layers and disrupts the mechanisms of formation of vortices. The evidence that the spanwise perturbation velocity w' is prominent in the region where the streamwise vorticity is more intense (figure (5.21)) confirms in a stability analysis framework that the presence of cross-flow perturbations enhances localised spanwise modifications of the base flow, which generate the additional components of vorticity, as explained in §5.4.

These considerations highlight the strong relation between the mechanisms of suppression of vortex shedding and the leading eigenmode, but some questions arise: how do the perturbations and the base flow interact? How does the interaction affect the stabilisation of the wake? To answer these questions let us start by considering the curl of the linearised Navier-Stokes equations, which describes the evolution of the vorticity perturbations $\boldsymbol{\omega'}$:

$$\frac{\partial \boldsymbol{\omega'}}{\partial t} + \boldsymbol{U} \cdot \nabla \boldsymbol{\omega'} = \boldsymbol{\omega'} \cdot \nabla \boldsymbol{U} + \boldsymbol{\Omega} \cdot \nabla \boldsymbol{u'} - \boldsymbol{u'} \cdot \nabla \boldsymbol{\Omega} + \frac{1}{Re} \nabla^2 \boldsymbol{\omega'}. \tag{5.16}$$

where $\boldsymbol{U}$ and $\boldsymbol{\Omega}$ represents the base flow velocity and its vorticity respectively. The first two terms on the left hand side of (5.16) represent the advection of the vorticity perturbations by the base flow, while the first and last term on the right hand side represent the tilting mechanisms by the base flow and the viscous dissipation respectively. The two additional terms present in the right hand side of equation (5.16) introduce a variation of the vorticity perturbations by the interaction between the base flow and the velocity perturbations. In particular, the term $\boldsymbol{u'} \cdot \nabla \boldsymbol{\Omega}$ acts as a potential trigger for the development of the instabilities and does not play a crucial role in the process. To verify this, let us consider the evolution of the perturbation enstrophy, which can be obtained by a scalar multiplication of equation (5.16) by $\boldsymbol{\omega'}$ and integrating over the domain:

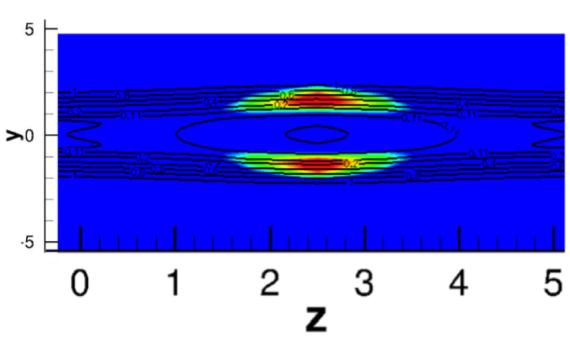

(a) $|u|/|u|_{max}$

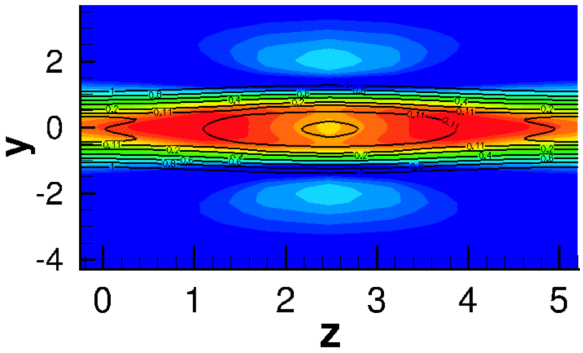

(b) $|v|/|v|_{max}$

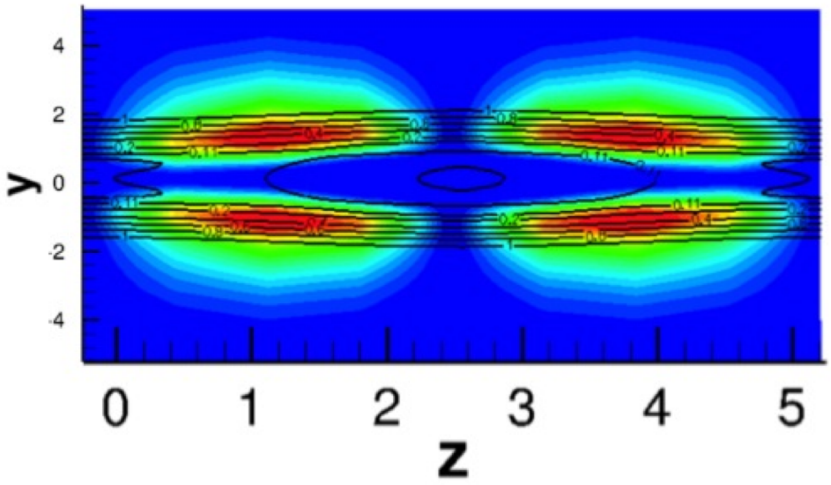

(c) $|w|/|w|_{max}$

Figure 5.24: Components of the perturbation velocity $\boldsymbol{u}'$ at $x = D$. Blue are the less intense regions, red the more intense ones.

$$\frac{1}{2}\frac{\partial}{\partial t}\int_V \boldsymbol{\omega'}\cdot\boldsymbol{\omega'}dV + \int_V (\boldsymbol{\omega'}\otimes\boldsymbol{\omega'}) : \nabla\boldsymbol{U}dV = \int_V (\boldsymbol{\omega'}\otimes\boldsymbol{\omega'}) : \nabla\boldsymbol{U}dV + \\ + \int_V (\boldsymbol{\omega'}\otimes\boldsymbol{\Omega'}) : \nabla\boldsymbol{u'}dV - \int_V (\boldsymbol{\omega'}\otimes\boldsymbol{u'})\nabla\boldsymbol{\Omega}dV + \frac{1}{2Re}\int_{\partial V}(\boldsymbol{\omega'}\otimes\boldsymbol{\omega'})\cdot\boldsymbol{n}dS + \\ - \frac{1}{Re}\int_V \nabla\boldsymbol{\omega'} : \nabla\boldsymbol{\omega'}dV \tag{5.17}$$

We can evaluate the contribution to the variation of the enstrophy perturbation from the tilting term (first term on the right hand side) and the interaction of the perturbations with the base flow (second and third term on the right hand side) when the perturbation is the leading eigenmode. The interaction of the base flow shear and the perturbations (third term on the right hand side) was seen to be about three order of magnitude smaller than the other ones. This confirms that once the flow is stabilised the interaction of the base flow shear and the perturbations does not have a significant influence on the dynamics of the system. The tilting term was seen to be the dominant one, of order 10^{-3}, although the interaction of the perturbation shear and the base flow is still quite relevant ($\approx 10^{-4}$). Therefore, this consideration suggests that the stabilisation is related to the combination of vortex tilting by the base flow shear and the subsequent interaction of the deformed vortices with the perturbations. The introduction of spanwise forcing in the base flow enhances tilting of the spanwise vorticity perturbation ω'_z and the development of streamwise and transverse components (ω'_x and ω'_y respectively). The vorticity is then subject to perturbations along every spatial direction and quickly becomes three-dimensional and interacts with the time-evolving perturbations $\boldsymbol{u'}$. A better quantitative characterisation of the phenomenon can be given using the Reynolds-Orr equation (4.7), which describes the evolution of the kinetic perturbation energy as a sum of two terms: the work of the Reynolds stresses again the base flow shear and the dissipation. The evaluation of the components which constitute the first term quantifies the amount of energy that the perturbations extract from the base flow. The dominant terms are reported in figure (5.25) and are $u'v'\frac{\partial U}{\partial y}$, $u'v'\frac{\partial V}{\partial x}$ and $v'^2\frac{\partial V}{\partial y}$.
This shows that the instability mechanisms that govern the stabilisation of the wake are mainly related to the work of the Reynolds stresses against the streamwise and transverse components of the base flow shear, whereas the terms involving the spanwise components are practically negligible. This result, as already discussed, is related to the fact that the stabilisation mechanism involves mainly the generation of a cross-flow velocity at the expense

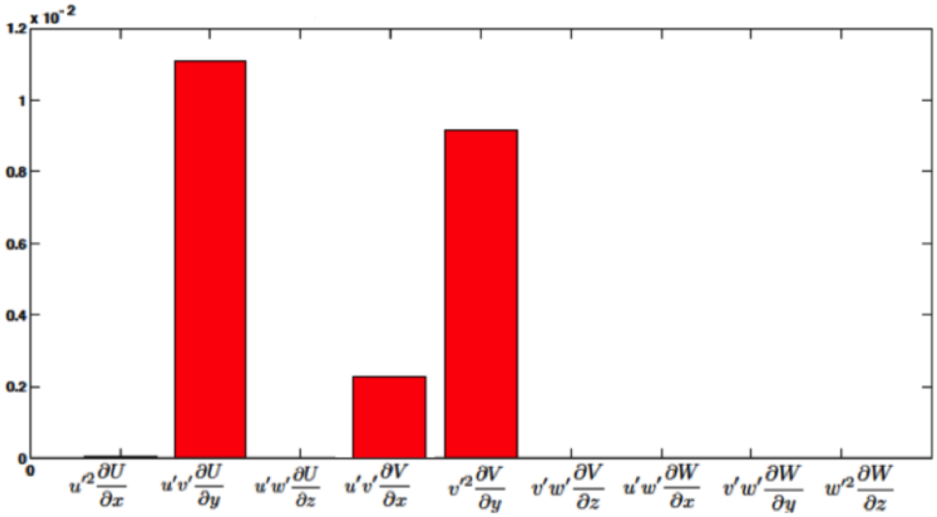

Figure 5.25: Energy budget analysis of the base flow forced with a Gaussian function of amplitude $A = 0.13$.

of the streamwise and transverse components. Therefore, the perturbations will act on the intensity of the streamwise and transverse components of the base flow shear and divert the energy into the spanwise direction. We can analyse the contribution of each of these three-terms by calculating their spatial distribution over the domain: positive values indicate an increase in the rate of change of perturbation kinetic energy, negative values a reduction. It is important to stress that while the increase of energy is uniquely related to the interaction with the base flow, the reduction of the perturbation kinetic energy is connected also to the viscous damping term, which always subtracts energy. The profiles are reported in figure (5.26). All these terms show a mild variation in the spanwise direction and the interaction is more pronounced in the recirculation bubble region. Therefore, the transverse components of the base flow shear act as the main source of energy for the perturbations; in particular, the term $u'v'\frac{\partial U}{\partial y}$ contributes most to the disturbance energy balance and it shows that the Reynolds-stresses give and takes energy away through interaction with the bottom and top shear layers respectively. Finally, the term $v'^2\frac{\partial V}{\partial x}$ indicates that the interaction with the transverse derivative $\frac{\partial V}{\partial y}$ is mainly along the centreplane, with a rather strong extraction of energy in the near-wake region.

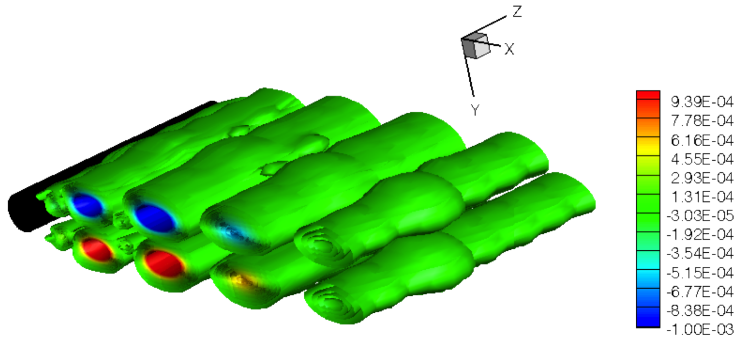

(a) $u'v'\frac{\partial U}{\partial y}$

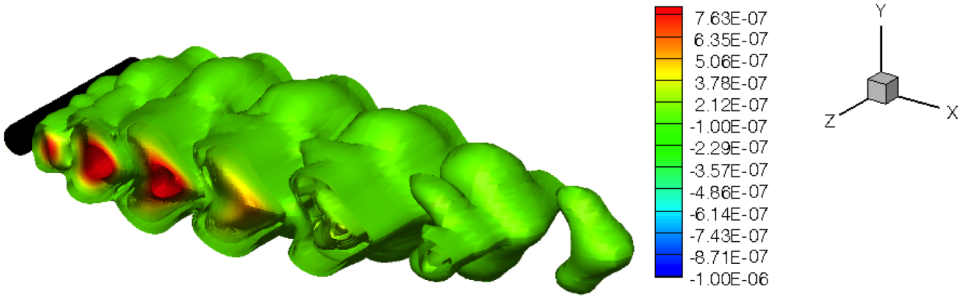

(b) $u'v'\frac{\partial V}{\partial x}$

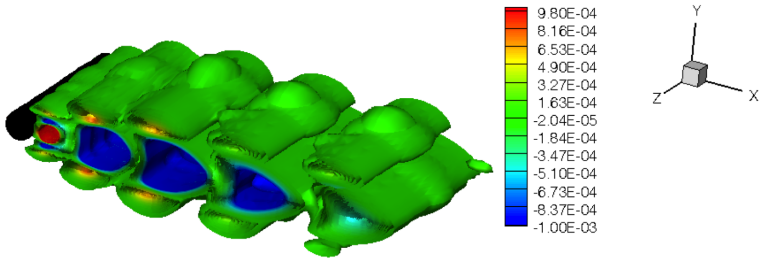

(c) $v'^2\frac{\partial V}{\partial y}$

Figure 5.26: Spatial distribution of the most significants components of the Reynolds-Orr term $\boldsymbol{u'} \otimes \boldsymbol{u'} : \nabla \boldsymbol{U}$

5.8 Receptivity analysis and structural sensitivities

The results of direct stability analysis helped us to understand the physics involved in the suppression of vortex shedding and confirmed that the spanwise modulation is responsible for the suppression of the near-wake absolute instabilities. However, the receptivity analysis provides additional indications on the capability of the control technique. Specifically, the global adjoint mode describes how the systems respond to momentum forcing. Therefore, the three-dimensional adjoint mode was computed in a similar manner to the direct one, and its profile is reported in figure (5.27). The profile shows a distinct variation in the spanwise direction, indicating that the regions more receptive to momentum forcing vary along the surface of the cylinder. We consider a $y-z$ section of the mode at $x = -0.17$, which intersects the cylinder at θ_c, where the peaks of forcing ϕ_{xy} was applied. The mode is located in a small layer in proximity of the cylinder and its width is roughly constant. The regions most receptive to momentum forcing are nearby the kinematic inflection points, at $z = L/4$ and $z = 3/4L_z$ respectively; this shows that the forced flow responds mostly to modifications close to these regions, which is consistent with the findings from the direct numerical simulations and direct stability analysis.

However, we need to evaluate the structural sensitivity to detect where the core of the instability is located. As discussed in §4.6.2, the structural sensitivity $\lambda(x, y, z)$ can be calculated as the spectral norm of the product of direct and adjoint modes and its profile is shown in figure (5.29). Along the streamwise direction, the profile is similar to the one of a two-dimensional unforced cylinder, described in §4.8, although some important modifications can be detected. The sensitivity still presents two lobes which are symmetrical with respect to the centreplane, at about $2D$ downstream from the cylinder. Both close to the cylinder (where the adjoint peaks) and far downstream (where the direct mode peaks), the product of the adjoint and direct modes is negligible, therefore these regions are not particularly important for the onset of the instabilities. However, these two lobes are slightly shifted towards the extremities of the domain, which is related to the diversion of the shear layers explained in §5.4. The largest drift of the eigenvalue is still at the same streamwise location of the unforced case, which is predicted by the dispersive-wave theory, but at the transverse locations of forcing. Structural perturbations on the centreplane do not have any impact; this result has a connection with the fact that the vortex sheets do not interact in this region, inhibiting the formation of vortex shedding. Finally the structural

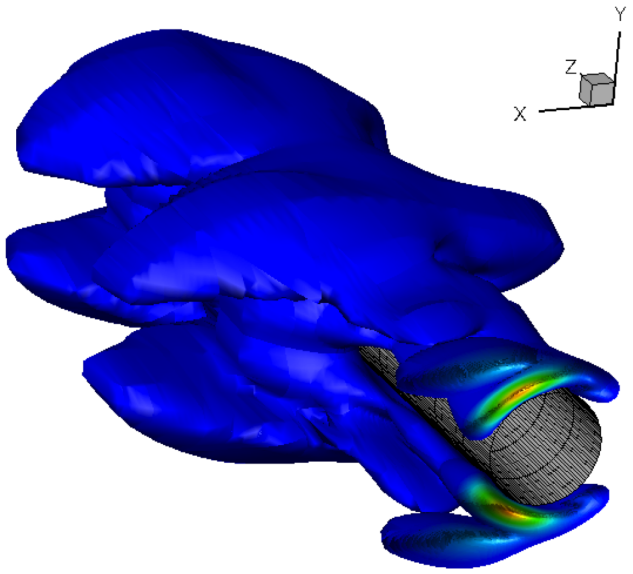

Figure 5.27: Three-dimensional perspective of the adjoint mode.

sensitivity does not show a pronounced variation in the spanwise direction as figure (5.29) shows.

This last result suggests that two-dimensional structural perturbations are more relevant than the spanwise ones to suppress the absolute instability. This leads us to ask the actual reason behind the high efficiency of the three-dimensional methods. A reasonable explanation relies on the structural sensitivity to base flow modifications. A structural perturbation in the flow produces a force proportional and parallel to the local velocity (spatial localised feedback), but it acts also on the steady base flow and its time-varying disturbance. The eigenvalue drift is then induced by two separate mechanisms: the feedback of the velocity perturbation onto itself and the perturbation induced by a modification of the base flow (Luchini & Bottaro, 2014). It is the combination of these two effects which describes properly the dynamics of the system. The structural sensitivity can be thought as the sensitivity of the frequency to a structural perturbation acting on the time-varying disturbance, leaving the base flow unperturbed. This is a theoretical approach to identify the wavemaker region, but it does not complete the discussion on the effects of our control strategy. The structural sensitivity to base flow modification permits us to understand how the introduction

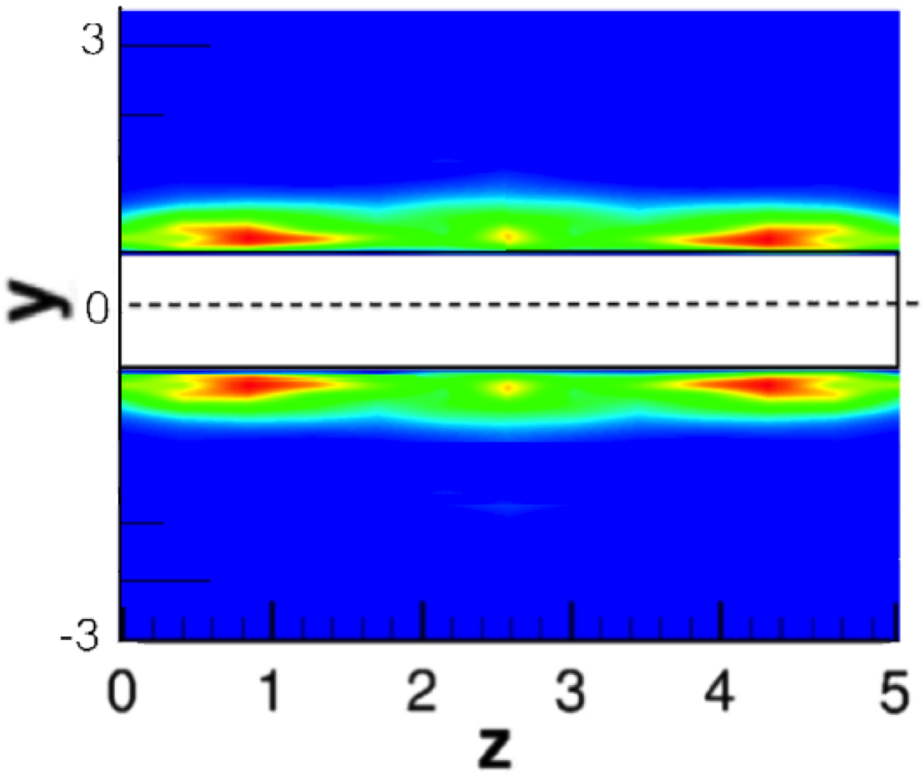

Figure 5.28: Section view of the adjoint mode at $x = -0.17$.

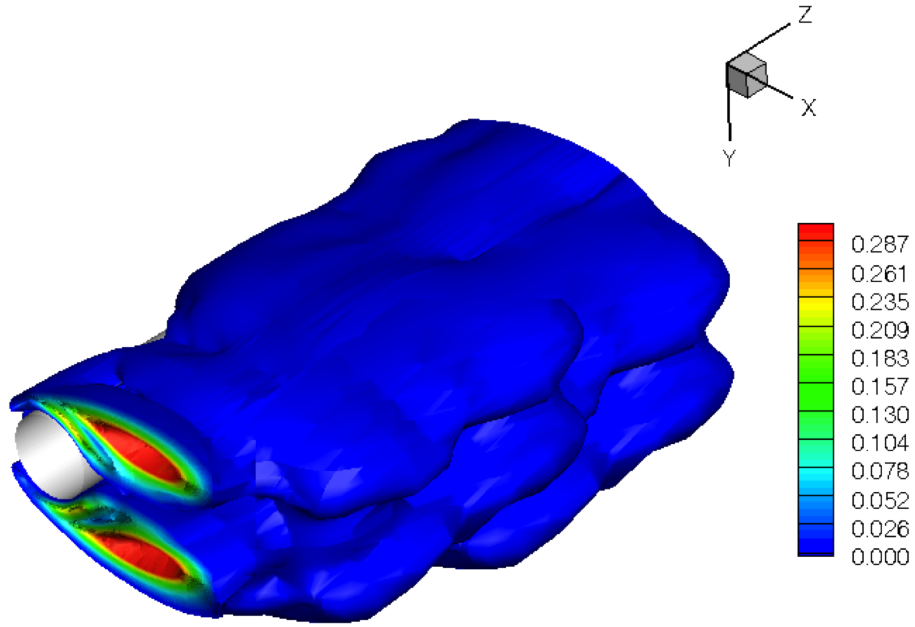

Figure 5.29: Three-dimensional perspective of the structural sensitivity $\lambda(x, y, z)$

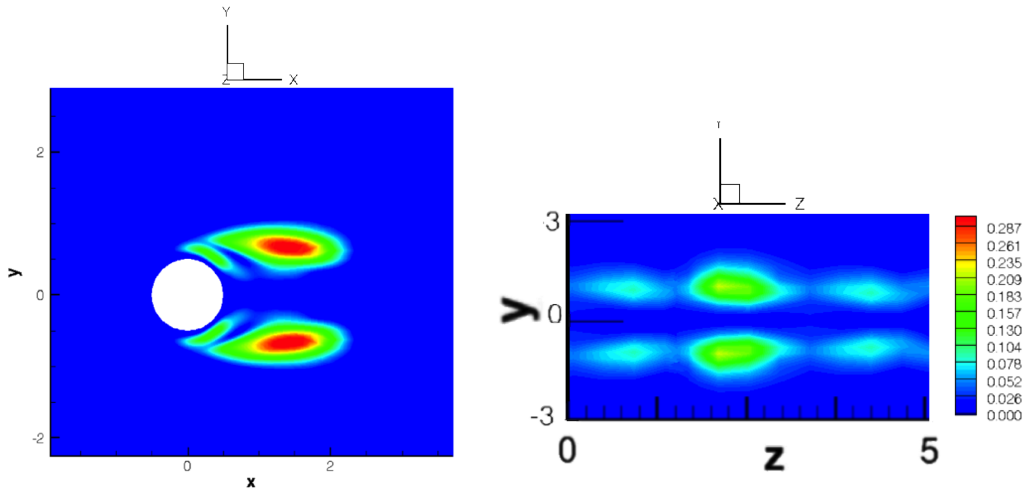

(a) (b)

Figure 5.30: Section views of the structural sensitivity: (a) profile along the streamwise section at $z = 0$, (b) $y - z$ section at $z = 2D$.

of surface bleed produces a variation of the leading eigenvalue. The structural sensitivity to base flow modifications is reported in figure (5.31). This sensitivity appears to be definitely stronger (about 3 times) than the sensitivity to perturbations and the maxima are attained just above and below the cylinder. This confirms what Hwang *et al.* (2013) hypothesised in the local stability approximation: the high efficiency of the three-dimensional control is mainly due to the severe distortion of the base flow caused by the modulation. Significant values of the sensitivity to base flow modifications are also attained in the lobes which identify the wavemaker regions.

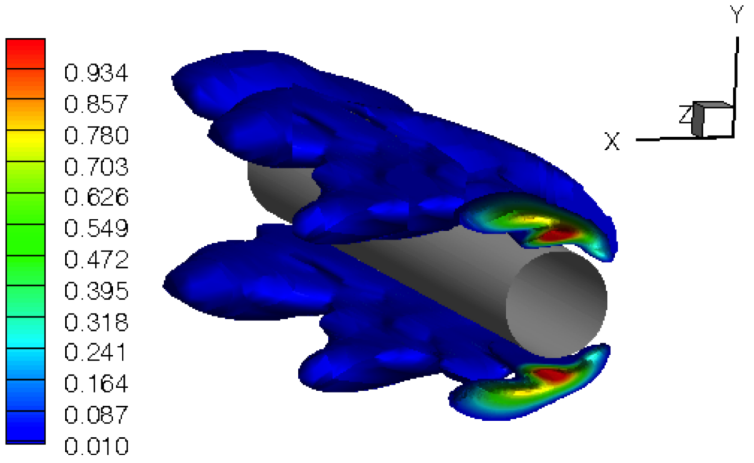

Figure 5.31: Perspective view of the structural sensitivity to base flow modifications.

5.9 Further investigations at $Re = 180$

The analysis performed so far is relative to a flow at $Re = 60$, just above the critical value for the onset of vortex shedding. In this section, we try to extend this result to a higher Reynolds number, $Re = 180$, to understand how the dynamics of the system changes within the two-dimensional vortex shedding regime. Following the approach used in the previous sections, DNS was used to study the dynamics of the base flow and then the linear stability analysis was performed to understand the role of forcing on the near-wake absolute instability.

5.9.1 Different regimes in the suppression of vortex shedding

Following the approach described in §5.4, spanwise Gaussian forcing expressed by (5.8) and (5.9) was applied on the surface of the cylinder at $\theta_c = \pm\pi/9$, as shown in figure (5.4). In the following simulations, the spanwise standard deviation of the Gaussian was chosen to be equal to 0.02, which was seen to be small enough to suppress the oscillation of vortex shedding[5]. We study the changes in the wake topology when forcing is increased. For very small values of forcing ($A < 0.2$), surface bleed is not able to suppress the von-Kármán street and unsteady coherent structures can be detected along the wake (regime I). These structures show a high degree of three-dimensionality and do not disappear or become weaker if longer times are considered. When $A \simeq 0.2$, a complete stabilisation of the wake was observed, with a profile very similar to the one obtained at $Re = 60$. The drag coefficient is subject to a reduction of about 17%, slightly smaller than the previous case at $Re = 60$, and the Strouhal frequency is zero. However, this behaviour is maintained only if the forcing amplitude is $A < 0.25$ (regime II). Higher amplitudes were found to generate a smaller drag reduction (about 15%) and large unsteady hairpin vortices were seen to emerge from the near-base structure (regime III), with a wake topology resembling the one of a sphere at low Reynolds number (Johnson & Patel 1999). A summary of these regimes is reported in figure (5.32). Following the intuition and the insight gained at lower Reynolds numbers, we can predict that the absolute instability is progressively weakened when the forcing amplitude is increased; when $A \simeq 0.2$ the flow has been stabilised, consistently with the complete suppression of vortex shedding. However, when $A \gtrsim 0.25$ a new type of unsteadiness was detected. We can pose the question whether higher forcing amplitudes destabilise wakes and what the most relevant mechanisms in this regime are. We are at sea since the results obtained so far do not shed any light; we need to perform the stability analysis again to understand how the modifications introduced by surface bleed affect the stability of the flow.

5.9.2 Stability analysis and stabilisation of the flow

Direct stability analysis was performed in all the three regimes and the profile of the growth rate as a function of the amplitude is reported in figure (5.33). The behaviour for regimes I and II is very similar to the study performed at $Re = 60$: a monotonic decrease can be detected, which is as-

[5] Analogous results can obviously be obtained using sinusoidal forcing functions.

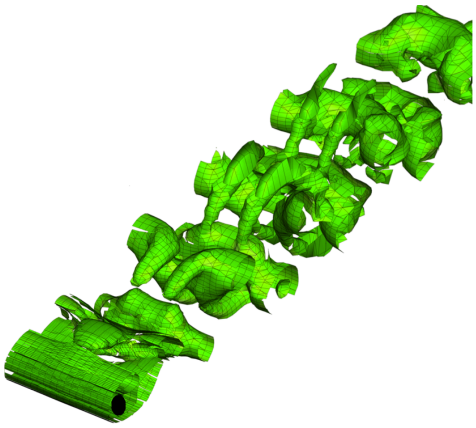

(a) regime I: $0 < A < 0.2$

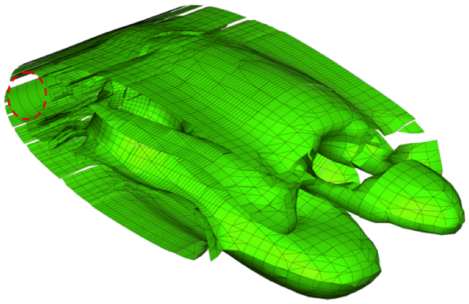

(b) regime II: $0.2 < A < 0.25$

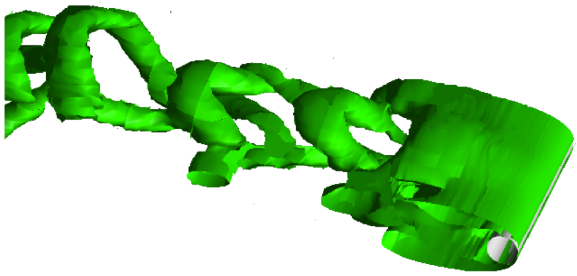

(c) regime III: $A > 0.25$

Figure 5.32: Wake topology for different regimes for spanwise Gaussian forcing at $Re = 180$.

sociated with a progressive weakening of the near-wake absolute instability. When $A \simeq 0.2$ the base flow was found to be stable and it confirms the intuitive speculations of the previous section. The main difference with respect to the simulations at the lower Reynolds number is a slower reduction of the growth rate with the forcing amplitude A, which is related the fact that we are operating at a Reynolds number closer to the on-set of a more complex three-dimensional instability (mode A). The main differences were detected in regime III: increasing the forcing amplitude, the decay rate is subject to a slight increase despite that the flow is still stable. Hence, we can conclude that in the range of the forcing amplitudes we considered (simulations were performed up to $A = 3$), the flow is still stable, but when $A \gtrsim 0.25$ the disturbances decay more slowly than in regime II. The general profile of the growth rate as function of the forcing amplitude is not a monotonic function, but shows a minimum.

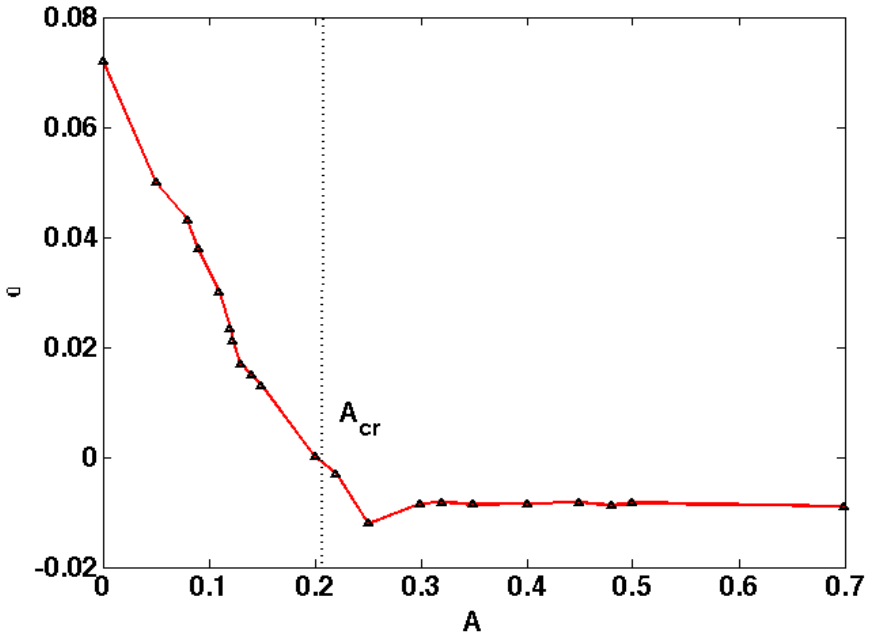

Figure 5.33: Profile of the growth rate as a function of the forcing amplitude for $Re = 180$.

Regarding the eigenmodes, in regimes I and II, the leading modes are similar to the profiles found at $Re = 60$. They progressively acquire a higher degree of three-dimensionality and tend to be located in the near-wake region. Since the behaviour of the global modes in regime I and II is almost identical to

the one showed in figure (5.21), they are not reported herein. The profile of the mode in regime III, for a forcing amplitude $A = 0.35$ is, instead shown in figure (5.34); other simulations in the same regime showed a qualitative comparable topology.

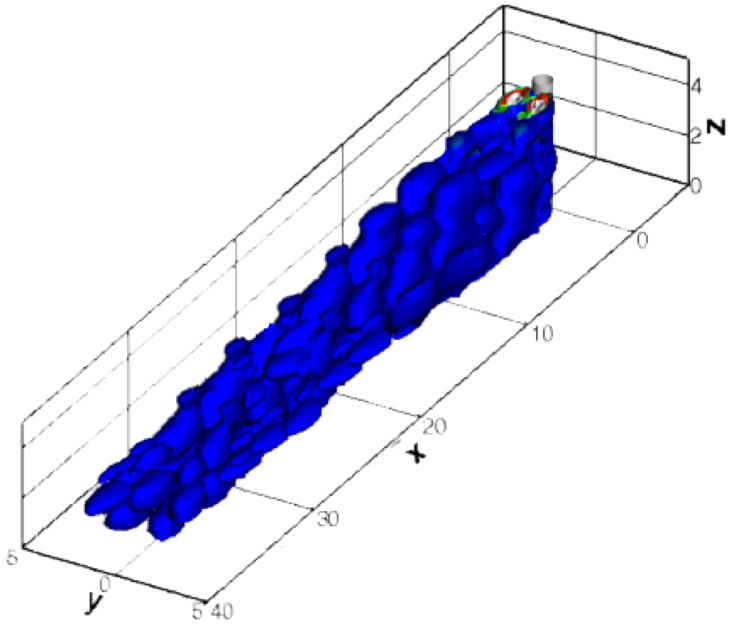

Figure 5.34: Profile of the eigenmode found for $A = 0.35$

Such a mode extends throughout the domain, even if the most intense region is still in the near-wake. This might indicate that the far wake plays a role on the stability of this configuration. The perturbations in the far-wake might be responsible for a local destabilisation, with subsequent convective instabilities. In particular, a transient growth analysis would provide additional information about the presence of convective instabilities and their relation with the development of hairpin vortices. This represents one of the main recommendations for further work. However, in the present thesis, we will try to study the dynamics of this regime using the equation of transport of vorticity perturbations (5.16). Repeating the analysis performed at $Re = 60$, we can deduct once again that the tilting mechanisms by the base flow shear represent the dominant ones (results are not reported for the sake of concision). Therefore, the tilting term $\boldsymbol{\omega}' \cdot \nabla \boldsymbol{U}$ represents the key factor for the stabilisation. Following Hwang's approach (Hwang *et al.* 2013), let us consider the modulation of a two-dimensional wake us-

ing spanwise sinusoidal forcing function with a sufficiently large spanwise wavelength. Equation (5.16) can then be written as:

$$\frac{D\omega_x'}{Dt} \sim \omega_z' E_{xz} \tag{5.18a}$$

$$\frac{D\omega_z'}{Dt} \sim \omega_x' E_{xz} \tag{5.18b}$$

where E_{xz} is the deformation rate tensor, which is related to the spanwise shear of the base flow. An illustration of the physical mechanisms is shown in figure (5.35); at the initial time, we have a spanwise vortex tube characterised by $\omega_z' < 0$. Equation (5.18a) suggests that the vortex tube is tilted downstream with the generation of positive ω_z' in the region where $\partial U/\partial z = E_{xz} > 0$. Analogously, in the region where $\partial U/\partial z = E_{xz} < 0$ the tube is tilted upstream, implying that the initial vortex gradually evolves into a hairpin structure.

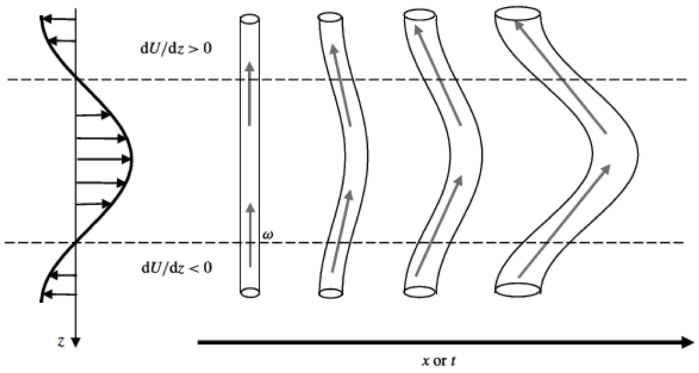

Figure 5.35: Evolution of a spanwise vortex. Adapted from Hwang *et al.* (2013)

Hence, according to Hwang's explanation, if $\boldsymbol{\omega}'$ is zero in a specific part of the domain, then the above-mentioned mechanism is inhibited downstream. This is what happens at moderate amplitude of forcing: the mode was seen to be located in a small streamwise region close to the cylinder, and so the perturbation vorticity (figure (5.36a)). This is not the case for higher forcing amplitudes, which show a perturbation vorticity extending in a wide portion of the domain (figure 5.36b) and the subsequent generation of arrays of alternating Λ-vortices. However, this analysis represents just a first explanation and additional investigations are recommended for future work.

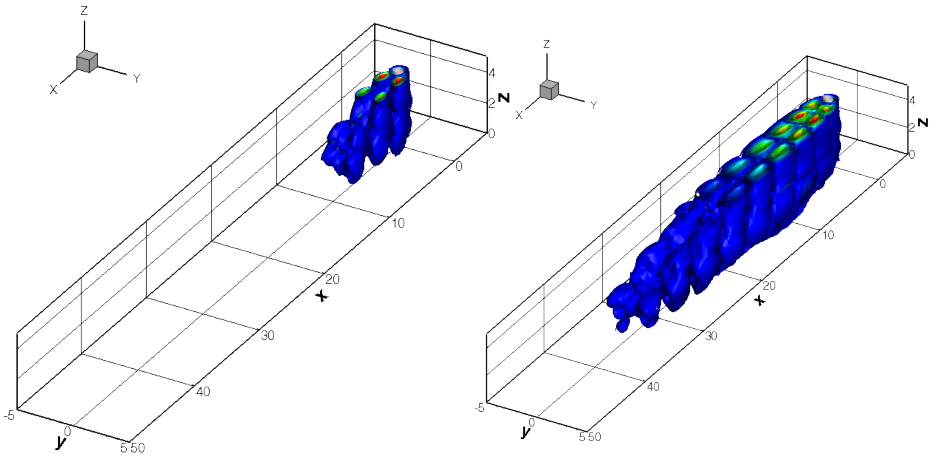

(a) (b)

Figure 5.36: Profile of the vorticity perturbation magnitude $|\boldsymbol{\omega}'|$ for (a) regime II ($A = 0.22$) and (b) regime III ($A = 0.35$).

Chapter 6

Floquet stability analysis of a flow in a compressor passage

> *Knowledge without application is like a book that is never read.*
>
> Christopher Crawford, *Hemel Hempstead*

In this chapter we present an application of Floquet stability analysis to a flow through a compressor passage. In the first part of the chapter the features of the base flow will be discussed, emphasising the physical mechanisms responsible for transition, while in the second part we will perform Floquet and transient growth analyses using the BiGlobal approach introduced in §3.

6.1 Overview of the problem

Studies of flows in turbomachines are relevant in aeronautical engineering and are currently subject to extensive investigations. These problems are particularly interesting due to the presence of relevant transitional phenomena, which might be associated to the presence of high adverse pressure gradients with the subsequent separation of the boundary layers and transition to turbulence. Wu & Durbin (2001) performed simulations of flows in a T106 turbine cascade with periodically incoming wakes. They observed that the incoming wakes triggered turbulent spots along the suction surface, which prevented further separation effects; besides this, two sets of streamwise vortices were observed on the pressure surface. Zaki &

Durbin(2005, 2006) suggested that such turbulent spots may be caused by transient growth phenomena. Jones *et al.* in 2008 simulated a flow over a NACA-0012 airfoil at 5° incidence at $Re = 5 \times 10^4$. The authors detected the presence of a laminar separation bubble located at about 15% of the axial cord, where the breakdown to turbulence was then observed; moreover, the flow was found to be absolutely unstable to three-dimensional perturbations. Abdessemed *et al.* (2009*b*) studied flow stability of a periodic array of a T106/300 low-pressure turbine at low Reynolds numbers ($Re < 5,000$) using Floquet stability analysis and showed that for increasing Reynolds numbers the flow becomes unstable at progressively larger wavelengths and energy transient growth phenomena are the most relevant. Studies on high-pressure turbine cascades are generally more complex, since the Reynolds numbers are generally one order of magnitude higher than low-pressure turbines and compressor cascades. Moreover, heat transfer is a critical issue. Recent studies by means of Large Eddy Simulations on high-pressure turbine passage showed instantaneous boundary layers with long, wavy, streamwise oriented streaky structures on both the suction and pressure sides of the blade. Stretching of vortices from the inlet turbulence around the leading edge, and subsequent transport of them into the blade passage, were found to be responsible of these boundary layer streaks (Bhaskaran 2010). Despite most studies focus on the low-pressure stages of turbines, several experimental and numerical investigations have been performed on flows in axial compressor geometries. Hughes & Walker (2001) investigated separation effects of the boundary layers on the suction surface of a compressor blade at $1.1 \times 10^5 < Re < 1.3 \times 10^5$, while other significant studies on the role of the free-stream turbulence or incoming wakes have been carried out (Zaki *et al.* 2009, Zaki *et al.* 2010, Schreiber *et al.* 2004, Sonoda *et al.* 2004). In particular, Zaki *et al.* (2009, 2010) performed DNS of a NACA-0065 geometry, detecting relevant transitional phenomena on both the pressure and suction surfaces. These phenomena were caused by both natural and by-pass transition, which was induced by incoming wakes or free-stream disturbances. The present study follows the previous investigations to characterise the behaviour of a flow through a compressor passage from a stability perspective. Although our investigations are performed at $Re = 138,500$, which is below the normal operational range of aircraft engines ($Re \geq 6 \times 10^5$), they are still important for the off-design of aeronautical engines because of the significant losses caused by the laminar separation. In the configuration adopted in the present work, due to the high adverse pressure gradient along the suction surface of the blade, the boundary layer profiles become inflectional and the flow might show an instability and high sensitivity to initial distur-

bances. Moreover, perturbations are subject to both temporal and spatial evolution downstream from the separation bubble because of the curvature of the blade and the unsteadiness of the flow (Zaki *et al.* 2010). Therefore, local studies at a fixed streamwise location are not able to describe properly the dynamics of the system, which is characterised by distinct vortex shedding along the suction surface. Global stability studies using time-averaged mean flows were seen able to be able to predict the frequency of the vortex shedding. However, since a well-defined periodicity of the flow is detected on the suction surface, downstream from the separation bubble, Floquet analysis would be an ideal approach to characterise transition. Unfortunately, this is not a feasible approach because this periodicity is located just in a restricted part of the domain. To overcome this limitation, the idea of our investigation is to compute a phase-averaged base flow, as we will discuss in §6.4. The unsteady base flow can then be sorted into a finite number of populations each having a constant phase. An ensemble average of each population with respect to the shedding periodicity can be used to build a sequence of frames of the instantaneous mean flow, where the vortices are frozen like in a photograph. This approach allows us to evaluate the behaviour of transition by computing the leading Floquet mode at different spanwise lengths and the eventual presence of convective instabilities.

6.2 Geometry and discretisation

In the present work, the geometry consists of a NACA-65 at Reynolds number $Re = 138,500$, which is identical to the studies performed by Zaki *et al.* (2009, 2010). At this Reynolds number transition was seen to be rather slow, therefore, in all the simulations performed in this chapter the flow can be considered laminar. The linear low pressure (LP) compressor cascade is based on the experimental studies performed at the University of Armed Forces in Munich (Hilgenfeld & Pfitzner 2004). Figure (6.1) shows a sketch of an aeronautical jet engine and the compressor passage we will simulate. We will consider just one passage of the compressor, using periodic boundary conditions on the upstream and downstream boundaries of the domain to take into account the cascade. The adoption of periodic boundary conditions to simulate such types of flows has already been used to simulate turbine passages (Wu & Durbin 2001, Wissink & Rodi 2006) and it generates synchronous vortex shedding of the trailing-edge vortices. The BiGlobal stability analysis performed by Abdessemed *et al.* on low-pressure turbine (LPT) blades showed that the adoption of two passages affects the dynamics of the shedding, which become asynchronous with relevant effects on the

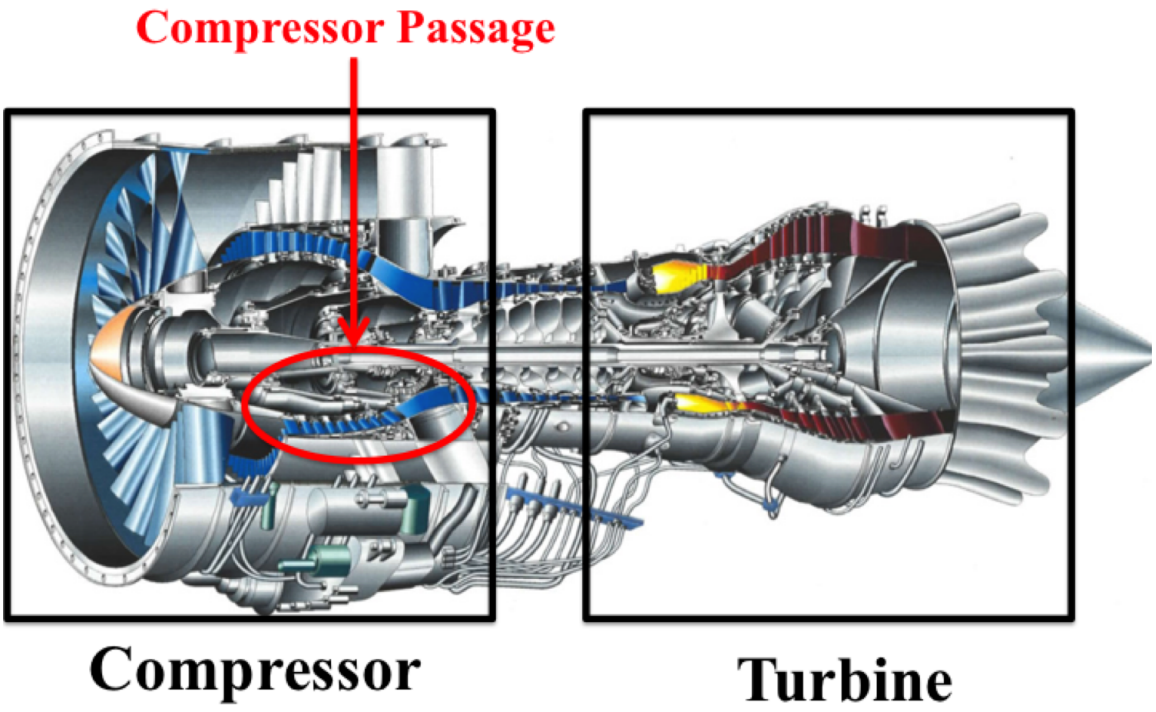

Figure 6.1: Sketch of an aeronautical jet engine. The compressor and turbine are visualised, while the passage in the red box is the object of the current investigation.

stability. However, as Zaki *et al.* (2010) noted, this phenomenon is relevant for the geometries where the flow is subject to strong turning effects. In the present configuration the velocity at the exit is nearly axial and the wake at the trailing-edge does not interact with the upstream flow, therefore no asyncronicity is present. Figure (6.2) shows a sketch of the geometry used. The vertical length of the domain L_p corresponds to one blade pitch $L_p = 0.6L$, where L is the axial chord of the blade. The inflow boundary $\partial\Omega_I$ is at a distance $L_I = -0.4L$ from the leading edge, while the outflow $\partial\Omega_O$ is at a distance $4L$ from the trailing edge. As already mentioned, periodic boundary conditions were used on the lower and upper boundaries ($\partial\Omega_{P_1}$ and $\partial\Omega_{P_1}$ respectively), while a velocity $(U_0\cos(\alpha), U_0\sin(\alpha))$ was assigned at the inflow boundary $\partial\Omega_I$, where $\alpha = 42^\circ$ and $U_0 = 1$. This configuration corresponds to the angle of attack at design, since its actual value in experiments could not be measured reliably. As discussed by Zaki *et al.* (2010), this choice generates some differences in the pressure distribution, but does not affect the mechanisms related to the boundary layer separation and transition to turbulence. Regarding the pressure, a high order boundary condition was used on the inflow boundary (Karniadakis *et al.* 1991). The main difficulty of the problem is the choice of appropriate boundary conditions for the outflow, due to the reflections that the outgoing flow experiences when it encounters the boundary. In the present work, an absorbing layer was used (Israeli & Orszag, 1981), which allows disturbances to pass out of the region of interest into a limited small region where they are dissipated. This can be achieved by adding a damping momentum forcing to the Navier-Stokes equations, $\boldsymbol{F} = -D(\boldsymbol{u} - \boldsymbol{u}|_{\partial\Omega_O})$, where D is the damping coefficient and is different from zero only in the damping region, while $\boldsymbol{u}|_{\partial\Omega_O}$ is the velocity on the boundary. Homogenous Neumann boundary conditions were used for the velocity on the downstream boundary $\partial\Omega_O$. The streamwise length of the artificial dumping region is $L_S = L$, while the damping coefficient was set to $D = 50$, which was observed to be sufficiently large to avoid numerical instabilities. No-slip boundary conditions were used on the surface of the blade. To summarise, the following boundary conditions were adopted:

$$\partial\Omega_W := \begin{cases} u = 0, \\ v = 0 \\ \frac{\partial p}{\partial n} = f(\boldsymbol{u}) \end{cases} \tag{6.1a}$$

$$\partial\Omega_I := \begin{cases} u = \cos(42^\circ) \simeq= 0.7431 \\ v = \sin(42^\circ) \simeq= 0.6691 \\ \frac{\partial p}{\partial x} = f(\boldsymbol{u}) \end{cases} \tag{6.1b}$$

$$\partial\Omega_O := \begin{cases} \frac{\partial u}{\partial x} = 0 \\ \frac{\partial v}{\partial x} = 0 \\ p = 0 \end{cases} \tag{6.1c}$$

$$\partial\Omega_{P_{1,2}} := \begin{cases} u|_{\partial\Omega_1} = u|_{\partial\Omega_2} \\ v|_{\partial\Omega_1} = v|_{\partial\Omega_2} \\ p|_{\partial\Omega_1} = p|_{\partial\Omega_2} \end{cases} \tag{6.1d}$$

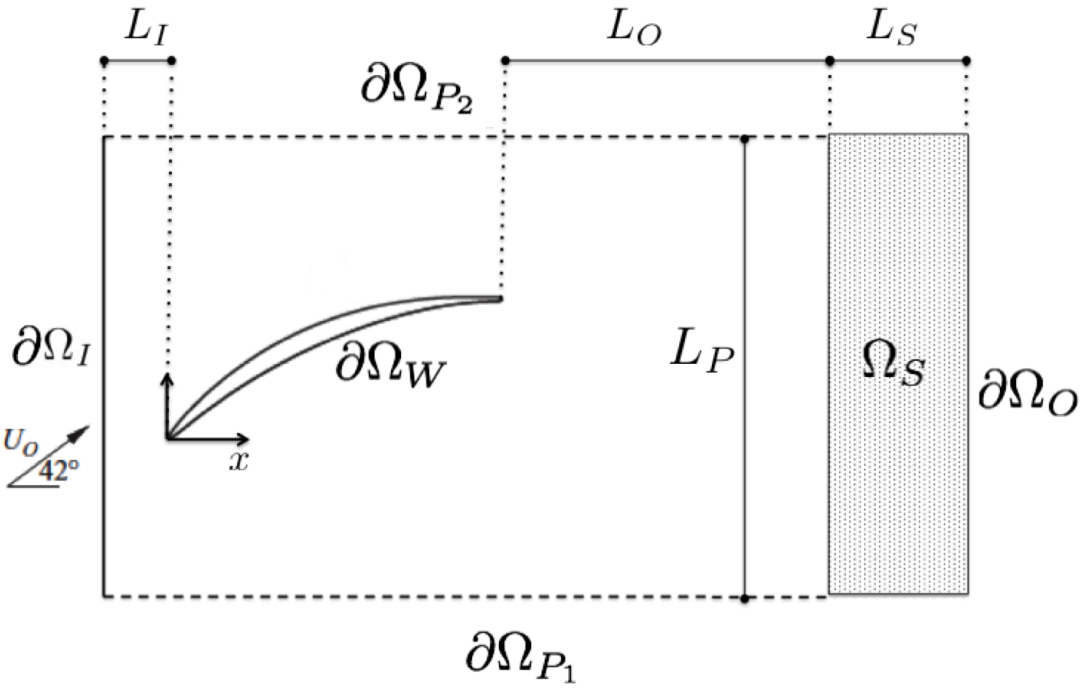

Figure 6.2: Sketch of the geometry of the problem.

Let us note that in the present work, the geometry of the compressor blade is slightly different from the case presented by Zaki *et al.* (2009) and Wu & Durbin (2001), where the pressure and suction surfaces were incorporated into the boundaries of the domain. Our choice is dictated by the need of a higher accuracy to capture the dynamics of the flow around the leading

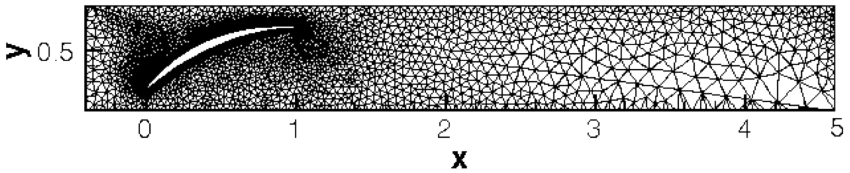

(a)

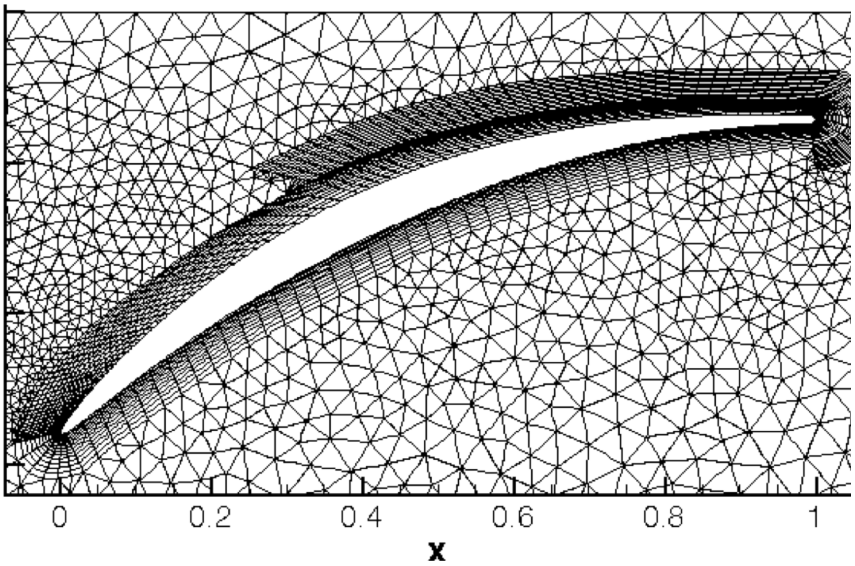

(b)

Figure 6.3: (*a*): mesh adopted for the simulations. (*b*): detail of the submesh around the surface of the blade.

and trailing edges to guarantee reliable results of stability analysis. This geometry was discretised using a spectral/*hp* element method with about 6,000 elements, as shown in figure (6.3a). The mesh is hybrid and composed of both triangular and quadrilateral elements. Close to the surfaces of the blade, where relevant separation effects are observed, a structured sub-mesh of quadrilaterals is adopted (figure (6.3b)), while triangles are used in the remaining part of the domain. Modal bases, described in §2.3.1 and §2.3.2, were used to interpolate the variables of the problem, using 8^{th} order polynomials. Finally, the splitting scheme described in §2.4 was adopted to solve the Navier-Stokes equations, using a second-order time integration technique with a time step $\Delta t = 1 \times 10^{-5}$.

6.3 Two-dimensional base-flow

In this section the behaviour of the base flow is discussed to provide an insight into the mechanisms of transition occurring on both the pressure and suction surfaces. Furthermore, the computation of the instantaneous fields provide a validation of our discretisation with respect to the previous results reported in the literature. Figure (6.4) shows the isocontours of the magnitude of the mean velocity, which was calculated averaging over about 100 time units once the flow has completely evolved through the passage. The velocity is subject to a deceleration of about 25% with respect to the inflow; this phenomenon is mainly related to a reduction of the transverse component of the velocity v, while the streamwise velocity u is slightly increased to compensate for the mass flow deficit associated to the development of the boundary layers (Zaki *et al.* 2010).

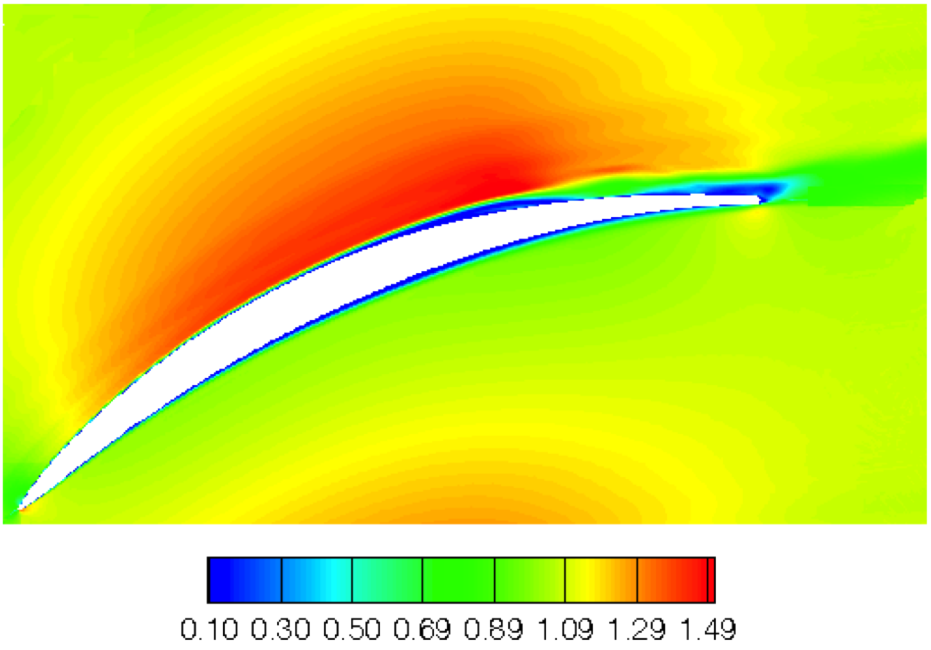

Figure 6.4: Isocontours of the magnitude of the mean velocity.

Important information about the dynamics of the flow can be given considering the distribution of the time-averaged pressure coefficient, defined as $C_P := (P - P_{ref})/(\rho U_0^2/2)$, where ρ is the density of the flow and P_{ref} a reference pressure, which is the inflow pressure in the present case. Figure (6.5) shows the profile of the pressure coefficient over the surface of the blade. The data are compared with the results obtained by Zaki *et al.* (2010) and match well, providing a validation of the discretisation and the parameters chosen in §6.2. The top curve represents the pressure surface, where an adverse pressure gradient can be detected up to about $x/L \simeq 0.8$, followed by a region of favourable pressure gradient. At $x/L \simeq 0.55$ the curve shows a kink, which is related to a mild separation of the boundary layer. However, the most relevant separation phenomena occur on the suction surface: the flow is subject to a strong acceleration until $x_L \simeq 0.2$, then a strong adverse pressure gradient is present. This is responsible for an evident flow separation, and in absence of free-stream perturbations (turbulence wakes or free-stream turbulence), a Kelvin-Helmholtz instability arises, characterised by a typical wake flow with rolls being shed from the separated boundary layer. However, these structures do not break up to turbulence and are convected just slightly away from the surface of the blade, as the instantaneous profiles will show. A small region of reverse flow can be detected on the suction surface even after the rolls are convected downstream; this region is known as *secondary bubble* and it moves at the same velocity of the Kelvin-Helmholtz rolls. The secondary bubble can be identified in figure (6.5) as a drop in the pressure coefficient within the separation region at about $x/L \simeq 0.6$ and it extends for about 10% of the axial chord.

Another relevant quantity is the skin friction coefficient $C_f := \mu \frac{\partial u_t}{\partial n}/(\rho U_0^2/2)$, where u_t represents the velocity tangential to the surface of the blade and n the unit-vector normal to the surface. The profile of the skin friction on the pressure and suction sides is reported in figure (6.6) and a good match with the results obtained by Zaki *et al.* (2010) was found again. Along the pressure surface, the skin friction is subject to a monotonic decrease until $x/L \simeq 0.35$, where separation occurs; downstream from the separation region, where the favourable pressure gradient was observed, the skin friction increases. Let us note that the reattachment at $x/L \simeq 0.55$ is in accordance with the distribution of the pressure coefficient.

Regarding the suction surface, separation of the boundary layer was observed at $x/L \simeq 0.44$ and laminar reattachment at $x/L \simeq 0.8$. As noted by Zaki *et al.* (2009), the separation bubble can be identified as the region with negative skin friction within the primary separation; downstream from this region, the skin friction increases in a short interval (up to $x/L \simeq 0.8$) and

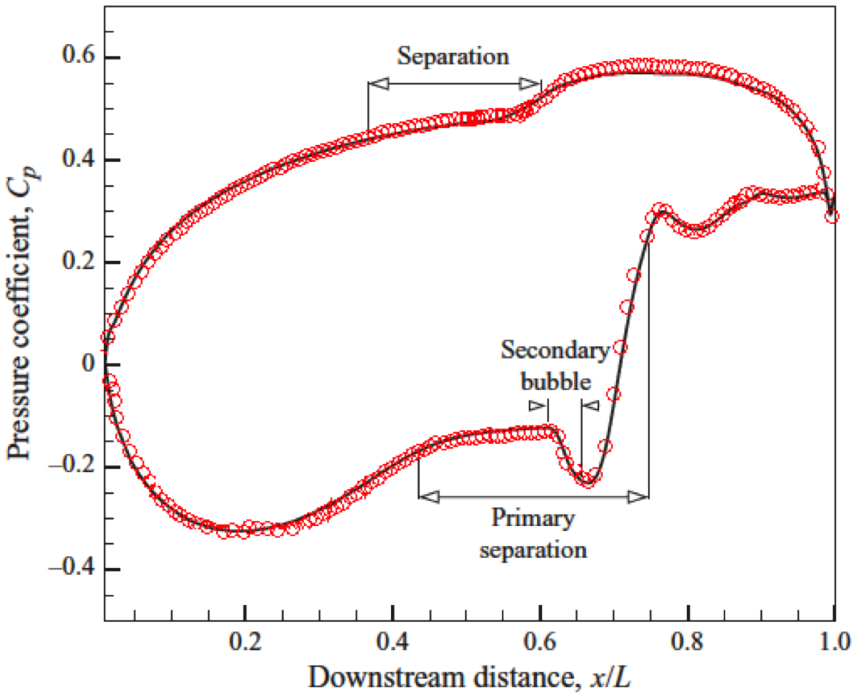

Figure 6.5: Distribution of the pressure coefficient C_p along the surface of the blade. Solid line represents the result from Zaki *et al.* (2010), while hollow circles the present results.

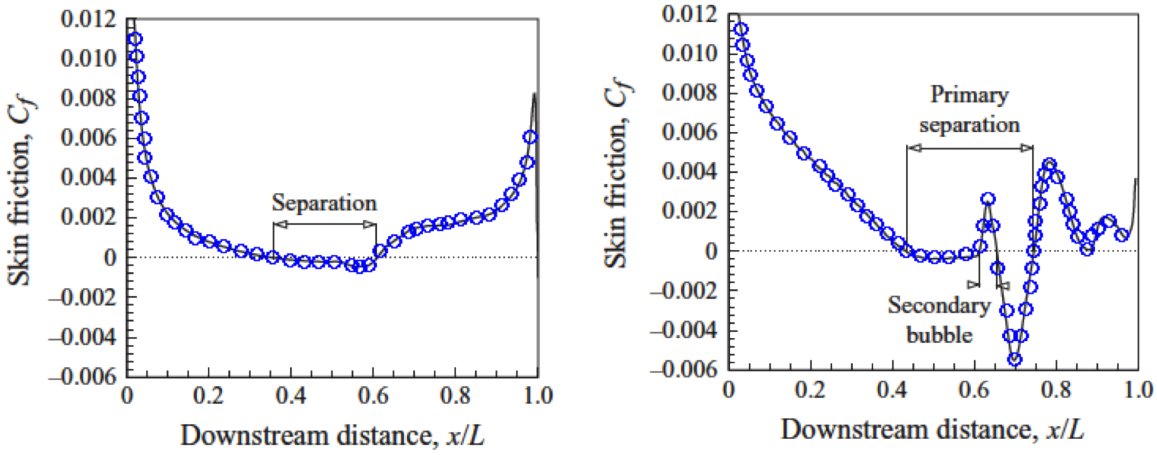

(a) (b)

Figure 6.6: Profiles of the skin friction coefficients on the pressure surface (a) and the suction surface (b). Hollow circles are the data obtained in the present work, while the solid line the results from Zaki *et al.* (2010)).

then is subject to a slight reduction.

All these physical mechanisms can be visualised considering the instantaneous profiles of the spanwise vorticity ω_z around the surface of the blade; the isocontours of the vorticity are shown in figure (6.7) . Although both surfaces show distinct separation effects, the dynamics of the flow on the suction surface is far more complex than the pressure surface. On the pressure surface a mild separation can be observed, but the coherent structures remain attached to the surface of the blade; conversely, on the suction surface, downstream from the separation bubble, the boundary layer is subject to a roll-up caused by the Kelvin-Helmholtz instability. The vortical structure are convected slightly away from the suction surface, but a small zone of reverse flow on the blade surface beneath them can be observed.
In order to characterise the behaviour of these structures, we consider of the profiles of the velocity along the separation region of the suction side. Specifically, we track the time evolution of the velocity in 4 points, $P_1 \equiv (x_1, y_1) = (0.66, 0.65)$, $P_2 \equiv (x_2, y_2) = (0.73, 0.67)$, $P_3 \equiv (x_3, y_3) = (0.82, 0.67)$, $P_4 \equiv (x_4, y_4) = (0.93, 0.68)$, which are distributed all along the separation region of the suction surface where the vortical structures were detected. The time evolution of the velocity shows a clear periodic behaviour of the structures, confirmed by the presence of a limit cycle, as figures (6.16)-(6.11) show. A total period $T = 0.22$ can be clearly identified, which corresponds

to a complete shedding cycle, as shown in figure (6.8). In the other parts of the domain, no other straightforward periodicity could be detected.

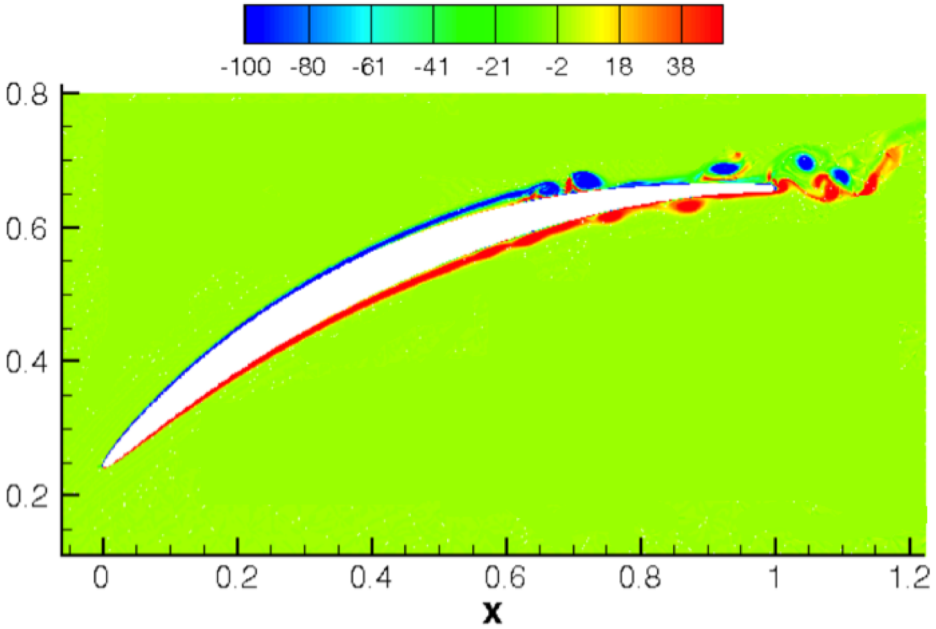

Figure 6.7: Profile of the spanwise vorticity ω_z.

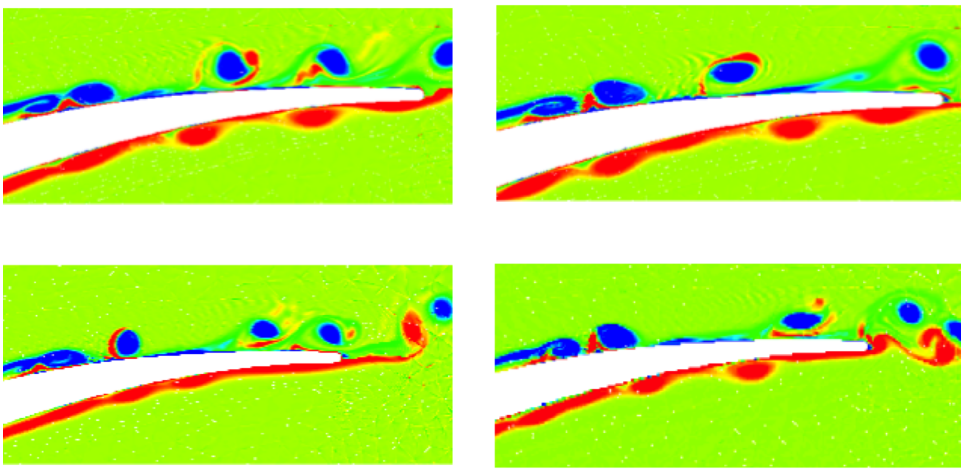

Figure 6.8: Vorticity profile for four different phases of the shedding cycle.

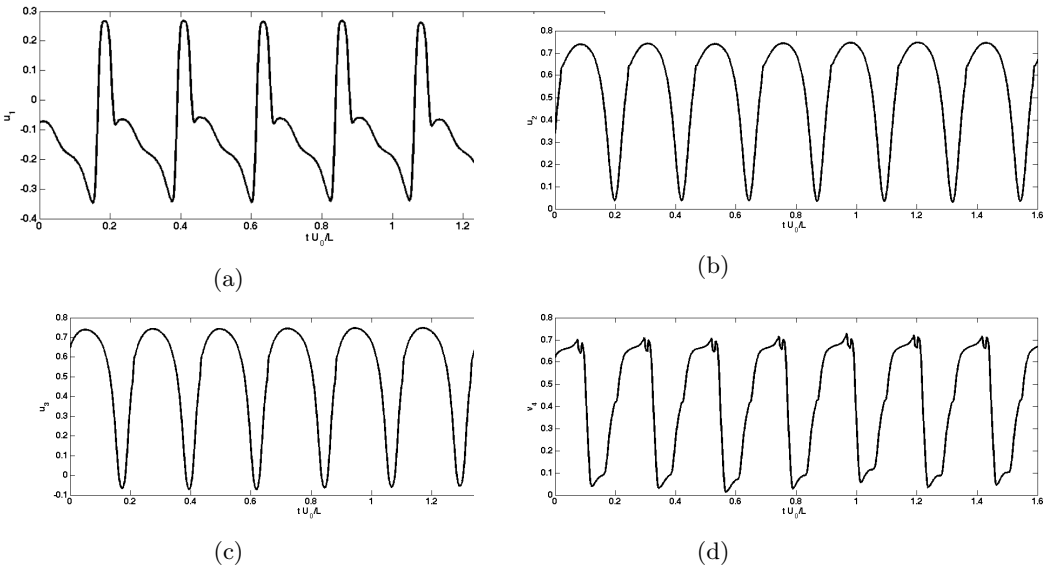

Figure 6.9: Time evolution of the streamwise velocity u'; (a) $P_1 \equiv (x_1, y_1) = (0.66, 0.65)$, (b) $P_2 \equiv (x_2, y_2) = (0.73, 0.67)$, (c) $P_3 \equiv (x_3, y_3) = (0.82, 0.67)$, (d) $P_4 \equiv (x_4, y_4) = (0.93, 0.68)$.

6.4 Phase-averaged base flow

As described in § 6.3, the flow past a compressor blade has a complex behaviour, in particular on the suction surface, where relevant separation effects are enhanced by the high adverse pressure gradient. Besides this, we found a periodic motion of the coherent structures which appear in the region downstream from the separation bubble region. To characterise the stability of the Kelvin-Helmholtz rolls, we need to perform stability analysis. However, Floquet stability analysis cannot be applied, since it requires the time-periodicity on the whole domain. Hence, we need to seek other techniques to sort out this problem; a common approach is to perform the stability analysis using a time-averaged mean flow as basic state. Barkley (2006) used this technique to study the flow past a circular cylinder and

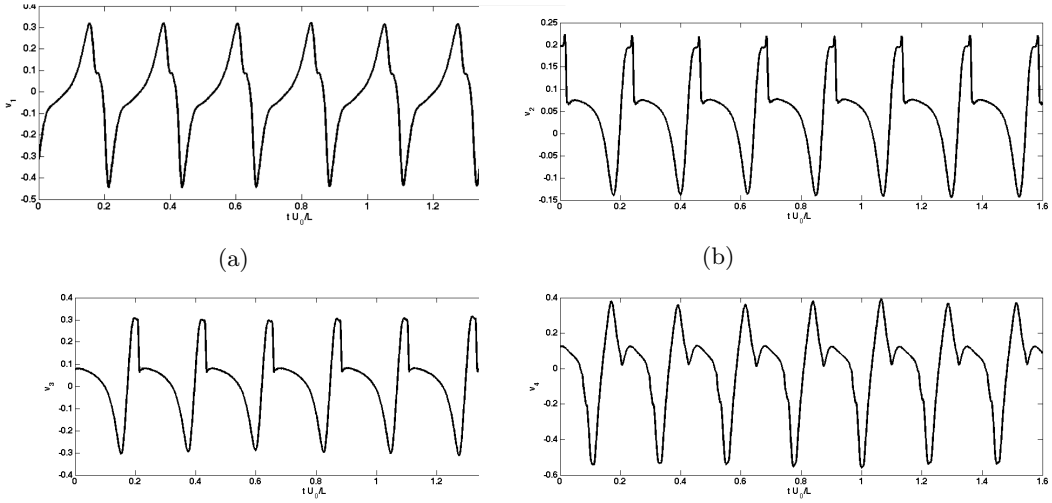

(a) (b) (c) (d)

Figure 6.10: Time evolution of the transverse velocity v'; (a) $P_1 \equiv (x_1, y_1) = (0.66, 0.65)$, (b) $P_2 \equiv (x_2, y_2) = (0.73, 0.67)$, (c) $P_3 \equiv (x_3, y_3) = (0.82, 0.67)$, (d) $P_4 \equiv (x_4, y_4) = (0.93, 0.68)$.

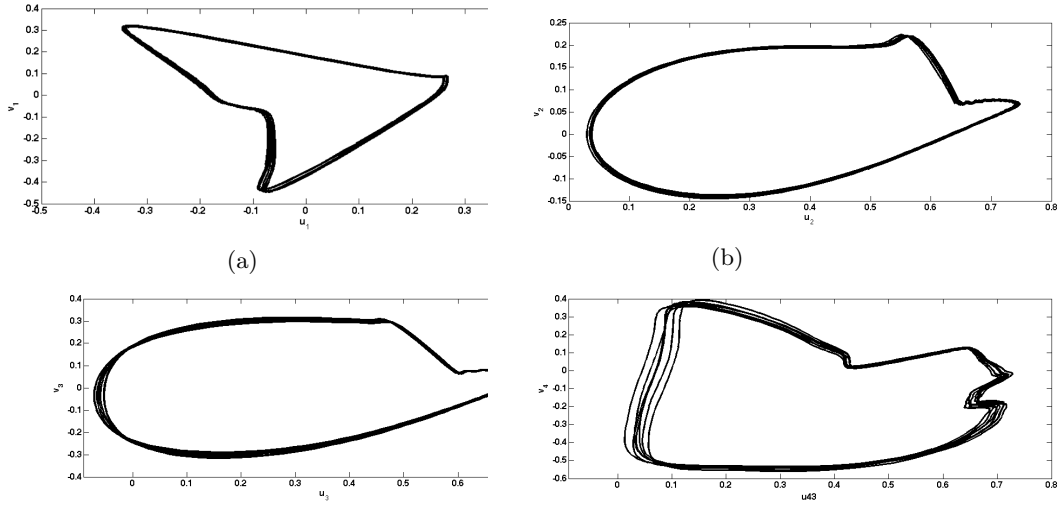

(a) (b) (c) (d)

Figure 6.11: Detection of the limit cycle (transverse component v as a function of the streamwise component u; (a) $P_1 \equiv (x_1, y_1) = (0.66, 0.65)$, (b) $P_2 \equiv (x_2, y_2) = (0.73, 0.67)$, (c) $P_3 \equiv (x_3, y_3) = (0.82, 0.67)$, (d) $P_4 \equiv (x_4, y_4) = (0.93, 0.68)$.

showed that the eigenfrequency of the mean flow recovers almost exactly the Strouhal number of vortex shedding, even if this methodology often produces growth rates which are not relevant to the physical solution. An alternative approach, which combines both the Floquet stability analysis and the mean base flow, is the computation of a phase-averaged mean flow. This technique allowed us to sort the flow into several groups, each corresponding to a small interval associated to the phase of the shedding cycle. Following Cantwell & Coles (1983), we can decompose the instantaneous flow field into the sum of a global mean component $\bar{\boldsymbol{u}}$, a periodic mean component $\tilde{\boldsymbol{u}}$ and a random component $\boldsymbol{u}'$ (Reynolds & Hussain (1972)):

$$\boldsymbol{u} = \bar{\boldsymbol{u}} + \tilde{\boldsymbol{u}} + \boldsymbol{u}' \tag{6.2}$$

The global mean $\bar{\boldsymbol{u}}$ is defined as an ensemble average of the N samples which are computed in a single period of the shedding cycle T:

$$\bar{\boldsymbol{u}} = \frac{1}{N}\sum_{i=1}^{N} \boldsymbol{u}_i \tag{6.3}$$

where $\boldsymbol{u}_i$ indicates a single sample. We divided the N-samples into a specific number of subpopulations N_P, 50 in the present study, each one associated to a particular phase interval of the shedding. Within each subpopulation, composed by N_i samples, we can define a mean at constant phase $\langle \boldsymbol{u} \rangle$:

$$\langle \boldsymbol{u} \rangle = \frac{1}{N_i}\sum_{j=1}^{N_i} \boldsymbol{u}_j \quad i = 1, 2, \ldots, N_P \tag{6.4}$$

We can now define the periodic component $\tilde{\boldsymbol{u}}$ as the difference of the mean at constant phase and the global mean:

$$\tilde{\boldsymbol{u}} = \langle \boldsymbol{u} \rangle - \bar{\boldsymbol{u}} \tag{6.5}$$

Using these definitions, the average of the periodic motion over one cycle can be shown to be zero: $\bar{\tilde{\boldsymbol{u}}} = 0$, and the random fluctuations have zero mean at constant phase: $\langle \boldsymbol{u}' \rangle = 0$. Moreover, the periodic and random component are not correlated, which means that $\overline{\tilde{\boldsymbol{u}}\boldsymbol{u}'} = 0$. Let us consider the flow over one period: we can write that $\boldsymbol{u} = \langle \boldsymbol{u} \rangle + \boldsymbol{u}'$. Adopting the same decomposition also for the pressure, substituting into the Navier-Stokes equations and performing the phase average $\langle \cdot \rangle$, we obtain the Navier-Stokes equations for the mean flow at constant phase:

$$\frac{\partial \langle \boldsymbol{u} \rangle}{\partial t} + \langle \boldsymbol{u} \rangle \cdot \nabla \langle \boldsymbol{u} \rangle = -\nabla \langle p \rangle + \frac{1}{Re}\nabla^2 \langle \boldsymbol{u} \rangle - \nabla \cdot \langle \boldsymbol{u}'\boldsymbol{u}' \rangle \tag{6.6a}$$

$$\nabla \cdot \langle \boldsymbol{u} \rangle = 0 \tag{6.6b}$$

The equations for the global mean flow can be obtained substituting (6.2) into (2.3) and then time-averaging:

$$\bar{\boldsymbol{u}} \cdot \nabla \bar{\boldsymbol{u}} = -\nabla \bar{p} + \frac{1}{Re} \nabla^2 \bar{\boldsymbol{u}} - \nabla \cdot \left\langle \overline{\boldsymbol{u}' \boldsymbol{u}'} \right\rangle - \nabla \cdot (\overline{\tilde{\boldsymbol{u}} \tilde{\boldsymbol{u}}}) \tag{6.7a}$$

$$\nabla \cdot \overline{\boldsymbol{u}} \tag{6.7b}$$

Equation (6.7a) shows explicitly that the mean flow depends on both the random and periodic fluctuations of the Reynolds stresses, while (6.6a) just on the term related random fluctuations at constant phase $\left\langle \overline{\boldsymbol{u}' \boldsymbol{u}'} \right\rangle$. This last term is directly associated to the dynamics of the rolls and, as explained by Cantwell & Coles (1983), it operates at a lower level than the stresses present in equation (6.7a). This shows that the adoption of a phase-averaging technique to approximate the base-flow is more precise than using a Reynolds-averaged base-flow; the minimisation of the contributions of the Reynolds-stresses, by which the RANS and the Navier-Stokes solution differ, leads to smaller approximation errors and this may be important especially in the context of linear stability analysis. Figure (6.12) and (6.13) show the profiles of the phase-averaged vorticity at four different phases, where the phase-averaging was performed on over 100 cycle. Almost all the unsteady phenomena on the pressure surface have been smeared out by the averaging, while traces of roll-up of the boundary layer due to a Kelvin-Helmholtz instability are still detectable on the suction surface. Furthermore, the location where the separation of the shear layers occurs moves downstream, although it does not show any strong dependence on the phase, being constrained between $0.42 \lesssim x/L \lesssim 0.44$.

6.5 Floquet stability analysis

The phase-averaged base flow described in §6.4 can be used to investigate its capacity to amplify three-dimensional disturbances, using the BiGlobal approach (Theofilis 2003). Floquet analyses at different spanwise wavenumbers $\beta = 2\pi/L_z$ were performed to study the stability of the periodic states which characterise the region downstream from the separation bubble. Similarly to the other simulations performed in this thesis, an Arnoldi method was adopted: a dimension of the Krylov subspace $m = 12$ was used, while

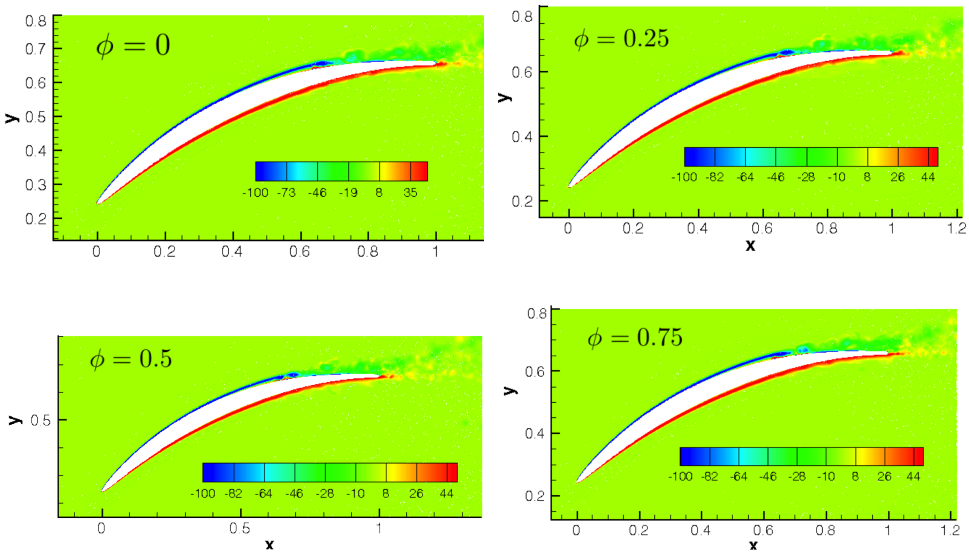

Figure 6.12: Contours of the phase-averaged vorticity at four different phases.

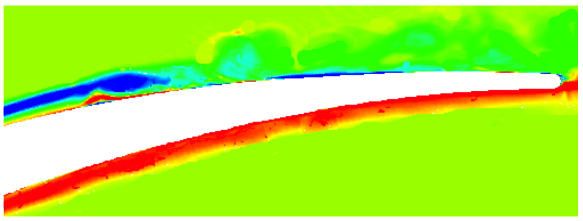

Figure 6.13: Detail of the phase-averaged base flow at $\phi = 0$, near the trailing edge

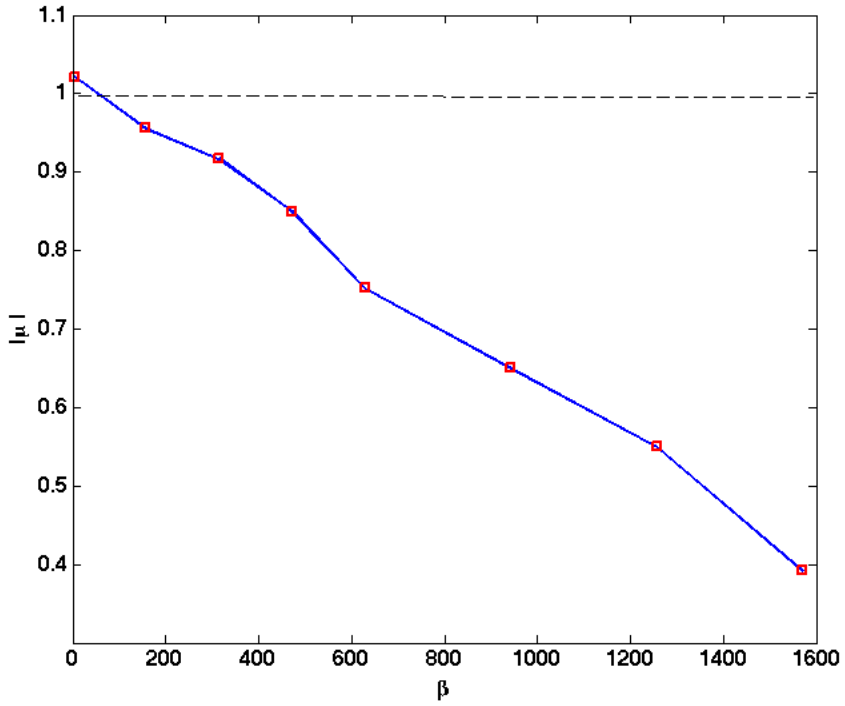

Figure 6.14: Floquet multipliers $|\mu$ as a function of the wavenumbers β.

the tolerance on the eigenvalues was set to 10^{-5}. Tests with $m \geq 12$ produced differences in the magnitudes of the leading Floquet modes of order 10^{-4}. Figure (6.14) shows the eigenspectrum, which reports the value of the Floquet multipliers with respect to the wavenumber β. All the Floquet multipliers are real and $|\mu| < 1$ denotes a decaying perturbation, while $|\mu| > 1$ a growing one. Therefore, they are related to stable and unstable modes respectively. An unstable Floquet mode was detected just for very small wavenumbers, $\beta < \pi/10$. This result is similar the findings of Abdessemed *et al.* (2009*b*), who suggested that in a low-pressure turbine, the instabilities arise at $\beta \to 0$ when $Re \to \infty$. However, to infer direct connections further studies are required due to the different physical mechanisms and the fact that the present study was performed at just one Reynolds number.

The structure of the normalised Floquet mode at $\beta = 500$ is reported in figure (6.15); the mode is located on the suction side, across the separation bubble, where the unsteady phenomena of the phase-averaged base flow

were observed. Its intensity becomes weaker approaching to the trailing-edge and, despite the general structure of the mode appears to be rather complex, a wake pattern can still be detected. The contributions of the velocity components $\hat{u}', \hat{v}', \hat{w}'$ is shown in figure (6.16).

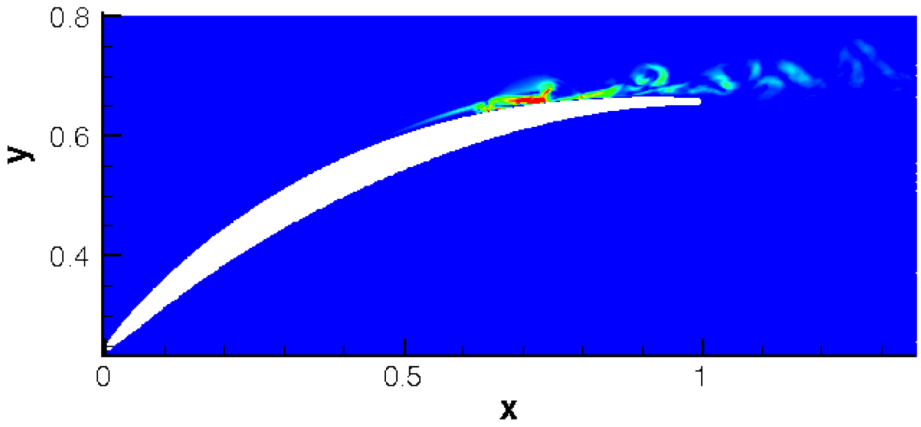

Figure 6.15: Magnitude of the dominant Floquet mode at $\beta = 500$.

Similarly to the approach used in §5.7, we can validate of the results of the Floquet analysis superposing the Floquet mode to the base flow $\boldsymbol{u}(x, y, t) + \varepsilon \hat{\boldsymbol{u}}'(x, t) \exp(\omega t + \beta z)$ and use the result as initial conditions to integrate the non-linear Navier-Stokes equations. In the present case, we chose $\varepsilon = 10^{-6}$ and the energy of the system $E = \frac{1}{2} \int_\Omega \|\boldsymbol{u}\|^2 d\Omega$ as a function of the non-dimensional time is reported in figure (6.17). The growth rate obtained from the DNS, corresponding to the slope of the curve at $t \simeq 0$, was found to be 0.885, while the stability analysis predicted a value $\mu = 0.891$. The difference of these two values is of order 10^{-3} and can be attributed mainly to the adoption of the phase-averaged base flow, which includes the additional presence of the Reynolds stresses, and the non-linearities of the Navier-Stokes equations.

6.6 Transient growth analysis

Floquet analysis described in the previous section showed that the region downstream from the separation bubble is characterised by a significant

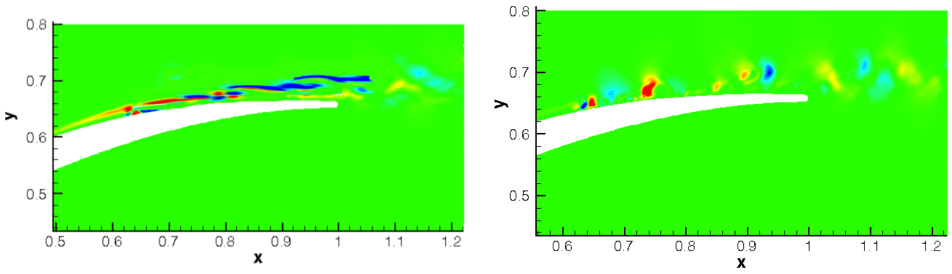

(a) $\hat{u}'$

(b) $\hat{v}'$

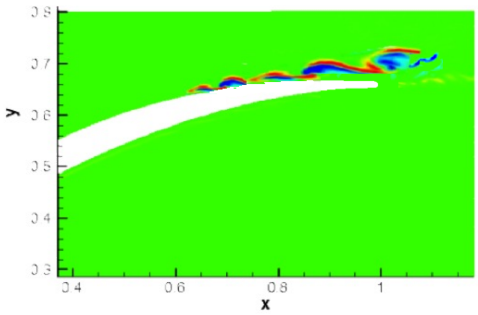

(c) $\hat{w}'$

Figure 6.16: Velocity component of the Floquet mode.

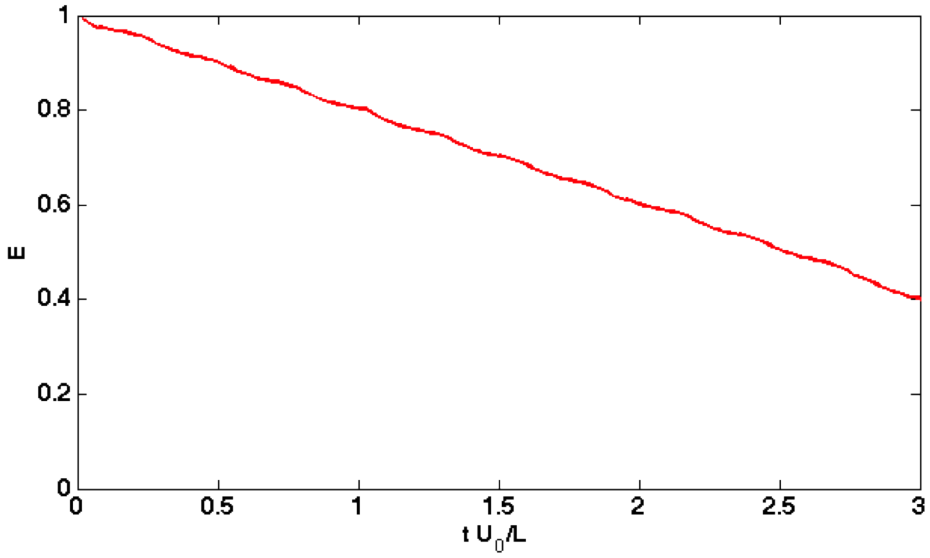

Figure 6.17: Time evolution of the energy of eigenmode associated at $\beta = 500$. The curve was obtained by a non-linear Navier-Stokes simulation.

concentration of energy; therefore, the interaction of stable modes might generate large energy transient growth phenomena. Transient growth analysis was performed using an approach similar to the one adopted in §6.5; the base flow consists again of 50 time slices, obtained by phase-averaging the non-linear Navier-Stokes equations, corresponding to one shedding cycle $T = 0.22$. The computational parameters are unaltered with respect to Floquet analysis, expect the Krylov subspace dimension which was chosen to be $m = 5$. The obtained results were compared with a study on the same configuration using a Lagrangian time-interpolation of the base flow (Mao X., priv comm). The comparison showed similar trends for the optimal energy growth, although differences of about 20% were detected due to the different techniques used to take into account the unsteadiness of the base flow. In the present study, two different time horizons were investigated, $\tau = 0.1$ and $\tau = 0.3$ respectively. The variation of the energy growth with the spanwise wavenumber β is shown in figure (6.18). Both cases are convectively unstable in a wide range of spawise wavenumbers, hence significant energy transient growth phenomena are present. The most energised wavenumber is $\beta \simeq 400\pi$ in both cases, which corresponds to a wavelength $L_z = 1/200$.

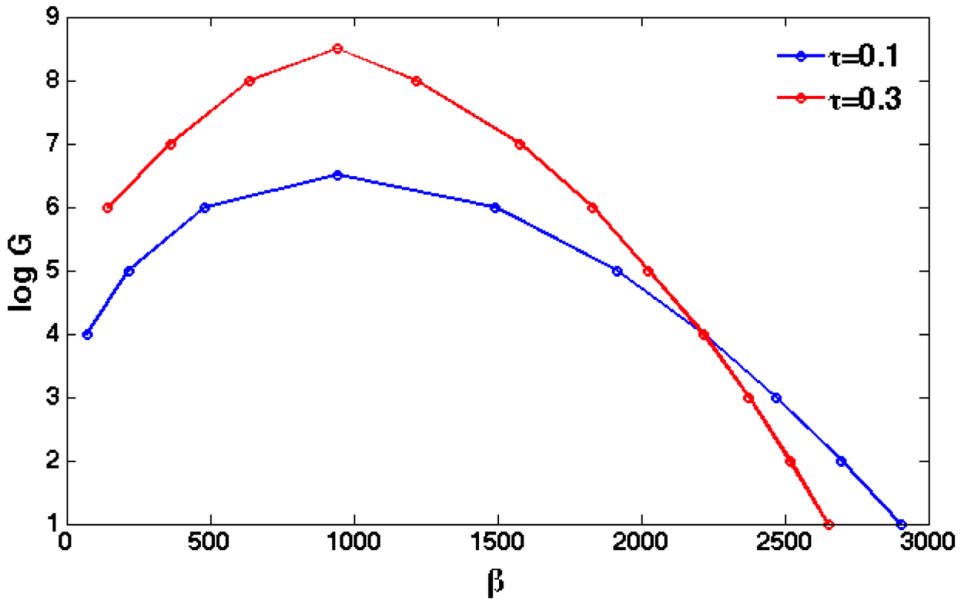

Figure 6.18: Variation of the optimal energy growth G with the spanwise wavenumber β for two different time horizons: $\tau = 0.1$ and $\tau = 0.3$ respectively.

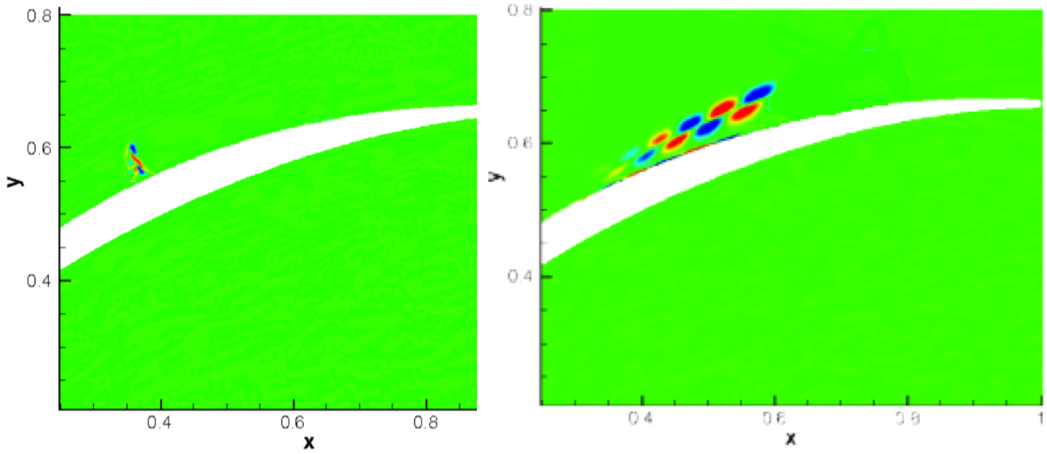

(a) $\tau = 0.1$ (b) $\tau = 0.3$

Figure 6.19: Spanwise vorticity of the optimal perturbations.

The profiles of the vorticity of the optimal perturbations are reported in figure (6.19); in both cases the optimal perturbations are located near the separation bubble and are convected downstream from the suction surface, exploiting the shear layers of the base flow. However, two different topologies can be detected for these optimal perturbations: the optimal perturbation at $\tau = 0.1$ has the shape of a thin shear layers, while the one at $\tau = 0.3$ extends over 10% of the axial chord from the primary separation region and it is composed of an array of alternating vortical structures.

The energy growth that the disturbances experience is reported in figure (6.20) for the two time horizons. This profile can be obtained time-marching the linearised Navier-Stokes equations using the optimal perturbations as initial conditions. For $t \leq 0.05$ the two curves are practically overlapped, but for longer times the energy growth associated to $\tau = 0.3$ is subject to a larger amplification. These behaviours are characteristic of the small time horizons we considered; if τ is large enough, the perturbations are expected to be convected further downstream and the energy amplification would drop.
Finally, figure (6.21) shows the time evolution of the disturbances. Two different mechanisms were detected: for $\tau = 0.15$ the thin shear layer rolls-up while being convected along the suction surface, experiencing a progressive increase in its strength. The optimal perturbation corresponding to $\tau = 0.3$

is instead subject to an Orr mechanism which results into a Kelvin-Helmtholz instability, confirming the results obtained by the DNS.

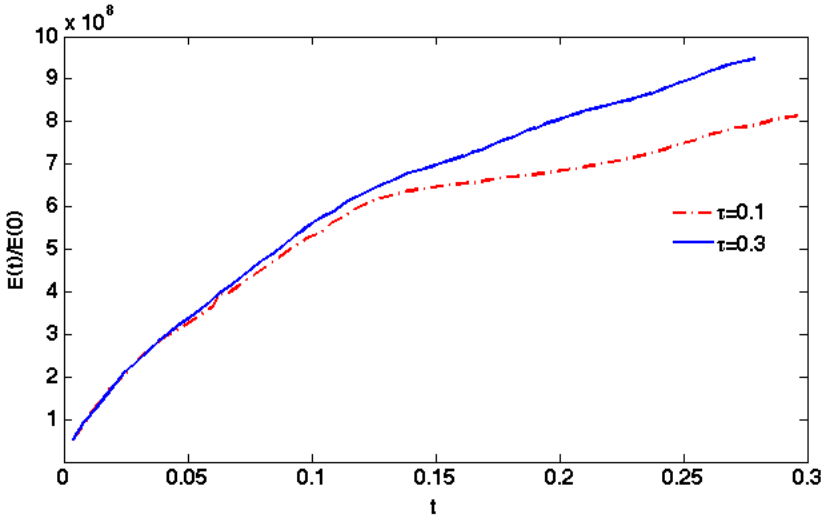

Figure 6.20: Transient responses at $\beta = 400\pi$ for two times horizons ($\tau =$ 0.15 and 0.3.

At last, we point out that even if the present study sheds light on the complex behaviour of the transition in flows through compressor passages, several questions remain unanswered. Specifically, investigation at other Reynolds numbers would be useful to understand the mechanisms behind the development of the instabilities and the role of three-dimensionality. Furthermore, stability analysis of the steady state and transient growth analyses in a wider range of time horizons could provide further validations of the results we obtained and be the starting point for a generalisation of the relevance of transient growth phenomena in flows which experience significant separation effects.

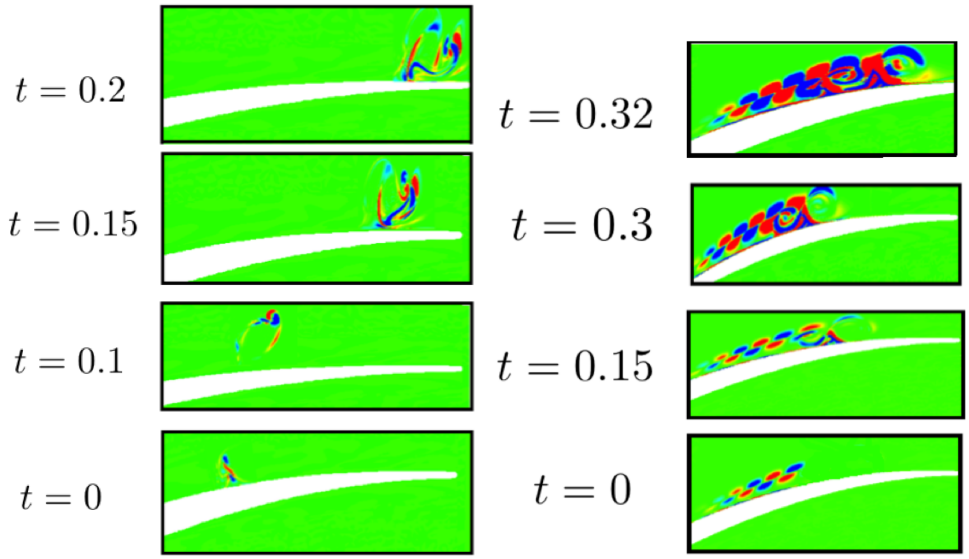

Figure 6.21: Time evolution of the optimal perturbations. (a): $\tau = 0.1$, (b): $\tau = 0.3$.

Chapter 7

Conclusions

> *James Joyce was a synthesiser, trying to bring in as much as he could. I am an analyser, trying to leave out as much as I can.*
>
> Samuel Beckett, *A History of Famous Literary Mentorships*

In this thesis we investigated hydrodynamic stability of vortical flows in complex geometries, where local approaches, based on the strong assumption of parallel flows, generally fail to provide a good prediction on the dynamics of the absolute instabilities. Specifically, we focused on flows past bluff bodies because of their importance in industrial applications, spanning from the automotive to the aeronautical and naval industries. As described in chapter §3, the dynamics of these types of flows is very complex even in simple configurations due to transition and separation effects, which generate remarkable fluctuations of the aerodynamic forces, vibrations and noise. Hence these phenomena must be carefully taken into account for the design of effective and efficient devices. The methodology to characterise accurately these phenomena is linear stability analysis, which was summarised in chapter §4. Linear stability analysis consists of two different steps. The first one is a direct numerical simulation of the flow, which can be obtained by solving analytically, or more often numerically, the incompressible Navier-Stokes equations; in particular, spectral/*hp* element discretisations were adopted for the present investigations, due to their flexibility and high-order accuracy. The second step of the methodology is hydrodynamic stability analysis of the computed base flow, which required the implementation of the linearised Navier-Stokes equations (direct stability analysis) coupled with

Arnoldi algorithms to retrieve the eigenspectra of the systems. Since one of the objectives of this project was the investigation of efficient control techniques, receptivity studies could not be ignored for an exhaustive analysis; therefore the adjoint solutions of the Navier-Stokes equations were considered. Moreover, the introduction of the adjoint evolution operator allowed us to evaluate the presence of energy transient growth phenomena, which can be detected by computing the solution of the eigenproblem obtained by combining the direct and adjoint operators together.
The description of the developed tools and the results of the two main applications are summarised in the following sections.

7.1 Developed tools

To perform the simulations described in this thesis, a significant effort has been made to improve and make more robust the incompressible Navier-Stokes solver implemented in Nektar++, an on-going inter-institutional project, entirely designed in C++, aimed at solving a wide range of partial differential equations using spectral/*hp* element methods. Tools to perform BiGlobal and TriGlobal stability analyses were implemented via a Fouier-Spectral element method and their validation was performed using several simple benchmark cases. Transient growth and receptivity analyses were implemented to perform accurate studies on stability of complex flows, together with *ad hoc* post-processing routines. All these features are included in the open-source code to make them more accessible and easy to use for the research community.

7.2 Suppression of vortex shedding

The first application is the investigation of the mechanisms behind the suppression of the von-Kármán street in a flow past a circular cylinder. Despite the simple geometry, this problem is still widely studied because of the rich and different transitional phenomena that the flow experiences when the Reynolds number is increased. From a control perspective, several techniques can be used to attenuate the unsteadiness caused by vortex shedding; in the present thesis, spanwise forcing was introduced on the top and bottom surfaces of a cylinder immersed in a flow at $Re = 60$, in order to stabilise the wake, similarly to the investigations of Kim & Choi (2005) and Darekar & Sherwin (2001). This technique was seen to generate relevant three-dimensional effects on the flow and it represents an interesting

method since it does not require any modification of the geometry of the system, differently from the widely adopted wavy cylinders. Two different spanwise forcing functions were tested: sinusoidal and Gaussian; Gaussian forcing was found to be more effective than the sinusoidal one since it generates a more prominent drag reduction (about 20% larger than the sinusoidal one) with a lower control velocity. The physical mechanisms behind the suppression were found to be related to the diversion of the shear layers, whose interaction in the near-wake region is inhibited. This mechanism is consistent with the presence of two counter-rotating vortices, which generate a cross flow and a redistribution of the spanwise vorticity along the streamwise and transverse directions. The evaluation of the enstrophy of the system allowed us to confirm that when the forcing amplitudes is sufficiently high, the dissipation effects are not able to inhibit the interaction of the shear layers and a global redistribution of the maxima of vorticity is observed, until vortex shedding is completely suppressed. A further study of the stabilisation mechanisms in the near-wake was performed by means of a fully three-dimensional direct stability analysis (TriGlobal stability); this analysis represents the most general approach to evaluating linear stability of flows, since no assumptions are made on the structure of the basic state. Results from this analysis confirmed a complete suppression of the near-wake instability and the three-dimensional mode was seen to be located close to the cylinder, maintaining a symmetric behaviour with respect to the centreplane. The main mechanisms predicted by the local stability theory (Hwang *et al.*, 2013) were confirmed and consist of tilting of the spanwise vortices followed by interactions with the modulated von-Kármán street. The evaluation of the work of Reynolds stresses against the base flow confirmed that the perturbations mainly extract the energy from the transverse components of the base flow shear, in particular in the region close to the cylinder. To evaluate the regions where the forced flow was more receptive to momentum forcing, the adjoint mode was computed. This mode shows a significant variation along the spanwise direction and the maxima are attained in the regions close to the kinematic inflection points, indicating that these are the areas more receptive to forcing. Finally, the proper superposition of the direct and adjoint mode provided the profile of the structural sensitivity, which is useful the detect the wavemaker region, where the instabilities arise, before being amplified in the remaining part of the domain. The profile reminds the one of the unforced flow (§4.8), even if the two lobes, which constitute the core of the instabilities, were seen to be shifted towards the regions where forcing was applied. Furthermore, the variation along the spanwise direction was found to be rather mild. However, it is the structural

sensitivity to the base modifications which provided the most significant insights into the mechanisms behind the suppression of the near-wake instability. This sensitivity was seen to be three-times larger than the structural sensitivity to perturbations and indicates that the largest drift of the leading eigenvalue can be achieved by modifying the base flow in proximity of the cylinder surface. A peculiar feature of this sensitivity is its prominent spanwise variation, therefore the adoption three-dimensional modifications is a key factor for the design of an efficient control. An extension of this study was performed at $Re = 180$, close to the on-set of Mode A. The most important differences with respect to the simulations at $Re = 60$ are the necessity of larger forcing amplitudes to suppress vortex shedding and the presence of unsteady hairpin vortices if forcing is increased over a critical value. Results from TriGlobal stability analysis pointed out that these structures do not destabilise the flow, but produce a small decrease of the decay rate of the disturbances. A first explanation on the reason behind the appearance of these structures can be obtained by the topology of the related eigenmode, which was seen to extend throughout the domain. A significant streamwise distribution of the vorticity perturbation is in fact directly associated to the gradual spatial evolution of the Λ-shaped structures.

7.3 Stability of a turbomachinery flow

The second application consists in performing stability analysis of a transitional flow over a NACA-65 airfoil. This problem evaluates the stability features of a flow in a linear compressor passage at $Re = 138,500$ and follows the studies of Zaki *et al.* (2009 and 2010) on the same configuration, where the transition was triggered by incoming wakes from the upstream stages and free-stream turbulence respectively. The boundary layers in the present geometry were seen to be subject to relevant separation effects on both the pressure and suction surfaces. However, in absence of external forcing the transition to turbulence was found to be very slow, allowing us to consider the flow laminar. Hence, the complexity of this study relies on the high Reynolds number and, in particular, the non-trivial geometry of the blade, which is based on laboratory experiments. An appropriate discretisation of the problem required an accurate refinement of the computational grid to capture properly the dynamics of the flow because, as discussed by Zaki *et al.* (2010), a lack of sufficient resolution in the region close to the suction surface might hinder the detection of important transitional phenomena, specifically the separation bubble close to the trailing edge. An hybrid mesh was designed, paying attention to generate a sufficiently refined grid in the

area surrounding the blade. Direct numerical simulations were performed to validate the discretisation by a direct comparison with the previous findings (Zaki *et al.* 2009, 2010) and to gain a detailed insight into the role of the favourable and adverse pressure gradients on both the pressure and suction surfaces. The adverse pressure gradient on the suction surface generates an inflection of the boundary layers, which might be subject to relevant instabilities. Specifically, the suction surface shows a Kelvin-Helmholtz instability in the region close to the trailing edge, with rolls being shed from the separated boundary layer. The peculiarity of these rolls is that they neither break up into turbulent eddies nor are convected away, but they remain coherent and create a small region of reverse flow on the blade surface beneath them. These structure were seen to have a well-defined time periodicity, which could be precisely detected. Floquet stability analysis was recognised to be the ideal approach to investigate the response of these structures to infinitesimal perturbations, but the fact that the periodicity was seen to be confined just in a small region of the domain prevented its direct application. The idea was to perform a phase-averaging of the flow, which is not other than the average over a sufficiently large ensemble of points with the same phase with respect to a reference oscillator. The main advantage of the phase-average is that only the organised motions are extracted, neglecting all the background unsteadiness; furthermore it can be shown that this approach leads to a better approximation of the flow features than the more conventional time-averaged technique, since the role of the Reynolds stresses is less prominent. Such an approach allowed us to sort out the base flow in a fixed number of time slices (fifty to be precise), where the vortical structures were "frozen", similar to a photograph. The BiGlobal Floquet stability analysis was then performed on the phase-averaged base flow for different values of the spanwise wavenumber β. All the leading Floquet multipliers were found to be real and the flow was found to be unstable just for small wavenumbers ($\beta \ll 1$), or equivalently very long wavelength ($L_z \gg 1$). The leading eigenmodes showed a high concentration of energy in the region where the separation bubble was detected, suggesting the presence of possible convective instabilities. Therefore, a transient growth analysis was performed for two different time horizons: $\tau = 0.1$ and $\tau = 0.3$ respectively, at $\beta = 400\pi$, which was seen to be the wavenumber of maximum energy growth. In both cases the flow was found to be convectively unstable in a large range of wavenumbers, and the evolution of the optimal perturbations showed two different mechanisms: a rolling of a thin shear layer perturbation at $\tau = 0.1$ and an Orr-mechanism, leading to the Kelvin-Helmholtz instability, at $\tau = 0.3$.

7.4 Final remarks and recommendations for further work

The main aim of the current project was to use advanced methods to investigate stability of flows in complex geometries, which can be found in a wide range of engineering applications. In chapter 5, we used TriGlobal stability analysis to investigate the physical mechanisms behind the surface bleed, an innovative three-dimensional technique to stabilise vortex shedding. This control method has already been successfully used on a model of a vehicle (Kim *et al.*, 2004) and the present study extends its application to the adoption of Gaussian functions, which were found to generate an additional drag reduction and an improvement in the global efficiency with respect to sinusoidal forcing. The results from the TriGlobal stability analysis offered a wide set of information for an improvement in the design of controllers, in particular the necessity to introduce forcing in specific regions to maximise the effects of the stabilisation. However, there are several questions that were not addressed in the present project and the following recommendations cover the areas that should be investigated further:

- the suppression of vortex shedding in flows past a cylinder via surface bleed should be studied for higher Reynolds numbers in order to address the actual capability of this method. The present work showed that the important changes in the dynamics of the flow happen at higher Reynolds numbers, even within the laminar vortex shedding regime, where the presence of vortex hairpins was detected. Extending this study to other regimes and turbulent wakes is essential to test its potentiality in industrial relevant geometries.

- A systematic comparison with spanwise wavy cylinder would highlight the differences between kinematic and geometric modifications of the base flow.

- Transient growth analysis should be performed to address the dynamics of the convective instabilities in the far-wake.

- Different types of forcing should be investigated and additional comparisons with experiments would be ideal to understand the applicability of this method.

- Applications of TriGlobal stability analysis to complex geometries certainly represents one of the most challenging development of the cur-

rent work. Investigations of flows past airfoils or vehicles may offer important advancements in the aerodynamic design.

The study discussed in chapter 6.3 represents a first step attempt to investigate the role of the transition in the compressor stages of turbomachines by means of stability analysis. While the low pressure turbine stages have received a noteworthy attention, flows through compressors are less studied. The phase-averaging technique is an interesting method to characterise the transition in presence of local periodic oscillations, like on the suction surface of the current configuration. The following recommendations are suggested to provide a better insight of the problem:

- transient growth analysis should be extended to a wider range of time horizons and wavelengths, to detect how these parameters affect the evolution of convective instabilities.
- Simulations of the same geometry at different Reynolds numbers would be useful to characterise more precisely transition. Our results suggest that at lower Reynolds numbers the instabilities might be more relevant in a wider range of wavelengths, similarly to the findings of Abdessemed *et al.* (2009*b*). However, further studies are necessary to infer it more precisely.
- Simulations at higher Reynolds numbers, close to the operating conditions of aircraft engines, could provide relevant hints for a more efficient aerodynamic design.
- Stability analysis of the steady solution would offer an interesting comparison with the present study.
- Fully three-dimensional simulations and TriGlobal stability analysis could shed some light on the role of spanwise variations on the aerodynamic performances of the problem.

Bibliography

Abdessemed, N., Sharma, A.S., Sherwin, S.J. & Theofilis, V. 2009*a* Transient growth analysis of the flow past a circular cylinder. *Physics of Fluids* **21** (044103).

Abdessemed, N., Sherwin, S.J. & Theofilis, V. 2009*b* Linear instability analysis of low-pressure turbine flows. *J. Fluid Mech.* **628**, 57–83.

Abergel, F. & Teman, R. 1990 On some control problems in fluid mechanics. *Theor. Comput. Fluid Dyn.* **303-325**.

Achenbach, E. 1972 Experiments on the flow past spheres at very high reynolds numbers. *J. Fluid Mech.* **54**, 565–575.

Achenbach, E. 1974 The effect of surface roughness and tunnel blockage on the flow past spheres. *J. Fluid Mech.* **65**, 113–125.

Akervik, E., Hoepffner, J., Ehrenstein, U. & Henningson, D.S. 2007 Optimal growth, model reduction and control in a separated boundary-layer flow using global eigenmodes. *J. Fluid Mech.* **579** (1), 305–314.

Amon, C.H. & Patera, A.T. 1989 Numerical calculation of stable three-dimensional tertiary states in grooved channel flow. *Physics of Fluids* **1** (2005-2009).

Arnoldi, W.E. 1951 The principle of minimized iterations in the solution of the matrix eigenvalue problem. *Quart. J. Appl. Math.* **9**, 17–29.

Bagheri, S., Schlatter, P., Schmid, P.J. & Henningson, D.S. 2009 Gloabl stability of a jet in crossflow. *J. Fluid Mech.* **624**, 33–44.

Barkley, D. 2006 Linear analysis of the cylinder wake mean flow. *Europhysics Letters* **75** (5), 750–756s.

Barkley, D., Blackburn, H.M & Sherwin, S.J. 2008 Direct optimal growth analysis for timesteppers. *Int. J. Numer. Meth. Fluids* **57**, 1435–1458.

Barkley, D. & Henderson, D.R. 1996 Three-dimensional floquet stability analysis of the wake of a circular cylinder. *J. Fluid Mech* **322**, 215–241.

Bearman, P.W. 1965 Investigation of the flow behind a two-dimensional model with a blunt trailing edge and fitted with splitter plates. *J. Fluid Mech* **21**, 241.

Bearman, P.W. 1967 The effect of base bleed on the flow behind a two-dimensional model with a blunt trailing edge. *Aeronaut. Q.* **18**, 207–224.

Bearman, P.W. 1969 On vortex shedding from circular cylinder in the critical reynolds number regime. *J. Fluid Mech.* **37**, 577.

Bearman, P.W. 1992 Challenging problems in bluff bodies wakes. In *Bluff-body Wakes, Dynamics and Instabilites, IUTAM Symposium*.

Bearman, P.W. & Owen, J.C. 1998 Special brief note: reduction of bluff-body drag and suppression of vortex shedding by introduction of wavy separation lines. *Journal of Fluids and Structures* **12**, 123–130.

Bell, J.H. & Mehta, R.D. 1993 Effects of imposed spanwise perturbations on plane mixing-layer structure. *J. Fluid Mech.* **257**, 33.

Bender, C.M. & Orszag, S.A. 1978 *Advanced Mathematical Methods for Scientiests and Engineers*. New York: McGrawHill.

Berger, E. 1967 Suppression of vortex shedding and turbulence behind oscillating cylinders. *Physics of Fluids* **10**, S191–193.

Berger, E. & Wille, R. 1972 Periodic flow phenomena. *Annu. Rev. Fluid Mech.* **4**, 313.

Bhaskaran, R. 2010 Large eddy simulation of high pressure turbine cascade. PhD thesis, Stanford University.

Blackburn, H.M. 2002*a* Three-dimensional instability and state selection in an oscillatory axisymmetric swirling flow. *Physics of Fluids* **14** (11), 3983–3996.

Blackburn, H.M. 2002*b* Three-dimensional instability and state selection in an oscillatory axysymmetric swirling flow. *Physics of Fluids* **14** (3893).

Blackburn, H.M., Barkley, D. & Sherwin, S.J. 2008 Convective instabilities and transient growth in a flow over a backward-facing step. *J. Fluid Mech.* **603**, 271–304.

Blackburn, H.M. & Lopez, J.M. 2003a On three-dimensional quasiperiodic floquet instabilities of two-dimensional bluff body wakes. *Physics of Fluids* **15**, L57–L60.

Blackburn, H.M., Marques, F. & Lopez, J.M. 522 Symmetry breaking of two-dimensional time-periodic wakes,. *J. Fluid Mech.* pp. 395–411.

Blackburn, H.M. & Melbourne, W.H. 1996 The effect of free-stream turbulence on sectional lift forces on a circular cylinder. *J. Fluid Mech.* **385**, 267–292.

Blevins, R. 1990 *Flow-Induced Vibrations.*, 2nd edn. New York: Van Nostrand Reinhold.

Bloor, M.S. 1964 The transition to turbulence in the wake of a circular cylinder. *J. Fluid Mech.* **19**, 290.

Bolis, A. 2013 Fourier spectral/hp element method: Investigation of time-stepping and parallelisation strategies. PhD thesis, Imperial College London.

Bottaro, A., Corbett, P. & Luchini, P. 2003 The effect of base flow variation on flow stability. *J. Fluid Mech* **476**, 293–303.

Brede, M., Eckelmann, H. & Rockwell, D. 1996 On secondary vortices in the cylinder wake. *Physics of Fluids* **8**, 2117–2124.

Cantwell, B. & Coles, D. 1983 An experimental study of entrainment and transport in the turbulent near wake of a circular cylinder. *J. Fluid Mech.* **136**, 321–374.

Cantwell, C.D. & Barkley, D. 2010 Computational study of subcritical response in flow past a circular cylinder/. *Phys. Rev. E* **82** (026315).

Canuto, C., Hussaini, M., Quarteroni, A. & Zang, T. 2006 *Spectral Methods. Fundamentals in Single Domains*. Springer Verlag.

Chakraborty, P., Balachandar, S. & Adrian, R.J. 2005 On the relationships between local vortex identification schemes. *J. Fluid Mech.* **535**, 189–214.

Choi, H., Woo-Pyung, J. & Kim, J. 2008 Control of flow over a bluff body. *Annu. Rev. Fluid Mech.* **40**, 113–139.

Choi, J., Jeon, W.-P. & H.Choi 2006 Mechanism of drag reduction by dimples on a sphere. *Physics of Fluids* **18** (041702).

Chomaz, J.-M. 2005 Global instabilities in spatially developing flows: non-normality and nonlinearity. *Annu. Rev. Fluid Mech.* **37** (357-392).

Chong, M.S., Perry, A.E. & Cantwell, B.J. 1990 general classification of three-dimensional flow fields. *Physics of Fluids A* **2**, 765–777.

Chun, S., Lee, I. & Sung, H.S. 1990 Effect of spanwise-varying local forcing on turbulent separated flow over backward-facing step. *Exp. Fluids* **26**, 437.

Collis, S.S., Lele, S.K., Moser, R.D. & Rogers, M.M. 1994 The evolution of a plane mixing layer with spanwise nonuniform forcing. *Physics of Fluids* **6**, 381.

Cornelius, K.C. 1985 Three-dimensional wave development during boundary layer transition. *Tech. Rep.*. Lockheed Georgia Res. Rep. LG85RR0004.

Cortelezzi, L. 1996 Nonlinear feedback control of the wake past a plate with a suction point on the downstream wall. *J. Fluid Mech.* **327**, 303–324.

Courant, R. & Hilbert, D. 1989 *Methods for mathematical physics*, , vol. 1. Wiley, New York.

Coutanceau, M. & Bouard, R. 1977 Experimental determination of the main features of the viscous flow in the wake of a circular cylinder in uniform translation. part 1. steady flow. *J. Fluid Mech* **79**, 231–256.

Daniel, J., Gragg, W.B., Kaufman, L. & Stewart, G.W. 1976 Reorthognalization and stable algorithms for updating the gram-schmidt qr factorization. *Math. Comp.* **30** (772-795).

Darekar, R.M. & Sherwin, S.J. 2001 Flow past a square-section cylinder with a wavy stagnation face. *J. Fluid Mech.* **426**, 263–295.

Del Guercio, G., Cossu, C. & Pujals, G. 2014 Stabilizing effect of optimally amplified streaks in parallel wakes/. *J. Fluid Mech.* **739**, 37–56.

Delbende, I. & Chomaz, J.M. 1998 Nonlinear convective/absolute instabilities in parallel two-dimensional wakes. *Physics of Fluids* **10**, 2724–2736.

Dennis, S.R.C. & Chang, G. 1970 Numerical solutions for steady flow past a circular cylinder at reynolds number up to 100. *J. Fluid Mech* **42**, 471–489.

Drazin, P.G. & Reid, W.H. 1981 *Hydrodynamic Stability.*. Cambridge University Press.

Eisenlohr, H. & Eckelmann, H. 1989 Vortex splitting and its consequences in the vortex street wake of cylinders at low reynolds number. *Physics of Fluids A* **1**, 189.

Eriksson, L.E. & Rizzi, A. 1985 Computer-aided analysis of the convergence to steady state of discrete approximations to the euler equations. *J. Comput. Phys.* **57** (90-128).

Fornberg, B. 1980 A numerical study of steady viscous flow past a circular cylinder. *J. Fluid Mech* **98**, 819–855.

Gerrard, J.H. 1966 The mechanics of the vortex formation region of vortices behind bluff bodies. *J. Fluid Mech* **25** (401).

Gerrard, J.H. 1978 The wakes of cylindrical bluff bodies at low reynolds number. *Philos. Trans. R. SOC. London Sex A* **288**, 351.

Giannetti, F., Camarri, S. & Luchini, P. 2010 Structural sensitivity of the secondary instability in the wake of a circular cylinder. *J. Fluid Mech* **651**, 319–337.

Giannetti, F. & Luchini, P. 2007 Structural sensitivity of the first instability of the cylinder wake. *J. Fluid Mech* **581** (167-197).

Giannetti, F., Luchini, P. & Marino, L. 2009 inear stability analysis of three-dimensional lid-driven cavity flow. In *Atti 19th Congr. AIMETA Mecc. Teor. Appl., Ancona, Italy* (ed. Aras Edizioni), , vol. 738.

Glezer, A. & Amitay, M. 2002 Synthetic jets. *Annu. Rev. Fluid Mech.* **34**, 503–529.

Goldhammer, M. 2009 The next decade in commercial aircraft aerodynamics: a boeing perspective. In *Proc. KATnet II Conf. of Key Aerodynamic Technologies, Bremen*. Boeing Commercial Airplanes, Seattle, USA.

Gomez, F., Hermida, J., Gomez, R., Theofilis, V., Carmo, B. & Meneghini, J. 2014 Three-dimensional transition of the flow past a cylinder fitted with helical strakes. In *Instability and Control of Massively Separated Flow*.

Gottlieb, D. & Orszag, S.A. 1977 Numerical analysis of spectral methods: theory and applications. *SIAM-CMBS* .

Graham, W.R., Peraire, J. & Tang, K.Y. 1999 Optimal control of vortex shedding using low-order models. part ii: model-based control. *Int. J. Numer. Methods Eng.* **44**, 973–990.

Griffin, O.M. & Ramberg, S.E. 1974 The vortex street wakes of vibrating cylinders. *J. Fluid Mech* **66**, 553.

Hall, P. & Horseman, N. 1991 The linear inviscid secondary instability of longitudi nal vortex structures in boundary layers. *J. Fluid Mech.* **232**, 357–375.

Hama, F.R. 1957 Three-dimensional vortex pattern behind a circular cylinder. *J. Aeronaut. Sci.* **24**, 156.

Hammache, M. & Gharib, M. 1991 An experimental study of the parallel and oblique vortex shedding from circular cylinders. *J. Fluid Mech.* **232**, 567.

Haynes, T. S. & Reed, H. L. 1996 Computations in nonlinear sturation of stationary crossflow vortices in swept-wing boundary layer. *AIAA paper* **96** (0182).

Henderson, R.D. 1994 Unstructured spectral element methods: parallel algorithms and simulations. PhD thesis, Princeton University.

Henderson, R.D. 1995 Details of the drag curve near the onset of vortex shedding. *Physics of Fluids* **7** (9), 2012–2014.

Henderson, R.D. 1997 Nonlinear dynamics and pattern formation in turbulent transition. *J. Fluid Mech.* **352**, 65–112.

Henderson, R.D. & Barkley, D. 1996 Secondary instability in the wake of a circular cylinder. *Physics of Fluids* **8** (6), 1683–1685.

Henningon, D. S. 1987 Stability of inviscid shear flow with mean spanwise variation. *Tech. Rep.* FFA-TN 1987-57. Aeronautical Research Institute of Sweden, Bromma.

Herbert, T. 1988 Secondary instability of boundary layers. *Annu. Rev. Fluid Mech.* **20**, 487–526.

Hilgenfeld, L. & Pfitzner, M. 2004 Unsteady boundary development due to wake passing effects on a highly loaded linear compressor cascade. *J. Turbomach.* **493**, 493–500.

Hill, D. 1992 A theoretical approach for analyzing the re-stabilization of wakes. *AIAA paper* **92** (0067).

Hill, D.C. 1995 Adjoint systems and their role in the receptivity problem for boundary layers. *J. Fluid Mech* **292**, 183–204.

Holmes, P., Lumley, J.L. & Berkooz, G. 1996 *Turbulence, Coherent Structures, Dynamical Systems and Symmetry.*. Cambridge, UK: Cambridge Univ. Press.

Horton, G. 2006 Forecasts of co2 emissions from civil aircraft for ipcc. *Tech. Rep.* 06/02392. Qinetiq.

Huang, X. 1996 Feedback control of vortex shedding from a circular cylinder. *Exp. Fluids* **20**, 218–224.

Huerre, P. & Monkewitz, A. 1990 Local and global instabilities in spatially developing flows. *Annu. Rev. Fluid Mech.* **22**, 473–537.

Huerre, P. & Monkewitz, P.A. 1995 Absolute and convective instabilities in free shear layers. *J. Fluid Mech* **159**, 151–168.

Hughes, J.D. & Walker, G.J. 2001 Natural transition phenomena on an axial flow compressor blade. *J. Turbimach.* **123**, 392–401.

Hunt, J.C.R., Wray, A.A. & Moin, P. 1988 Eddies, stream, and convergence zones in turbulent flows. *Tech. Rep.*. Center of Turbulence Research Report CTR-S88.

Hwang, Y. & Choi, H. 2006 university-based scientists and engineers in industry, with each group recognizing and responding creatively to the priorities andcontrol of absolute instability by basic-flow modification in a parallel wake at low reynolds number. *J. Fluid Mech.* **560** (465-475).

Hwang, Y., Kim, J. & Choi, H. 2013 Stabilization of absolute instability in spanwise wavy two-dimensional wakes. *J. Fluid Mech.* **727**, 346–378.

Ilak, M., Schlatter, P., Bagheri, S. & Henningson, D.S. 2012 Bifurcation and stability analysis of a jet in crossflow. onset of global instability at a low velocity. *J. Fluid Mech.* **695**, 94–121.

Ince, E.L. 1926 *Ordinary Differential Equations*. Dover.

Israeli, M. & Orszag, S.A. 1981 Approximation of radiation boundary conditions. *J. Comput. Phys.* **41**, 115–135.

Jeong, J. & Hussain, F. 1995 On the identification of a vortex. *J. Fluid Mech.* **285**, 69–94.

Johnson, T. A. & Patel, V.C. 1999 Flow past a sphere up to reynolds number of 300. *J. Fluid Mech.* **378**, 19–70.

Jones, L.E., Sandberg, R.D. & Sandham, N.D. 2008 Direct numerical simulations of forced and unforced separation bubbles on a airfoil at incidence. *J. Fluid Mech.* **602**, 175–207.

Joseph, D.D. 1966 Nonlinear stability of boussinesque equations by method of energy. *Arch. Rat. Mech. Anal.* **22**, 163–184.

Kachanov, Y. S. & Levchenko, V.Y 1984 The resonant interaction of disturbances at laminar-turbulent transition in boundary layer. *J. Fluid Mech.* **138**, 209–247.

Karniadakis, G.E. 1990 Spectral element-fourier methods for incompressible turbulent flows. *C.M.A.M.E* **80**, 362.

Karniadakis, G.E., Israeli, M. & Orszag, S.A. 1991 High-order splitting methods for incompressible navier-stokes equations. *J. Comput. Phys.* **97**, 414.

Karniadakis, G.E. & Sherwin, S.J. 2005 *Spectral/hp element methods for computational fluid dynamics*, 2nd edn. Oxford University Press.

Karniadakis, G.E. & Triantafyllou, G.S. 1992 Threedimensional dynamics and transition to turbulence in the wake of bluff objects. *J. Fluid Mech.* **238**, 1.

Kim, J. & Choi, H. 2005 Distributed forcing of flow over a circular cylinder. *Physics of Fluids* **17** (033103).

Kim, J., Hahn, S., Kim, J.S., Lee, D.K., Choi, J., Jeon, W.-P. & Choi, H. 2004 Active control of turbulent flow over a model vehicle for drag reduction. *J. Turbulence* **5** (019).

Kim, J., Kim, D. & Choi, H. 2001 An immersed-boundary finite-volume method for simulations of flow in complex geometries. *J. Comput. Phys.* **171**, 132–150.

Kimura, T. & Tsutahara, M. 1991 Fluid dynamic effects of grooves on a circular cylinder surface. *AIAA J.* pp. 2062–2068.

Kirby, R.M. & Sherwin, S.J. 2006 www.nektar.info.

Kiya, M., Suzuki, Y., Arie, M. & Hagino, M. 1982 A contribution to the free-stream turbulence effect on the flow past a circular cylinder. *J. Fluid Mech.* **115**, 151–164.

Klebanoff, P.S., Tidstrom, K.D. & Sargent, L.M. 1962 The three-dimensional nature of boundary-layer instability. *J. Fluid Mech.* **12**, 1–34.

Küchermann, R. 1965 Report on the iutam symposium on concentrated vortex motion in fluids. *J. Fluid Mech.* **21**, 1–20.

Larson, R. 2012 *Elementary Linear Algebra*, 7th edn. Richard Stratton.

Lascheras, L. & Choi, H. 1989 Three-dimensional instability of a plane free shear layer: an experimental study of the formation and evolution of streamwise vortices. *J. Fluid Mech.* **189**, 53–86.

Lehoucq, R.B., Sorensen, D.C. & Yang, C. 1998 *Arpack: Solution of Large-Scale Eigenvalue Problems with Implicitly Restarted Arnoldi Methods*. Siam.

Leschziner, M.A., Choi, H. & Choi, K.S. 2011 Flow-control approaches to drag reduction in aerodynamics: progress and prospects. *Phil. Trans. R. Soc. A* **369**.

Lewis, C.G. & Gharib, M. 1992 An e xploration of w ake t hree d imensionalities c aused by a l ocal d iscontinuity in c ylinder d iameter an e xploration of w ake t hree d imensionalities c aused by a l ocal d iscontinuity in c ylinder d iameter an exploration of wake three dimensionalities caused by a local discntinuity in cylinder diameter. *Physics of Fluids A* pp. 104–117.

Li, F. & Aubry, N. 2003 Feedback control of a flow past a cylinder via transverse motion. *Physics of Fluids* **15**, 2163–2176.

Luchini, P. & Bottaro, A. 2014 Adjoint equations in stability analysis. *Annu. Rev. Fluid Mech.* **46**, 493–517.

Luchini, P., Giannetti, F. & Pralits, J.O. 2008 Structural sensitivity of linear and nonlinear global modes. In *AIAA Paper*. Seattle, Washington.

Luchini, P., Giannetti, F. & Pralits, J.O. 2009 Structural sensitivity of the finite-amplitude vortex shedding behind a circular cylinder. In *IUTAM Symp. on Unsteady Separated Flows and Their Control.*, , vol. 14, pp. 151–160. Springer.

Lundbladh, A. 1993 Simulation of bypass transition to turbulence in wall bounded shear flows. PhD thesis, Royal Institute of Technology, Stockholm, Sweden.

Marques, F., Lopez, J.M. & Blackburn, H.M. 2004 Bifurcations in systems with Z2 spatio-temporal and O(2) spatial symmetry. *Physica D* **189**, 247–276.

Marquet, O., Sipp, D. & Jacquin, L. 2008a Sensitivity analysis and passive control of cylinder flow. *J. Fluid Mech* **615** (221-252).

Maxworthy, T. 1969 Experiments on the flow around a sphere at high reynolds numbers. *J. Appl. Mech. E* **36**, 598–607.

Meiburg, E. & Lasheras, J.C. 1988 Experimental and numerical investigation of the threedimensional transition in plane wakes. *J. Fluid Mech.* **190**, 1.

Miller, G.D. & Williamson, C.H.K. 1994 Control of three-dimensional phase dynamics in a cylinder wake. *Exp. Fluids* **18**, 26.

Min, C. & Choi, H. 1999 Suboptimal feedback control of vortex shedding at low reynolds numbers. *J. Fluid Mech.* **401**, 123–156.

Mittal, S. 2010 Stability of flow past a cylinder: energy budget of the eigenmodes. *Int. J. Numer. Meth. Fluids* **63**, 533–547.

Morzynski, M. & Thiele, F. 2008 Finite element method for global stability analysis of 3d flows. In *Presented at Fluid Dyn. Conf. Exhib., 38th, Seattle, AIAA Pap.*, pp. 2008–3865.

Nagata, M. 1990 Three-dimensional finite-amplitude solutions in plane coutte flow bifurcation from infinity. *J. Fluid Mech* **217**, 519–527.

Natarajan, R. & Acrivos, A. 1993 The instability of the steady flow past spheres and disks. *J. Fluid Mech.* **254**, 323–344.

Nishioka, M. & Sato, H. 1974 Measurements of velocity distributions in the wake of a circular cylinder at low reynolds numbers. *J. Fluid Mech.* **765**, 97–112.

Noack, B. R. & Eckelmann, H. 1994 A global stability analysis of the steady and periodic cylinder wake. *J. Fluid Mech.* **270**, 297–330.

Nygaard, K.J. & Gletzer, A. 1994 The effect of phase variations and cross-shear vortical structures in plane mixing layer. *J. Fluid Mech.* **276**, 21.

Owen, J.C. 2001 Passive control of vortex shedding in the wakes of bluff bodies. PhD thesis, Imperial College London.

Owen, J.C., Szewczyk, A.A. & Bearman, P.W. 2000 Suppression of Kármán vortex shedding. *Physics of Fluids* **S9 (Gallery of Fluid Motion)**.

Papangelou, A. 1992 Vortex shedding from slender cones. *J. Fluid Mech.* **242**, 229–321.

Park, H., Lee, D., Jeon, W.-P., Choi, H., Yoo, J.Y. & Kim, J. 2006 Drag reduction in flow over a twodimensional bluff body with a blunt trailing edge using a new passive device. *J. Fluid Mech.* **563**, 389–414.

Perry, A.E., Chong, M.S. & Lim, T.T. 1982 The vortex shedding eocess behind two-dimensional bluff bodies. *J. Fluid Mech* **116**, 77.

Peters, P.M., Middel, J. & Hoolhorst, A. 2005 Fuel efficiency of commercial aircraft, an overview of historical and future trends. *Tech. Rep.* 20905-669. NLR-CR.

Petrusma, M.S. & Gai, S.L. 1994 The effect of geometry on the base pressure recovery of the segmented blunt trailing edge. *Aeronaut. J.* **98**, 267–274.

Pier, B. 2008 Local and global instabilities in the wake of a sphere. *J. Fluid Mech.* **603**, 39–61.

Pierrehumbert, R.T. 1986 niversal shortwave instability of two-dimensional eddies in an inviscid fluid. *Phys. Rev. Lett.* **57**, 2157–2159.

Pierrehumbert, R.T. & Widnall, S.E. 1982 The two- and three-dimensional instabilities of a spatially periodic shear layer. *J. Fluid Mech.* **114**, 58–82.

Pralits, J.O., Brandt, L. & Giannetti, F. 2010 Instability and sensitivity of the flow around a rotating circular cylinder. *J. Fluid Mech* **650**, 513–536.

Provansal, M., Mathis, C. & Boyer, L. 1987 Bernard-von karman instability: transient and forced regimes. *J. Fluid Mech.* **182**, 1.

Reynolds, W.C. & Hussain, A.K.M.F. 1972 The mechanics of an organized wave in turbulent shear flow. part 3. theoretical models and comparisons with experiments. *J. Fluid Mech.* **54** (263-288).

Robichaux, J., S., S. Balachandar & Vanka, S. P. 1999 Three-dimensional floquet instability of the wake of a square cylinder. *Physics of Fluids* **11** (3), 560–578.

Rodriguez, O. 1991 Base drag reduction by the control of three-dimensional unsteady vortical structures. *Exp. Fluids* **11**, 228–226.

Roshko, A. 1955*a* On the development of turbulent wakes from vortex streets. *Tech. Rep.* 1191. NACA Rep.

Roshko, A. 1955*b* On the wake and drag of bluff bodies. *J. Aeronaut. Sci.* **22** (124-132).

Roshko, A. 1993 Perspectives on bluff body aerodynamics. *J. Wind Ind. Aerodyn.* **49**, 79.

Roussopoulos, K. 1993 Feedback control of vortex shedding at low reynolds numbers. *J. Fluid Mech.* **248**, 267–296.

Schmid, P.J. 2007 Nonmodal stability theory. *Annu. Rev. Fluid Mech.* **39** (129-162).

Schmid, P.J. & Henningson, D.S. 2001 *Stability and Transition in Shear Flows*. Springer.

Schreiber, H., Steinert, W., Sonoda, T. & Arima, T. 2004 Advanced high turning compressor airfoils for low reynolds number conidition. part ii: Experimental and numerical analysis. *J. Turbimach.* **126** (4), 482–492.

Semeraro, O., Bagheri, S., Brandt, L. & Henningson, D.S. 2013 Transition delay in boundary lauer flow using active control. *J. Fluid Mech.* **731** (288-311).

Sherwin, S.J. & Blackburn, H.M. 2005 Three-dimensional instabilities and transition of steady and pulsatile flows in an axisymmetric stenotic tube. *J. Fluid Mech.* **533**, 297–327.

Shewe, G. 1983 On the force fluctuations acting on a circular cylinder in crossflow from subcritical up to transcritical reynolds numbers. *J. Fluid Mech.* **133**, 265.

Smith, B.L. & Glezer, A. 1998 The formation and evolution of synthetic jets. *Physics of Fluids* **31**, 2281–2297.

Sonoda, T., Yamaguchi, Y., Arima, T., Olhoder, M., Sendhoff, B. & Schreiber., H.A. 2004 Advanced high turning compressor airfoils for low reynolds number. part i: design and optimization. *J. Turbimach.* **126** (3), 350–359.

Sorensen, D.C. 1992 Implicit application of polynomial fiters in a k-step arnoldi methods. *SIAM J. Marix Anal. Appl.* **13** (1), 101–137.

Spalart, P.R. & McLean, J.D. 2011 Drag reduction: enticing turbulence, and then an industry. In *Phil. Trans. R. Soc. A*, , vol. 369.

Squire, H.B. 1933 On the stability for threedimensional disturbances of viscous fluid flow between parallel walls. *Proc. R. Soc. London Ser. A.* **142**, 621.

Stansby, P.K. 1974 The effects of end plates on the base pressure coefficient of a circular cylinder. *Aerosp. J.* **36-37**.

Strykowski, P.J. & Sreenivasan, K.R. 1990 On the formation and suppression of vortex 'shedding' at low reynolds number. *J. Fluid Mech* **218**, 71–107.

Tang, S. Aubry 1997 On the symmetry breaking instability leading to vortex shedding. *Physics of Fluids* **9**, 2550–2561.

Tanner, M. 1972 A method of reducing the base drag of wings with blunt trailing edges. *Aeronaut. Q.* **23**, 15–23.

Tezuka, A. & Suzuki, K. 2006 Three-dimensional global linear stability analysis of flow around a spheroid. *AIAA J.* **44**, 1697–1708.

Theofilis, V. 2003 Advances in global linear instability analysis of nonparallel and threedimensional flows. *Prog. Aerosp. Sci.* **39** (4), 249–315.

Theofilis, V. 2011 Global linear instability. *Annu. Rev. Fluid Mech.* **43**, 319–352.

Thompson, M.C., Leweke, T. & Williamson, C.H.K. 2000 Transition in bluff body wakes: is transition elliptic? In *2000 IUTAM Symposium on Bluff-Body Wakes and Vortex-Induced-Vibrations*.

Thompson, M.C., Leweke, T. & Williamson, C.H.K. 2001 The physical mechanism of transition in bluff body wakes. *Journal of Fluids and Structures* **15**, 607–616.

Tokumaru, P.T. & Dimotakis, P.E. 1991 Rotary oscillatory control of a cylinder wake. *J. Fluid Mech.* **224**, 77–90.

Tombazis, N. & Bearman, P.W. 1997 A study of three-dimensional aspects of vortex shedding from a bluff body with a mild geometric disturbance. *J. Fluid Mech.* **330**, 85–112.

Trefethen, L. N., Trefethen, A. E., Reddy, S. C. & Driscoll, T. A. 1993 Hydrodynamic stability without eigenvalues. *Science* **261**, 578–584.

Tritton, D.J. 1959 Experiments on the flow past a circular cylinder at low reynolds numbers. *J. Fluid Mech.* **6**, 574.

Tuckerman, L.S. & Barkley, D. 2000 Bifurcation analysis for timesteppers. *Numerical methods for bifurcation problems and large-scale dynamical systems* .

Wei, T. & Smith, C.R. 1986 Secondary vortices in the wake of circular cylinders. *J. Fluid Mech.* **169**, 513.

Williams, J. Ffowcs & Zhao, B. 1989 The active control of vortex shedding. *Journal of Fluids and Structures* **3**, 114–122.

Williamson, C.H.K. 1988a Defining a universal and continuous strouhal-reynolds number relationship for the laminar vortex shedding of a circular cylinder. *Physics of Fluids* **31**, 2742.

Williamson, C.H.K. 1988b The existence of two stages in the transition to threedimensionality of a cylinder wake. *Physics of Fluids* **31**, 3165.

Williamson, C.H.K. 1989 Oblique and parallel modes of vortex shedding in the wake of a circular cylinder at low reynolds numbers. *J. Fluid Mech.* **206**, 579.

Williamson, C.H.K. 1992a The natural and forced formation of spot-like dislocations in the transition of a wake. *J. Fluid Mech.* **243** (393-441).

Williamson, C.H.K. 1996a Three-dimensional wake transition. *J. Fluid Mech.* **328**, 345–407.

Williamson, C.H.K. 1996b Vortex dynamics in the cylinder wake. *Annu. Rev. Fluid Mech.* **28**, 477–539.

Wissink, J.G. & Rodi, W. 2006 Direct numerical simulation of flow and heat transfer in a turbine cascade with incoming wakes. *J. Fluid Mech.* **596**, 209–247.

Wood, C.J. 1964 The effect of base bleed on a periodic wake. *J. R. Aeronaut. Soc.* **68**, 477–482.

Wu, X. & Durbin, P.A. 2001 Evidence of longitudinal vortices evolved from distorted wakes in a turbine passage. *J. Fluid Mech.* **446**, 199–228.

Ye, T., Mittal, R., Udaykumar, H.S. & Shyy, W. 1999 An accurate cartesian grid method for viscous incompressible flows with complex immersed boundaries. *J. Comput. Phys.* **156**, 209–240.

Yoon, J. 2005 Control of flow over a circular cylinder using wake disrupter. Master's thesis, Seoul National University, South Korea.

Zaki, T.A. & Durbin, P.A. 2005 Mode interaction and the bypass route to transition. *J. Fluid Mech.* **531**, 85–111.

Zaki, T.A., Wissink, J.C., Durbin, P.A. & Rodi, W. 2009 Direct computations of boundary layers distorted by migrating wakes in a linear compressor cascade. *Flow, Turbulence and Combustion* **83**, 307–322.

Zaki, T.A., Wissink, J.G., Rodi, W. & Durbin, P. 2010 Direct numerical simulations of transition in a compressor cascade: the influence of free-stream turbulence. *J. Fluid Mech.* **665**, 57–98.

Zdravkovich, M.M. 1981 Review and classification of various aerodynamic and hydrodynamic means for suppressing vortex shedding. *J. Wind Eng. Ind. Aerodyn.* **7**, 145–189.

Zebib, A. 1987 Stability of viscous flow past a circular cylinder. *J. Eng. Maths* **21** (155-165).

Zhang, H., Fey., U., Noack, B.R., König, M. & Eckelmann, H. 1995 On the transition of the cylinder wake. *Physics of Fluids* **7**, 779–794.

Zhang, M., Cheng, L. & Zhou, Y. 2004 Closed-loop-controlled vortex shedding and vibration of a flexibly supported square cylinder under different schemes. *Physics of Fluids* **16**, 1439–1448.

Zhou, J., Adrian, R.J., Balachandar, R.J. & Kendall, T. M. 1990 Mechanisms for generating coherent packets of hairpin vortices. *J. Fluid Mech.* **387**, 353–396.

Appendix A

Numerical solutions of eigenproblems

One of the main challenge of the global stability analysis is the necessity to solve demanding eigenproblems in order to determine the dominant eigenvalue of an operator $\mathcal{A}$ (§4.4.2). However, the systems are generally too large to construct a discrete representation of the operator through a matrix $\boldsymbol{A}$, so timestepping approaches are usually used and the classic QR algorithm is not a viable method. Thus, efficient alternatives are presented in this chapter.

A.1 The Power Method

The simplest technique to compute a single real eigenvalue is the power method. This application of this method leads to obtain the dominant eigenvalue of a matrix $\boldsymbol{A}$.

Definition

Let λ_i be the eigenvalues of a matrix $\boldsymbol{A} \in \mathbb{R}^{n \times n}$. λ_1 is called the **dominant** (or **leading**) **eigenvalue** of $\boldsymbol{A}$ if:

$$|\lambda_1| > |\lambda_i|, \quad i = 2, \ldots, n \tag{A.1}$$

The eigenvector corresponding to λ_1 is called **dominant** (or **leading**) **eigenvector** of $\boldsymbol{A}$.

Let us assume that the matrix $\boldsymbol{A} \in \mathbb{R}^{n\times n}$ has a dominant eigenvalue and choose an initial approximation of its dominant eigenvector $\boldsymbol{u}_0 \in \mathbb{R}^n_0$. The main idea behind the power method is the repeated application of the matrix $\boldsymbol{A}$ to $\boldsymbol{u}_0$, generating the sequence $\boldsymbol{A}^k\boldsymbol{u}_0$. For large powers of k, it is possible to demonstrate that $\boldsymbol{A}^k\boldsymbol{u}_0$ is a good approximation of the dominant eigenvector of $\boldsymbol{A}$. To determine the eigenvalue corresponding to a given eigenvector, we can to use the following theorem, which is credited to the English physicist John William Rayleigh (1842-1919).

Theorem

If $\boldsymbol{u}$ is an eigenvector of the matrix $\boldsymbol{A}$, then its corresponding eigenvalue is given by:

$$\lambda = \frac{\boldsymbol{u}^T\boldsymbol{A}\boldsymbol{u}}{\boldsymbol{u}^T\boldsymbol{u}} \tag{A.2}$$

which is called **Rayleigh quotient**.

Proof : since $\boldsymbol{u}$ is an eigenvector of the matrix $\boldsymbol{A}$, then $\boldsymbol{A}\boldsymbol{u} = \lambda\boldsymbol{u}$ and we can write:

$$\frac{\boldsymbol{u}^T\boldsymbol{A}\boldsymbol{u}}{\boldsymbol{u}^T\boldsymbol{u}} = \frac{\boldsymbol{u}^T\lambda\boldsymbol{u}}{\boldsymbol{u}^T\boldsymbol{u}} = \frac{\lambda(\boldsymbol{u}^T\boldsymbol{u})}{\boldsymbol{u}^T\boldsymbol{u}} \tag{A.3}$$

□

The convergence of the power method to the dominant eigenvalue is implied by the following theorem:

Theorem

If $\boldsymbol{A} \in \mathbb{R}^{n\times n}$ is a diagonalisable matrix with a dominant eigenvalue, then there exists a non-zero vector $\boldsymbol{u}_0$ such that the sequence of vector given by:

$$\boldsymbol{A}\boldsymbol{u}_0\,,\boldsymbol{A}^2\boldsymbol{u}_0,\ \boldsymbol{A}^3\boldsymbol{u}_0,\ \ldots,\ \boldsymbol{A}^k\boldsymbol{u}_0,\ \ldots \tag{A.4}$$

approaches a multiple of the dominant eigenvector of $\boldsymbol{A}$.

Proof : since $\boldsymbol{A}$ is diagonalisable, there exist n linearly independent eigenvectors $\boldsymbol{u}_i$ with their corresponding eigenvalues λ_i. Let us assume that λ_1 and $\boldsymbol{u}_1$ are respectively the dominant eigenvalue and eigenvector. Since the n eigenvectors are linearly independent, they are a basis for $\mathbb{R}^n$. Therefore we can write a generic vector $\boldsymbol{u}_0 \in \mathbb{R}^n$ as a linear combination of the eigenvectors:

$$\boldsymbol{u}_0 = \sum_{i=1}^{n} c_i \boldsymbol{u}_i \tag{A.5}$$

Multiplying both sides of the equation by $\boldsymbol{A}$:

$$\boldsymbol{A}\boldsymbol{u}_0 = \boldsymbol{A}\sum_{i=1}^{n} c_i \boldsymbol{u}_i = \sum_{i=1}^{n} c_i \left(\boldsymbol{A}\boldsymbol{u}_i\right) = \sum_{i=1}^{n} c_i \lambda_i \boldsymbol{u}_i \tag{A.6}$$

Iterating the last multiplication, we obtain:

$$\boldsymbol{A}^k \boldsymbol{u}_0 = \sum_{i=1}^{n} c_i \left(\lambda_i^k \boldsymbol{u}_i\right) \tag{A.7}$$

which implies:

$$\boldsymbol{A}^k \boldsymbol{u}_0 = \lambda_1^k \left[c_1 \boldsymbol{u}_1 + \sum_{i=2}^{n} c_i \left(\frac{\lambda_i}{\lambda_1}\right) \boldsymbol{u}_i \right] \tag{A.8}$$

From the assumption of existence of the dominant eigenvalue, λ_1:

$$\frac{\lambda_i}{\lambda_1} < 1 \quad i = 2, \ldots n \tag{A.9}$$

As consequence:

$$\lim_{k \to +\infty} \left(\frac{\lambda_i}{\lambda_1}\right) = 0 \tag{A.10}$$

Expression (A.10) implies that the approximation $\boldsymbol{A}^k \boldsymbol{u}_0 \approx \lambda_1^k c_1 \boldsymbol{u}_1$ is valid if k is sufficiently large. Since $\boldsymbol{u}_1$ is the dominant eigenvector, it follows that any scalar multiple of $\boldsymbol{u}_1$ is also a dominant eigenvector.

□

The proof of the previous theorem is important because it provides some insights about the rate of convergence of the power method. If the eigenvalues are ordered such that:

$$|\lambda_1| > |\lambda_2| \geq |\lambda_3| \geq \cdots \geq |\lambda_n| \tag{A.11}$$

then the rate of convergence depends on the ratio $|\lambda_2|/|\lambda_1|$ (A.11) shows the main drawback of the power method, which is not able to compute the dominant eigenvalue in case the spectrum is clustered in a small area of the complex plane, since convergence could be extremely slow or even non-existent. Furthermore, this method is not able to compute a block of eigenvalues. Deflation schemes and/or block variants may be employed to compute more eigenvalues and spectral transformations may be used to accelerate convergence and focus on subset of eigenvalues (Larson, 2012). Other more efficient techniques, exploiting the power method sequence, to solve eigenproblems are discussed in the next sections.

A.2 Arnoldi Method

In this section we discuss the solution of eigenproblems by means of the Arnoldi method (Arnoldi, 1951), which belongs to a class of algorithms called Krylov subspace projection methods, which take advantage of the intricate structure of the sequence of vectors naturally produced by the power method. The sequence of vectors produced by the power method contains a considerable amount of information about the eigenvector directions, corresponding to more eigenvalues than the dominant one. The expansion coefficients of the vectors in the sequence evolve, in fact, in a very structured way. Therefore, a linear combination of these vectors can be constructed to enhance convergence to additional eigenvectors.
The first step is to consider the definition of a Krylov subspace:

Definition

Given a matrix $\boldsymbol{A} \in \mathbb{R}^{n\times n}$ and a vector $\boldsymbol{u}_1 \in \mathbb{R}^n$, we define **Krylov subspace** of order n the linear subspace spanned by the images of $\boldsymbol{u}_1$ under the first k powers of $\boldsymbol{A}$.

$$\mathcal{K}_k(\boldsymbol{A}, \boldsymbol{u}_1) = Span\{\boldsymbol{u}_1, \boldsymbol{A}\boldsymbol{u}_1, \boldsymbol{A}^2\boldsymbol{u}_1, \ldots, \boldsymbol{A}^{k-1}\boldsymbol{u}_1\} \tag{A.12}$$

It is reasonable to construct approximate eigenpairs by imposing a Galerkin condition:

Definition

A vector $\boldsymbol{x} \in \mathcal{K}_k(\boldsymbol{A}, \boldsymbol{u}_1)$ is called **Ritz vector** with its corresponding **Ritz value** θ if the Galerkin condition:

$$\langle \boldsymbol{w}, \boldsymbol{A}\boldsymbol{x} - \boldsymbol{x}\theta \rangle = 0 \quad \forall \boldsymbol{w} \in \mathcal{K}_k(\boldsymbol{A}, \boldsymbol{u}_1) \tag{A.13}$$

is satisfied.

There are some immediate consequences of this definition. Let $\boldsymbol{W}$ be a matrix whose columns are an orthonormal basis for $\mathcal{K}_k \equiv \mathcal{K}_k(\boldsymbol{A}, \boldsymbol{u}_1)$. Let us consider the orthogonal projector onto $\mathcal{K}_k$, $\mathcal{P} = \boldsymbol{W}\boldsymbol{W}^H$ and define $\hat{\mathbf{A}} \equiv \mathcal{P}\boldsymbol{A}\mathcal{P} = \boldsymbol{W}\boldsymbol{G}\boldsymbol{W}^{\boldsymbol{H}}$ where $\boldsymbol{G} \equiv \boldsymbol{W}^{\boldsymbol{H}}\boldsymbol{A}\boldsymbol{W}$. The following theorem can be shown:

Theorem

For all the quantities defined above,

- $(\boldsymbol{x}, \theta)$ is a Ritz pair $\iff$ $\boldsymbol{x} = \boldsymbol{W}\boldsymbol{s}$ with $\boldsymbol{G}\boldsymbol{s} = \boldsymbol{s}\theta$.
- $\|(\boldsymbol{I} - \mathcal{P})\boldsymbol{A}\boldsymbol{W})\| = \left\|(\boldsymbol{A} - \hat{\mathbf{A}})\boldsymbol{W})\right\| \leq \|(\boldsymbol{A} - \boldsymbol{M})\boldsymbol{W}\| \quad \forall \boldsymbol{M} \in \mathbb{C}^{n\times n} : \boldsymbol{M}\mathcal{K}_k \subset \mathcal{K}_k$
- The Ritz pairs $(\boldsymbol{x}, \theta)$ and the minimum value $\|(\boldsymbol{I} - \mathcal{P})\boldsymbol{A}\boldsymbol{W})\|$ are independent of the choice of the basis $\boldsymbol{W}$.

Proof: Omissis.

This theorem has important algorithmic consequences, in fact it can be shown that $\mathcal{K}_k$ is an invariant subspace for $\boldsymbol{A}$ if and only if the starting vector $\boldsymbol{u}_0$ is a linear combination of vectors spanning an invariant subspace of $\boldsymbol{A}$. An important example of this result can be deducted choosing $\boldsymbol{u}_0$ as a partial Shur decomposition of $\boldsymbol{A}$.

Theorem

Given $\boldsymbol{A} \in \mathbb{C}^{n\times n}$, then there is a unique matrix $\boldsymbol{Q}$ and an upper triangular matrix $\boldsymbol{R}$ such that

$$\boldsymbol{AQ} = \boldsymbol{QR} \tag{A.14}$$

This is called **Shur decomposition** and the diagonal element of $\boldsymbol{R}$ are the eigenvalues of $\boldsymbol{A}$.

Proof: Omissis.

A Schur decomposition is not unique, in fact the eigenvalues of the matrix $\boldsymbol{A}$ can appear on the diagonal of $\boldsymbol{R}$ in any order. Therefore for a specified set of k eigenvalues of $\boldsymbol{A}$, there is a Schur decomposition such that these k eigenvalues appear as the diagonal elements of the leading principal submatrix $\boldsymbol{R}_k$ associated to $\boldsymbol{R}$. If $\boldsymbol{Q}_k$ denotes the k columns of the corresponding unitary matrix $\boldsymbol{Q}$, then it is possible to obtain a *partial Schur decomposition* by equating these columns on both sides of (A.14):

$$\boldsymbol{AQ}_k = \boldsymbol{Q}_k\boldsymbol{R}_k \tag{A.15}$$

It is possible to write a partial Schur decomposition of $\boldsymbol{A}$ and use as the initial vector of the Kylov subspace as $\boldsymbol{u}_0 = \boldsymbol{Q}_k\boldsymbol{s}$. We can construct a convenient orthonormal basis $\boldsymbol{U} = \boldsymbol{WQ}$,which provides a convenient choice to build the basis vectors. A $k\times k$ unitary $\boldsymbol{Q}$ can be constructed using standard Householder transformations such that $\boldsymbol{u}_0 = \boldsymbol{Ue}_1$ and $\boldsymbol{H} = \boldsymbol{Q}^H\boldsymbol{GQ}$, where $\boldsymbol{H}$ is an upper-Hessenberg matrix with non-negative subdiagonal elements[1]. It is also possible to show that in this basis:

$$\boldsymbol{AU} = \boldsymbol{UH} + \boldsymbol{fe}_k^T \quad \text{where} \quad \boldsymbol{f} = \gamma\hat{p}(\boldsymbol{A})\boldsymbol{u}_1 \tag{A.16}$$

with $\boldsymbol{U}^H\boldsymbol{f} = \boldsymbol{0}$ implied by the projection property and $\hat{p}(\lambda) = \det(\lambda\boldsymbol{I} - \boldsymbol{H})$, where $\gamma \in \mathbb{R}$. If it is possible to obtain $\boldsymbol{u}_1$ as a linear combination of k eigenvectors of $\boldsymbol{A}$, then $\boldsymbol{f} = 0$ and $\boldsymbol{U}$ is an orthonormal basis for an invariant subspace of $\boldsymbol{A}$. Hence, the Ritz values of $\boldsymbol{sH}$ are the eigenvalues of $\boldsymbol{A}$ and the corresponding Ritz vectors are the eigenvectors. This idea

[1] an upper Hessenberg matrix is a matrix that has zero entries below the first subdiagonal.

of using a partial Schur decomposition for the initial vector of the Krylov subspace, which leads to (A.16), is the starting point of the Arnoldi method.

A.2.1 Arnoldi factorisation

Definition

Given $\boldsymbol{A} \in \mathbb{C}^{n\times k}$, we define a **k-step Arnoldi factorisation** a relation of the form:

$$\boldsymbol{A}\boldsymbol{U}_k = \boldsymbol{U}_k\boldsymbol{H}_k + \boldsymbol{f}_k\boldsymbol{e}_k^T \tag{A.17}$$

where $\boldsymbol{U}_k \in \mathbb{C}^{n\times k}$ has orthonormal columns, $\boldsymbol{U}_k^H\boldsymbol{f}_k = 0$, and $\boldsymbol{H}_k \in \mathbb{C}^{k\times k}$. If $\boldsymbol{A}$ is hermitian then $\boldsymbol{H}_k$ is real, symmetric and tridiagonal and the relation is called **k-step Lanczos factorisation** of $\boldsymbol{A}$.

An alternative way of writing the factorisation (A.17) is:

$$\boldsymbol{A}\boldsymbol{U}_k = (\boldsymbol{U}_k, \boldsymbol{u}_{k+1})\begin{pmatrix}\boldsymbol{H}_k \\ \beta_k\boldsymbol{e}_k^T\end{pmatrix}, \quad \text{where} \quad \beta_k = \|\boldsymbol{f}_k\| \quad \text{and} \quad \boldsymbol{u}_{k+1} = \frac{1}{\beta_k}\boldsymbol{f}_k \tag{A.18}$$

If $\boldsymbol{H}_k\boldsymbol{s} = \boldsymbol{s}\theta$ then the vector $\boldsymbol{x} = \boldsymbol{U}_k\boldsymbol{s}$ satisfies:

$$\|\boldsymbol{A}\boldsymbol{x} - \boldsymbol{x}\theta\| = \|(\boldsymbol{A}\boldsymbol{U}_k - \boldsymbol{U}_k\boldsymbol{H}_k)\,\boldsymbol{s}\| = \left|\beta_k\boldsymbol{e}_k^T\boldsymbol{s}\right| \tag{A.19}$$

The value $\left|\beta_k\boldsymbol{e}_k^T\boldsymbol{s}\right|$ is called *Ritz estimate* of the Ritz pair $(\boldsymbol{x}, \theta)$ and is an approximate eigenpair of $\boldsymbol{A}$. If $(\boldsymbol{x}, \theta)$ is a Ritz pair then:

$$\theta = \boldsymbol{s}^H\boldsymbol{H}_k\boldsymbol{s} = (\boldsymbol{U}_k\boldsymbol{s})^H\boldsymbol{A}(\boldsymbol{U}_k\boldsymbol{s}) = \boldsymbol{x}^H\boldsymbol{A}\boldsymbol{x} \tag{A.20}$$

is the Rayleigh quotient assuming $\|\boldsymbol{s}\| = 1$ and the residual $\boldsymbol{r}(\boldsymbol{x}) \equiv \boldsymbol{A}\boldsymbol{x} - \boldsymbol{x}\theta$ is:

$$\|\boldsymbol{r}(\boldsymbol{x})\| = \left|\beta_k\boldsymbol{e}_k^T\boldsymbol{s}\right| \tag{A.21}$$

The main goal of Arnoldi method is to drive $\|\boldsymbol{r}(\boldsymbol{x})\| \to 0$ so that the Ritz pair $(\boldsymbol{x}, \theta)$ approximates an eigenpair of $\boldsymbol{A}$. When $\boldsymbol{f} = 0$, $\boldsymbol{U}$ is an invariant subspace of $\boldsymbol{A}$ and the Ritz values and vectors are precisely eigenvalues

and eigenvectors of $\boldsymbol{A}$. An efficient algorithm to compute numerically the Arnoldi factorisation is the following one:

Algorithm 1 The k-step Arnoldi factorisation

Input: $(\boldsymbol{A}, \boldsymbol{u}_0)$

Put $\boldsymbol{u}_0 = \boldsymbol{u}/\left\|\boldsymbol{u}_0\right\|$; $\quad \boldsymbol{w} = \boldsymbol{A}\boldsymbol{u}_0$; $\quad \alpha_1 = \boldsymbol{u}_0^H \boldsymbol{w}$;

Put $\boldsymbol{f}_0 \leftarrow \boldsymbol{w} - \boldsymbol{u}_0\alpha$; $\quad \boldsymbol{U}_0 \leftarrow (\boldsymbol{u}_0)$; $\quad \boldsymbol{H}_0 \leftarrow (\alpha_0)$;

for $j = 1, 2, \ldots, k-1$ **do**

$\beta_j = \left\|\boldsymbol{f}_j\right\|$; $\quad \boldsymbol{u}_{j+1} \leftarrow \boldsymbol{f}_j/\beta_j$;

$\boldsymbol{U}_{j+1} \leftarrow (\boldsymbol{U}_j, \boldsymbol{u}_{j+1})$; $\quad \hat{\mathbf{H}}_j \leftarrow \begin{pmatrix} \boldsymbol{H}_j \\ \beta_j \boldsymbol{e}_j^T \end{pmatrix}$;

$\boldsymbol{w} \leftarrow \boldsymbol{A}\boldsymbol{u}_{j+1}$;

$\boldsymbol{h} \leftarrow \boldsymbol{U}_{j+1}^H \boldsymbol{w}$; $\quad \boldsymbol{f}_{j+1} \leftarrow \boldsymbol{w} - \boldsymbol{U}_{j+1}\boldsymbol{h}$;

$\boldsymbol{H}_{j+1} \leftarrow (\hat{\mathbf{H}}_j, \boldsymbol{h})$;

end

In exact arithmetic, the columns of $\boldsymbol{U}$ form an orthonormal basis for the Krylov subspace, however in finite precision arithmetic, explicit re-orthogonalisation of the columns of $\boldsymbol{U}$ is necessary. This task can be accomplished a the Gram-Schmidt process with t-steps of iterative refinement (Daniel *et al.*, 1976).
The Arnoldi factorisation is entirely dependent on the choice of the starting vector $\boldsymbol{u}_0$ and it is uniquely determined by the choice of $\boldsymbol{u}_0$ until a subdiagonal element of $\boldsymbol{H}$ is zero. At this point an invariant subspace has been computed and the factorisation continues with a new choice of the starting vector.

A.2.2 Implicit Restarting technique

Generally we want the starting vector $\boldsymbol{u}_0$ to be prominent in the subspace spanned by the desired eigenvectors, with very small components in the other directions. As we improve the knowledge of the desired eigenvectors, we would like to adaptively refine $\boldsymbol{u}_0$ to be a linear combination of the approximate eigenvectors and restart the Arnoldi factorisation with this new vector. A convenient and stable way to do this operation without explicitly computing a new Arnoldi factorisation is given by the implicitly restarted Arnoldi method (IRAM), which is based on an implicitly shifted QR factorisation (Sorensen, 1992).
Let us consider a m-step Arnoldi factorisation and let us apply an arbitrary complex shift μ to $\boldsymbol{H}_m \in \mathbb{C}^{m\times m}$. Since the dimensions of $\boldsymbol{H}_m$ are relatively small, we can factor $\boldsymbol{H}_m - \mu\boldsymbol{I} = \boldsymbol{Q}_m\boldsymbol{R}_m$. The following equivalent

statements can be obtained:

$$\boldsymbol{A}\boldsymbol{U}_m = \boldsymbol{U}_m\boldsymbol{H}_m + \boldsymbol{f}_m\boldsymbol{e}_m^T \tag{A.22a}$$

$$(\boldsymbol{A} - \mu\boldsymbol{I})\boldsymbol{U}_m - \boldsymbol{U}_m(\boldsymbol{H}_m - \mu\boldsymbol{I}) = \boldsymbol{f}_m\boldsymbol{e}_m^T \tag{A.22b}$$

$$(\boldsymbol{A} - \mu\boldsymbol{I})\boldsymbol{U}_m - \boldsymbol{U}_m\boldsymbol{Q}_m\boldsymbol{R}_m = \boldsymbol{f}_m\boldsymbol{e}_m^T \tag{A.22c}$$

$$(\boldsymbol{A} - \mu\boldsymbol{I})\boldsymbol{U}_m\boldsymbol{Q}_m - \boldsymbol{U}_m\boldsymbol{Q}_m\boldsymbol{R}_m\boldsymbol{Q}_m = \boldsymbol{f}_m\boldsymbol{e}_m^T\boldsymbol{Q}_m \tag{A.22d}$$

$$\boldsymbol{A}(\boldsymbol{U}_m\boldsymbol{Q}_m) - (\boldsymbol{U}_m\boldsymbol{Q}_m)(\boldsymbol{R}_m\boldsymbol{Q}_m + \mu\boldsymbol{I}) = \boldsymbol{f}_m\boldsymbol{e}_m^T\boldsymbol{Q}_m \tag{A.22e}$$

$$\boldsymbol{A}\boldsymbol{U}_m^+ = \boldsymbol{U}_m^+\boldsymbol{H}_m^+ + \boldsymbol{f}_m\boldsymbol{e}_m^T\boldsymbol{Q}_m \tag{A.22f}$$

where $\boldsymbol{U}_m^+ = \boldsymbol{U}_m\boldsymbol{Q}_m$ has orthonormal columns since it is the product of the $\boldsymbol{U}_m$ and an orthogonal matrix $\boldsymbol{Q}$. It also turns out that $\boldsymbol{H}_m^+ = \boldsymbol{R}_m\boldsymbol{Q}_m + \mu\boldsymbol{I}$ is an upper Hessenberg matrix. Therefore, a complex shifting μ does not alter the structure of the Arnoldi factorisation. The result of these operations is that the first column of $\boldsymbol{U}_m^+$ is equal to $(\boldsymbol{A} - \mu\boldsymbol{I})\boldsymbol{u}_1$, where $\boldsymbol{u}_1$ is the first column of $\boldsymbol{U}$. It is possible to extend this procedure to a $(k+p)$-step Arnoldi factorisation:

$$\boldsymbol{A}\boldsymbol{U}_{k+p} = \boldsymbol{U}_{k+p}\boldsymbol{H}_{k+p} + \boldsymbol{f}_{k+p}\boldsymbol{e}_{k+p}^T \tag{A.23}$$

When p-implicit shifts are then applied to the factorisation, then the following new factorisation is obtained:

$$\boldsymbol{A}\boldsymbol{U}_{k+p}^+ = \boldsymbol{U}_{k+p}^+ + \boldsymbol{f}_{k+p}\boldsymbol{e}_{k+p}^T\boldsymbol{Q} \tag{A.24}$$

where $\boldsymbol{U}^+ = \boldsymbol{U}_{k+p}\boldsymbol{Q}$, $\boldsymbol{H}^+ = \boldsymbol{Q}^H\boldsymbol{H}_{k+p}\boldsymbol{Q}$ and $\boldsymbol{Q} = \boldsymbol{Q}_1\boldsymbol{Q}_2\ldots\boldsymbol{Q}_p$ (each matrix $\boldsymbol{Q}_i$ is associated to the factorisation $(\boldsymbol{H} - \mu\boldsymbol{I}) = \boldsymbol{Q}_i\boldsymbol{R}_i$).The first $k-1$ entries of $\boldsymbol{e}_{k+p}\boldsymbol{Q}$ are zero, so that a new k-step Arnoldi factorisation can be obtained by equating the first k columns on each side:

$$\boldsymbol{A}\boldsymbol{U}_k^+ = \boldsymbol{U}_k^+\boldsymbol{H}_k^+ + \boldsymbol{f}_k^+\boldsymbol{e}_k^T \tag{A.25}$$

We can now iterate the process of applying shifts and then condensing. The payoff is that every iteration implicitly applies a p^{th}-degree polynomial in $\boldsymbol{A}$ to the initial vector $\boldsymbol{u}_0$. The roots of the polynomial are the p-shifts that were applied to the factorisation. Therefore, we can efficiently filter the starting vector $\boldsymbol{u}_0$ so that its components are prominent in the direction of the desired eigenvectors. We can then present the full implicitly restarted Arnoldi method:

Algorithm 2 Implicitly restarted Arnoldi method

Input:

- matrix $\boldsymbol{A} \in \mathbb{C}^{n \times n}$;
- k, the number of eigenvalues to be computed;
- p, the number of implicit shifts to apply to the Arnoldi factorisation at each iteration;
- criterion to determine the requested eigenvalue (i.e. largest magnitude);
- a starting vector $\boldsymbol{u}_0$;
- requested tolerance τ.

Result: $(\boldsymbol{x}_k, \lambda_k)$, approximation of the k-eigenvalues of $\boldsymbol{A}$.

Generate the k-step Arnoldi factorisation starting from $\boldsymbol{u}_0$.

for $j = 1, 2, \ldots,$ *convergence* **do**

  Extend the k-step Arnoldi factorisation to a $k + p$ steps.

  Let $\boldsymbol{q} = \boldsymbol{e}_{k+p}$.

  Sort the spectrum of $\boldsymbol{H}$, $\sigma(\boldsymbol{H})$ and take $\mu_1, \mu_2, \ldots, \mu_p$ to be the p "worst" eigenvalues.

  for $j = 1, 2, \ldots, p$ **do**

    Factor $\boldsymbol{H} - \mu_j \boldsymbol{I} = \boldsymbol{Q}\boldsymbol{R}$.

    $\boldsymbol{H} \leftarrow \boldsymbol{Q}^H \boldsymbol{H} \boldsymbol{Q}$.

    $\boldsymbol{U} \leftarrow \boldsymbol{U}\boldsymbol{Q}$.

    $\boldsymbol{q} \leftarrow \boldsymbol{q}^H \boldsymbol{Q}$.

  end

  $\boldsymbol{f} \leftarrow \boldsymbol{U}(:, 1:k) \cdot \boldsymbol{H}(k+1, k) + \boldsymbol{f} \cdot \boldsymbol{q}(k)$.

  Take the first k-column on each side of the factorisation to get:

  $\boldsymbol{U} = \boldsymbol{U}(:, 1:k)$; $\boldsymbol{H} = \boldsymbol{H}(1:k, 1:k)$.

  Take as eigenpair approximation the Ritz pairs of the problem.

end

The repeated update of the starting vector $\boldsymbol{u}_0$ through the implicit restarting method enhances the components of this vector to be prominent in the directions of the desired eigenvectors, damping the unwanted ones. Let us express $\boldsymbol{u}_0$ as a linear combination of eigenvectors $\boldsymbol{x}_k$ of $\boldsymbol{A}$:

$$\boldsymbol{u}_0 = \sum_{k=0}^{k=n} \gamma_k \boldsymbol{x}_k \tag{A.26}$$

Each shift cycle results into the implicit application of a polynomial in $\boldsymbol{A}$ of degree p to the starting vector:

$$\boldsymbol{u}_0 \leftarrow \psi(\boldsymbol{A})\boldsymbol{u}_0 \quad \text{with} \quad \psi(\lambda) = \prod_{i=1}^{p}(\lambda - \mu_i) \tag{A.27}$$

Therefore:

$$\psi(\boldsymbol{A})\boldsymbol{u}_0 = \sum_{j=1}^{n} \gamma_j \boldsymbol{x}_j \psi(\lambda_j) \tag{A.28}$$

If the same polynomial is applied each time, then after l iteration, the j-th original expansion coefficient is attenuated by the following factor:

$$\left(\frac{\psi(\lambda_j)}{\psi(\lambda_1)}\right)^l, \tag{A.29}$$

where the eigenvalues have been ordered according to the decreasing values of $|\psi(\lambda_j)|$. The leading k eigenvalues become dominant in the expansion and the remaining ones become less significant as the iterations proceed. Adaptive choices of shifts yield to the isolation of the specified components in this expansion, resulting in better approximations.

A.3 Shift-and-invert

If the eigenvalues to be computed are requested to be close to a specific shift σ of the spectrum, convergence could be rather slow. The eigenvectors corresponding to the eigenvalues of largest magnitude would resurface despite the attempt to eliminate them from the Arnoldi basis. The accumulated round-off error during one iteration, in the direction of the eigenvector of largest magnitude, could be enough to cause this eigenvector to resurface in the next iteration. To avoid this issue, it is possible to use a shift-and-invert technique to compute the k-eigenvalues close to a selected shift σ. In this case, the k-eigenvalues of the matrix $(\boldsymbol{A} - \sigma\boldsymbol{I})^{-1}$ must be evaluated and then it is possible to recover the desired eigenvalues using the spectral transformation:

$$\lambda_j = \sigma + \frac{1}{\nu_j} \quad \text{where} \quad \nu_j = \frac{1}{\lambda_j - \sigma} \tag{A.30}$$

A.4 Implementation of the Arnoldi method

In this thesis, the Implicitly Restarted Arnoldi Method has been used in the code by means of `ARPACK` (ARnoldi PACKage, Lehoucq *et al.* 1998), a

collection of Fortran 77 routines which are capable of solving large-scale Hermitian, non-Hermitian, standard or generalised eigenvalue problems. The main advantage of using this library is that it is possible to compute a desired number of eigenvalues with a user-defined criterion (largest real/imaginary part, largest absolute value, largest algebraic value for the symmetric case, etc.). Since `ARPACK` requires just the action of the operator on the a vector is required, its use is particularly attractive when time-stepping algorithms are adopted, because no evolution matrix is generally built. Furthermore, `ARPACK` requires just a fix pre-determined storage, which is generally $n \cdot \mathcal{O}(k) + \mathcal{O}(k^2)$, where k is the number of eigenvalues and n the dimension of the eigenproblem. An alternative modified Arnoldi method method, referred as "Modified Arnoldi" (Barkley *et al.* 2008) was implemented in the present work and it was verified to compare well with `ARPACK`, in fact the differences of the dominant eigenvalues were generally found to be of order less than 10^{-5}. The main advantage of the Modified Arnoldi Algorithm is that it uses just basic library calls and it is straightforward to evaluate how far the eigenvalues are from convergence.
Regarding the starting vector $\boldsymbol{u}_0$, it is generated using a quasi-random routine and the divergence-free of the velocity is enforced by the time integration algorithm.